UNIVERSIDADE FEDERAL DE SANTA MARIA
CENTRO DE CIÊNCIAS NATURAIS E EXATAS
PROGRAMA DE PÓS-GRADUAÇÃO EM FÍSICA

Rafael Maroneze

SIMULAÇÃO NUMÉRICA DOS REGIMES DA CAMADA LIMITE ESTÁVEL.

Santa Maria, RS
2019

Rafael Maroneze

SIMULAÇÃO NUMÉRICA DOS REGIMES DA CAMADA LIMITE ESTÁVEL.

Tese de Doutorado apresentada ao Programa de Pós-Graduação em Física, Área de Concentração em Áreas clássicas da fenomenologia e suas aplicações, da Universidade Federal de Santa Maria (UFSM, RS), como requisito parcial para obtenção do grau de **Doutor em Física**.

ORIENTADOR: Prof. Otávio Costa Acevedo

Santa Maria, RS
2019

Maroneze, Rafael
SIMULAÇÃO NUMÉRICA DOS REGIMES DA CAMADA LIMITE ESTÁVEL. / Rafael Maroneze.- 2019.
156 p.; 30 cm

Orientador: Otávio Costa Acevedo
Tese (doutorado) - Universidade Federal de Santa Maria, Centro de Ciências Naturais e Exatas, Programa de Pós-Graduação em Física, RS, 2019

1. Turbulência 2. Camada limite estável I. Costa Acevedo, Otávio II. Título.

Sistema de geração automática de ficha catalográfica da UFSM. Dados fornecidos pelo autor(a). Sob supervisão da Direção da Divisão de Processos Técnicos da Biblioteca Central. Bibliotecária responsável Paula Schoenfeldt Patta CRB 10/1728.

Endereço: Rua Agrimensor João Alves dos Santos, 55
Fone (0xx) 55 99946 4846; End. Eletr.: rafaelmaroneze@gmail.com

Rafael Maroneze

SIMULAÇÃO NUMÉRICA DOS REGIMES DA CAMADA LIMITE ESTÁVEL.

Tese de Doutorado apresentada ao Programa de Pós-Graduação em Física, Área de Concentração em Áreas clássicas da fenomenologia e suas aplicações, da Universidade Federal de Santa Maria (UFSM, RS), como requisito parcial para obtenção do grau de **Doutor em Física**.

Aprovado em 11 de novembro de 2019:

_____

Otávio Costa Acevedo, Dr. (UFSM)
(Presidente/Orientador)

_____

Gervásio Annes Degrazia, Dr. (UFSM)

_____

José Carlos Merino Mombach, Dr. (UFSM)

_____

Maria Assunção Faus da Silva Dias, Phd. (USP) (videoconferência)

_____

Nelson Luís da Costa Dias, Dr. (UFPR) (videoconferência)

Santa Maria, RS
2019

DEDICATÓRIA

à meus pais, avós e irmão.

AGRADECIMENTOS

À Universidade Federal de Santa Maria pelo suporte ao longo desses 9 anos, o que possibilitou eu cursar e concluir graduação, mestrado e doutorado.

À CAPES pelo financiamento dessa pesquisa, mas também agradeço pelo suporte financeiro dado à grande parte da pesquisa brasileira.

À minha família que sempre me apoiou e incentivou ao longo da minha formação. Gostaria de agradecer em especial a meus pais Valmir e Rosa que sempre me apoiaram e ajudaram quando mais precisava. Também não posso esquecer de agradecer ao meu colega de quarto e irmão Adriano pelo seu companheirismo, e é claro aos meus avós Mario e Maria, que sempre estiveram ao meu lado.

Aos professores Otávio Costa Acevedo e Felipe Denardin Costa pelas ideias, dedicação, confiança e amizade que foram fundamentais no desenvolvimento deste trabalho. Não existem palavras que possam expressar minha gratidão a vocês.

Aos meus amigos e colegas do Grupo de Turbulência Atmosférica de Santa Maria (GruTA): Daiaa, Ivan Mauricio, Michel e Osmar.

Aos meus amigo Viviane Guerra, Giuliano Demarco, Franciano Scremin Puhales, Luis Gustavo Nogueira Martins e Alessandro Eugenio Denardin Pozzobon, Vagner Anabor, Gervásio Annes Degrazia e Luca Mortarini.

Aos membros da comissão examinadora pelas contribuições nesse trabalho.

O único lugar onde o sucesso vem antes do trabalho é no dicionário.

(Albert Einstein)

RESUMO

SIMULAÇÃO NUMÉRICA DOS REGIMES DA CAMADA LIMITE ESTÁVEL.

AUTOR: Rafael Maroneze
ORIENTADOR: Otávio Costa Acevedo

Estudos recentes mostraram que a camada limite estável (CLE) apresenta dois regimes distintos. No regime pouco estável a turbulência é contínua e relações de similaridade são válidas e no muito estável a turbulência é intermitente ou ausente e relações de similaridade não funcionam. Na presente tese, são abordadas as dificuldades de simular numericamente os dois regimes e a transição entre eles. O estudo é dividido em 4 artigos. No primeiro deles,] diferentes modelos numéricos, são comparados quanto à sua capacidade de reproduzir dois regimes da CLE. Esse artigo indica que a inclusão de equações mais prognósticas aos modelos fazem com os regimes da CLE sejam reproduzidos de uma maneira mais semelhantes às observadas na natureza. No segundo artigo, a transição do regime pouco estável para muito estável, é analisada através dos dados provenientes de uma torre de 140 metros situada em Linhares, no estado de Espírito Santos. Foi observado que a transição entre os regimes era precedida por um resfriamento abrupto da camada, acompanhado de uma redução na energia cinética turbulenta, e da intensidade da velocidade do vento. Além disso, foi observado que o máximo do fluxo de calor, em módulo, ocorre no regime pouco estável. No terceiro artigo, transições semelhantes, às apresentadas no segundo artigo, foram investigadas com auxilio de um modelo numérico de segunda ordem, em que a transição é impulsionada pelo decréscimo da intensidade do vento no topo do domínio. Nesse artigo é mostrado que os processos radiativos e propriedades térmicas da superfície do solo são determinantes para transição entre os regimes da CLE. No quarto artigo, diferentes parametrizações de camada limite planetária presentes no "Weather Research and Forecasting - Single Column Model" foram comparados e avaliados quanto a sua capacidade de simular os regimes da CLE. Nesse artigo foi mostrado que ambos os esquemas Mellor-Yamada-Nakanishi-Niino de nível 2.5 apresentam o melhor desempenho, conseguindo resolver tanto o regime pouco estável quanto o regime muito estável. Porém, a transição entre esses regimes ocorre sob condições de vento geostrófico de menor intensidade que observado. Os resultados apresentados no presente trabalho indicam que o fluxo de calor exerce um grande controle nos regimes da camada limite estável. Logo, a inclusão de uma equação prognóstica para o fluxo de calor nos esquemas de turbulência, presentes no WRF, significaria um importante avanço.

Palavras-chave: Turbulência. Camada limite estável. Regimes. Fluxos turbulentos.

ABSTRACT

NUMERICAL SIMULATION OF THE STABLE BOUNDARY LAYER REGIMES.

AUTHOR: Rafael Maroneze
ADVISOR: Otávio Costa Acevedo

Recent studies have shown that the stable boundary layer (SBL) presents two distinct regimes. In the weakly stable regime, turbulence is continous and similarity relationships are valid, while in the very stable regime turbulence is intermittent or absent and similarity relationships do not work properly. In the present thesis, the difficulties associated with the numerical simulation of both regimes and transition between them are addressed. This study has been divided into 4 articles. In the first article different numerical models, are compared for their ability to reproduce the two SBL regimes. This paper indicates that the inclusion of more prognostic equations in the models cause the SBL regimes to be reproduced more similarly to what is observed in nature. In the second article, the transition from the weakly stable to the very stable regime is analyzed through data from a 140-meter tower located in Linhares, Espirito Santos state. It was observed that the transition between the regimes was preceded by an abrupt cooling of the layer, accompanied by a reduction in turbulent kinetic energy, and wind speed intensity. Also, it has been observed that the maximum absolute heat flux occurs in the weakly stable regime. In the third article, similar transitions to those presented in the second article were investigated with a second-order numerical model, where the transition is driven by decreasing wind intensity at the top of the domain. In this paper, it is shown that the radiative processes and thermal properties of the soil are determinant for the transition between SBL regimes. In the fourth article, different planetary boundary layer parameterizations in the Weather Research and Forecasting - Single Column Model have been compared and evaluated for their ability to simulate SBL regimes. In this article, it has been shown that both 2.5-level Mellor-Yamada-Nakanishi-Niino have the best performance both in the weakly and the very stable regime. However, the transition between these regimes occurs under lower geostrophic wind than observed in nature. The results indicate that the heat flux exerts large control in the stable boundary layer regimes. Therefore, the inclusion of a prognostic equation for heat flux in the WRF turbulence schemes would be an important advance in the future developments.

Keywords: Turbulence. Stable boundary layer. Regimes. Turbulence flux

LISTA DE ABREVIATURAS E SIGLAS

$\overline{u}$	Componente zonal do vento
$\overline{v}$	Componente meridional do vento
ψ	Direção do vento
l	Comprimento de mistura
ω	Velocidade angular da terra
κ	Constante de Von Kármám
$\overline{e}$	Energia cinética turbulenta
$\overline{\theta}$	Temperatura potencial do ar
$\overline{\theta_g}$	Temperatura do solo
$\overline{u'^2}$	Componente zonal da variância da velocidade do vento
$\overline{v'^2}$	Componente meridional da variância da velocidade do vento
$\overline{w'^2}$	Componente vertical da variância da velocidade do vento
$\overline{\theta'^2}$	Variância da temperatura potencial
K_m	Difusividade turbulenta de momentum
K_H	Difusividade turbulenta de calor
u_g	Componente zonal do vento geostrófico
v_g	Componente meridional do vento geostrófico
Q_c	Cobertura de nuvens
u_*	Velocidade de fricção
θ_*	Escala de temperatura
c_g	Capacidade térmica da superfície por unidade de área
H_0	Fluxo de calor sensível superficial
$I_\downarrow$	Radiação de onda longa proveniente da atmosfera
Ri_g	Número de Richardson gradiente

Ri_f	Número de Richardson fluxo
$\overline{w'\theta'}$	Fluxo de energia na forma de calor sensível
$\overline{u'w'}$	Componente zonal do fluxo de momentum
$\overline{v'w'}$	Componente meridional do fluxo de momentum
V_{TKE}	Escala de velocidade turbulenta

SUMÁRIO

1 INTRODUCAO 19
2 EQUAÇÕES BÁSICAS DA CLP 31
2.0.1 Equação de estado 31
2.0.2 Conservação da massa (Equação da continuidade) 31
2.0.3 Segunda Lei de Newton 32
2.0.4 Conservação da energia térmica (1º lei da termodinâmica) 33
2.0.5 Equações médias 33
2.1 PROBLEMA DO FECHAMENTO 37
3 ARTIGO 1 - SIMULATING THE REGIME TRANSITION OF THE STABLE BOUNDARY LAYER USING DIFFERENT SIMPLIFIED MODELS 39
4 ARTIGO 2 - THE NOCTURNAL BOUNDARY LAYER TRANSITION FROM WEAKLY TO VERY STABLE. PART I: OBSERVATIONS 57
5 ARTIGO 3 - THE NOCTURNAL BOUNDARY LAYER TRANSITION FROM WEAKLY TO VERY STABLE. PART II: NUMERICAL SIMULATION WITH A SECOND-ORDER MODEL 73
6 ARTIGO 4 - HOW IS THE TWO-REGIME STABLE BOUNDARY LAYER SOLVED BY THE DIFFERENT PBL SCHEMES IN WRF 89
7 DISCUSSÃO 129
8 CONCLUSÕES 137
ANEXO A – ENERGIA CINÉTICA TURBULENTA 141
ANEXO B – FLUXO DE CALOR SENSíVEL 147
ANEXO C – VARIÂNCIA DE TEMPERATURA 151
REFERÊNCIAS BIBLIOGRÁFICAS 153

1 INTRODUCAO

A camada limite planetária (CLP) é a parte da troposfera onde o escoamento do fluido e os fluxos de momentum, energia na forma de calor sensível e outros são influenciados pela presença da superfície terrestre, que os torna turbulentos. A turbulência, por sua vez, tem caráter altamente difusivo, sendo um processo bastante eficiente no transporte e na mistura de quantidades ao longo da CLP. Assim, a turbulência faz com que a presença da superfície terrestre seja efetivamente sentida até o topo da CLP, que pode ser da ordem de quilômetros.

Os escoamentos turbulentos são caraterizados por uma enorme variabilidade tanto espacial como temporal das variáveis físicas que os descrevem. Ao observar a figura 1.1 pode-se ver esta variabilidade temporal para as três componentes do vento e a temperatura. As flutuações ocorrem em torno de uma média bem definida, sendo em geral proporcional à intensidade da turbulência.

Figura 1.1 – Representa a evolução temporal das componentes do vento e da temperatura potencial de um escoamento atmosférico noturno acima de uma floresta de araucária localizada em São João do Triunfo, Paraná.

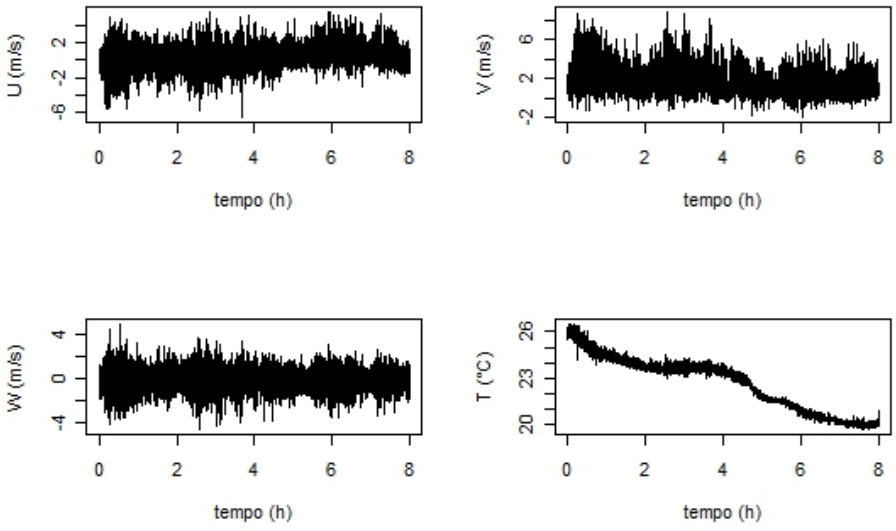

A estatística desempenha um papel fundamental no estudo de turbulência na CLP. Esta ferramenta permite decompor as variáveis associadas aos escoamentos em uma parte média e outra turbulenta (Decomposição de Reynolds, como por exemplo, $u = \overline{u}+u'$). Com isto, alguns momentos estatísticos representam quantidades com significado físico bem definido. Por exemplo, as covariâncias estatísticas entre variáveis do escoamento e componentes da velocidade do vento estão relacionadas aos fluxos turbulentos de determinadas quantidades, como por exemplo $\overline{w'\theta'}$, covariância entre a componente vertical da velocidade e a temperatura potencial, está associada ao fluxo vertical de energia na forma

de calor sensível através da relação $H = \rho c_p \overline{w'\theta'}$.

A energia cinética turbulenta (ECT) é definida como energia cinética das flutuações turbulentas de velocidade por unidade de massa e é dada por $\overline{e} = \frac{1}{2}(\overline{u'^2} + \overline{v'^2} + \overline{w'^2})$, onde $\overline{u'^2}, \overline{v'^2}$ e $\overline{w'^2}$ representam as variâncias das três componentes turbulentas do vento. Isto evidencia a importância da estatística no presente estudo, citada no parágrafo anterior. A ECT é uma das quantidades mais importantes utilizadas no estudo de turbulência na camada limite (STULL, 1988).

Durante o dia, a superfície do solo é aquecida pela radiação eletromagnética de onda curta proveniente do sol, deixando a temperatura do solo maior que a temperatura da atmosfera. Isto acarreta o surgimento de um fluxo de energia na forma de calor sensível do solo para a atmosfera, que aquece as camadas de ar adjacentes ao solo e as torna menos densas que as superiores, dando início a um movimento convectivo. Esse processo está associado à produção térmica de turbulência. Durante o dia, há também a produção mecânica de turbulência devido ao cisalhamento do vento. A camada limite que se desenvolve durante o dia é caracterizada pela produção térmica e mecânica de turbulência e é denominada camada limite convectiva (CLC). A altura dessa camada é da ordem de um quilômetro.

Ao pôr do sol, o fluxo de energia na forma de calor sensível inverte o sinal, passando a ser da atmosfera para a superfície do solo. Isso ocorre porque a superfície do solo esfria-se mais rapidamente que a atmosfera, devido à radiação eletromagnética de onda longa emitida pela superfície exceder a emissão correspondente da atmosfera para a superfície. Com isso, os níveis inferiores ficam com uma temperatura menor que os superiores e qualquer movimento ascendente tende a ser desacelerado devido a ação das forças de empuxo. A atuação das forças de empuxo tornam a camada estável, ou seja, uma parcela de fluido que por algum motivo é deslocada verticalmente de baixo para cima encontra regiões mais quentes e portanto menos densas, sendo forçada a descer. O processo descrito anteriormente representa à destruição térmica de turbulência. A camada acima da superfície caracterizada pelos resquícios e pela dissipação da CLC é denominada camada limite residual.

Junto à superfície, a camada limite que se desenvolve durante a noite e que é caracterizada pela destruição térmica e pela produção mecânica de turbulência é denominada camada limite estável (CLE).

Muitos estudos, tanto observacionais (MALHI, 1995; OHYA; NEFF; MERONEY, 1997; MAHRT, 1998; ACEVEDO; FITZJARRALD, 2003; SUN et al., 2012; ACEVEDO et al., 2016; LAN et al., 2018; ACEVEDO et al., 2019) quanto de modelagem numérica (MCNIDER et al., 1995; WIEL et al., 2002b; COSTA et al., 2011; MARONEZE et al., 2019) evidenciam a existência de dois regimes distintos na camada limite estável. A CLE é usualmente classificada como muito estável ou pouco estável, mas estas classificações podem variar entre os estudos (MAHRT, 1998).

O regime pouco estável normalmente ocorre em condições de ventos intensos e/ou com uma cobertura de nuvens significativa, caracterizando uma camada limite quase neutra ou pouco estratificada. Nesse regime, a turbulência é bem desenvolvida e contínua tanto no espaço quanto no tempo sendo, em geral, bem descrita pela teoria da similaridade (MAHRT, 2014). Já, o regime muito estável normalmente ocorre em condições de ventos fracos e de céu claro (MAHRT, 1998), de modo que a perda radiativa superficial seja intensa e, como consequência, uma intensa estratificação térmica é desenvolvida. No regime muito estável a mistura turbulenta é drasticamente reduzida, podendo ser intermitente. Escoamentos turbulentos, muito estratificados, não são bem descritos pelos conceitos clássicos, e sua descrição completa permanece sendo um desafio (MAHRT, 2014).

Figura 1.2 – Velocidade de fricção na noite do dia 25 para 26 de janeiro de 2001.

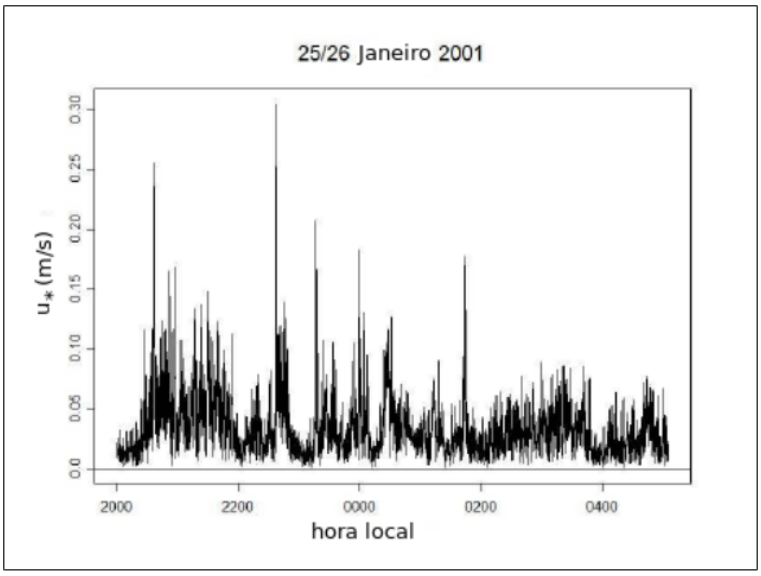

Fonte: Costa et al.(2011)

Na CLE é frequentemente observado que a turbulência é não continua no espaço e no tempo. Essa descontinuidade temporal caracteriza a turbulência intermitente, que causa alterações na evolução média da camada limite atmosférica estratificada e que pode resultar em comportamento oscilatório da temperatura do ar, do vento e dos fluxos turbulentos próximos à superfície (WIEL et al., 2002a). Chama-se intermitência global quando todas as escalas do escoamento turbulento são suprimidas e restabelecidas de maneira sucessiva e não previsível, caracterizando uma alternância entre períodos de turbulência de baixa intensidade ou de turbulência quase inexistente, e períodos turbulentos intensos ao longo de uma mesma noite (figura 1.2) (COSTA et al., 2011). A intermitência global é um fenômeno comum na camada limite muito estável, cuja compreensão e descrição matemática ainda é limitada.

Uma das primeiras formas de classificar os regimes da camada limite estável foi

através da dependência do fluxo de energia na forma de calor sensível com a estabilidade do escoamento (figura 1.3). No regime fracamente estável, também chamado de pouco estável, a magnitude do fluxo de energia na forma de calor sensível cresce com a estabilidade do escoamento devido ao aumento do gradiente vertical de temperatura até atingir um valor máximo. No regime muito estável, a magnitude do fluxo de energia na forma de calor sensível decresce com o aumento da estabilidade do escoamento, devido à forte redução da atividade turbulenta. Entretanto, de acordo com Monahan et al. (2015), parâmetros de estabilidade, como o comprimento de Obukhov ou o número de Richardson, por si só não são capazes de distinguir os regimes da CLE. Além disso, Acevedo et al. (2019) observaram que o máximo do fluxo de calor, em módulo, ocorre no regime pouco estável, portanto esta quantidade não deve ser utilizada como um marcador da transição entre os regimes da CLE.

Figura 1.3 – Fluxo de energia na forma de calor sensível em função da estabilidade.

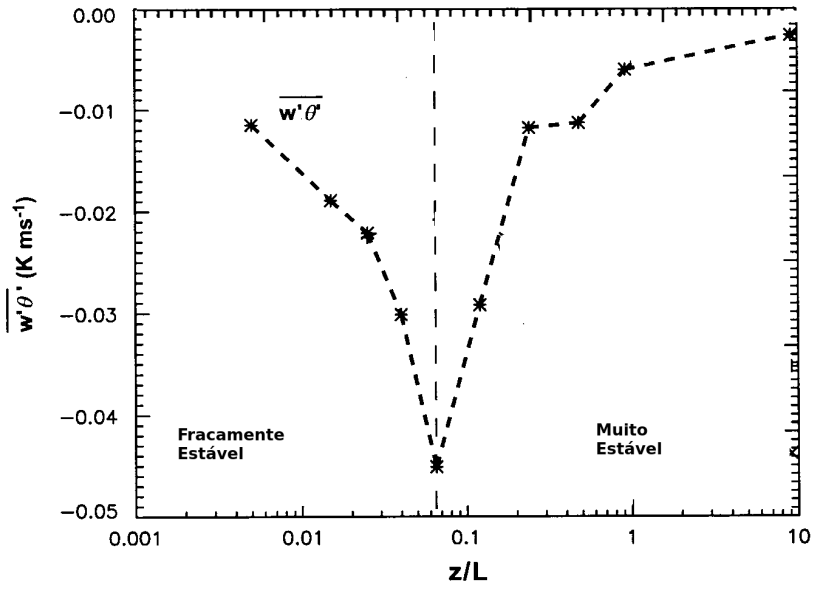

Fonte: Adaptado de Mahrt, 1998.

Sun et al. (2012) exploraram a dependência da turbulência com velocidade média do vento. Uma escala de velocidade turbulenta é definida como $V_{TKE} = \sqrt{e}$ e está associada à intensidade da turbulência. A relação entre V_{TKE} e velocidade horizontal média do vento, V, observado por Sun et al. (2012) para cada nível atmosférico é mostrado na figura 1.4. Eles observaram que a relação entre V_{TKE} e a velocidade do vento muda abruptamente em um valor crítico de velocidade do vento. A partir daí, propuseram dois regimes, sendo que no primeiro V_{TKE} é pouco intenso e aumenta lentamente com V, e no segundo regime V_{TKE} aumenta rapidamente com o V após essa quantidade exceder o valor crítico. Além disso, identificaram que a transição entre os dois regimes ocorre de forma abrupta (Figura 1.5).

Figura 1.4 – Dependência da turbulência com velocidade média do vento obtida experimentalmente por Sun et al. (2012).

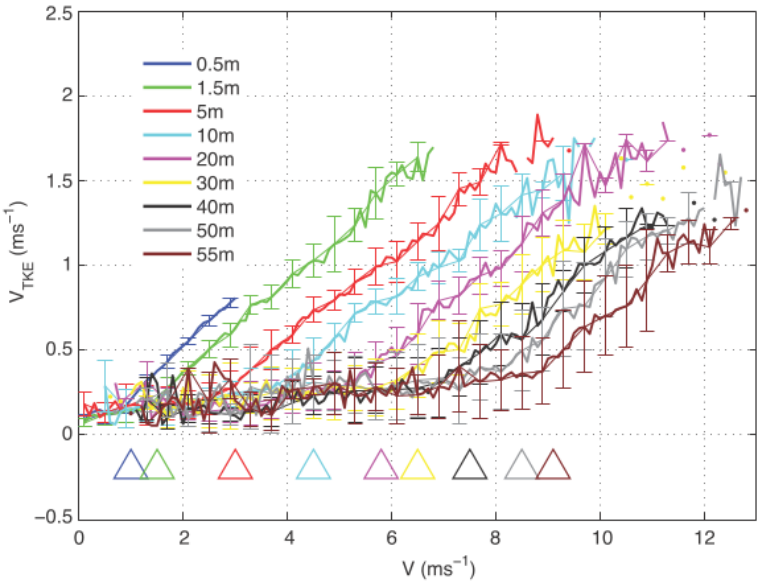

Fonte: Sun et al. (2012)

De acordo com Sun et al. (2012), quando a intensidade do vento é menor que o valor limite, a turbulência é controlada pelo cisalhamento do vento local, enquanto que é o cisalhamento global do vento ao longo de toda CLE que controla a turbulência quando esse limite é excedido. Esse conceito indica uma situação em que a CLE está verticalmente acoplada ao topo da camada, quando os ventos excedem o valor limite. Uma classificação alternativa, porém não excludente da anterior, da CLE, é relacionada com o estado de acoplamento das parcelas de ar próximas à superfície e dos níveis superiores da atmosfera. Em condições turbulentas, diferentes níveis da atmosfera mantém-se unidos entre si e a ao topo da CLE, representando o estado acoplado, que geralmente coincide com o regime pouco estável. Por outro lado, se não há ocorrência de ventos de intensa magnitude, a superfície tende a se desacoplar dos níveis atmosféricos superiores. O estado desacoplado, pode ser relacionado ao regime muito estável da CLE (COSTA et al., 2011).

Outra forma objetiva de classificar os regimes da CLE é através da relação entre a inversão térmica e a intensidade da velocidade do vento, Vignon et al. (2017) observaram a existência de dois limites assintóticos para essa relação, coincidindo com cada um dos regimes da CLE. No regime muito estável, esse valor assintótico, em geral, é superior a 3-5 K, pois o fluxo turbulento de calor não é intenso suficiente para manter a superfície acoplada aos níveis superiores da CLE, mais quentes, então devido a perda radiativa do solo uma intensa estratificação térmica se desenvolve. No regime pouco estável esse limite se aproxima de zero, pois a intensidade da turbulência é suficiente para que as camadas de ar mais quentes, dos níveis superiores da CLE, passem a influenciar o que ocorre na superfície, reduzindo a estratificação térmica. Entre esses dois limites assintóticos,

Figura 1.5 – Representação esquemática da dependência da turbulência com velocidade média do vento observada experimentalmente por Sun et al. (2012).

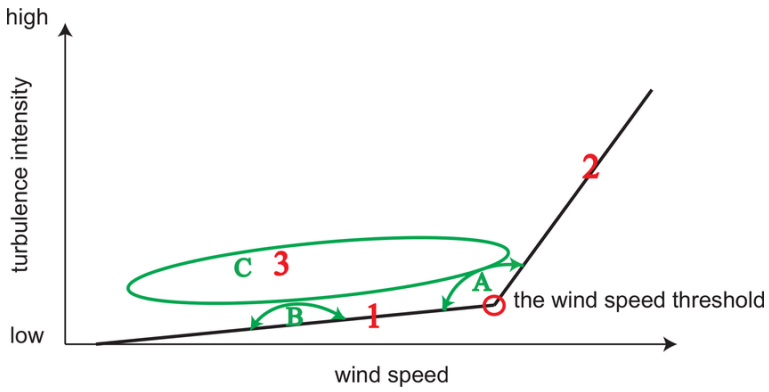

Fonte: Sun et al.(2015)

a inversão térmica passa a ter uma dependência com a intensidade da velocidade do vento, Vignon et al. (2017) mostraram que está dependência pode variar de acordo com alguns parâmetros externos como, por exemplo, a perda radiativa superficial (Figura 1.6). A inversão térmica em função da velocidade do vento tem o formato típico de um "S" (Figura 1.7).

Muitos estudos estudos mostram que podem haver variações de V_{TKE} em função de $\overline{V}$ em relação ao caso canônico observado por Sun et al. (2012), e da inversão térmica em função da intensidade da velocidade do vento em relação ao caso observado por Vignon et al. (2017). Essas diferenças em geral podem ser atribuídos a características, específicas, do sítio (ACEVEDO et al., 2016; DIAS-JÚNIOR et al., 2017; SUN; FRENCH, 2016; WIEL et al., 2017). A velocidade da transição entre os regimes da CLE pode variar de sítio para sítio, e também ao longo da mesma noite em resposta a determinados fatores externos.

Mahrt et al. (2013) observaram que transição entre os regimes da CLE ocorre em condições de vento mais intenso sobre superfícies mais regulares. Escoamentos sobre superfícies irregulares tendem a ser mais turbulentos, permitindo que o acoplamento entre a superfície e a atmosfera ocorra com ventos de menor intensidade. Sun e French (2016) observaram que a transição entre os regimes ocorre em condições de ventos mais intensos sobre o oceano do que sobre o continente, evidenciando que o acoplamento entre a superfície e atmosfera se torna menos eficaz com o aumento da capacidade térmica da superfície. Com auxilio de um modelo conceitual que resolve o balanço de energia na superfície do solo, Wiel et al. (2017) atribuiu o controle da transição entre os regimes à "intensidade de acoplamento" entre a superfície e a atmosfera. A "intensidade de acoplamento" está diretamente ligado ao balanço da energia na superfície do solo, portanto, quantidades como a cobertura de nuvens e propriedades térmicas da superfície, importantes para esse balanço, o controlam. A "intensidade de acoplamento" é diretamente proporcional à cobertura de nuvens e à rugosidade da superfície, inversamente proporcional à capacidade

Figura 1.6 – Diferença de temperatura entre 10 metros e a temperatura da superfície em função da intensidade da velocidade do vento em 10 metros para quatro diferentes faixas de perda radiativa superficial, especificada no topo de cada painel, obtidas por Vignon et al. (2017) com as medidas meteorológicas provenientes de uma torre de 45 metros localizada em Dome C.

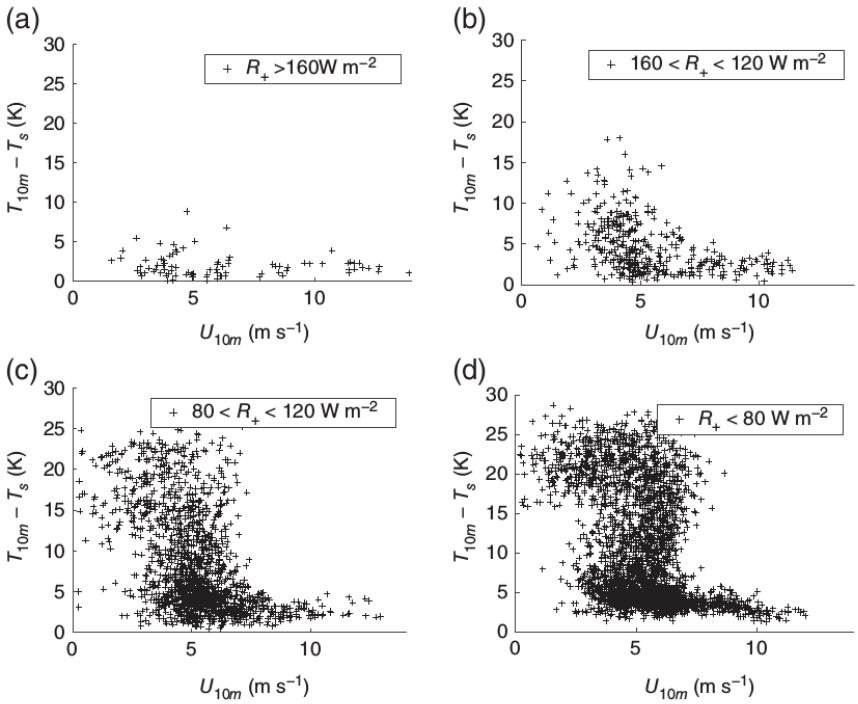

Fonte: Vignon et al.(2017)

calorífica do solo e por fim é diretamente proporcional a temperatura do substrato, que está diretamente ligado ao fluxo molecular de calor no solo. Um acréscimo na cobertura de nuvens faz com que a radiação de onda longa, de maior intensidade, chegue à superfície do solo, mantendo-a mais quente, e consequentemente o escoamento torna-se menos estável e mais turbulento do que em uma situação semelhante sem nuvens. Quando a capacidade térmica da superfície do solo é reduzida observa-se um efeito semelhante ao descrito anteriormente, pois nesse caso a superfície esfria a uma taxa menor do que esfriaria um solo de maior capacidade térmica, sob as mesma condições de perda radiativa. Um substrato mais quente faz com que a transferência de calor, das camadas mais profundas do solo em direção à superfície do solo, seja mais intenso, mantendo a superfície do solo mais quente do que ela estaria se substrato estivesse mais frio. "Intensidades de acoplamento" maiores permitem que a transição entre os regimes da CLE, pouco estável e muito estável, ocorra com ventos de menor intensidade.

A existência de dois regimes distintos na CLE também pode ser estabelecida através da relação entre o número de Richardson fluxo (Ri_f) e o número de Richardson gradiente (Ri_g) (ZILITINKEVICH et al., 2013; BOU-ZEID et al., 2018). Tanto observações (OHYA, 2001; PARDYJAK; MONTI; FERNANDO, 2002) quanto simulações numéricas (NA-

Figura 1.7 – Representação esquemática da inversão térmica e a intensidade do vento, observada por Vignon et al. (2017).

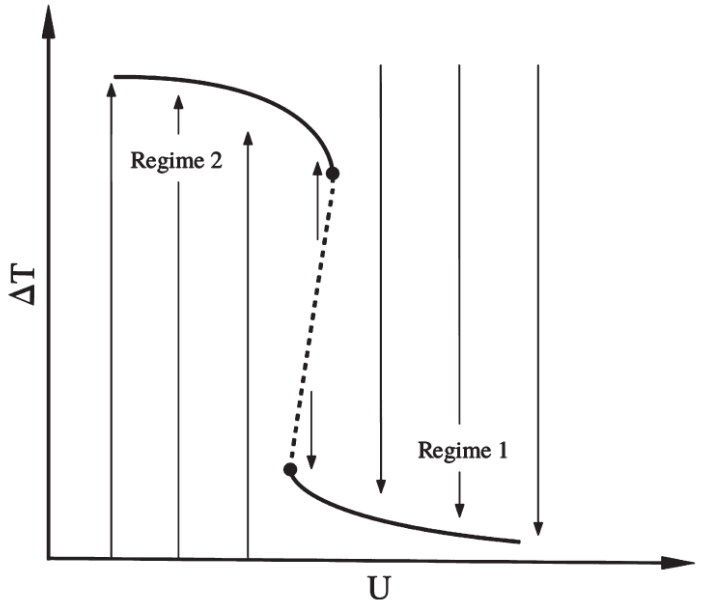

Fonte: Vignon et al.(2017)

KANISH, 2001) mostram que Ri_f cresce, aproximadamente, linearmente com Ri_g no regime pouco estável. Quando Ri_g excede um valor crítico (normalmente em torno de 0,25), Ri_f se torna aproximadamente constante e independente de Ri_g, caracterizando o regime muito estável (Figura 1.8). A razão Ri_g/Ri_f também conhecida como número turbulento de Prandtl (Pr_T), é aproximadamente constante no regime pouco estável, e cresce linearmente com Ri_g no regime muito estável, implicando na redução da difusão turbulenta de calor em relação à difusão turbulenta de momentum (ZILITINKEVICH et al., 2013). Bou-Zeid et al. (2018) mostraram que o de termo de retorno à isotropia presente, no balanço das componentes da variância, justifica a ocorrência de um máximo teórico para o número de Richardson fluxo.

Uma camada limite pouco estável é relativamente bem descrita pela teoria da similaridade e por modelos em condições horizontalmente homogênea. Já a estimativa adequada dos fluxos turbulentos em condições muito estáveis ainda é um grande desafio para os modelos numéricos que descrevem o comportamento médio da camada limite estável (CLE), uma vez que não podem ser descritos pela teoria da similaridade local. Embora, na média, muitas características do escoamento sejam reproduzidas, a variação intermitente da intensidade da turbulência não é reproduzida por grande parte dos modelos atmosféricos. Além disso, o regime muito estável, e a transição entre os regimes da CLE, ainda, não são bem compreendidas e descritos pelos modelos numéricos.

Em 1979, Blackadar propôs um modelo simplificado com intenção de simular a interação superfície-atmosfera, resolvendo equações prognósticas para as componentes zonal

Figura 1.8 – Relação entre Ri_f e Ri_g observada por Zilitinkevich et al. (2013).

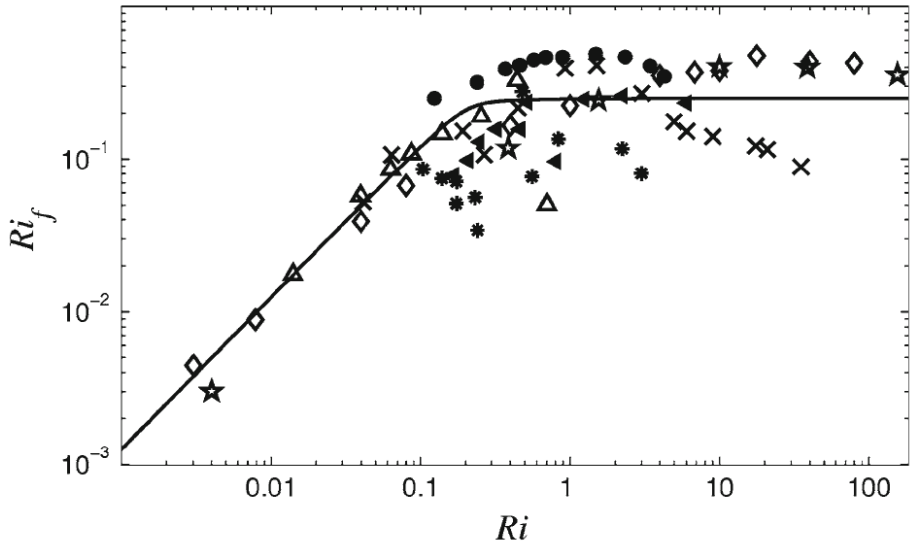

Fonte: Zilitinkevich et al.(2017)

e meridional da velocidade vento, temperatura potencial do ar e da superfície. Nesse simples modelo, os fluxos turbulentos são estimados através dos gradientes das quantidades médias e funções de estabilidade, caracterizando um fechamento de primeira ordem . McNider et al. (1995) observaram que o modelo de Blackadar é sensível a pertubações na intensidade do vento geostrófico, onde pequenas pertubações podem ser suficientes para que ocorra a mudança de regime da CLE.

Costa et al. (2011) propuseram um modelo simplificado, capaz de reproduzir alguns eventos intermitentes, no qual as componentes do fluxo turbulento de momentum são estimadas diretamente a partir da mistura turbulenta local, dada pelo valor local da ECT. Todavia, a estimativa do fluxo de energia na forma de calor sensível é feita através da escala de temperatura. O fato de parametrizar o fluxo de energia na forma de calor sensível pode reduzir o número de graus de liberdade do sistema, além de limitar o realismo físico do modelo, principalmente devido às evidencias já apresentadas que esta variável tem papel dominante na determinação do regime da CLE.

Wiel et al. (2012), propuseram um "modelo bulk" para explicar a relação entre a velocidade do vento no topo da camada e a intensidade da turbulência na camada limite noturna, e mostraram que a transição entre os estados da CLE também é controlado pela velocidade do vento. Eles mostraram que o colapso da turbulência na CLE é essencialmente causado pelo fato que o fluxo de calor sensível em camadas limites estratificadas é limitado a um valor máximo para um determinado forçante mecânico. Para casos em que os ventos geostróficos são intensos, o transporte turbulento de energia na forma de calor sensível é intenso o suficiente para compensar a perda de energia radiativa da superfície. Entretanto, para o caso em que os forçantes mecânicos são de pequena intensidade, o va-

lor máximo do fluxo de energia na forma de calor sensível é pequeno quando comparado à taxa de resfriamento radiativo da superfície. Nesse caso, o gradiente de temperatura cresce rapidamente, sobre superfícies com baixa capacidade térmica, e a turbulência, em grande parte, é suprimida pela intensa estratificação. Eles também mostraram que há um limite de velocidade do vento (sendo este da ordem de $5,0\ \mathrm{m/s}$) abaixo do qual a turbulência é pouco intensa para sustentar o fluxo de calor turbulento necessário para compensar a perda de energia radiativa da superfície para as camadas de ar adjacentes a ela. A discussão realizada por Wiel et al. (2012) mostra que o fluxo de energia na forma de calor exerce grande controle no colapso da turbulenta na CLE e também na transição entre os regimes. Este fato foi corroborado por Acevedo et al. (2016), que mostraram que o termo da destruição térmica de turbulência na equação de balanço de ECT tem importância relativa no balanço total muito maior no estado desacoplado.

Estudos sobre o comportamento e a estimativa adequada dos fluxos turbulentos em uma camada limite estável são de grande importância para diferentes áreas da sociedade. Entre essas estão: a agricultura, meio ambiente (através do estudo da dispersão de poluentes), geração de energias renováveis (energia eólica), mudanças climáticas, entre outras. Na agricultura, a estimativa correta da temperatura mínima é muito importante para a previsão de geadas. Por exemplo, a ocorrência de geada, na primavera, é prejudicial para prática agrícola, de modo que o congelamento das flores de uma árvore frutífera provoca perdas significativas na produtividade. Já na aviação, isso se traduz na redução no número de voos devido à ocorrência de neblina, o que pode causar perdas econômicas significativas. O desenvolvimento de parametrizações para CLE que seja capaz capaz de resolver tanto o regime muito estável como o pouco estável é fundamental para estudos como de controle de ar, dispersão de poluentes, a previsão de temperaturas mínimas, entre outros.

A presente tese visa identificar os principais mecanismos responsáveis pela transição entre os regimes da camada limite estável, e contribuir no desenvolvimento de uma nova parametrização para camada limite planetária que seja capaz de reproduzir adequadamente os dois regimes da CLE, e futuramente sua implementação no modelos atmosféricos, tais como o WRF.

Há anos conhece se bem a existência dos dois regimes da CLE, pouco e muito estável, sabe-se a ocorrência de um ou de outro regime está extremamente associada a intensidade do vento, forçante mecânico, e ao balanço de energia da superfície do solo, forçantes externos ao escoamento (SUN et al., 2012; ACEVEDO et al., 2016; WIEL et al., 2017; MARONEZE et al., 2019, entre outros). Entretanto, embora seja conhecido que alguns forçantes externos ao escoamento, como cobertura de nuvens, está associado a ocorrência do regime pouco estável ou do regime muito estável, ainda não sabe-se bem como cada um desses fatores controla os regimes da CLE. Além disso, não existe consenso de como ocorre a transição entre os regimes das CLE. Devido a esses motivos e a outros motivos, modelar uma camada limite estável permanece sendo grande desafio.

A presente tese está divida em 4 diferentes artigos. No artigo 1 ("Simulating the Regime Transition of the Stable Boundary Layer Using Different Simplified Models", publicado na revista *Boundary-Layer Meteorology*) serão comparados três diferentes modelos numéricos baseados no modelo proposto por Costa et al. (2011), de uma ordem e meia, que são utilizados para descrever o comportamento médio de uma camada limite noturna. No modelo $e - F_H$, o fluxo de energia na forma de calor sensível será estimado através de uma equação prognóstica. Uma vez que a equação prognóstica para o fluxo de energia na forma de calor sensível depende da variância da temperatura potencial, no modelo $e - F_H - \sigma_\theta$ será incluída uma equação prognóstica para a variância da temperatura, a fim de acrescentar mais graus de liberdade ao sistema e de modo a acrescentar detalhamento físico à solução. Ao longo desse artigo, serão realizadas comparações entre as diferentes soluções obtidas pelos modelos variando diferentes parâmetros. Além disso, esse trabalho visa determinar o menor número de equações prognósticas necessário para que um modelo de coluna simples consiga reproduzir os dois regimes da CLE, adequadamente.

Acevedo et al. (2018) realizaram uma descrição detalhada dos dados micrometeorológicos provenientes de uma torre de 140 metros situada em Linhares, no estado de Espírito Santos, sudoeste do Brasil. Uma grande variedade de fenômenos micrometeorológicos foram observados, em detalhes, nessa torre, como por exemplo, a ocorrência de dois regimes na CLE e a transição entre eles ao longo de uma mesma noite. Com a ocorrência do regime pouco estável durante a primeira metade da noite, enquanto na segunda metade a ocorrência do regime muito estável. Utilizando esse mesmo conjunto de dados micrometeorológicos, Acevedo et al. (2019) (artigo 2, "The nocturnal boundary layer transition from weakly to very stable. Part I: Observations", publicado na revista *Quarterly Journal of the Royal Meteorological Society*) observaram, em muitas noites, um resfriamento abrupto da camada acompanhado de uma redução na energia cinética turbulenta (ECT), e na intensidade da velocidade do vento. Nesse estudo Acevedo et al. (2019) propuseram que a transição entre o regime pouco estável e o muito estável ocorre simultaneamente com o máximo resfriamento do níveis inferiores da camada limite. No artigo 3 ("The nocturnal boundary layer transition from weakly to very stable. Part II: Numerical simulation with a second-order model", publicado na revista *Quarterly Journal of the Royal Meteorological Society*), transições semelhantes, as observadas por Acevedo et al. (2019), são investigadas com auxilio de um modelo numérico unidimensional de segunda ordem, com o balanço de energia resolvido na superfície, através do método "Force-Restore" proposto por Blackadar (1979). Nesse modelo, a transição é impulsionada pelo decréscimo da intensidade da velocidade do vento no topo do domínio, simulações com diferentes coberturas de nuvens e propriedades térmicas da superfície são realizadas.

Os esquemas de turbulência hoje utilizados nos modelos numéricos de previsão de tempo e clima (MNPTC) são de primeira ordem, onde apenas as equações prognósticas para variáveis médias são resolvidas e todos os momentos estatísticos de ordem mais alta

são parametrizados, ou são modelos ECT, em que a energia cinética turbulenta é resolvida prognosticamente. Os esquemas de turbulência presentes no WRF são equivalentes aos modelos Mellor-Yamada 1-, 2-, 2.5 e 3-nível, em que o fluxo de calor é parametrizado. Maroneze et al. (2019) (artigo 1) mostraram que o regime muito estável da CLE só é representado adequadamente quando o fluxo de calor e a variância de temperatura são resolvidos prognosticamente. Assim, no artigo 4 ("How is the two-regime stable boundary layer solved by the different PBL schemes in WRF?", submetido para revista *Geophysical Research Letters*), cinco diferentes esquemas de turbulência para CLP, com diferentes configurações, presentes no "Weather Research and Forecasting - Single Column Model"(WRF-SCM) serão comparadas e avaliadas quanto a capacidade de resolver adequadamente os regimes da CLE. Esse esquemas são: Mellor-Yamada-Nakanishi-Niino (MYNN,Nakanishi e Niino (2006), Nakanishi e Niino (2009)), Mellor-Yamada-Janjic (MYJ, Janjić (1994)), "Quasi-Normal Scale Elimination "(QNSE, Sukoriansky, Galperin e Perov (2005)), "University of Washington (TKE) Boundary Layer Scheme"(UWBLS, Bretherton e Park (2009)) e Bougeault-Lacarrere (BouLac,Bougeault e Lacarrere (1989)).

2 EQUAÇÕES BÁSICAS DA CLP

Os movimentos atmosféricos obedecem os princípios fundamentais da Física, tais como a conservação da energia (primeira lei da termodinâmica), conservação da massa, conservação do momentum (segunda lei de Newton) e a lei dos gases ideais. As leis fundamentais da mecânica de fluídos e da termodinâmica, que governam os movimentos atmosféricos, podem ser expressas em termos de equações diferencias parciais que envolvem as variáveis do campo (velocidade do vento, temperatura, umidade, etc) como variáveis dependentes, o espaço e o tempo como variáveis independentes (HOLTON, 2004).

2.0.1 Equação de estado

O estado termodinâmico dos gases presentes na camada limite, como uma boa aproximação, podem ser descritos pela lei dos gases ideais:

$$p = \rho R' T_v \ , \tag{2.1}$$

onde p é a pressão, ρ é a densidade do ar úmido, R' é constante dos gases para o ar seco $(R' = 287 J.K^{-1} kg^{-1})$ e T_v é a temperatura absoluta virtual que é dada por $T_v = T(1 + 0,6r)$, sendo que r representa a úmidade específica.

2.0.2 Conservação da massa (Equação da continuidade)

A equação da continuidade, ou de conservação da massa, pode ser dada por:

$$\frac{\partial \rho}{\partial t} + \frac{\partial \left(\rho U_j\right)}{\partial x_j} = 0 \ , \tag{2.2}$$

onde U_j são as componentes da velocidade do vento. Pode-se dizer que um escoamento é incompressível quando a divergência da velocidade do vento é nula $\left(\frac{\partial U_j}{\partial x_j} = 0\right)$.

2.0.3 Segunda Lei de Newton

A segunda lei de Newton aplicada a um fluído pode ser escrita na notação tensorial como:

$$\underset{I}{\frac{\partial U_i}{\partial t}} + \underset{II}{U_j \frac{\partial U_i}{\partial x_j}} = \underset{III}{-\delta_{i3} g} \underset{IV}{- f \varepsilon_{ij3} U_j} \underset{V}{- \frac{1}{\rho} \frac{\partial p}{\partial x_i}} + \underset{VI}{\frac{1}{\rho} \frac{\partial \tau_{ij}}{\partial x_j}} \ . \tag{2.3}$$

$I \rightarrow$ Variação Euleriana de velocidade.

$II \rightarrow$ Transporte advectivo de velocidade.

$III \rightarrow$ Aceleração da gravidade efetiva. Aceleração da gravidade efetiva é a soma da aceleração gravitacional com a aceleração centrifuga devido a rotação da Terra, ou seja a Terra é um sistema de referencia não inercial.

$IV \rightarrow$ Aceleração devido à força de Coriolis, proveniente da rotação da Terra.

$V \rightarrow$ Aceleração devido ao gradiente de pressão.

$VI \rightarrow$ Dissipação, devido viscosidade do fluido.

As equações para as componentes da velocidade do vento zonal, meridional e vertical, desconsiderando o termo de dissipação molecular, podem ser escritas respectivamente como:

$$\frac{du}{dt} = -\frac{1}{\rho} \frac{\partial p}{\partial x} - fv \ , \tag{2.4}$$

$$\frac{dv}{dt} = -\frac{1}{\rho} \frac{\partial p}{\partial y} + fu \ , \tag{2.5}$$

$$\frac{dw}{dt} = -\frac{1}{\rho} \frac{\partial p}{\partial z} - g \ , \tag{2.6}$$

O vento geostrófico é definido como o vento horizontal que resulta de um equilíbrio entre a força devido ao gradiente de pressão (horizontal) e a força de Coriolis. Na micrometeorologia é comum aproximar o termo do gradiente de pressão horizontal utilizando a conceito de vento geostrófico:

$$f u_G = -\frac{1}{\rho} \frac{\partial p}{\partial y} \qquad e \qquad f v_G = \frac{1}{\rho} \frac{\partial p}{\partial x} \ , \tag{2.7}$$

sendo u_G e v_G as componentes do vento geostrófico, respectivamente, zonal e meridional.

A temperatura potencial θ é definida como a temperatura que uma parcela de ar teria se fosse expandida ou comprimida adiabaticamente de seu estado real de pressão e temperatura a um valor referência de pressão:

$$\theta = T \left(\frac{p_0}{p} \right)^{\frac{R}{C_p}} \ .$$

onde $P_0 = 1000$ mb, R é a constante dos gases para o ar e C_P o calor específico do ar a

pressão constante.

2.0.4 Conservação da energia térmica (1º lei da termodinâmica)

A primeira lei da termodinâmica descreve a conservação da entalpia, com a contribuição tanto da transferência de energia na forma de calor sensível quanto latente. O vapor de água presente no ar não apenas absorve e libera energia na forma de calor sensível associada à sua temperatura, mas também pode absorver e liberar energia na forma de calor latente durante alguma mudança de fase. A equação associada a conservação da energia térmica pode ser escrita como:

$$\underset{I}{\frac{\partial\theta}{\partial t}} + \underset{II}{U_j\frac{\partial\theta}{\partial x_j}} = \underset{III}{\nu_\theta\frac{\partial^2\theta}{\partial x_j^2}} - \underset{IV}{\frac{1}{\rho c_p}\frac{\partial Q}{\partial x_j}} - \underset{VI}{\frac{L_p E}{\rho c_p}} \ . \tag{2.8}$$

$I \rightarrow$ Variação Euleriana da temperatura potencial.

$II \rightarrow$ Transporte advectivo de temperatura potencial.

$III \rightarrow$ Termo de difusão molecular.

$IV \rightarrow$ Termo associado à divergência da radiação.

$VI \rightarrow$ Está associado à liberação de energia na forma de calor latente durante as mudanças de fase.

Na equação acima, E, ν_θ, L_p e c_p representam, respectivamente, a informação sobre a mudança de fase, a difusividade térmica, o calor latente associado à mudança de fase E e o calor específico para o ar úmido.

2.0.5 Equações médias

A partir das equações de conservação de momentum e energia, considerando o equilíbrio hidrostático, um ambiente idealizado seco e horizontalmente homogêneo, utilizando a decomposição de Reynolds e aplicando a média de Reynolds, obtem-se as equações para as variáveis médias do escoamento (Costa et al., 2011):

$$\frac{\partial\overline{u}}{\partial t} = f(\overline{v} - v_g) - \frac{\partial(\overline{u'w'})}{\partial z} \ , \tag{2.9}$$

$$\frac{\partial\overline{v}}{\partial t} = -f(\overline{u} - u_g) - \frac{\partial(\overline{v'w'})}{\partial z} \ , \tag{2.10}$$

$$\frac{\partial\overline{\theta}}{\partial t} = -\frac{\partial(\overline{w'\theta'})}{\partial z} \,. \tag{2.11}$$

Nas equações anteriores e nas seguintes, não aparecem os termos de advecção horizontal pelo vento médio. Isto ocorre porque o presente trabalho foca nos processos de interação entre a superfície e a atmosfera, considerando para tanto uma coluna vertical, sem transportes horizontais. Entretanto, no mundo real estes termos advectivos são importantes, sendo frequentemente dominantes. Da mesma forma, termos viscosos, de divergência de fluxos radiativo e de aquecimento por liberação de energia na forma de calor latente não foram incluídos.

Equações prognóstica para as componentes horizontais da variâncias da velocidade do vento $\left(\overline{u'^2}, \overline{v'^2}\right)$, em condições de homogeneidade horizontal, podem ser escritas como (Anexo A, equação A.20):

$$\frac{\partial\overline{u'^2}}{\partial t} = \underbrace{-2\overline{u'w'}\frac{\partial\overline{u}}{\partial z}}\underbrace{-\frac{\partial\overline{w'u'^2}}{\partial z}}\underbrace{-\frac{2}{\overline{\rho}}\frac{\partial\overline{u'p'}}{\partial x}}\underbrace{+\frac{2}{\overline{\rho}}\overline{p'\frac{\partial u'}{\partial x}}}\underbrace{-\epsilon_u}\,, \tag{2.12}$$

$$\frac{\partial\overline{v'^2}}{\partial t} = \underbrace{-2\overline{v'w'}\frac{\partial\overline{v}}{\partial z}}_{I}\underbrace{-\frac{\partial\overline{w'v'^2}}{\partial z}}_{II}\underbrace{-\frac{2}{\overline{\rho}}\frac{\partial\overline{v'p'}}{\partial y}}_{III}\underbrace{+\frac{2}{\overline{\rho}}\overline{p'\frac{\partial v'}{\partial y}}}_{IV}\underbrace{-\epsilon_v}_{V}\,. \tag{2.13}$$

$I \rightarrow$ Termo associado à a produção da variância devido ao cisalhamento do vento.

$II \rightarrow$ Termo associado ao transporte turbulento de variância ao longa da vertical vertical.

$III \rightarrow$ Termo associado ao transporte turbulento de variância devido as flutuações de pressão.

$IV \rightarrow$ Termo associado a redistribuição de pressão (retorno à isotropia).

$V \rightarrow$ Termo associado à dissipação viscosa da variância.

A equação prognóstica para componente vertical da variância da velocidade do vento, é dada por:

$$\frac{\partial\overline{w'^2}}{\partial t} = \underbrace{+2\frac{g}{\overline{\Theta}}\overline{w'\theta'}}_{I}\underbrace{-\frac{\partial\overline{w'w'^2}}{\partial z}}_{II}\underbrace{-\frac{2}{\overline{\rho}}\frac{\partial\overline{w'p'}}{\partial y}}_{III}\underbrace{+\frac{2}{\overline{\rho}}\overline{p'\frac{\partial w'}{\partial z}}}_{IV}\underbrace{-\epsilon_w}_{V}\,. \tag{2.14}$$

$I \rightarrow$ Termo associado à produção (durante o dia) ou destruição (durante a noite) térmica de turbulência devido à estratificação térmica da CLP.

$II \rightarrow$ Termo associado ao transporte turbulento de variância ao longa da vertical vertical.

$III \rightarrow$ Termo associado ao transporte turbulento de variância devido as flutuações de pressão.

$IV \rightarrow$ Termo associado a redistribuição de pressão (retorno à isotropia).

$V \rightarrow$ Termo associado à dissipação viscosa da variância.

A principal fonte de variância na equação 2.14 é o termo de redistribuição de pressão, que transfere energia das componentes horizontais da variância do vento para o componente vertical. Esse termo não é totalmente compreendido e desempenha um papel importante na equação 2.14. Portanto, uma forma para determinar a componente vertical da variância da velocidade vento é através da definição da ECT (DEARDORFF, 1974).

Através da definição da energia cinética turbulenta e de algumas manipulações algébricas das equações acima, pode-se escrever uma equação prognóstica para ECT, considerando a turbulência horizontalmente homogênea. A derivação detalhada desta equação é mostrada no Anexo A.

$$\frac{\partial \overline{e}}{\partial t} = \underbrace{-\overline{u'w'}\frac{\partial \overline{u}}{\partial z} - \overline{v'w'}\frac{\partial \overline{v}}{\partial z}}_{I} \underbrace{+\frac{g}{\Theta}\overline{w'\theta'}}_{II} \underbrace{-\frac{\partial}{\partial z}\left[(\overline{w'e'}) + \frac{\overline{p'w'}}{p_0}\right]}_{III} \underbrace{-\epsilon}_{IV} . \tag{2.15}$$

$I \rightarrow$ Termo associado à produção mecânica de turbulência devido ao cisalhamento do vento.

$II \rightarrow$ Termo associado à produção (durante o dia) ou destruição (durante a noite) térmica de turbulência devido à estratificação térmica da CLP.

$III \rightarrow$ Termo associado ao transporte turbulento de ECT na vertical.

$IV \rightarrow$ Termo associado à dissipação viscosa de ECT.

De forma análoga à utilizada para a obtenção da equação prognóstica para ECT, pode-se obter uma equação prognóstica para o fluxo turbulento de energia na forma de calor sensível. Quando a turbulência é considerada horizontalmente homogênea, está pode ser escrita como: (Anexo B)

$$\frac{\partial \overline{w'\theta'}}{\partial t} = \underbrace{-\overline{w'^2}\frac{\partial \overline{\theta}}{\partial z}}_{I} \underbrace{-\frac{\partial(\overline{w'w'\theta'})}{\partial z}}_{II} \underbrace{+\overline{\theta'^2}\frac{g}{\Theta}}_{III} \underbrace{+\frac{1}{\overline{\rho}}\overline{\theta'\frac{\partial p'}{\partial z}}}_{IV} . \tag{2.16}$$

$I \rightarrow$ Produção (durante a noite) ou destruição (durante o dia) de fluxo de energia na forma de calor sensível.

$II \rightarrow$ Termo associado ao transporte do fluxo de energia na forma de calor sensível.

$III \rightarrow$ Destruição (durante a noite) ou produção (durante o dia) de fluxo de energia na forma de calor sensível devido as flutuações de temperatura.

$IV \rightarrow$ Termo associado ao transporte do fluxo de energia devido as flutuações de pressão.

De forma análoga à utilizada para a obtenção da equação prognóstica para fluxo

de calor sensível, pode-se obter as equações prognósticas para o fluxo turbulento de momentum. Quando a turbulência é considerada horizontalmente homogênea, está pode ser escrita como:

$$\frac{\partial \overline{u'w'}}{\partial t} = \underbrace{-\overline{w'^2}\frac{\partial \overline{u}}{\partial z}}\underbrace{-\frac{\partial(\overline{w'u'w'})}{\partial z}}\underbrace{+\overline{\frac{p'}{\overline{\rho}}\left[\frac{\partial u'}{\partial z}+\frac{\partial w'}{\partial x}\right]}}, \tag{2.17}$$

$$\frac{\partial \overline{v'w'}}{\partial t} = \underbrace{-\overline{w'^2}\frac{\partial \overline{v}}{\partial z}}_{I}\underbrace{-\frac{\partial(\overline{w'v'w'})}{\partial z}}_{II}\underbrace{+\overline{\frac{p'}{\overline{\rho}}\left[\frac{\partial v'}{\partial z}+\frac{\partial w'}{\partial y}\right]}}_{III}. \tag{2.18}$$

$I \rightarrow$ Produção (durante a noite) ou destruição (durante o dia) de fluxo de energia na forma de calor sensível.
$II \rightarrow$ Termo associado ao transporte do fluxo de energia na forma de calor sensível.
$III \rightarrow$ Termo associado ao transporte do fluxo de energia devido as flutuações de pressão.

De forma análoga à utilizada para a obtenção da equação prognóstica para ECT, pode-se obter uma equação prognóstica para a variância da temperatura potencial. Quando a turbulência é considerada horizontalmente homogênea, está pode ser escrita como:(Anexo C)

$$\frac{\partial \overline{\theta'^2}}{\partial t} = \underbrace{-2\overline{w'\theta'}\frac{\partial \overline{\theta}}{\partial z}}_{I}\underbrace{-\frac{\partial \overline{w'\theta'^2}}{\partial z}}_{II}\underbrace{-\epsilon_{\theta'^2}}_{III}. \tag{2.19}$$

$I \rightarrow$ Termo de produção associado aos movimentos turbulentos na presença de um gradiente temperatura médio.
$II \rightarrow$ Termo associado ao transporte da variância de temperatura ao longo da vertical.
$III \rightarrow$ Termo associado à dissipação viscosa.

A temperatura da superfície ($\overline{\theta_g}$) pode determinada através do método "Force-Restore" proposto por Blackadar (1979):

$$\frac{\partial \overline{\theta_g}}{\partial t} = \frac{1}{c_g}(I_{\downarrow} - \sigma\overline{\theta_g^4} - H_0) - k_m(\overline{\theta_g} - \overline{\theta_m}). \tag{2.20}$$

onde σ representa a constante de Stefan-Boltzman; k_m é o coeficiente de transferência de calor; ρ é a densidade do ar; θ_m é temperatura do substrato; H_0 é fluxo de calor sensível superficial que pode ser dado como $H_0 = \rho C_p \overline{w'\theta'}$; C_p é calor específico do ar à pressão constante; c_g é a capacidade térmica da superfície por unidade de área; $I_{\downarrow}$ está associado à radiação de onda longa proveniente da atmosfera, que depende da cobertura de nuvens Q_c, umidade específica Q_a em uma altura de referência e da temperatura no topo da CLP:

$$I_{\downarrow} = \sigma(Q_c + 0,67(1 - Q_c)(1670Q_a)^{0,08})\theta^4 \ . \tag{2.21}$$

Na equação 2.20, é utilizado um método que considera o balanço de energia em uma pequena camada de solo (Figura 2.1), em que o modelo considera as trocas de energia entre o subtrato e essa camada e dessa camada com a atmosfera (BLACKADAR, 1979; MCNIDER et al., 1995). Essa equação é conhecida como método "Force-restore", porque a perda radiativa líquida $(I_{\downarrow} - \sigma\overline{\theta_g^4})$ e fluxo de calor turbulento (H_0) na superfície são modificados pelo fluxo calor molecular, nessa pequena camada de solo, que tende a restaurar a temperatura da superfície à temperatura do substrato. Se o termo forçante $(I_{\downarrow} - \sigma\overline{\theta_g^4} - H_0)$ for removido, o termo restaurador da equação 2.20 fará com que $\overline{\theta_g}$ se aproxime exponencialmente de $\overline{\theta_m}$ (ARYA, 2001).

Figura 2.1 – Balanço de energia em uma pequena camada de solo.

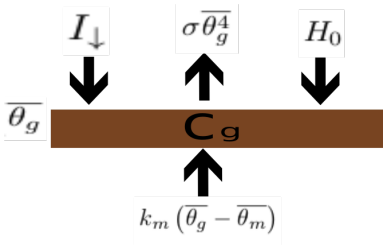

Segundo Blackadar (1979) a capacidade térmica da superfície por unidade de área pode ser dada por:

$$c_g = 0.95\left(\frac{\lambda c_s}{2\omega}\right)^{1/2} \ , \tag{2.22}$$

sendo λ a condutividade térmica do solo, ω a frequência angular da Terra e c_s a capacidade térmica do solo por unidade de volume.

2.1 PROBLEMA DO FECHAMENTO

Ao escrever equações básicas da CLP para as variáveis médias surgem novas incógnitas, associadas a momentos estatísticos de segunda ordem. Isto acarreta em um sistema de equações aberto. Assim, qualquer solução deste sistema requer que faça o seu fechamento.

Há duas maneiras para resolver o problema do fechamento:

a) Reduzir o número de incógnitas, através de parametrizações, como a clássica teoria K na qual, em analogia a processos moleculares, os fluxos turbulentos de determinadas quantidades são relacionados aos gradientes médios em questão na direção dos fluxos considerados.

b) Escrever equações prognósticas para as incógnitas, através de manipulações algébricas das equações básicas da CLP.

Entretanto, ao escrever as equações prognósticas para os momentos de segunda ordem, surgem incógnitas de terceira ordem, como pode ser visto nas equações 2.15-2.19, que são prognósticas para momentos de segunda ordem e apresentam sempre alguns termos de terceira ordem. Assim, a solução de escrever equações prognósticas para todas as novas incógnitas nunca resolve o problema do fechamento, pois sempre surgirão novas incógnitas, mantendo o número de variáveis maior que o de equações. Portanto, sempre será necessário que os momentos estatísticos de alguma ordem sejam parametrizados em termos dos de ordem mais baixa para que seja possível obter solução (normalmente numérica) para o sistema de equações básicas da CLP para as variáveis médias.

As aproximações ou premissas de fechamento são nomeadas através das equações prognósticas de maior ordem mantidas no sistemas de equações utilizadas para descrever o escoamento. Assim, por exemplo, para o fechamento de primeira ordem as equações prognósticas para os momentos estatísticos de primeira ordem são mantidas, enquanto os momentos de segunda ordem são aproximados ou parametrizados. Analogamente, para um fechamento de segunda ordem são mantidas as equações para os momentos estatísticos de primeira e de segunda ordem, aproximando os termos de terceira ordem.

Nem sempre é necessário escrever equações prognósticas para todos momentos estatísticos de segunda ou terceira ordem, pois algumas quantidades tem maior importância física que outros. Portanto, sistemas de equações que mantém equações prognósticas para energia cinética turbulenta e variância da temperatura, além das equações para os momentos estatísticos de primeira ordem, podem ser classificados como um sistema com fechamento de uma ordem e meia, intermediários aos de primeira e segunda ordem, pois resolvem alguns momentos estatísticos de segunda ordem, mas não todos (STULL, 1988).

Assim, modelos numéricos, como o proposto no artigo 1, que resolvem equações prognósticas para velocidade do vento, temperatura, energia cinética turbulenta, fluxo de energia na forma de calor sensível e para a variância da temperatura são classificados como modelos de uma ordem e meia. Já, o modelo proposto no artigo 3 corresponde à um modelo de segunda ordem completa.

Mellor e Yamada (1974) propuseram quatro diferentes níveis para fechamento da turbulência. Os níveis 1 e 2 são basicamente esquemas de primeira ordem, sem equações prognósticas para quaisquer variáveis turbulentas. Já, o nível 3 equações prognósticas para ECT e variância de temperatura são resolvidas. Por fim o nível 4, todos os momentos estatísticos de segunda ordem, como fluxo de momentum, de calor e as variâncias das componentes da velocidade do vento e da temperatura potencial, são resolvidas prognosticamente. Posteriormente, Mellor e Yamada (1982) propuseram o fechamento de nível 2.5, em que a ECT é o único momento de segunda ordem resolvido prognóstico.

3 ARTIGO 1 - SIMULATING THE REGIME TRANSITION OF THE STABLE BOUNDARY LAYER USING DIFFERENT SIMPLIFIED MODELS

Boundary-Layer Meteorology
https://doi.org/10.1007/s10546-018-0401-3

RESEARCH ARTICLE

Simulating the Regime Transition of the Stable Boundary Layer Using Different Simplified Models

Rafael Maroneze[1] · Otávio C. Acevedo[1] · Felipe D. Costa[2] · Jielun Sun[3]

Received: 27 April 2018 / Accepted: 23 October 2018

Abstract
The transition between the stable and the near-neutral regimes corresponding to weak and strong winds in the stable boundary layer is investigated using four one-dimensional numerical models with increasing numbers of prognostic equations for turbulent variables. The basic state for all the models includes prognostic equations for mean horizontal wind speed, and air and surface temperatures. The simplest model of the four has turbulence variables parametrized using a long-tail stability function and the gradient Richardson number. The complexity of the other three models increases by introducing one more prognostic equation to each model to reduce the number of parametrized turbulent variables: a prognostic equation for turbulent kinetic energy (TKE, e model), an additional prognostic equation for heat fluxes (e-F_H model), and an additional prognostic equation for temperature variances (e-F_H-σ_θ model). Results for all modells are similar in the strong-wind regime. The two stability regimes can be identified in the relationship between the turbulence velocity scale derived from TKE and mean wind speed from the three models with resolved TKE. However, the weak-wind regime can only be resolved with heat fluxes and temperature variance solved by prognostic equations. Simulations with the removal of the buoyancy term associated with heat fluxes in the TKE equation only result in the strong-wind regime, showing that this term controls the regime transition.

Keywords Stable boundary layer · Strong-wind regime · Transition · Weak-wind regime

1 Introduction

Many studies have shown the existence of two regimes or states in the stable boundary layer (SBL), usually classified as very or weakly stable (Malhi 1995; Oyha et al. 1997; Mahrt 1998), although this classification criterion varies between studies. The weakly stable regime normally occurs in the presence of consistently strong winds and/or cloud cover

Rafael Maroneze
rafaelmaroneze@gmail.com

1 Departamento de Física, Universidade Federal de Santa Maria, Santa Maria, RS, Brazil

2 Universidade Federal do Pampa-Campus, Alegrete, RS, Brazil

3 NorthWest Research Associates, Boulder, CO 80301, USA

Published online: 13 November 2018

(Acevedo and Fitzjarrald 2003), such that strong shear-generated turbulent mixing reduces the boundary-layer stratification, or cloud cover reduces air–surface temperature differences. The very stable regime, on the other hand, is characterized by weak winds and clear skies, corresponding to strong net radiative cooling at the surface (Mahrt 1998). In the very stable regime the turbulent mixing is weak and possibly intermittent.

A method to identify the two SBL regimes uses the relation between heat flux and stability due to Mahrt (1998). In the weakly stable regime the heat-flux magnitude increases with stability due to the increase of vertical temperature gradient as a result of the upward transfer of cold near-surface air. In the very stable regime, the heat-flux magnitude decreases with stability because turbulent mixing is suppressed by the atmospheric stable stratification. An alternative SBL classification refers to the coupling state between near-surface air and the upper SBL levels. When mechanical forcing for turbulence generation is strong the weakly stable SBL is coupled to the surface. In contrast, when the mechanical forcing is weak, the atmosphere above tends to be decoupled from the surface, corresponding to the very stable SBL regime (Costa et al. 2011).

Sun et al. (2012) observed that the relationship between the turbulence velocity scale (V_{TKE}) and mean wind speed abruptly changes at a critical value of mean wind speed ($\overline{V}$) at a given height, characterizing the hockey stick transition between the stable (weak wind) and the near-neutral (strong wind) regimes (Sun et al. 2015). For the weak-wind regime, V_{TKE} increases slightly with $\overline{V}$, and for the strong-wind regime V_{TKE} increases rapidly with $\overline{V}$ when $\overline{V}$ exceeds the critical value.

For some decades simple models have been used to describe the interactions between turbulence, mean wind speed and stability whitin the SBL. Blackadar (1979) introduced a model for air–surface interactions in which prognostic equations for the velocity components, air and surface temperatures are solved. Turbulent fluxes are estimated using a first-order closure with the gradients of mean quantities and stability functions. McNider et al. (1995) showed that in the Blackadar model very small pertubations of the geostrophic wind speed are sufficient to force the SBL to switch regimes.

It is not yet entirely clear why there are two different regimes with such contrasting characteristics, and the abrupt transition between them illustrated in the modelling results of McNider et al. (1995) and observations presented by Acevedo and Fitzjarrald (2003). Using simple reasoning based on energy budget and similarity arguments, van de Wiel et al. (2012a) argued that there is a minimum wind speed above which the turbulent energy is able to totally transfer the cold air from the radiatively cooled surface to the atmosphere above. Sun et al. (2016) suggested that in the weak-wind regime the energy supplied by the mean wind shear is partially converted to turbulent potential energy (TPE), defined as $TPE \equiv 1/2\,[(g/\Theta N)]^2\,\overline{\theta'^2}$, where g is the acceleration due to gravity, Θ is the reference temperature, N is the Brunt-Vaisala frequency and $\overline{\theta'^2}$ is the temperature variance, limiting the increase of turbulent kinetic energy (TKE). In the strong-wind regime, on the other hand, TPE is reduced because the thermal gradient is reduced by turbulent mixing, allowing most of the shear-generated energy to be converted to TKE.

The present study tests the hypothesis that simple models are able to capture important aspects of the regime transition if the main physical processes driving the transition are included in their formulations. Four different numerical models with an increasing number of prognostic equations are considered and their ability to reproduce the regime transition is evaluated. The simplest one (long-tail model) solves prognostic equations for mean wind speed, mean temperature and surface temperature and uses a long-tail stability function to estimate turbulence as a function of the atmospheric stability. In the second model (e model),

TKE is directly solved by a prognostic equation. In addition to the set-up of the e model, a prognostic equation for heat fluxes is added in the third model (e-F_H model). Finally, an additional prognostic equation for $\overline{\theta'^2}$ is also considered in the fourth model (e-F_H-σ_θ model). Through this systematic approach, we address the role of the heat flux and $\overline{\theta'^2}$ in the observed regime transition.

2 Models

2.1 Historical Background

In early studies, turbulence in the atmospheric boundary layer was parametrized and only mean variables are solved by prognostic equations. These are the first-order schemes. In general, turbulence is parametrized similarly to molecular diffusion except that an eddy diffusivity (K) is applied rather than molecular diffusivity to relate fluxes to the mean gradients. The eddy diffusivity K was first assumed to be invariant (e.g., Ekman 1905; Taylor 1915), then to be an exponential function of height z (e.g., Köhler 1933),and later to be the widely used $K = \kappa u_* z$, where κ is the von Karman constant, u_* is the friction velocity. Following the suggestions of similarity approaches by Heisenberg (1948), Blackadar (1962) proposed $K = l^2 S$, where $l = \kappa z$ is the mixing length and S is the local wind shear.

Solving selected turbulence variables with prognostic equations while defining the others through parametrizations is commonly referred as a higher-order closure scheme, which was introduced in the 1960s (Donaldson and Rosenbaum 1968; Kline et al. 1968). Mellor and Yamada (1974) classified the sophistication of the turbulence closure in four levels. Their definitions of levels 1 and 2 are basically first-order schemes with no prognostic equations for any turbulence variables. Their level-3 scheme solves prognostic equations for TKE and temperature variances. In their level-4 scheme, all the turbulence variables of second-order moments, such as momentum and heat fluxes and variances of velocity components and temperature, are solved prognostically. Later on, Mellor and Yamada (1982) proposed a 2.5-level scheme, in which TKE is the only second-order moment that is solved prognostically. Meanwhile, Wyngaard and Coté (1974) proposed to add a prognostic equation for the turbulence dissipation rate to simulate the convective boundary layer (CBL). Applying the same approach, Wyngaard (1975) demonstrated its success in simulating the SBL.

A major problem with lower-order schemes concerns their excessive turbulent mixing, a commonly used solution for which is the use of a stability function, which forces the reduction of mixing as the stability increases. Commonly used stability functions may be described as short-tail, when turbulence is reduced to zero at a Richardson number larger than a critical value; or long-tail, when turbulent mixing never totally disappears even at large stability. The short-tail stability function is used in the Mellor and Yamada levels-1, -2, and -2.5 schemes, the long-tail stability function such as those developed by Louis (1979) and Delage (1997) are widely used in numerical weather and climate models because of their ability to mantain finite turbulent mixing even in very stable conditions. It is a means of simulating localized turbulence activity, which in nature may occur in parts of a numerical grid cell. Besides, maintaining weak turbulence provides an effective means of avoiding the so-called runaway cooling problem (Louis 1979; Steeneveld et al. 2006) that may occur when turbulence is suppressed abruptly by a short-tail approach, causing the surface to be cooled indefinitely through longwave radiation loss.

2.2 Basic Equations

For a dry atmosphere without consideration of advection and radiative flux divergence, the equations that describe the mean atmospheric variables can be written as (Blackadar 1979; McNider et al. 1995; Costa et al. 2011),

$$\frac{\partial \overline{u}}{\partial t} = f(\overline{v} - v_G) - \frac{\partial \overline{u'w'}}{\partial z}, \tag{1}$$

$$\frac{\partial \overline{v}}{\partial t} = f(u_G - \overline{u}) - \frac{\partial \overline{v'w'}}{\partial z}, \tag{2}$$

$$\frac{\partial \overline{\theta}}{\partial t} = -\frac{\partial \overline{w'\theta'}}{\partial z}, \tag{3}$$

and the surface temperature is determined by the force-restore method (Blackadar 1979)

$$\frac{\partial \overline{\theta_g}}{\partial t} = \frac{1}{c_g}(I_\downarrow - \sigma \overline{\theta_g^4} - H_0) - k_m(\overline{\theta_g} - \overline{\theta_m}) \,, \tag{4}$$

where $\overline{u}$, $\overline{v}$, $\overline{\theta}$ and $\overline{\theta_g}$ are the east–west, north–south velocity components, potential temperature and surface temperature, respectively. The Coriolis parameter is represented by f, while u_G and v_G are the zonal and meridional horizontal components of the geostrophic velocity above the atmospheric boundary layer. Specifying geostrophic velocity is equivalent to specifying external mechanical forcing due to the horizontal pressure gradient in models. In Eq. 4, c_g is the thermal capacity of the soil layer per unit area, k_m is the soil heat transfer coefficient, θ_m is the soil temperature below the surface, σ is the Stefan–Boltzmann constant. The term $H_0 = \rho c_P \overline{w'\theta'}_0$ is the surface sensible heat flux, where ρ is the air density, and c_P is the specific heat of air at constant pressure. The longwave radiative flux from the atmosphere $I_\downarrow$ is given by (Staley and Jurica 1972)

$$I_\downarrow = \sigma(Q_c + 0,67(1 - Q_c)(1670 Q_a)^{0.08})\theta_a^4 \,, \tag{5}$$

where Q_c is the cloud fraction, Q_a is the specific humidity at a reference height, and θ_a is the potential temperature at the boundary-layer top (50 m). The thermal capacity of the soil layer is given by (Blackadar 1979)

$$c_g = 0.95 \left(\frac{\lambda c_s \rho_s}{2\omega} \right)^{\frac{1}{2}}, \tag{6}$$

where λ is the surface thermal conductivity, ω is the earth angular frequency, c_s is the soil specific heat, and ρ_s represents soil density (Blackadar 1979).

2.2.1 The *e* Model

For a horizontally homogenous atmosphere, the TKE prognostic equation is

$$\frac{\partial \overline{e}}{\partial t} = -\overline{u'w'}\frac{\partial \overline{u}}{\partial z} - \overline{v'w'}\frac{\partial \overline{v}}{\partial z} + \frac{g}{\Theta}\overline{w'\theta'} - \frac{\partial}{\partial z}\left[\overline{w'e'} + \frac{\overline{p'w'}}{\rho_0}\right] - \epsilon_e, \tag{7}$$

where $\overline{e}$ is mean TKE, p is pressure, ρ_o is a reference density and Θ is a reference temperature. The terms on the right-hand side (r.h.s.) of Eq. 7 are the turbulence shear production (first and second terms), turbulence buoyant destruction (for stable conditions, third term), vertical

transport of TKE both by turbulence and by pressure fluctuations (fourth term), and the viscous dissipation of TKE (fifth term). The prognostic TKE equation is used to approximate the friction velocity as $u_* = \overline{e}^{\frac{1}{2}}/4$. This practice of solving TKE and hence determining u_* as a constant fraction of $\overline{e}^{\frac{1}{2}}$ is common in models (André et al. 1978; Therry and Lacarrere 1983; Duynkerke 1988; Xu and Taylor 1997, among others). According to Acevedo et al. (2014), the purely turbulent value of $\overline{e}u_*^{-2}$ at neutral conditions approaches 4, when the contributions of the low-frequency flow fluctuations are removed.

The fluxes in Eqs. 1–3 are parametrized as $-\overline{u'w'} = u_*^2 \cos\psi$ and $-\overline{v'w'} = u_*^2 \sin\psi$, where $\psi = \tan^{-1}\left[(\partial\overline{v}/\partial z)\,/\,(\partial\overline{u}/\partial z)\right]$. The shear production term is parametrized as Ωu_*^2, where Ω is the mean wind gradient that is defined as $\partial\sqrt{\overline{u}^2 + \overline{v}^2}/\partial z$ (Pielke 2013). The sensible heat flux is parametrized as $-\overline{w'\theta'} = u_*\theta_*$ (Wyngaard 1975; McNider et al. 1995), where θ_* is a temperature scale given by

$$\theta_* = K_H \frac{\partial\overline{\theta}}{\partial z}/u_*, \tag{8}$$

where K_H is the heat eddy diffusivity.

The exchange coefficient for momentum is parametrized as $K_m = u_* l$, where l is the mixing length given by $l = \kappa z$ (Pielke 2013). For simplicity, the turbulent Prandtl number (Pr_t) is assumed to be 1, so that the heat eddy diffusivity can be evaluated as $K_H = K_m/Pr_t$. Therefore, the buoyant destruction term in Eq. 7 can be rewritten $(g/\Theta)\overline{w'\theta'} = -Ri\Omega u_*^2$, where Ri is the gradient Richardson number, given by

$$Ri = \frac{g}{\Theta}\frac{\left(\partial\overline{\theta}/\partial z\right)}{\left(\partial\overline{u}/\partial z\right)^2 + \left(\partial\overline{v}/\partial z\right)^2}. \tag{9}$$

Following Duynkerke (1988), the TKE transport term is given by

$$-\left[\overline{w'e'} + \frac{\overline{p'w'}}{\rho_0}\right] = \frac{K_m}{\sigma_E}\frac{\partial\overline{e}}{\partial z}, \tag{10}$$

where σ_E is the turbulent Prandtl number for TKE (Duynkerke 1988). A value of 2.5 is assumed for σ_E in all simulations (Costa et al. 2011). The TKE viscous dissipation term is parametrized as $c_\varepsilon \overline{e}^{3/2}/l$ and can be rewritten as $c_e u_*^3/l$ using the relationship $\overline{e}u_*^{-2} = 4$, where c_ε and c_e are numerical constants. Following Cuxart et al. (2006), values from 0.08 to 0.7 have been used for c_ε so that values of c_e may vary from 0.64 to 5.6. We assume $c_e = 1.2$, because the results are very weakly sensitive to c_e at this range. Equation 7 can be rewritten as

$$\frac{\partial\overline{e}}{\partial t} = \Omega u_*^2 - Ri\Omega u_*^2 + \frac{\partial}{\partial z}\left(\frac{K_m}{\sigma_E}\frac{\partial\overline{e}}{\partial z}\right) - c_e\frac{u_*^3}{l}, \tag{11}$$

and with these parametrizations for the second-order moments, Eqs. 1–4 and 11 constitute a closed system of five equations for five unknown variables, $\overline{u}$, $\overline{v}$, $\overline{e}$, $\overline{\theta}$ and $\overline{\theta_g}$, which will be referred as the e model. This model is mathematically equivalent to the 2.5-level model proposed by Mellor and Yamada (1982).

2.2.2 Long-Tail Model

In this model u_* is directly dependent on the gradient Richardson number through a stability function $\phi(Ri)$ (Louis 1979)

$$u_* = \frac{\kappa z}{\phi^2(Ri)}\frac{\partial\overline{V}}{\partial z}, \tag{12}$$

where the stability function $\phi(Ri)$ is given by Louis (1979)

$$\phi(Ri) = 1 + 4.7Ri. \tag{13}$$

It is a long-tail formulation because it allows the existence of turbulent activity even at the limit of very large stability. As in the e model, the heat eddy diffusivity is given by $K_H = \kappa u_* z$, while the heat fluxes are given by the K theory. This scheme is equivalent to Mellor–Yamada level 1, but in that case a short-tail stability function is used.

2.2.3 e-F_H Model

The third model, that is, the e-F_H model consists of the equations from the e model, with the addition of a prognostic equation for the heat flux.

The heat-flux prognostic equation for a horizontally homogenous atmosphere is

$$\frac{\partial \overline{w'\theta'}}{\partial t} = -\overline{w'^2}\frac{\partial \overline{\theta}}{\partial z} + \overline{\theta'^2}\frac{g}{\Theta} - \frac{\partial \overline{w'w'\theta'}}{\partial z} + \frac{1}{\overline{\rho}}\overline{\theta'\frac{\partial p'}{\partial z}}\,, \tag{14}$$

where the first term on the r.h.s. of Eq. 14 represents the thermal gradient production of downward heat flux in the SBL. The second term is buoyant destruction, while the third and fourth terms represents the transport by turbulence and pressure fluctuations, respectively. Therry and Lacarrere (1983) suggested that the last term of Eq. 14 can be parametrized as a sum of two contributions, the first being proportional to the heat flux itself and the second being proportional to the temperature variance

$$\frac{1}{\overline{\rho}}\overline{\theta'\frac{\partial p'}{\partial z}} = -C_1\frac{\epsilon_e}{\overline{e}}\overline{w'\theta'} - C_2\frac{g}{\Theta}\overline{\theta'^2} = -C_2\frac{g}{\Theta}\overline{\theta'^2} - C_\theta\frac{u_*}{l}\overline{w'\theta'} \tag{15}$$

where C_1, C_2 and C_θ are numerical constants. Therry and Lacarrere (1983) suggested $C_2 = 0.4$ but had no suggestion for C_θ; we used $C_\theta = 2$.

Therefore, with all these approximations, Eq. 14 can be rewritten as

$$\frac{\partial \overline{w'\theta'}}{\partial t} = -\overline{w'^2}\frac{\partial \overline{\theta}}{\partial z} + (1 - C_2)\overline{\theta'^2}\frac{g}{\Theta} + \frac{\partial}{\partial z}\left[\frac{K_m}{\sigma_1}\frac{\partial \overline{w'\theta'}}{\partial z}\right] - C_\theta\frac{u_*}{l}\overline{w'\theta'}. \tag{16}$$

The turbulent transport term is parametrized in analogy to its equivalent term in the TKE equation

$$-\frac{\partial \overline{w'w'\theta'}}{\partial z} = \frac{\partial}{\partial z}\left[\frac{K_m}{\sigma_1}\frac{\partial \overline{w'\theta'}}{\partial z}\right] \tag{17}$$

where σ_1 is a numerical constant $= 2$.

The e-F_H model, therefore, consists of a 6-equation system, composed of Eqs. 1–4, 11 and 16. The additional unknowns in Eq. 16 are parametrized as $\overline{w'^2} = 1.44u_*^2$ (Acevedo et al. 2014) and as $\overline{\theta'^2} = 4\theta_*^2$. This model may be compared to Mellor and Yamada's level 3, except the heat flux instead of the temperature variance is solved with a prognostic equation, which is important as shown later.

2.2.4 e-F_H-σ_θ Model

In the e-F_H-σ_θ model, the temperature variance that appears in Eq. 16 is also solved through its prognostic equation, rather than parametrized. For a horizontally homogeneous atmosphere, and neglecting radiative terms, such a prognostic equation is

Table 1 Soil parameters

λ	Surface thermal conductivity	0.06 W m^{-1} K^{-1}
c_s	Soil specific heat	1.92×10^3 J kg^{-1} K^{-1}
ρ_s	Soil density	0.30×10^3 kg m^{-3}

$$\frac{\partial \overline{\theta'^2}}{\partial t} = -2\overline{w'\theta'}\frac{\partial \overline{\theta}}{\partial z} - \frac{\partial \overline{w'\theta'^2}}{\partial z} - \epsilon_\theta, \tag{18}$$

where the first term in the r.h.s. is the heat-flux production of temperature variance, the second is the turbulent transport of temperature variance and the third is its molecular dissipation. Using analogous parametrizations for the second and third terms to those employed for the corresponding terms in the TKE equation, the temperature variance prognostic equation becomes

$$\frac{\partial \overline{\theta'^2}}{\partial t} = -2\overline{w'\theta'}\frac{\partial \overline{\theta}}{\partial z} - \frac{\partial}{\partial z}\left[\frac{K_m}{\sigma_1}\frac{\partial \overline{\theta'^2}}{\partial z}\right] - C_3\frac{\overline{e}^{\frac{1}{2}}}{l}\overline{\theta'^2}, \tag{19}$$

where C_3 is a numerical constant $= 8$.

Therefore, the e-F_H-σ_θ model consists of Eqs. 1–4, 11, 16 and 19. In Mellor and Yamada's hierarchy it lies near level 4, with the important difference that momentum fluxes are not directly solved.

2.3 Model Integration

The methodology utilized to solve the prognostic equations Eqs. 1–3, 11, 16 and 19 is similar to that used by McNider et al. (1995), van de Wiel et al. (2002) and Costa et al. (2011), employing method of lines (Kreiss and Lorenz 1989). A 50-m deep SBL is assumed between the surface ($z = 0$) and $h = 50$ m. In this layer five main levels are considered, with the first fixed at $z_1 = 5$ m and the other levels being equally spaced between the first level and the top. To estimate the turbulent-flux divergences at the main levels, the prognostic equations for TKE, heat flux and temperature variance are calculated at intermediate levels (z_i), which are set up in between the main levels. Discrete forms of Eqs. 1–4, 11, 16, 19 are integrated in time by using a fourth-order Runge–Kutta algorithm for 20 h, with a timestep of 0.1 s.

At the domain top, the mean variables are assumed to be $\overline{u}(t,h) = u_G$, $\overline{v}(t,h) = 0$ and $\overline{\theta}(t,h) = \Theta$, where $\Theta = 300$ K. At the surface, the no-slip condition is assumed ($\overline{u}(t,0) = \overline{v}(t,0) = 0$), and the substrate temperature is considered as $\theta_m = 282$ K. At the first level, the initial condition for zonal velocity component is $\overline{u}(0,z_1) = 0.1$ m s^{-1} and this quantity varies linearly between this level and the domain top are the wind speed assumed geostrophic. For the meridional velocity component, the initial condition at all levels is $\overline{v}(0,z) = v_G = 0$. The initial condition for the surface and air temperatures is the same: $\theta_g(0) = \Theta$ and $\overline{\theta}(0,z) = \Theta$. The initial value for TKE at all the intermediate levels is set to be $\overline{e}(0,z_i) = \overline{e}_0 = 0.005$ m^2 s^{-2}, which is also assumed to be the minimum TKE value at any height to ensure numerical stability Costa et al. (2011). The surface heat flux $\overline{w'\theta'}_0$ is assumed to be the same as the heat flux calculated at the first intermediate level with Eq. 16, while the surface temperature variance is assumed to be zero. The soil constants are shown in Table 1.

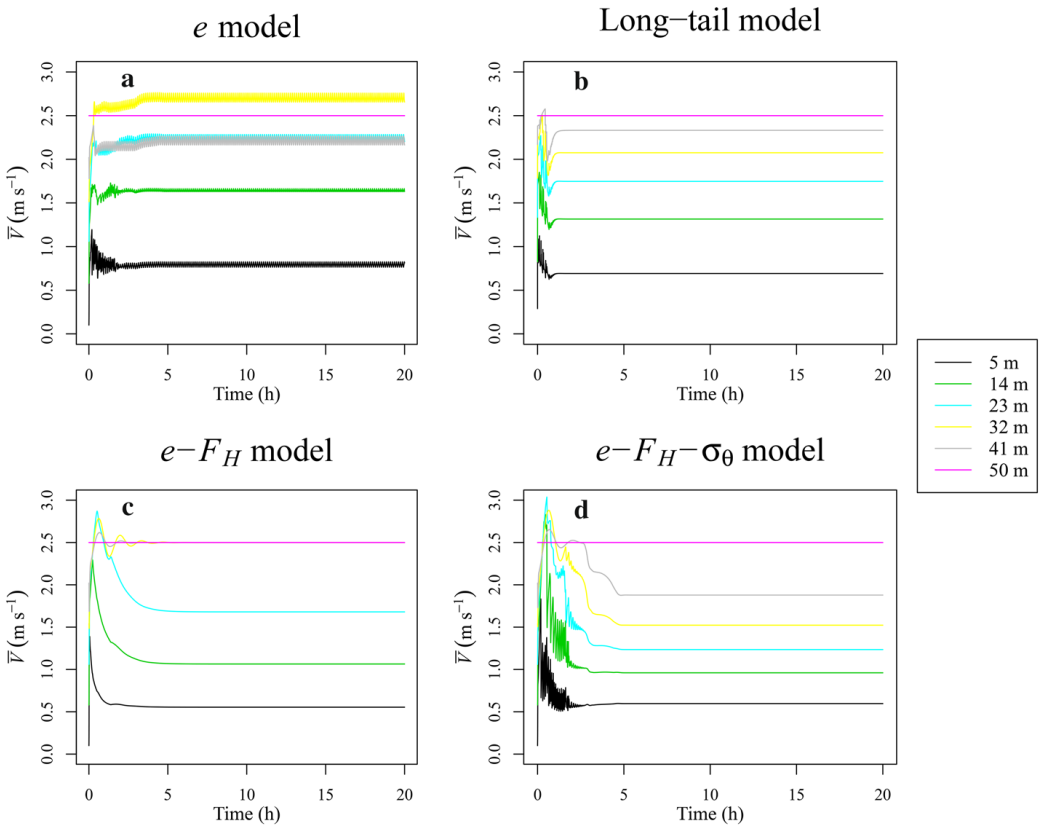

Fig. 1 Wind speed solved by the different models (as identified above each panel) for the different vertical levels, as given by legend. A geostrophic wind speed of $u_G = 2.5$ m s^{-1} was used

3 Results

We present results from the four models: the long-tail model, the e model, the e-F_H model and the e-F_H-σ_θ model. All the models reach an equilibrium state after 2–5 h of simulation (Fig. 1). All the figures are based on the results averaged over the last 5 h of simulation, that is, between hours 15 and 20 into each simulation. Looking at equilibrium conditions allows identifying how the SBL reaches the weak-wind or the strong-wind stability in each model.

The results from the three models with the solved TKE differ between each other for $u_G = 1.75$ m s^{-1}, and are similar for $u_G = 9$ m s^{-1} (Fig. 2). With $u_G = 1.75$ m s^{-1}, the e model results in the greatest wind speeds (Fig. 2a), highest temperature (Fig. 2d), and lowest TKE (Fig. 2g). The highest temperature from the e model is due to its largest parametrized surface heat flux with K theory (-0.04 K m s^{-1}) in comparison with the solved heat fluxes from the e-F_H and the e-F_H-σ_θ models (-0.0034 K m s^{-1} and -0.0017 K m s^{-1}, respectively). The larger heat fluxes in the e model are a consequence of a larger vertical temperature gradient near the surface than in the other two models. The large stability near the surface also reduces the TKE in the e model, a situation that changes when a empirically developed long-tail stability function is considered. In that case, the equilibrium surface heat flux from the long-tail model (-0.0055 K m s^{-1}) is closer to that from the e-F_H and from the e-F_H-σ_θ models, resulting in profiles of mean wind speed, temperature, and TKE that are similar to those from the e-F_H-σ_θ model. This results indicate that, with low u_G, the long-tail stability function provides small turbulent heat fluxes, similar to those resolved

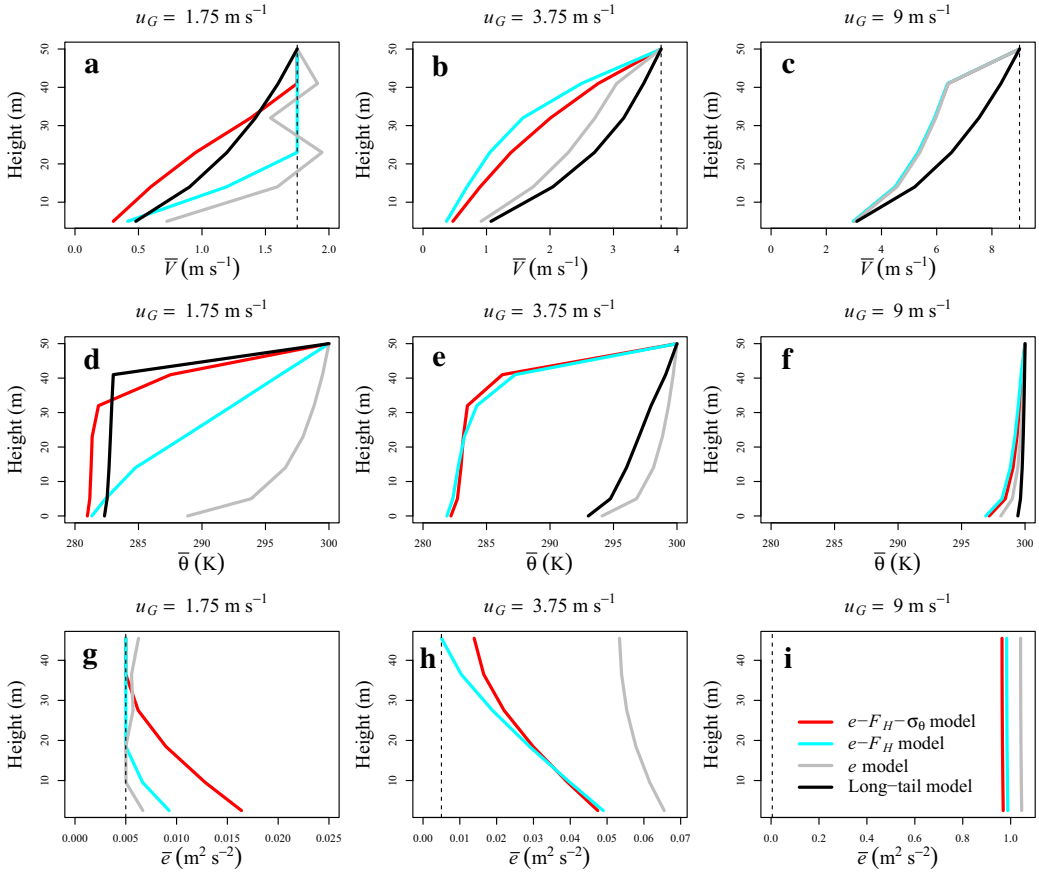

Fig. 2 Vertical profiles of wind speed (**a**, **b**, **c**), potential temperature (**d**, **e**, **f**) and TKE (**g**, **h**, **i**) averaged for the last five hours of the 5-level simulation for $u_G = 1.75$ m s^{-1} (**a**, **d**, **g**), $u_G = 3.75$ m s^{-1} (**b**, **e**, **h**) and $u_G = 9$ m s^{-1} (**c**, **f**, **i**). Different lines indicate the different models, as given by legend at panel (**i**). The TKE panels (**g**, **h**, **i**) do not present results from the long-tail model as this variable is not solved prognostically in this case

from the flux prognostic equation. Because TKE decreases rapidly with height for low u_G, the e model with the smallest TKE, reaches the preset minimum TKE e_0 at a low height. With the additrional prognostic equations introduced in the e-F_H and the e-F_H-σ_θ models, their TKE values reach e_0 at higher levels (Fig. 2g).

As the geostrophic wind speed increases to $u_G = 3.75$ m s^{-1}, TKE in the entire SBL from the e model becomes the largest among all the models while its stratification is largest. The largest TKE is associated with the fact that this model has experienced the regime transition at this value of u_G, while the others have not yet done so (Fig. 3).

Meanwhile, the profiles of mean wind speed, $\overline{\theta}$, and TKE from the e-F_H and the e-F_H-σ_θ models converge. With $u_G = 9$ m s^{-1}, all the profiles are similar regardless of the models (Fig. 2c, f, i).

Because the simulated air temperatures from all the models increase with geostrophic wind speed, the stability regime change in the boundary layer can be studied based on the surface–air coupling as a function of geostrophic wind forcing (Acevedo et al. 2012). Investigation of the air temperature at the lowest level as a function of geostrophic wind speed indicates that the stability regime change occurs for all the models, but the transition between the weak and the strong stability regimes occurs abruptly around 5 m s^{-1} for the

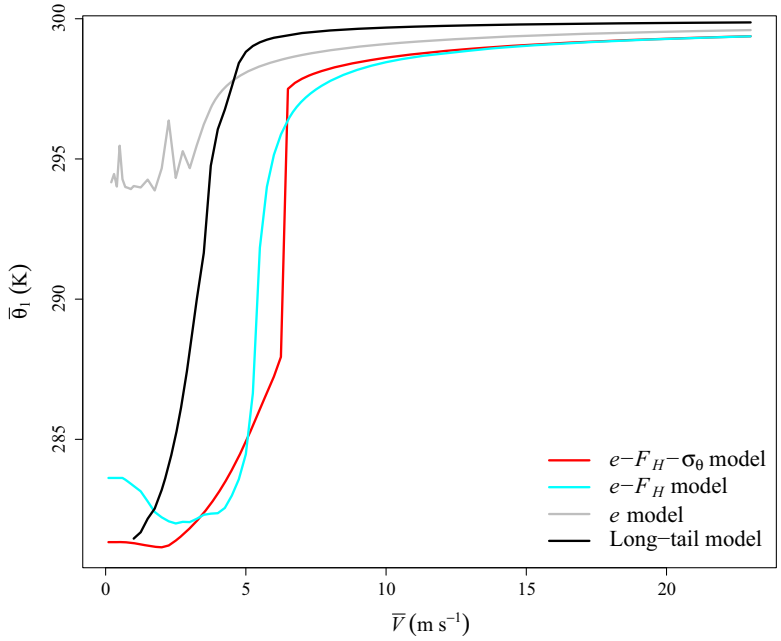

Fig. 3 Equilibrium temperature at the lowest vertical level as a function of the geostrophic wind speed for each of the formulations considered, according to legend

e-F_H and the e-F_H-σ_θ models. Acevedo et al. (2012) compared simple TKE schemes with or without stability functions, and found that the use of stability functions causes the transition to become less abrupt than when they are not used. This value is close to the range of the minimum geostrophic wind speed for maintaining moderate to strong turbulence found by van de Wiel et al. (2012a, b), based on similarity and energy budget arguments. Similarly, using an extensive observational dataset, van der Linden et al. (2017) showed that quantities such as friction velocity and sensible heat flux have, on the average, magnitudes substantially larger than zero only for geostrophic wind speeds > 4 m s^{-1}. The use of a stability function causes surface air temperatures to approach those from the e-F_H and e-F_H-σ_θ models in the weak-wind regime. However, the regime transition of the model that uses stability function occurs at the same low geostrophic wind speed that drives the regime transition in the e model.

The relationship between the turbulence velocity scale V_{TKE} and the mean wind speed $\overline{V}$ at a given height has been used to determine the SBL stability regimes (Sun et al. 2012). The results from the three models with TKE solved show distinctively different relationships between both quantities (Fig. 4), and in the strong-wind regime, the relationship is very similar among the models. That is, V_{TKE} increases linearly with $\overline{V}$, and the rate of increase varies with height. At all the levels, the $V_{TKE} \times \overline{V}$ lines from the strong-wind regime may be extrapolated towards the origin ($\overline{V} = 0$ and $V_{TKE} = 0$) (dashed lines in Fig. 4). The main differences between the models occur in the weak-wind regime and, more importantly, in the transition between the weak-wind and the strong-wind regimes. In the simple e model, V_{TKE} varies significantly and is nearly independent of $\overline{V}$ for wind speeds smaller than the transition threshold wind speed V_T (Fig. 4a). This near independence between V_{TKE} and $\overline{V}$ in the weak-wind regime is not largely affected when a prognostic equation for the heat flux is included (Fig. 4b). However, the additional inclusion of a prognostic equation for the temperature variance in the e-F_H-σ_θ makes it possible to define a weak-wind regime where V_{TKE} linearly

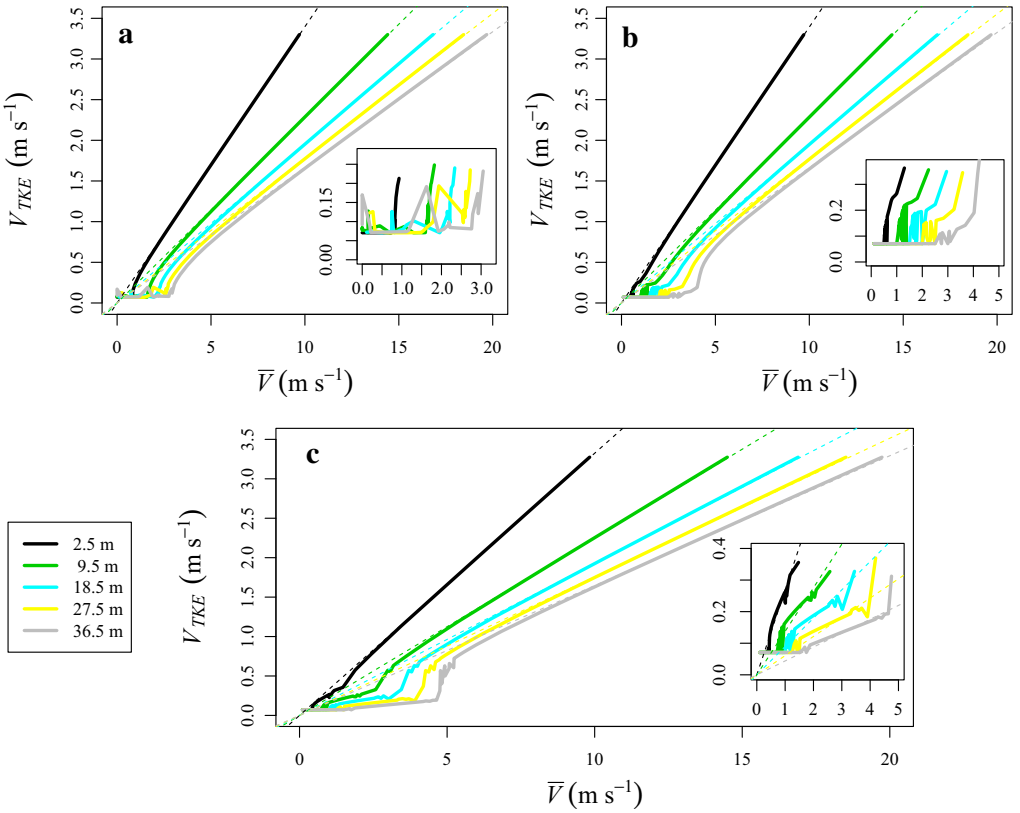

Fig. 4 Average dependence of turbulence velocity scale V_{TKE} on the mean wind speed $\overline{V}$ for the e model (**a**), e-F_H model (**b**) and e-F_H-θ_θ model (**c**) at the different vertical levels (according to legend). Insets show zooms on the weak-wind regime

increases with mean wind speed. Furthermore, similarly to what occurs in the strong-wind regime, the $V_{TKE} \times \overline{V}$ lines for the weak-wind regime may also be extrapolated towards the origin (Fig. 4c, inset), but with smaller slopes. When the buoyancy term, $(g/\Theta)\overline{w'\theta'}$, is removed from Eq. 7 in all the models (Fig. 5), the $V_{TKE} \times \overline{V}$ diagrams display a single regime that coincides with those for the strong-wind regime in Fig. 4. This simple result shows that the transition is, in all cases, fully driven by the TKE buoyant destruction term.

The fact that $V_{TKE} \times \overline{V}$ lines from the strong-wind regime may be extrapolated towards the origin shows that the ratio between the two quantities is constant in that regime, and varies vertically. Such a ratio is, in fact, proportional to the square root of the drag coefficient, defined as $C_D \equiv (u_*/\overline{V})^2$, given that all schemes assume $\overline{e}/u_*^2 = 4$. Therefore, all schemes provide constant drag coefficients in the strong-wind regime, decreasing with height (Fig. 6). Such a result was not observed by Sun et al. (2012) for the CASES-99 dataset, where the slope of the $V_{TKE} \times \overline{V}$ lines in the strong-wind regime is nearly independent of height, and with finite and variable intercepts (the $V_{TKE} \times \overline{V}$ lines from the different levels are nearly parallel to each other). In such a case, the observed drag coefficients vary with mean wind speed for any given height. On the other hand, the $V_{TKE} \times \overline{V}$ diagram presented by Acevedo et al. (2016) for the FLOSSII site indicates relationships between the two variables in the strong-wind regime that resemble those simulated by the models used herein. They present variable slopes with near-zero intercepts, which lead to drag coefficients independent of mean wind speed for a given height. It is possible therefore, that site characteristics dictate whether drag coefficients depend on mean wind speed or not in the strong-wind regime. As

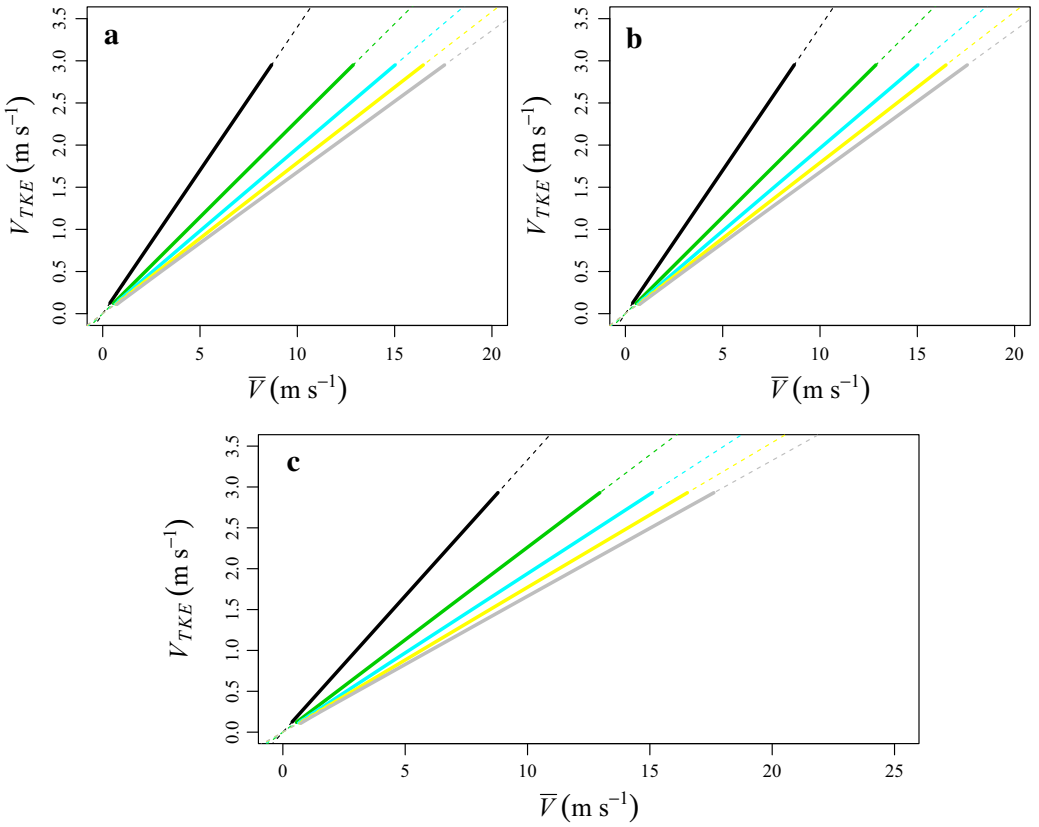

Fig. 5 The same as in Fig. 4, but for the cases when the buoyant term from the TKE prognostic equation is set to zero: **a** e model; **b** e-F_H model; **c** e-F_H-σ_θ model

shown in Fig. 4, the e-F_H-σ_θ model also presents a range in the weak-wind regime where the $V_{TKE} \times \overline{V}$ lines may be extrapolated towards the origin, although with a smaller slope than occurs in the strong-wind regime. Therefore, such a scheme also presents a range of mean wind speeds in the weak-wind range for which the drag coefficients are near constant and height dependent (Fig. 6c). Such a range is broader at the higher levels. The drag coefficients obtained when the buoyant term is set to zero in Eq. 7 are shown as dashed lines in Fig. 6, confirming that in the strong-wind limit the relationship between turbulence and mean wind speed is unaffected by buoyancy.

In all the model simulations, the threshold wind speed for the transition between the weak-wind and strong-wind stability regimes V_T increases with height, which is similar to that observed in both Sun et al. (2012) and Acevedo et al. (2016). However, the magnitudes of V_T from all the models are much smaller than the observed values. Nonetheless, the modelled V_T increases with the increasing number of turbulence variables resolved with prognostic equations. Overall, the results indicate that the solution of more prognostic equations in the model tends to cause its transition to occur at conditions more similar to those observed in nature (Fig. 7).

Furthermore, other quantities in the e-F_H-σ_θ model are also qualitatively similar to what has been observed in both regimes. The heat flux converges to a constant value at the strong-wind limit (Fig. 8a, b), which is in agreement with the observations from Mahrt (2017) and van der Linden et al. (2017). At the regime transition the heat-flux dependence on wind speed presents an inflection point, as found by Acevedo et al. (2016). When the fluxes are referred

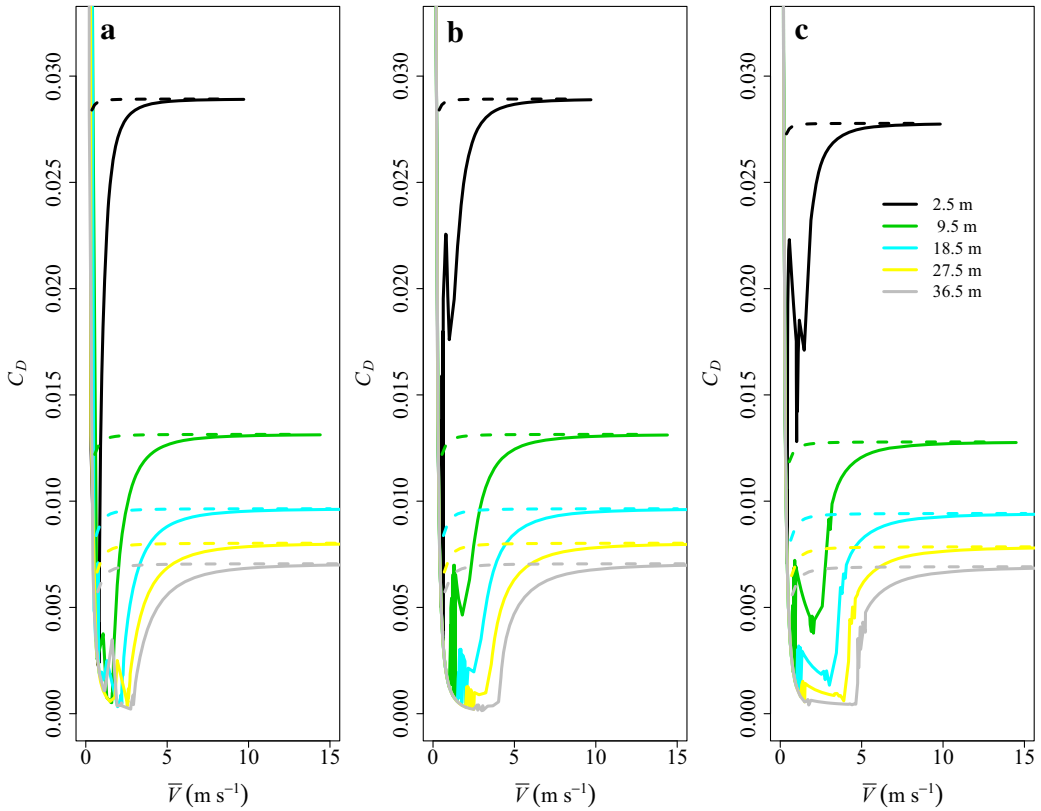

Fig. 6 Solid line show the drag coefficients as a function of the mean wind speed for models e (**a**), e-F_H (**b**) and e-F_H-σ_θ (**c**) (solid lines) at the different vertical levels, according to legend in panel (**c**). The dashed lines represent the same drag coefficients when the buoyant term from the TKE prognostic equation is set to zero

to the mean wind speed at a fixed level (Fig. 8b), it is seen that the equilibrium solution of the model has constant fluxes with height, as imposed by the equilibrium state of Eq. 3. The temperature scale, $\theta_* \equiv -\overline{w'\theta'}/u_*$, peaks at the transition (Fig. 8c, d), which is in agreement with observations in Sun et al. (2012). This result was explained by Sun et al. (2016): in the weak-wind regime the increase of TKE near the surface is constrained by the energy used for increasing TPE through the buoyancy flux. In the strong-wind regime, on the other hand, all the energy may be used to increase TKE, so that TPE peaks at the transition. The modelled TPE is indeed shown to have a maximum value at the regime transition at a given height (Fig. 8e, f), which is consistent with the Sun et al. (2016) explanation.

4 Conclusions

Many recent studies (Mahrt 1998; Sun et al. 2012; van Hooijdonk et al. 2015; Acevedo et al. 2016) have observed the existence of two regimes in the stable boundary layer (SBL) separated by a wind-speed threshold. In the present study we determined the least number of prognostic equations that needs to be solved in a simplified model to properly reproduce the observed characteristics of the transition between these two regimes.

The most important result is that the realistic simulation of the transition between the two regimes requires that heat fluxes are solved using a prognostic equation instead of being

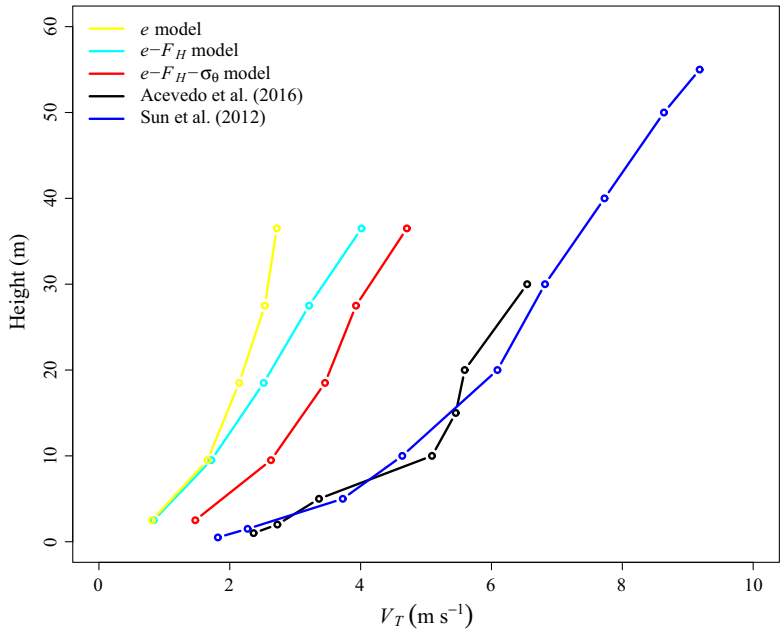

Fig. 7 Mean wind speed at which the transition between regimes occour at the different vertical levels in the different models and the values observed by Sun et al. (2012) for the CASES-99 experiment and by Acevedo et al. (2016) for the FLOSSII experiment

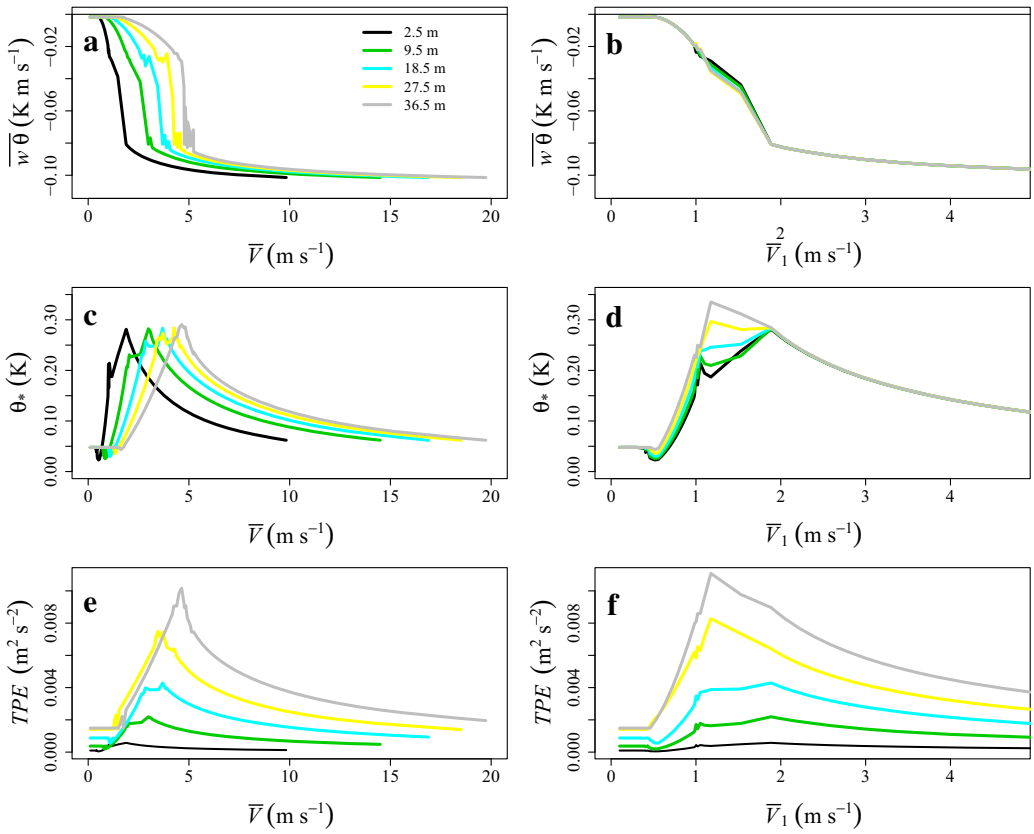

Fig. 8 Average dependence of **a**, **b** the sensible heat flux, **c**, **d** temperature scale and **e**, **f** turbulent potential energy on the mean wind speed $\overline{V}$ at each level (**a**, **c**, **e**) and on the mean wind speed at the lowest atmospheric level (**b**, **d**, **f**)

parametrized. This result confirms the role of heat fluxes in determining the regime transition found in previous studies. For example, van de Wiel et al. (2012a) associated the threshold wind speed with the maximum downward heat flux through the surface energy balance; Sun et al. (2016) found the small increase of TKE with wind speed in the weak-wind regime with the heat flux through its effect on turbulent potential energy; Acevedo et al. (2016) showed that the buoyant destruction is relatively much more important to the TKE budget in the weak-wind than in the strong-wind regime.

The present study further demonstrates that the strong-wind regime is approximately independent of heat fluxes and can be achieved regardless of the number of prognostic equations being used and whether or not the buoyant term is included in the TKE budget equation. Therefore, in the strong-wind regime the turbulent flow is mainly driven by shear production and dissipation, while in the weak-wind regime, complex variations of the turbulent variables are controlled by heat fluxes. In addition, the observed increase of TKE with mean wind speed in the weak-wind regime can only be simulated when the prognostic equation for temperature variance is included. Future studies may address the question whether additional prognostic equations further improve the representation of the weak-wind regime.

Turbulence schemes used in numerical weather and climate models are either first-order, in which case they solve prognostic equations for mean variables and parametrize all higher-order moments, or they are TKE models, for which the only higher-order moment solved is TKE (Cuxart et al. 2006; Svensson et al. 2011). These are equivalent to the Mellor–Yamada 1-, 2- and 2.5-level models. We have shown that inclusion of an additional prognostic equation for heat fluxes can directly solve the effects of heat transfer on atmospheric motions so that stability functions, which are empirically developed based on simple similarity theories, are no longer required. In addition, the transition between the two stability regimes can be simulated more realistically. Considering current difficulties current performing numerical weather prediction of the SBL especially in the weak-wind (stable) regime (Battisti et al. 2017), the addition of prognostic equations for heat transfer may be highly beneficial for their performance.

Acknowledgements The study was supported by Conselho Nacional de Desenvolvimento Científico e Tecnológico (CNPq) (Grant No. 307024/2017-2) and by Coordenação de Aperfeiçoamento de Pessoal de Nível Superior (CAPES).

References

Acevedo OC, Fitzjarrald DR (2003) In the core of the night-effects of intermittent mixing on a horizontally heterogeneous surface. Boundary-Layer Meteorol 106(1):1–33

Acevedo OC, Costa FD, Degrazia GA (2012) The coupling state of an idealized stable boundary layer. Boundary-Layer Meteorol 145(1):211–228

Acevedo OC, Costa FD, Oliveira PE, Puhales FS, Degrazia GA, Roberti DR (2014) The influence of submeso processes on stable boundary layer similarity relationships. J Atmos Sci 71(1):207–225

Acevedo OC, Mahrt L, Puhales FS, Costa FD, Medeiros LE, Degrazia GA (2016) Contrasting structures between the decoupled and coupled states of the stable boundary layer. Q J R Meteorol Soc 142(695):693–702. https://doi.org/10.1002/qj.2693

André J, De Moor G, Lacarrere P, Du Vachat R (1978) Modeling the 24-hour evolution of the mean and turbulent structures of the planetary boundary layer. J Atmos Sci 35(10):1861–1883

Battisti A, Acevedo OC, Costa FD, Puhales FS, Anabor V, Degrazia GA (2017) Evaluation of nocturnal temperature forecasts provided by the weather research and forecast model for different stability regimes and terrain characteristics. Boundary-Layer Meteorol 162(3):523–546

Blackadar A (1979) High resolution models of the planetary boundary layer. Adv Environ Sci Eng 1(1):50–85

Blackadar AK (1962) The vertical distribution of wind and turbulent exchange in a neutral atmosphere. J Geophys Res 67(8):3095–3102

Costa FD, Acevedo OC, Mombach JC, Degrazia GA (2011) A simplified model for intermittent turbulence in the nocturnal boundary layer. J Atmos Sci 68(8):1714–1729

Cuxart J, Holtslag AAM, Beare RJ, Bazile E, Beljaars A, Cheng A, Conangla L, Ek M, Freedman F, Hamdi R, Kerstein A, Kitagawa H, Lenderink G, Lewellen D, Mailhot J, Mauritsen T, Perov V, Schayes G, Steeneveld GJ, Svensson G, Taylor P, Weng W, Wunsch S, Xu KM (2006) Single-column model intercomparison for a stably stratified atmospheric boundary layer. Boundary-Layer Meteorol 118(2):273–303

Delage Y (1997) Parameterising sub-grid scale vertical transport in atmospheric models under statically stable conditions. Boundary-Layer Meteorol 82(1):23–48

Donaldson C, Rosenbaum H (1968) Calculation of turbulent shear flows through closure of the Reynolds equations by invariant modelling. Aeronautical Research Associates of Princeton, p 127

Duynkerke PG (1988) Application of the e−ϵ turbulence closure model to the neutral and stable atmospheric boundary layer. J Atmos Sci 45(5):865–880. https://doi.org/10.1175/1520-0469(1988)045<0865:AOTTCM>2.0.CO;2

Ekman VW (1905) On the influence of the earth's rotation on ocean currents. Ark Mat Astr Fys 2:11

Heisenberg W (1948) On the theory of statistical and isotropic turbulence. Proc R Soc Lond A 195(1042):402–406

Kline S, Morkovin M, Sovran G, Cockrell D (1968) Computation of turbulent boundary layers. In: AFOSR-IFP-stanford conference, vol 2

Köhler H (1933) Meteorologische turbulenz untersuchungen. K Seven vetenskakad handl 13

Kreiss HO, Lorenz J (1989) Initial-boundary value problems and the Navier–Stokes equations, vol 47. SIAM, New Delhi, p 420

Louis JF (1979) A parametric model of vertical Eddy fluxes in the atmosphere. Boundary-Layer Meteorol 17(2):187–202. https://doi.org/10.1007/BF00117978

Mahrt L (1998) Nocturnal boundary-layer regimes. Boundary-Layer Meteorol 88(2):255–278. https://doi.org/10.1023/A:1001171313493

Mahrt L (2017) Stably stratified flow in a shallow valley. Boundary-Layer Meteorol 162(1):1–20. https://doi.org/10.1007/s10546-016-0191-4

Malhi YS (1995) The significance of the dual solutions for heat fluxes measured by the temperature fluctuation method in stable conditions. Boundary-Layer Meteorol 74(4):389–396. https://doi.org/10.1007/BF00712379

McNider RT, England DE, Friedman MJ, Shi X (1995) Predictability of the stable atmospheric boundary layer. J Atmos Sci 52(10):1602–1614. https://doi.org/10.1175/1520-0469(1995)052<1602:POTSAB>2.0.CO;2

Mellor GL, Yamada T (1974) A hierarchy of turbulence closure models for planetary boundary layers. J Atmos Sci 31(7):1791–1806

Mellor GL, Yamada T (1982) Development of a turbulence closure model for geophysical fluid problems. Rev Geophys 20(4):851–875

Oyha Y, Neff DE, Meroney RN (1997) Turbulence structure in a stratified boundary layer under stable conditions. Boundary-Layer Meteorol 83(1):139–162. https://doi.org/10.1023/A:1000205523873

Pielke RA Sr (2013) Mesoscale meteorological modeling, vol 98. Academic Press, New York

Staley D, Jurica G (1972) Effective atmospheric emissivity under clear skies. J Appl Meteorol 11(2):349–356

Steeneveld GJ, van de Wiel BJH, Holtslag AAM (2006) Modeling the evolution of the atmospheric boundary layer coupled to the land surface for three contrasting nights in "CASES-99". J Atmos Sci 63(3):920–935. https://doi.org/10.1175/JAS3654.1

Sun J, Mahrt L, Banta RM, Pichugina YL (2012) Turbulence regimes and turbulence intermittency in the stable boundary layer during "CASES-99". J Atmos Sci 69(1):338–351

Sun J, Mahrt L, Nappo C, Lenschow DH (2015) Wind and temperature oscillations generated by waveturbulence interactions in the stably stratified boundary layer. J Atmos Sci 72(4):1484–1503. https://doi.org/10.1175/JAS-D-14-0129.1

Sun J, Lenschow DH, LeMone MA, Mahrt L (2016) The role of large-coherent-Eddy transport in the atmospheric surface layer based on "CASES-99" observations. Boundary-Layer Meteorol 160(1):83–111. https://doi.org/10.1007/s10546-016-0134-0

Svensson G, Holtslag AAM, Kumar V, Mauritsen T, Steeneveld GJ, Angevine WM, Bazile E, Beljaars A, de Bruijn EIF, Cheng A, Conangla L, Cuxart J, Ek M, Falk MJ, Freedman F, Kitagawa H, Larson VE, Lock A, Mailhot J, Masson V, Park S, Pleim J, Söderberg S, Weng W, Zampieri M (2011) Evaluation of the diurnal cycle in the atmospheric boundary layer over land as represented by a variety of single-column models: the second "GABLS" experiment. Boundary-Layer Meteorol 140(2):177–206

Taylor MG (1915) I: Eddy motion in the atmosphere. Philos Trans R Soc Lond A 215(523–537):1–26

Therry G, Lacarrere P (1983) Improving the Eddy kinetic energy model for planetary boundary layer description. Boundary-Layer Meteorol 25(1):63–88. https://doi.org/10.1007/BF00122098
van Hooijdonk IGS, Donda JMM, Clercx HJH, Bosveld FC, van de Wiel BJH (2015) Shear capacity as prognostic for nocturnal boundary layer regimes. J Atmos Sci 72(4):1518–1532. https://doi.org/10.1175/JAS-D-14-0140.1
van der Linden SJA, Baas P, van Hooft JA, van Hooijdonk IGS, Bosveld FC, van de Wiel BJH (2017) Local characteristics of the nocturnal boundary layer in response to external pressure forcing. J Appl Meteorol Clim 56(11):3035–3047. https://doi.org/10.1175/JAMC-D-17-0011.1
van de Wiel B, Ronda R, Moene A, De Bruin H, Holtslag A (2002) Intermittent turbulence and oscillations in the stable boundary layer over land "part I": a bulk model. J Atmos Sci 59(5):942–958
van de Wiel BJH, Moene AF, Jonker HJJ, Baas P, Basu S, Donda JMM, Sun J, Holtslag AAM (2012a) The minimum wind speed for sustainable turbulence in the nocturnal boundary layer. J Atmos Sci 69(11):3116–3127. https://doi.org/10.1175/JAS-D-12-0107.1
van de Wiel BJH, Moene AF, Jonker HJJ (2012b) The cessation of continuous turbulence as precursor of the very stable nocturnal boundary layer. J Atmos Sci 69(11):3097–3115. https://doi.org/10.1175/JAS-D-12-064.1
Wyngaard JC (1975) Modeling the planetary boundary layer: extension to the stable case. Boundary-Layer Meteorol 9(4):441–460. https://doi.org/10.1007/BF00223393
Wyngaard JC, Coté O (1974) The evolution of a convective planetary boundary layera higher-order-closure model study. Boundary-Layer Meteorol 7(3):289–308
Xu D, Taylor PA (1997) On turbulence closure constants for atmospheric boundary-layer modelling: neutral stratification. Boundary-Layer Meteorol 84(2):267–287

4 ARTIGO 2 - THE NOCTURNAL BOUNDARY LAYER TRANSITION FROM WEAKLY TO VERY STABLE. PART I: OBSERVATIONS

Received: 26 March 2019 | Revised: 1 August 2019 | Accepted: 7 August 2019

DOI: 10.1002/qj.3642

RESEARCH ARTICLE

Quarterly Journal of the Royal Meteorological Society RMetS

The nocturnal boundary layer transition from weakly to very stable. Part I: Observations

Otávio C. Acevedo[1] | Rafael Maroneze[1] | Felipe D. Costa[2] | Franciano S. Puhales[1] | Gervásio A. Degrazia[1] | Luis G. Nogueira Martins[1] | Pablo E. Soares de Oliveira[1] | Luca Mortarini[1,3]

[1]Department of Physics, Universidade Federal de Santa Maria, Santa Maria, Brazil

[2]Universidade Federal do Pampa, Alegrete, Brazil

[3]Institute of Atmospheric Sciences and Climate - National Research Council, Turin, Italy

Correspondence
Otávio C. Acevedo, Departamento de Física, Universidade Federal de Santa Maria, Santa Maria, RS 97105-900, Brazil.
Email: otavio@ufsm.br

Abstract

The nocturnal boundary-layer regime transition from weakly stable (strong wind) to very stable (weak wind) is analyzed using 10 levels of turbulence observations made at a 140 m micrometeorological mast near the southeastern Brazilian coast. The combination of synoptic and local flow favors the systematic occurrence of such a transition, typically 5 to 7 h after sunset. The regime transition is marked by decreases in temperature, wind speed, turbulent kinetic energy (TKE) and absolute heat flux. The decrease in temperature is often abrupt and the inflection point in the temperature series marks the regime transition. Absolute heat flux peaks before the transition during the weakly stable period, while temperature variance peaks near the transition. Composites from 36 cases when the cooling rate exceeded 2 °C/h are used to describe the vertical structure of the stable boundary layer (SBL) in both regimes. For these abrupt transitions, dimensionless variables that relate thermal and mechanical properties of the flow are compared as indicators of the SBL regime, and the gradient Richardson number is found to be better for that purpose. The absolute heat flux is shown to be proportional to the cube of the wind speed only in the strong wind limit of the very stable regime. Simulations of similar transitions using a second-order model are described in Part II.

KEYWORDS

heat flux, regime transitions, stable boundary layer, very stable regime, weakly stable regime

1 | INTRODUCTION

The stable boundary layer (SBL) has been characterized as a two-regime system by a number of studies in recent years. Since Mahrt *et al.* (1998), the two regimes have been referred to as *weakly stable* and *very stable*, and they also suggested there should be a transitional regime between the two. In terms of numerical modeling, McNider *et al.* (1995) showed that a very simplified two-layer scheme that represents the exchange between the surface and the SBL is also bi-stable. Along these lines of identifying two contrastingly different regimes of the SBL, Van de Wiel *et al.* (2003) identified that there are situations when the occurrence of intermittency is favored, while in others turbulence remains fully developed. The former may be associated with the very stable regime and the latter with the weakly stable regime. This classification has been corroborated numerically by Costa *et al.* (2011), who showed that surface-generated intermittent turbulence may arise in a simplified model, but only in the very stable regime.

More recently, different studies have shown that there is a wind speed threshold that triggers the transition between the two regimes, so that the very stable regime has been also called the *weak-wind* regime, and the weakly stable

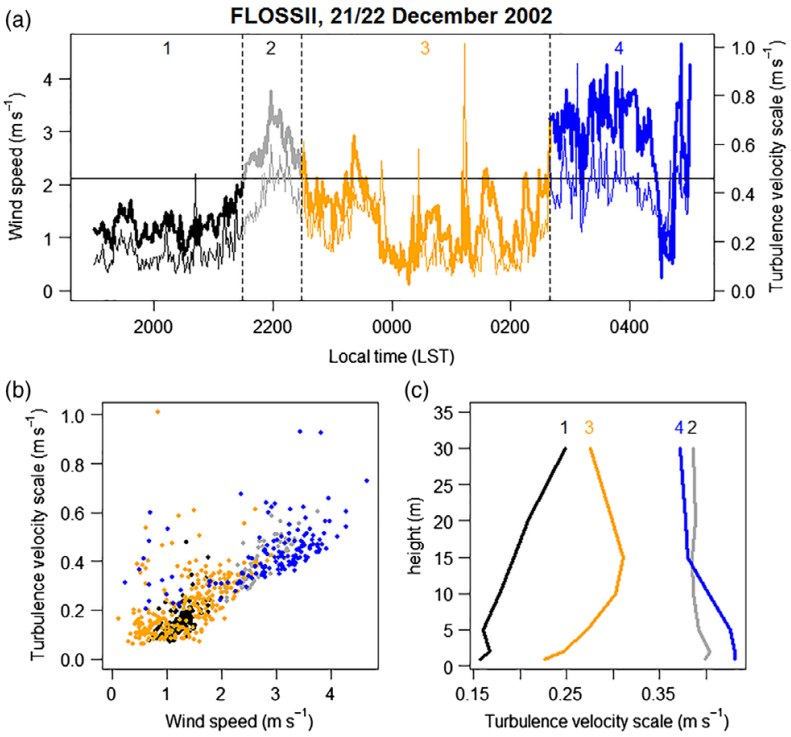

FIGURE 1 (a) Temporal evolution of 1 m mean wind speed (thick lines, scale at the left side) and turbulence velocity scale (thin lines, right side) on the night of 21/22 December 2002 at the FLOSSII site (Colorado, USA). Different colors indicate different periods of the night, based on the mean wind speed with respect to the threshold of 2.11 m/s. (b) 1 m turbulence velocity scale dependence on 1 m mean wind speed for the same night, where colors indicate the corresponding period shown in (a). (c) Average vertical profiles of turbulence velocity scale for each of the night-time periods considered, as given by colors and numbers [Colour figure can be viewed at wileyonlinelibrary.com].

regime is also referred to as the *strong-wind* regime. Sun *et al.* (2012) showed that the relationship between turbulent quantities and the mean wind speed abruptly changes at the transition. Sun *et al.* (2016) explained the differences based on the relationship between turbulent kinetic energy (TKE) and turbulent potential energy (TPE): in the very stable regime the shear-produced turbulence enhances both TKE and TPE, while in the weakly stable regime the thermal gradient has been mostly suppressed, favoring its total allocation in the form of TKE. Van de Wiel *et al.* (2007; 2012a) introduced the maximum sustainable heat flux (MSHF) theory, according to which there is a wind-speed dependent maximum heat flux. If the mean wind speed allows the turbulent heat flux to transfer enough energy to the surface to equilibrate the radiatively induced losses, the SBL remains in the weakly stable regime and turbulence is self-sustainable. Otherwise, turbulence collapses and the very stable regime is established. Acevedo *et al.* (2016) showed that TKE gradients switch sign at the transition and that the relative magnitudes of the dominant terms in the TKE and heat flux budgets also change at the transition. The MSHF framework has been further elaborated by Van de Wiel *et al.* (2017), who combined effects of different processes that affect the surface radiative budget into a lump parameter. They showed that the wind speed at which the regime transition occurs depends universally on such a parameter.

Sometimes, the SBL regime is considered a feature of a given night, which is assumed to be in that regime during the entire nocturnal period. Under this premise, Van Hooijdonk *et al.* (2015) introduced the shear capacity, a parameter based on radiative and wind observations at sunset, with the specific purpose of predicting the regime of a given night. Although this concept may be true on many occasions, observations show that the SBL state may switch regimes multiple times through the night. This is exemplified in Figure 1, where a night from the Fluxes Over Snow Surfaces (FLOSS-II) campaign (Mahrt and Vickers, 2006) is presented. As the wind speed crosses the threshold for regime transition (Figure 1a), the relationship between the turbulence velocity scale ($V_{\mathrm{TKE}} \equiv e^{1/2}$, where e is TKE) and the mean wind speed (V) changes appreciably (Figure 1b). Observations from weak-wind periods 1 and 3 show little dependence of V_{TKE} on V, while those from strong-wind periods 2 and 4 show V_{TKE} generally increasing with V. The TKE vertical gradient also switches sign between periods. TKE increases

with height in the very stable periods and decreases with height in the weakly stable ones (Figure 1c).

Although previous studies, such as those by Sun *et al.* (2012; 2015; 2016), Van de Wiel *et al.* (2012a; 2012b; 2017) and Van Hooijdonk *et al.* (2015) provide explanations on the physical controls of the mean wind speed for the SBL regime, there are still many doubts regarding the triggering of the transition and how the vertical structure of the SBL changes from one to the other regime. Detailed observations of such transitions offer a good opportunity to understand why there are two contrasting regimes in the SBL, but it is crucial that the timing of the transition is precisely determined in such an analysis. In the present study, we look at observations made at a 140 m micrometeorological tower in southeastern Brazil, equipped with 11 turbulence observation levels (Acevedo *et al.*, 2018). A very systematic pattern of progressive increase in static stability through the night is observed at the site when large-scale northerly winds prevail. In this situation, the first hours of the night are always weakly stable, while the latest portions are systematically in the very stable regime. Moreover, in most cases the transition between the two regimes is abrupt, marked by an intense cooling that may reach more than 1 °C over 10 min, causing a temperature inflection point. The present study aims at describing these occurrences, looking at the vertical structure of mean and turbulent quantities before and after the transition. In a companion article (Maroneze *et al.*, 2019), similar transitions from the weakly to the very stable regime are simulated using a second-order model for the SBL. Therefore, this first part, based on observations, is primarily descriptive of the SBL state in each of the regimes and during the transition between them. The second part (Maroneze *et al.*, 2019) is primarily explanatory, addressing the budgets of the second-order moments as well as the role of external forcings.

2 | OBSERVATIONS

The observations used in the study have been performed at a 140 m micrometeorological mast in southeastern Brazil (Acevedo *et al.*, 2018), between August 2016 and June 2017. There were initially 11 levels of turbulence observations, at the heights of 1, 2, 5, 9, 20, 37, 56, 75, 94, 113 and 132 m from the ground. They were made with sonic anemometers CSAT3B, from Campbell Sci., Inc. at all levels, except for 20 m, where an Infrared Gas Analyser and Sonic Anemometer (IRGASON) was used. The 1 m CSAT3B was removed in December 2016, and because of that the 2 m level is used in this article as a reference for observations near the ground. The IRGASON data failed in January 2017, so the data from 20 m are only used until that date.

Statistical moments of the quantities sampled by the sonic anemometer are determined for 1-minute data windows. The choice of a small data window follows recent practice in SBL studies (Mahrt *et al.*, 2013; Acevedo *et al.*, 2016; Stiperski *et al.*, 2019) and is chosen to avoid contamination from low-frequency fluctuations, especially in the horizontal wind components and vertical fluxes.

The tower is located next to a thermal power plant, at 4 km from the coastline. Roughness elements near the tower consist of a group of 9 m trees to the east, and the power plant buildings, about 150 m to the south. When mean winds are southerly, they flow past the plant before reaching the tower, largely affecting both turbulence and thermal structure (Acevedo *et al.*, 2018). For this reason, in the present study only nights when the mean wind speed had constantly a northerly component have been used. This is the dominant wind direction in post-frontal situations, so that a total of 113 nights with such a condition are available. The main focus of the study is the commonly observed nocturnal transition from the weakly to the very stable regime. It is a systematic feature at the site on nights when the large-scale flow has a northerly meridional component. As will be shown in section 4, the transition is initiated by a mean wind speed that decreases steadily in magnitude at higher levels. This is a combination between a northerly synoptic flow (Figure 2), that keeps the meridional component of the mean wind at the top of the tower roughly constant throughout the night (Figure 3, black line), and a varying sea-breeze component in the zonal direction (Figure 3, blue line), characterized by offshore flow in the afternoon that steadily decreases in magnitude, eventually switching to onshore in the middle of the night.

3 | CASE-STUDIES

A typical transition from the weakly to the very stable regime occurred on the night of 31 December 2016 (Figure 4). The transition happened between 2300 and 0000 LST (UTC – 3 h), when the 2 m temperature dropped 2 °C over 1 h. Further cooling followed, but at a slower rate. Besides the sharp surface decreases in mean wind speed (Figure 4a), temperature (Figure 4b), TKE (Figure 4c) and absolute heat flux (Figure 4d), the two regimes have contrasting vertical structures. A strong thermal stratification only sets up after the transition (Figure 4b), and although the entire tower layer cools faster after the transition than it does before it, the cooling is appreciably larger at the lowest 20 m than above these levels. Episodes of enhanced heat flux occur intermittently in the very stable regime both near the surface and at higher levels (Figure 4d).

Similar transitions occur in most of the nights when the large-scale winds have a northerly component, characteristic of post-frontal situations. However, some aspects of the transition may differ largely among the different nights. It may occur earlier, such as is the case in Figure 5a, when it happened near 2100 LST, or later, as in Figure 5b, when it

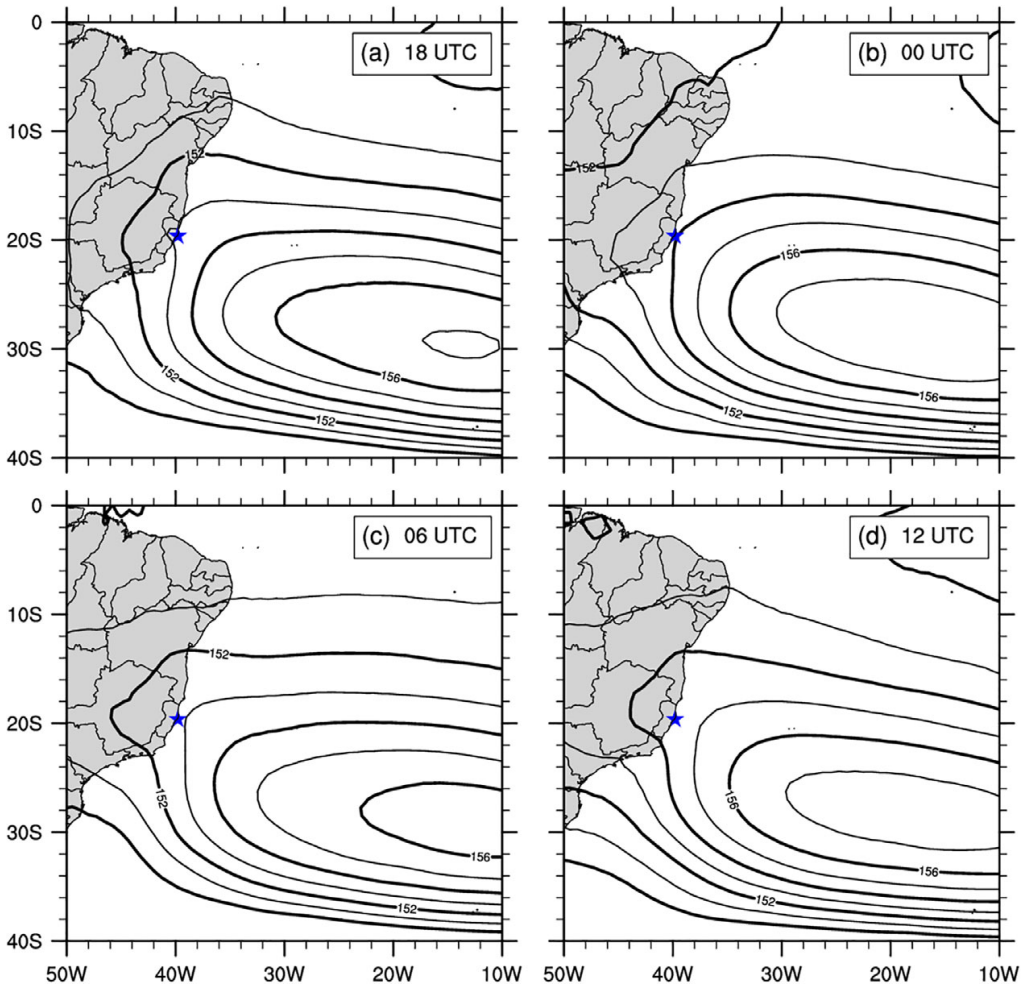

FIGURE 2 (a–d) Composite 850 hPa geopotential (dam) distributions for the 36 nights used in section 4, at the times (hour UTC) labeled at each panel. Reanalysis data from ERA-Interim (Dee *et al.*, 2011) have been used. In all panels, the location of the tower is indicated by a blue star [Colour figure can be viewed at wileyonlinelibrary.com].

occurred around 0100 LST. Besides, it is possible that turbulent mixing resumes after the initial transition, driving surface warming (Figure 5c,d). This mixing may affect the entire tower layer, causing potential temperatures near the surface and the tower top to approach each other, as occurs on 18 September 2016 near 0240 LST (Figure 5c) and 18 October 2016 near 0330 LST (Figure 5d). Curiously, in the latter case a more intense turbulent event happened before, at 0200 LST, but with no corresponding changes to the 132 m temperature. In some cases (Figure 5a,c), the transition is accompanied by an abrupt wind direction shift from northeasterly to northwesterly. Such a shift means that winds are from the ocean before the transition and from land afterwards, and it may suggest that the contrasting characteristics between the two regimes are, in this case, at least partially caused by different patterns of horizontal advection. However, there are also cases when the wind direction shifts a few hours after the abrupt surface cooling (Figure 5b,d) and in these cases the same patterns of cooling and abrupt reduction of wind speed, TKE and sensible-heat flux are observed. Besides, in the accompanying study of Maroneze *et al.* (2019), it is shown that the wind direction shift also occurs in the column model, characterizing it as an intrinsic characteristic of the transition and evidencing that the observed transition is mainly controlled by the internal SBL dynamics, although it is possible that advective patterns contribute to enhance the contrast between the two regimes in some cases.

Using the time of the abrupt cooling to mark the transition (vertical dotted lines in all panels of Figure 5), it is possible to characterize the two regimes separately. The different

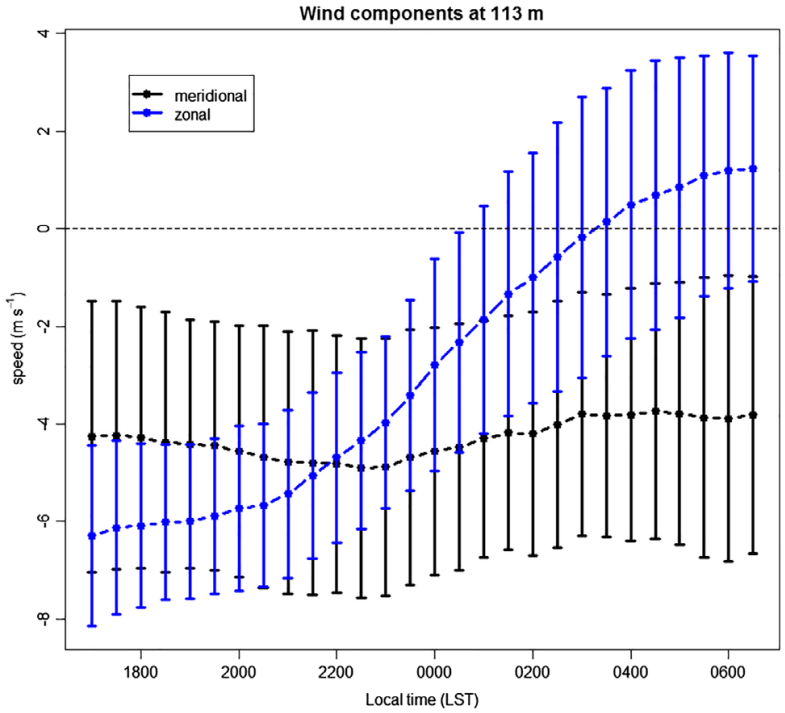

FIGURE 3 Average temporal evolution of the meridional (black) and zonal (blue) wind components at 113 m for the 113 nights with northerly meridional wind component [Colour figure can be viewed at wileyonlinelibrary.com].

dependence of turbulent mixing (shown as the turbulence velocity scale V_{TKE}) on mean wind speed between the two regimes is evident (Figure 6). As shown by Sun *et al.* (2012), V_{TKE} increases steadily with wind speed in the strong-wind, weakly stable regime, which in the present case precedes the transition (Figure 6, grey dots). In the very stable regime, on the other hand, in most cases it is difficult to identify any dependence of V_{TKE} on wind speed. In the study of Sun *et al.* (2012) and others such as Mahrt *et al.* (2015) and Acevedo *et al.* (2016), it has been shown that V_{TKE} increases with wind speed in the weak-wind, very stable regime, although at a much smaller rate (and with much larger temporal variability) than in the weakly stable regime. The observations in Figure 6 indicate that often turbulence is independent of the mean wind speed unless the threshold wind speed is exceeded. Therefore, it is possible that the dependence observed in previous studies is simply driven by sporadic events that are included in averages performed over a large number of nights. Nevertheless, a detailed analysis of the dependence of V_{TKE} on the mean wind speed for each regime separately is presented in section 5 of the present study. The V_{TKE}x V diagrams in Figure 6 also show curious occurrences on the different nights. In the two cases with intermittent turbulence events (Figures 6c,d), the points associated with these events (blue dots) behave similarly to those in the weakly stable regime, although the events happen after the transition. In the case of 17/18 September 2016 (Figure 5c), V_{TKE} depends differently on V during the intermittent event than it had before the transition. In fact, Sun *et al.* (2012) also identified a third regime, which they related to intermittent turbulence and that occupied a similar region of the diagram as those points during the intermittent event in Figure 6c.

4 | COMPOSITES

In this section, the transition is characterized based on composites of 36 cases. The cases chosen are all those when a cooling rate of at least 2 °C/h was observed at any portion of the night. The moment of most abrupt cooling was then assigned to represent the transition, assumed to happen at $t = 0$. It is important to notice that only 3 out of the total 113 nights did not show a clear transition in wind and temperature near the surface. Therefore, 110 nights had a transition, which could be abrupt or smooth. For compositing, it is essential to precisely determine the time of the transition, something that may not be possible in the smooth cases. Therefore, only the most abrupt cases have been chosen and, as described in section 2 it is possible that such abruptness is driven by a feedback between the wind direction shift and horizontal advection.

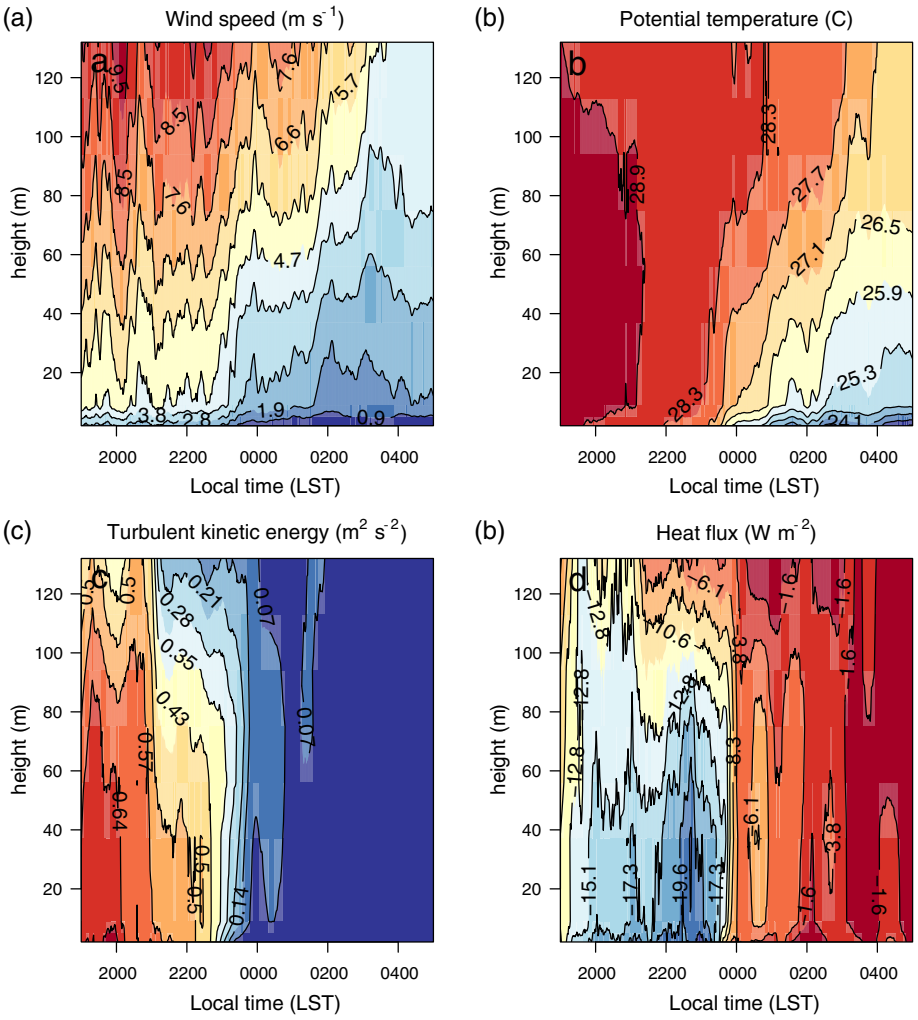

FIGURE 4 Nocturnal evolution of (a) mean wind speed, (b) potential temperature, (c) TKE and (d) heat flux, at all levels on the night of 31 December 2016/1 January 2017 [Colour figure can be viewed at wileyonlinelibrary.com].

The composites are averages of 10-hour time windows, from 5 h before to 5 h after the transition, over the 36 nights. Transitions have been found to occur as early in the night as 2037 LST and as late as 0210 LST but the vast majority (27 out of 36) happened between 2300 and 0100 LST.

Typically, temperature, mean wind speed and TKE all decrease near the surface in the strong-wind (weakly stable) period that precedes the transition (Figure 7a). The rate of decrease of all these quantities in the first 4.5 h of the composites is appreciably smaller than what is observed in the hour centered at the time of most abrupt cooling. At the pre-transition period, mean wind speed, temperature and TKE are all coupled to each other. The external large-scale forcing drives the mean wind speed decrease, which reduces TKE shear production and, therefore, TKE itself. At the same time, radiative loss at the surface cools the surface and the air in contact with it, by conduction. As TKE and the heat flux are still intense enough, the air cooled near the surface is transported to upper levels, over the entire tower layer. The absolute heat flux ($-\overline{w'\theta'}$) peaks about 3 h before the transition, on average (Figure 7b). It implies that such a maximum happens in the weakly stable period, when mean wind speed and temperature are still decaying at a small rate. The initial heat flux increase in magnitude may be attributed to the fact that many of the composites start shortly after sunset. In that case, the absolute heat flux increase is driven by thermal gradient production (*TGP*), the term in the heat flux budget that is proportional to the thermal gradient (which largely increases after sunset) and to the vertical velocity variance (still large in the period). At some point, the thermal gradient increase is

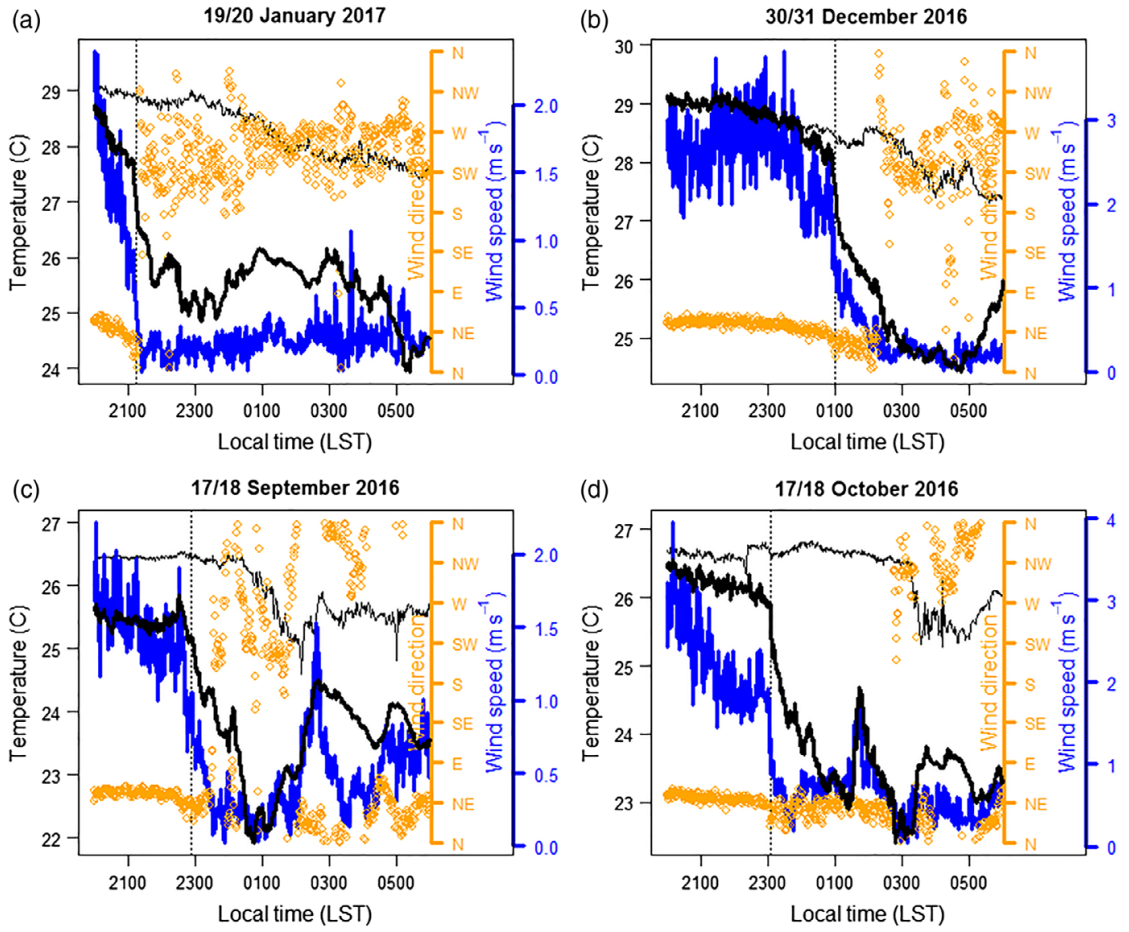

FIGURE 5 (a–d) Temporal evolutions of 2 m temperature (thick black lines), 132 m temperature (thin black lines), 2 m wind speed (blue lines) and 2 m wind direction (orange dots) on four different nights. Vertical dotted lines show the time of most abrupt cooling at 2 m [Colour figure can be viewed at wileyonlinelibrary.com].

no longer large enough to counteract the fact that the turbulent mixing is decreasing, and the absolute heat flux decreases in magnitude. A detailed analysis of the heat flux budget is presented by Maroneze *et al.* (2019), where the second-order model is used to produce all relevant budget terms. It is important to notice that $-\overline{w'\theta'}$ starts decreasing in magnitude much (some hours) before the TKE collapse and the intense surface cooling that mark the regime transition. In fact, the tendencies of variables such as temperature, mean wind speed and TKE in the weakly stable regime are insensitive to whether $-\overline{w'\theta'}$ increases or decreases. This is important because the maximum in the absolute surface heat flux has been used to classify the SBL regime (Acevedo and Fitzjarrald, 2003; Van Hooijdonk *et al.*, 2015; Baas *et al.*, 2018), and the present results do not support such an inference. In the present case, the maximum is a temporal one, but stability increases monotonically in time, so the association may be used to refer to the absolute heat flux dependency on stability, as is commonly done. Monahan *et al.* (2015) found a similar result, concluding that the separation between the two regimes could not be associated with a heat flux threshold. The one quantity that depends on the temporal tendency of $-\overline{w'\theta'}$ in the weakly stable regime is the temperature variance ($\overline{\theta'^2}$, Figure 7b). While the absolute heat flux increases in magnitude, $\overline{\theta'^2}$ steadily increases as well, but it becomes steady when the heat flux magnitude starts to decrease.

About 30 min before the time of maximum cooling rate, temperature, mean wind speed and TKE all start decaying at a much faster rate than before (Figure 7a). The mean wind speed at the top of the tower varies little at the time, indicating that the changes that take place near the surface are internal to the SBL, driven by its internal dynamics. The absolute heat flux and temperature variance also abruptly decrease in magnitude at the same time (Figure 7b). After the transition,

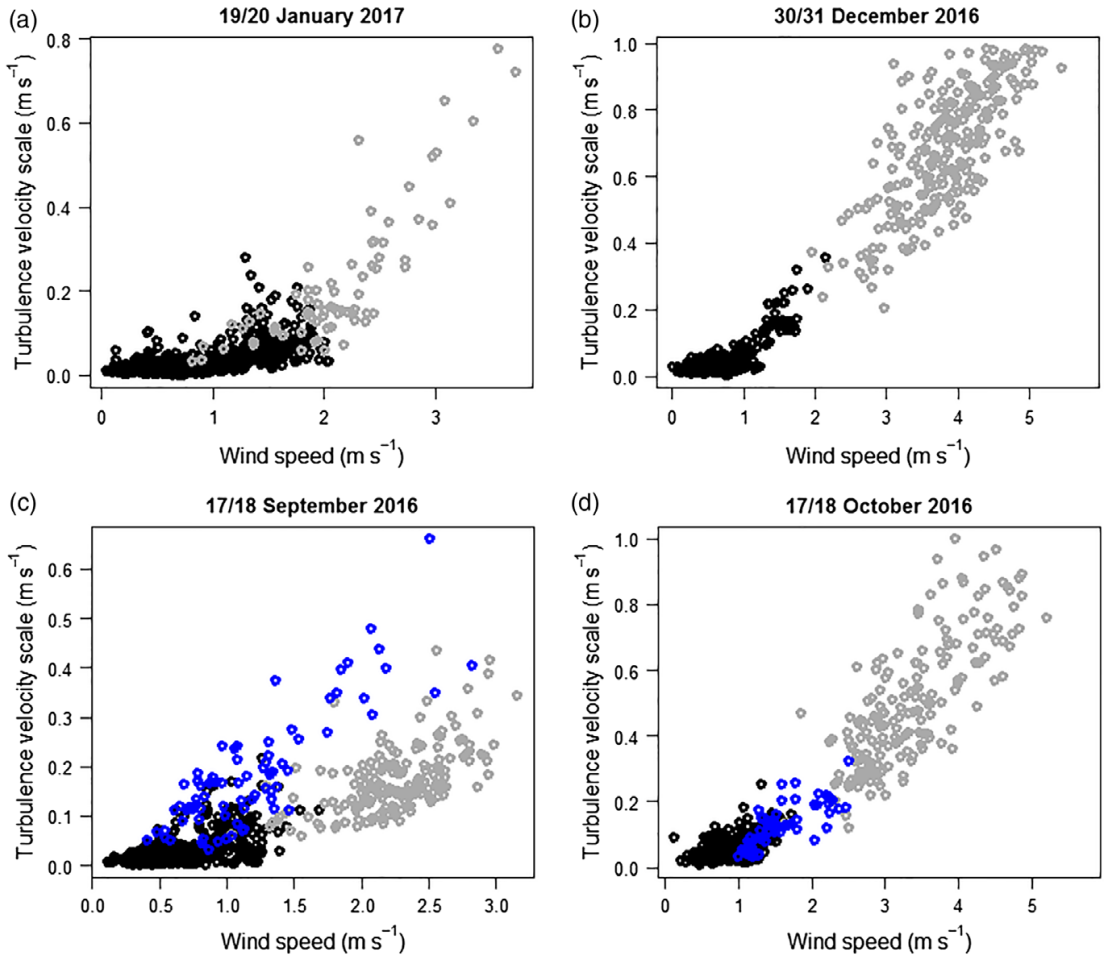

FIGURE 6 (a–d) Turbulence velocity scale as a function of mean wind speed for the four nights shown in Figure 5. Grey dots observations occurred before the instant of the most abrupt cooling at 2 m, and black dots have been observed after that occurrence. Blue dots refer to intermittent turbulence events (see text) [Colour figure can be viewed at wileyonlinelibrary.com].

only intermittent events such as the one shown in Figure 4b cause significant changes in the mean and turbulent quantities, but they average out in the composites. Mean temperature decreases at a rate similar to what happened before the transition, but it is no longer accompanied by a mean wind speed decrease, evidencing that thermal and mechanical structures have become disconnected from each other.

The vertical structure of the composites is seen in Figure 8. They show typical features that are generally common before and after the transition, despite case-to-case variability. Abraham (2019) presented similar composites for eight different sites, with different surface characteristics. The temperature composites show that the cold layer after the transition spans almost the entire extension of the tower (Figure 8a), indicating that regardless of the TKE decay, the turbulent heat flux is transferring the cold air from the surface upwards. A similar result was found at the five land sites, but not at the three oceanic ones considered by Abraham (2019). Cooling rates generally decrease with height, being largest near the surface. This result contrasts with those found by Baas *et al.* (2019) in Antarctica, where the temperature variations were larger at 10 m than close to the surface. The wind speed decreases more intensely at lower levels (Figure 8b), so that the composite profiles are nearly logarithmic before the transition, becoming nearly linear after it. This feature and the large mean wind speed decrease from the weakly stable to the very stable regime has been observed by Abraham (2019) at two of five land sites they analyzed (Boulder and Los Alamos). The sign inversion of the vertical TKE gradient is also a general feature, observable in the composites (Figure 8c). TKE decreases with height before the transition and increases vertically after it. Abraham (2019) made a similar analysis for

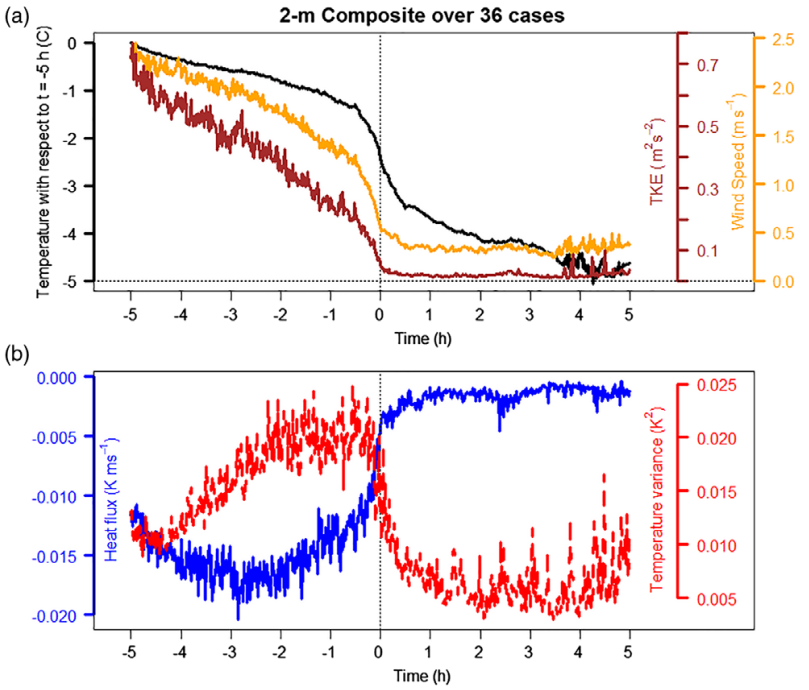

FIGURE 7 (a) Composited evolutions of temperature difference from that observed 5 h before the transition (black line), mean wind speed (orange) and TKE (brown); (b) Composited evolutions of heat flux (blue) and temperature variance (red). All quantities are shown at 2 m; composites are made from 36 cases of abrupt transitions [Colour figure can be viewed at wileyonlinelibrary.com].

three land sites, finding that only at Cabauw the same occurs consistently enough as to show in the composites. The wind direction evolution at higher levels is, as discussed in section 2, caused by a combination of a northerly large-scale forcing and a sea-breeze circulation that affects the mean zonal flow at upper levels. The composite shows that the wind direction changes first at lower levels (Figure 8d). The heat flux (Figure 8e) has an organized structure before the transition, with a maximum absolute value at −2.5 h at all levels. After the transition, on the other hand, the intermittent nature of most heat flux events causes a disorganized pattern even for the composited heat flux. Temperature variance peaks before the transition at lower levels, as shown in Figure 7b, but from 20 to 80 m the maximum occurs exactly at the transition (Figure 8f).

It is interesting to use this dataset consisting of cases with a clear transition and definition of both regimes to address whether there is a dimensionless number that unambiguously classifies the SBL regime. The comparison includes:

- the Richardson number $\mathrm{Ri} \equiv g\Theta^{-1}\overline{w'\theta'}(\overline{u'w'}\partial\overline{u}/\partial z)^{-1}$, which is the ratio between buoyant destruction (BD) and shear production terms in the TKE budget equation. Here, the fluxes are determined at 2 m, and the wind shear is determined between 2 and 5 m;
- the gradient Richardson number $\mathrm{Ri_g} \equiv g\Theta^{-1}\Delta z\Delta\overline{\theta}(\Delta\overline{V})^{-2}$. All gradients are determined between 2 and 37 m;
- the stability parameter zL^{-1} where L is the Obukhov length $L \equiv -u_*^3\Theta(\kappa g\overline{w'\theta'})^{-1}$. All quantities are taken at 2 m;
- the ratio between the BD and TGP in the heat flux budget equation, $BD\,TGP^{-1} \equiv -g\Theta^{-1}\overline{\theta'^2}\left(\frac{\overline{w'^2}\partial\overline{\theta}}{\partial z}\right)^{-1}$. Second-order moments are determined at 2 m, while the temperature gradient is considered between 2 and 5 m.

The three first dimensionless ratios are common choices to represent stability in observational and modeling studies of the atmospheric boundary layer. The fourth, the ratio $BD\,TGP^{-1}$ has been chosen because Acevedo *et al.* (2016) showed that it changes sign near the surface between the two regimes, as BD is larger than TGP in the very stable regime, while the opposite occurs in the weakly stable regime. Besides, it also equals the ratio between TPE and the vertical contribution to TKE. Sun *et al.* (2016) associated the regime transition with the change in the ratio between TPE and TKE.

The composite evolution of the four dimensionless numbers is shown in Figure 9. These were determined as the ratio between the average composites of the corresponding quantities, rather than as the average composite of the ratios for

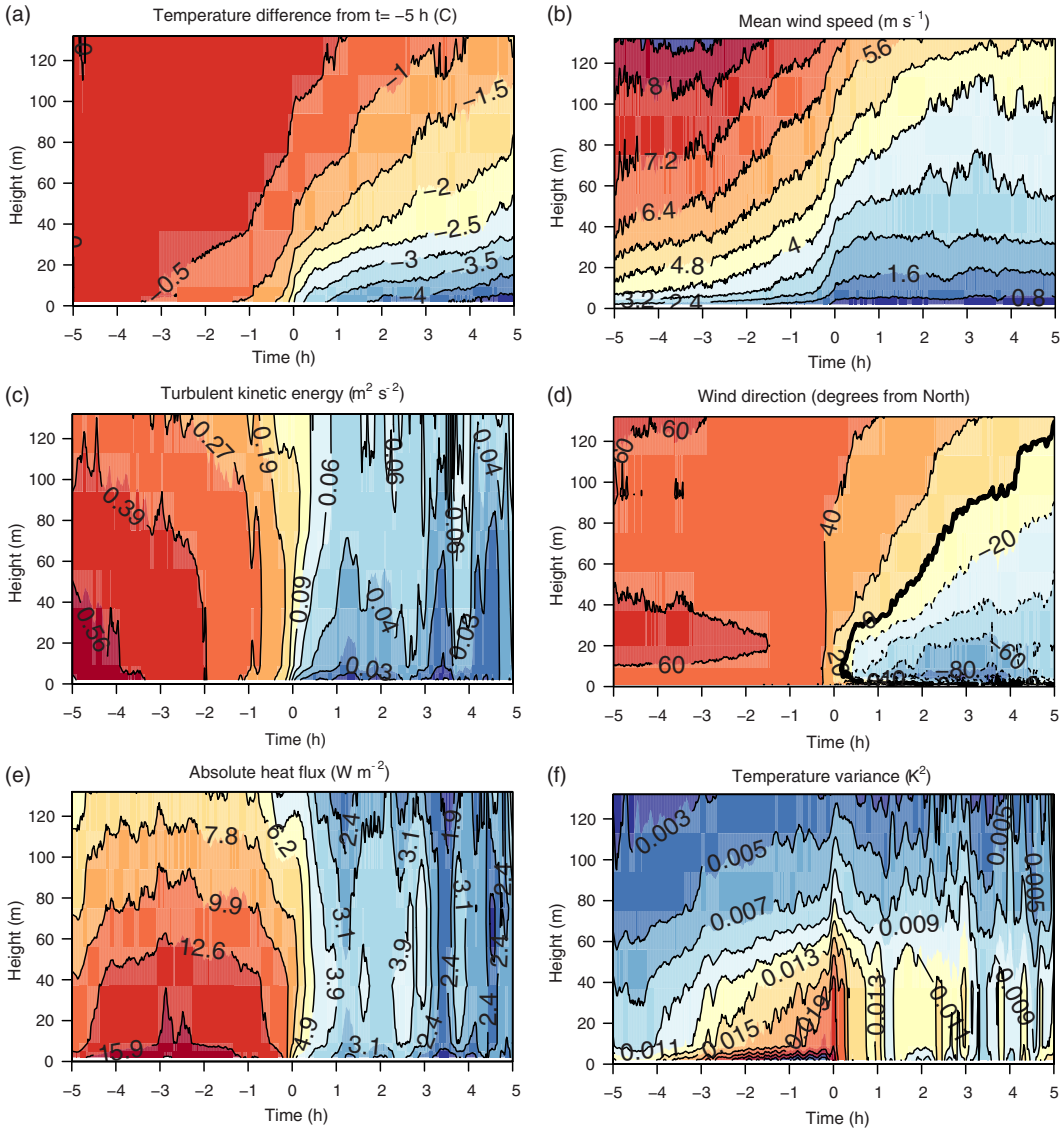

FIGURE 8 Composited evolution of (a) the temperature difference from that 5 h before the transition, (b) mean wind speed, (c) TKE, (d) wind direction, (e) absolute heat flux and (f) temperature variance, for 36 cases with abrupt transitions. In (d), the thick line indicates northerly wind direction [Colour figure can be viewed at wileyonlinelibrary.com].

each case. On the other hand, the probability distributions at the left of each panel are done using individual values from each of the 37 nights in the composite, allowing assessment of the case-to-case variability. All quantities change abruptly at the transition. Small values occur at the weakly stable regime, and large values occur in the very stable regime (Table 1). The critical values of the ratios are determined by their composite values at $t = 0$ h. For both forms of the Richardson number, the critical values are close to the typically accepted 0.2 and 0.25 (Grachev *et al.*, 2013; Van Hooijdonk *et al.*, 2015; Freire *et al.*, 2019; *inter alia*). The critical value of the stability parameter zL^{-1} at the transition is 0.18. The maximum absolute heat flux happens at a much smaller zL^{-1}, 0.02, close to the 0.025 value found by Grachev *et al.* (2005), but smaller than those of 0.06 (Mahrt *et al.*, 1998; Acevedo *et al.*, 2014), 0.08 (Moraes *et al.*, 2004) and 0.2 (Malhi, 1995). The large variability among results suggests that the stability parameter for the maximum absolute heat flux is site-dependent, but all these results except for those of Malhi (1995) indicate that the maximum heat flux occurs in the weakly stable regime.

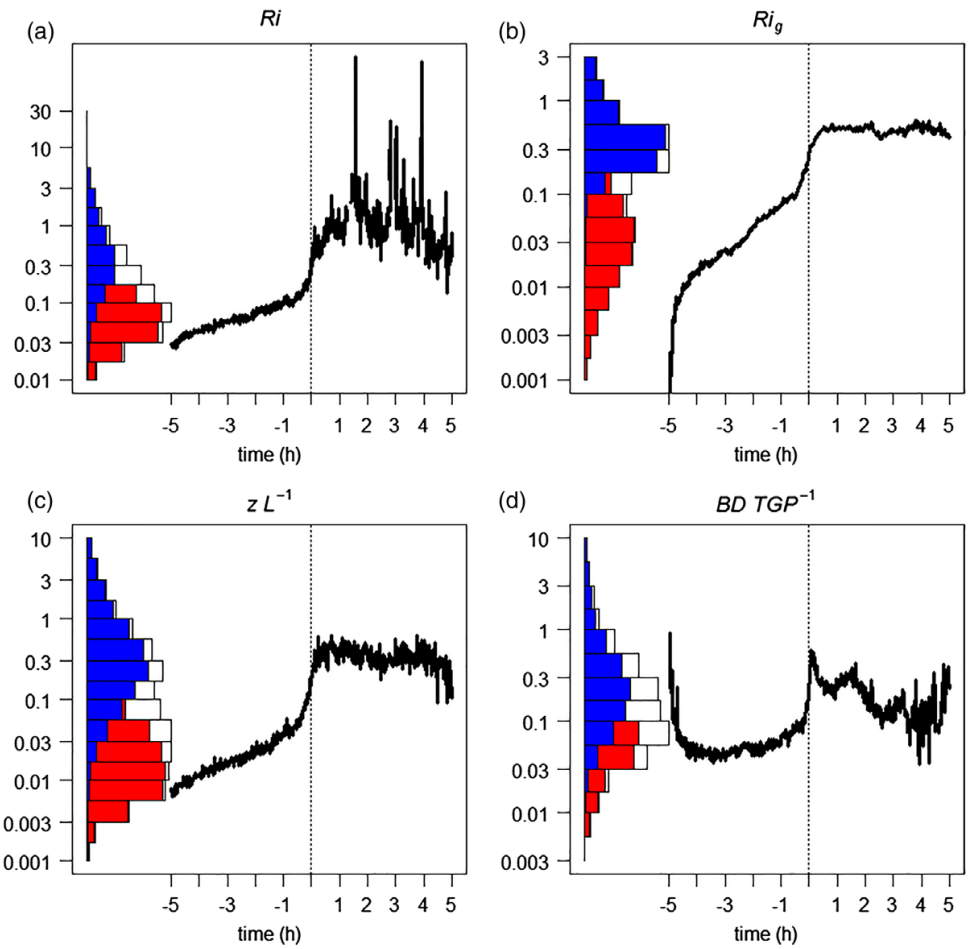

FIGURE 9 Black lines show the composite evolutions of (a) Ri, (b) Ri_g, (c) z/L and (d) BD/TGP, all determined from the composite values of the quantities that define each ratio, from the 36 cases of abrupt transitions. The horizontal bars show the frequency distributions of the same quantities as determined from the values of the quantities on each night. Red bars are for cases before the transition and blue bars are for cases after it [Colour figure can be viewed at wileyonlinelibrary.com].

Of all parameters considered, Ri_g is the most stable, fluctuating the least in both regimes. Besides, along with zL^{-1} but not with the others, their logarithms present two well-defined modes, one for each regime. These advantages of Ri_g may be because it is the only one that is entirely determined from first-order moments, which statistically converge faster than the second-order moments necessary for all other parameters. Besides, it is not a local parameter, reflecting the stability over a deeper layer. Therefore, this result indicates that bulk stability represents the SBL regime better than equivalent local quantities. The ratio $BD\ TGP^{-1}$ is not a good parameter to represent the transition in this study. It has large values at the beginning of the composites, which are caused by the fact that in many cases the composites begin when the thermal gradient is near zero. Besides, despite the abrupt change at the transition, the composited $BD\ TGP^{-1}$ decreases soon after it. This result contrasts with that from the companion modeling study, where Maroneze *et al.* (2019) found that this ratio does not fluctuate largely and has the advantage of having a critical value that is the least dependent on cloud cover.

TABLE 1 Values of the dimensionless ratios at different times in the composites, as given in the first row

Ratio	Average before transition	Average after transition	Critical value	Value at maximum heat flux
Ri	0.073	2.36	0.29	0.07
Ri_g	0.047	0.48	0.27	0.04
z/L	0.027	0.34	0.17	0.02
BD/TGP	0.061	0.19	0.24	0.05

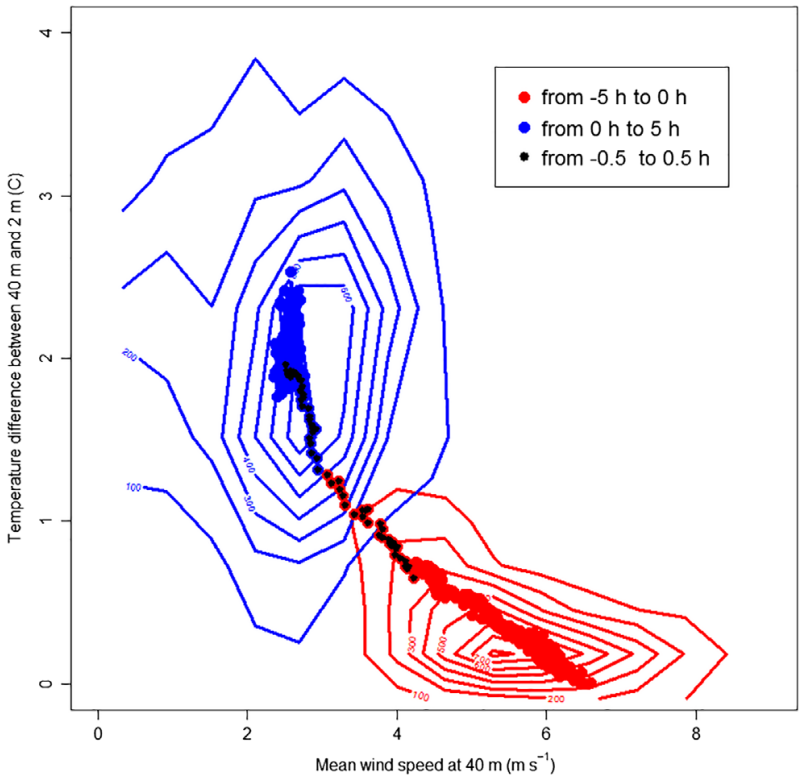

FIGURE 10 Composite temperature difference between 40 and 2 m as a function of the mean wind speed at 40 m before (red dots) and after the transition (blue dots) from the 36 cases of abrupt transitions. Black dots indicate a 1 h period centered at the transition. Red and blue contours show the probability distribution of individual occurrences before and after the transition, respectively [Colour figure can be viewed at wileyonlinelibrary.com].

5 | WIND SPEED CONTROLS

Van de Wiel *et al.* (2017) compared the mean wind speed to thermal stratification at both SBL regimes, finding that the stratification increases over a narrow range of wind speeds, and that in the very stable regime thermal stratification stays at a maximum as the mean wind speed decreases. A similar behavior is found in the present case, and this comparison further evidences the contrasting connection between the mechanical and thermal structures in both regimes (Figure 10). Before the transition, the composited mean stratification increases steadily as the mean wind speed decreases (Figure 10, red dots), but after the transition these quantities are virtually independent of each other (Figure 10, blue dots). The probability distributions in both regimes show much larger variability after the transition than before it. This is because in the very stable regime there are both occurrences of wind speed variations without stratification change and of stratification variations with no appreciable change of the mean wind speed. Such occurrences are much rarer in the weakly stable regime, even when individual cases are considered. The composite thermal gradient dependence on mean wind speed changes exactly at the transition, as evidenced by a change in the slope between blue and red dots in Figure 9. The independence between the two quantities only starts tens of minutes after the transition, as the average thermal gradient increases steadily as the mean wind speed decreases for 30 min after the regime transition (Figure 10, black dots with a blue background).

When the comparison between V_{TKE} and V is split by SBL regime, some details of the dependence found by Sun *et al.* (2012) can be better understood. At lower levels, there is a subtle slope change in such a relationship from the very stable (Figure 11, blue dots) to the weakly stable regime (red dots). At 37 m and higher levels, V_{TKE} is virtually independent of the mean wind speed in the very stable regime, while there is a linear relationship between the two quantities in the weakly stable case. At each level, there is a range of mean wind speeds for which the SBL may be in either regime, in agreement with the findings from Van de Wiel *et al.* (2017). The classical dependence found at upper levels with a slight increase in V_{TKE} as V increases in the very stable regime

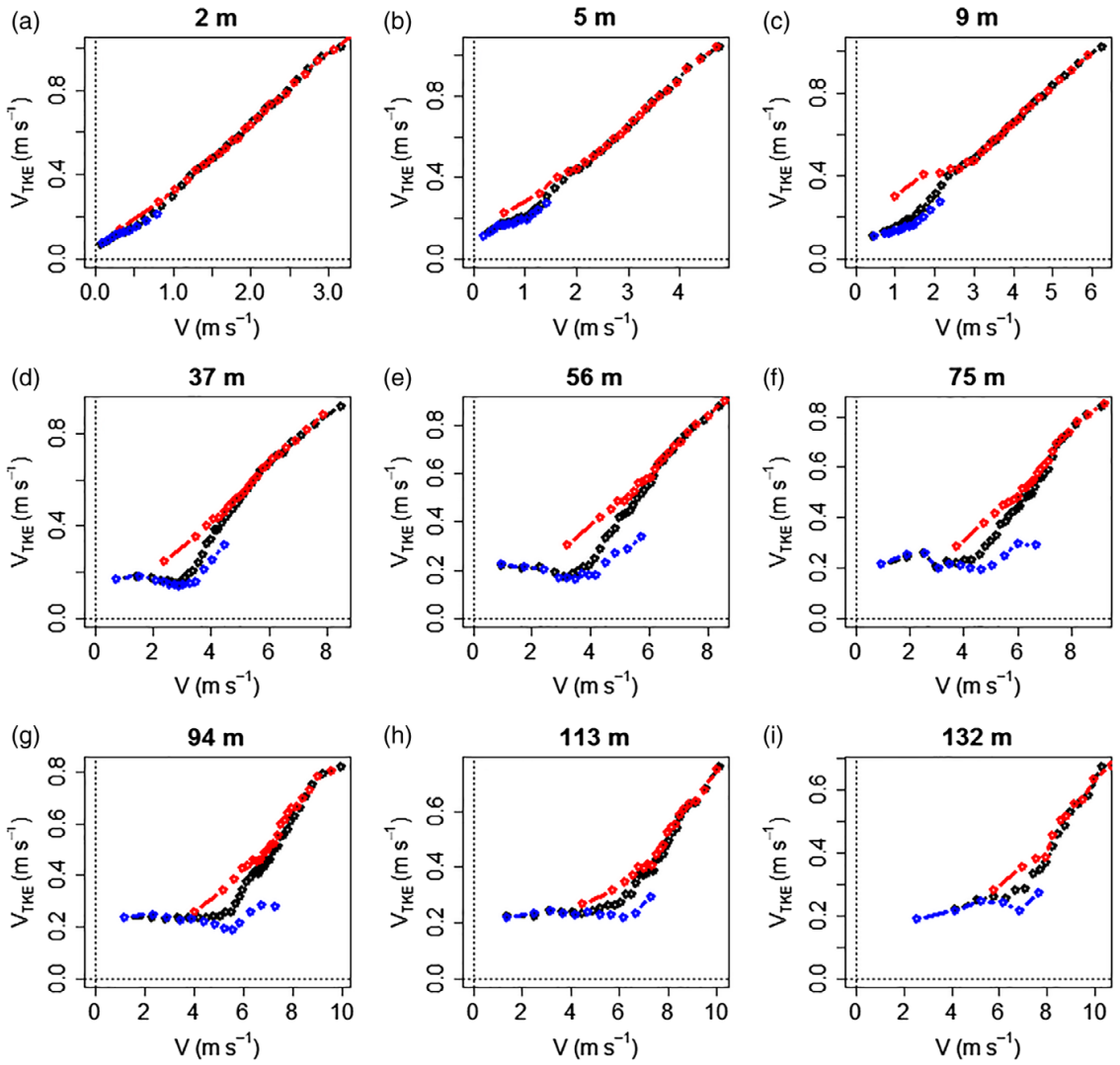

FIGURE 11 (a–i) Bin-averaged turbulence velocity scale as a function of the mean wind speed at each tower level, as indicated above each panel, for the entire dataset (black), before (red) and after (blue) the transition [Colour figure can be viewed at wileyonlinelibrary.com].

(Sun *et al.*, 2012; Acevedo *et al.*, 2016) likely arises, therefore, from clumping data from both regimes in the same mean wind speed bins. In the very stable regime, decoupling from the surface determines that V_{TKE} has no dependence on the mean wind. At 5 and 9 m there is a turbulence enhancement in the weak wind limit of the weakly stable regime, possibly caused because this is the height of the roughness elements around the tower.

Van de Wiel *et al.* (2012a) associated the SBL regime to a control exerted by the mean wind speed through its effect on the heat flux. Their reasoning is based on a cubic dependence of the heat flux on the mean wind speed proposed by Taylor (1971) from similarity-based relationships. The existence of such a cubic dependence is addressed here for both SBL regimes. In the weakly stable regime, the absolute heat flux increases with mean wind speed, but at a rate much smaller than cubic (Figure 12, red dots). In the very stable regime, on the other hand, the rate of absolute heat flux increase with mean wind speed is variable, approaching a cubic one in the large wind speed limit of the regime (Figure 12, blue dots). It is curious that when the heat fluxes are larger in magnitude (weakly stable regime), they are also less dependent on the mean wind speed. This is opposite to what happens with

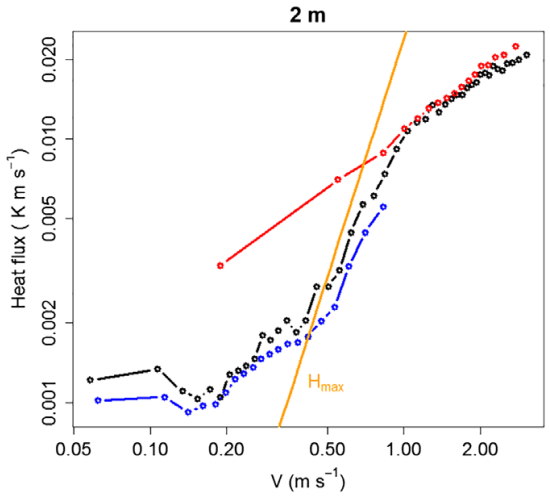

FIGURE 12 Bin-averaged 2 m heat flux as a function of the 2 m mean wind speed for the entire dataset (black), before (red) and after the transition (blue). Orange line is the maximum heat flux estimated from the relationship proposed by Van de Wiel *et al.* (2012a) [Colour figure can be viewed at wileyonlinelibrary.com].

both the thermal gradient (Figure 10) and TKE (Figure 11), which have a stronger dependence on wind speed in the weakly stable regime than in the very stable regime. However, these dependencies are in opposite directions, so that, as wind speed increases in the weakly stable regime, enhanced turbulence and reduced thermal gradients combine to produce a small heat flux dependence on mean wind speed. It also indicates, following the reasoning introduced by Sun *et al.* (2016) that, in this situation, most wind speed changes are used to change TKE, rather than TPE. Figure 12 supports the reasoning behind the MSHF theory introduced by Van de Wiel *et al.* (2012), according to which there is a maximum possible heat flux $H_{\max} = 0.15\kappa^2\Theta V^3(\alpha g z)^{-1}[\ln(z/z_0)]^{-2}$, where $\kappa = 0.4$ is the von Karman constant and $\alpha = 4$ is a constant dependent on the TKE decay with stability (Van Hooijdonk *et al.*, 2015). The theoretical $H_{\max}$ for 2 m is shown as an orange line in Figure 12. In the weakly stable regime, the maximum flux is never reached, because the existent flux is sufficient to totally transfer the radiatively cooled air from lower to upper levels. Hence, the heat flux increases at a smaller rate than a cubic one. The average heat flux approaches $H_{\max}$ in the strong wind limit of the very stable regime. For very weak winds, the heat flux exceeds $H_{\max}$, showing that in this case the fluxes are locally controlled and that the similarity relationship from Taylor (1971) used to support the $H_{\max}$ definition is no longer valid. Even exceeding $H_{\max}$, these fluxes are much smaller than the net radiative loss (not observed), therefore not being able to continually transfer the cold air to upper levels.

6 | CONCLUSION

The systematic transitions from weakly to very stable observed in the middle of the night at Linhares make this dataset especially appropriate for understanding what controls the SBL regime. Furthermore, the fact that such a transition often occurs abruptly allows a precise determination of its occurrence, making it possible to analyze separately the vertical structure of the weakly stable and of the very SBLs. Some important findings have been obtained from these observations of abrupt transitions from weakly to very SBL:

- The SBL regime is not only controlled by the mean wind speed, but also by thermal processes. This has been proposed by Van de Wiel *et al.* (2012a) under the MSHF framework. More recently, it has been generalized by Van de Wiel *et al.* (2017), to account for other factors that affect the surface radiative budget and consequently the regime transition, such as cloud cover and the surface thermal properties. Unfortunately, the lack of radiative observations at the site precluded a direct test of the theory from being performed at present. Such analysis is done in the companion article (Maroneze *et al.*, 2019), using a second-order closure numerical model. Nevertheless, it has been shown that different dimensionless numbers that incorporate stability effects are good indicators of the SBL regime. Gradient Richardson number is slightly superior for that purpose, possibly because it provides a bulk description of the SBL and also because it is entirely defined by first-order moments;
- The SBL has a maximum absolute heat flux, but it happens in the weakly stable regime. The maximum absolute heat flux does not, therefore, mark the regime transition, as suggested in previous studies (Acevedo and Fitzjarrald, 2003; Van Hooijdonk *et al.*, 2015; Baas *et al.*, 2018);
- Cooling in the very stable regime is more intense near the surface but it is sensed at an entire layer of a few tens of meters, showing that in such a regime the very small heat flux is still able to transfer the surface cooled air to upper levels;
- Turbulence-related quantities are independent of the mean wind speed in the very stable regime, and linearly dependent in the weakly stable regime. This finding supports the results from Sun *et al.* (2012), but it expands it by showing that the small dependence between these quantities in the very stable (weak-wind) regime may be simply a consequence of averaging observations in both regimes for a given mean wind speed;
- The heat flux is proportional to the third power of the mean wind speed, but only in the very stable regime, where it approaches the maximum heat flux proposed by MSHF.

In a companion article, Maroneze *et al.* (2019) extend the present analysis using a second-order model and addressing aspects that have not been discussed here, such as the role of cloudiness and surface thermal properties and the budgets of second-order moments such as turbulence kinetic energy, heat flux and temperature variance.

Although the systematic occurrence of the weakly to very stable transition at Linhares make the tower an appropriate laboratory to study this phenomenon, it is important to notice that the opposite transition, from very to weakly stable very rarely occurs there. Therefore, it is still unclear whether there is hysteresis in this transition and whether it is triggered by the same external factors found to be important in the present study. Besides, the fact discussed in the introduction that multiple transitions often occur in the same night has not been addressed here either. These are interesting analyses that may be done in the future, but they will certainly demand a different dataset.

ACKNOWLEDGEMENTS

The study has been developed within the context of a Research and Development project sponsored by companies Linhares Geração S.A. and Termelétrica Viana S.A., and named "*Desenvolvimento de um modelo operacional para simulação em tempo real da dispersão atmosférica de poluentes emitidos por termelétrica a gás natural*". The Project is within the context of the investment programme in Research and Development, regulated by Brazilian National Agency for Electric Energy. The authors thank deeply all support provided by these companies for the development of the present work. The study also has been partially supported by Brazilian funding agencies CNPq and CAPES. The latter funds graduate studies of the second author. Three anonymous reviewers offered valuable comments and suggestions.

ORCID

Otávio C. Acevedo https://orcid.org/0000-0003-2606-4726

Rafael Maroneze https://orcid.org/0000-0002-3025-9676

REFERENCES

Abraham C. (2019) *Regime occupation and transition information obtained from observable meteorological state variables in the stably stratified nocturnal boundary layer*. PhD Thesis, University of Victoria, Victoria, BC, Canada.

Acevedo, O.C., Costa, F.D., Oliveira, P.E.S., Puhales, F.S., Degrazia, G.A. and Roberti, D.R. (2014) The influence of submeso processes on stable boundary layer similarity relationships. *Journal of the Atmospheric Sciences*, 71, 207–225.

Acevedo, O.C., Degrazia, G.A., Puhales, F.S., Martins, L.G.N., Oliveira, P.E.S., Teichrieb, C.A., Silva, S.M., Maroneze, R., Bodmann, B., Mortarini, L., Cava, D. and Anfossi, D. (2018) Monitoring the micrometeorology of a coastal site next to a thermal power plant from the surface to 140 m. *Bulletin of the American Meteorological Society*, 99, 725–738. https://doi.org/10.1175/BAMS-D-17-0134.1.

Acevedo, O.C. and Fitzjarrald, D.R. (2003) In the core of the night – effects on intermittent mixing on a horizontally heterogeneous surface. *Boundary-Layer Meteorology*, 106, 1–33.

Acevedo, O.C., Mahrt, L., Puhales, F.S., Costa, F.D., Medeiros, L.E. and Degrazia, G.A. (2016) Contrasting structures between the decoupled and coupled states of the stable boundary layer. *Quarterly Journal of the Royal Meteorological Society*, 142, 693–702. https://doi.org/10.1002/qj.2693.

Baas, P., van de Wiel, B.J.H., van der Linden, S.J.A. and Bosveld, F.C. (2018) From near-neutral to strongly stratified: adequately modelling the clear-sky nocturnal boundary layer at Cabauw. *Boundary-Layer Meteorology*, 166, 217–238. https://doi.org/10.1007/s10546-017-0304-8.

Baas, P., van de Wiel, B.J.H., van Meijgaard, E., Vignon, E., Genthon, C., van der Linden, S.J.A. and de Roode, S.R. (2019) Transitions in the wintertime near-surface temperature inversion at Dome C, Antarctica. *Quarterly Journal of the Royal Meteorological Society*, 145(720), 930–946. https://doi.org/10.1002/qj.3450.

Costa, F.D., Acevedo, O.C., Mombach, J.C.M. and Degrazia, G.A. (2011) A simplified model for intermittent turbulence in the nocturnal boundary layer. *Journal of the Atmospheric Sciences*, 68, 1714–1729.

Dee, D.P., Uppala, S.M., Simmons, A.J., Berrisford, P., Poli, P., Kobayashi, S., Andrae, U., Balmaseda, M.A., Balsamo, G., Bauer, P., Bechtold, P., Beljaars, A.C.M., van de Berg, L., Bidlot, J., Bormann, N., Delsol, C., Dragani, R., Fuentes, M., Geer, A.J., Haimberger, L., Healy, S.B., Hersbach, H., Hólm, E.V., Isaksen, L., Kållberg, P., Köhler, M., Matricardi, M., McNally, A.P., Monge-Sanz, B.M., Morcrette, J.J., Park, B.K., Peubey, C., de Rosnay, P., Tavolato, C., Thépaut, J.N. and Vitart, F. (2011) The ERA-Interim reanalysis: configuration and performance of the data assimilation system. *Quarterly Journal of the Royal Meteorological Society*, 137, 553–597. https://doi.org/10.1002/qj.828.

Freire, L.S., Chamecki, M., Bou-Zeid, E. and Dias, N.L. (2019) Critical flux Richardson number for Kolmogorov turbulence enabled by TKE transport. *Quarterly Journal of the Royal Meteorological Society*, 145(721), 1551–1558. https://doi.org/10.1002/qj.3511.

Grachev, A.A., Andreas, E.L., Fairall, C.W., Guest, P.S. and Persson, P.O.G. (2013) The critical Richardson number and limits of applicability of local similarity theory in the stable boundary layer. *Boundary-Layer Meteorology*, 147, 51–82. https://doi.org/10.1007/s10546-012-9771-0.

Grachev, A.A., Fairall, C.W., Persson, P.O.G., Andreas, E.L. and Guest, P.S. (2005) Stable boundary-layer scaling regimes: the SHEBA data. *Boundary-Layer Meteorology*, 116, 201–235. https://doi.org/10.1007/s10546-004-2729-0.

Mahrt, L., Sun, J., Blumen, W., Delany, T. and Oncley, S. (1998) Nocturnal boundary-layer regimes. *Boundary-Layer Meteorology*, 88, 255–278.

Mahrt, L., Sun, J. and Stauffer, D. (2015) Dependence of turbulent velocities on wind speed and stratification. *Boundary-Layer Meteorology*, 155, 55–71. https://doi.org/10.1007/s10546-014-9992-5.

Mahrt, L., Thomas, C., Richardson, S., Seaman, N., Stauffer, D. and Zeeman, M. (2013) Non-stationarity generation of weak turbulence for very stable and weak-wind conditions. *Boundary-Layer Meteorology*, 147, 179–199.

Mahrt, L. and Vickers, D. (2006) Extremely weak mixing in stable conditions. *Boundary-Layer Meteorology*, 119, 19–39.

Malhi, Y.S. (1995) The significance of the dual solutions for heat fluxes measured by the temperature fluctuation method in stable conditions. *Boundary-Layer Meteorology*, 74, 389–396.

Maroneze, R., Acevedo, O.C., Costa, F.D., Puhales, F.S., Demarco, G. and Mortarini, L. (2019) The nocturnal boundary later transition from weakly to very stable. Part 2: Numerical simulation with a second-order model. *Quarterly Journal of the Royal Meteorological Society*.

McNider, R.T., England, D.E., Friedman, M.J. and Shi, X. (1995) Predictability of the stable atmospheric boundary layer. *Journal of the Atmospheric Sciences*, 52, 1602–1614.

Monahan, A., Rees, T., He, Y. and McFarlane, N. (2015) Multiple regimes of wind, stratification, and turbulence in the stable boundary layer. *Journal of the Atmospheric Sciences*, 72, 3178–3198. https://doi.org/10.1175/JAS-D-14-0311.1.

Moraes, O.L.L., Acevedo, O.C., Silva, R., Magnago, R. and Siqueira, A.C. (2004) Nocturnal surface-layer characteristics at the bottom of a valley. *Boundary-Layer Meteorology*, 112, 159–177.

Stiperski, I., Calaf, M. and Rotach, M.W. (2019) Scaling, anisotropy, and complexity in near-surface atmospheric turbulence. *Journal of Geophysical Research: Atmospheres*, 124, 1428–1448. https://doi.org/10.1029/2018JD029383.

Sun, J., Lenschow, D.H., LeMone, M.A. and Mahrt, L. (2016) The role of large-coherent eddy transport in the atmospheric surface layer based on CASES-99 observations. *Boundary-Layer Meteorology*, 160, 83–111.

Sun, J., Mahrt, L., Banta, R.M. and Pichugina, Y.L. (2012) Turbulence regimes and turbulence intermittency in the stable boundary layer during CASES-99. *Journal of the Atmospheric Sciences*, 69, 338–351.

Sun, J., Mahrt, L., Nappo, C. and Lenschow, D.H. (2015) Wind and temperature oscillations generated by wave-turbulence interactions in the stably stratified boundary layer. *Journal of the Atmospheric Sciences*, 72, 1484–1503.

Taylor, P.A. (1971) A note on the log-linear velocity profile in stable conditions. *Quarterly Journal of the Royal Meteorological Society*, 97, 326–329.

Van de Wiel, B.J.H., Moene, A.F., Hartogensis, O.K., de Bruin, H.A.R. and Holtslag, A.A.M. (2003) Intermittent turbulence in the stable boundary layer over land. Part III: A classification for observations during CASES-99. *Journal of the Atmospheric Sciences*, 60, 2509–2522.

Van de Wiel, B.J.H., Moene, A.F. and Jonker, H.J.J. (2012b) The cessation of continuous turbulence as precursor of the very stable nocturnal boundary layer. *Journal of the Atmospheric Sciences*, 69, 3116–3127.

Van de Wiel, B.J.H., Moene, A.F., Jonker, H.J.J., Baas, P., Basu, S., Donda, J.M.M., Sun, J. and Holtslag, A.A.M. (2012a) The minimum wind speed for sustainable turbulence in the nocturnal boundary layer. *Journal of the Atmospheric Sciences*, 69, 3097–3115.

Van de Wiel, B.J.H., Moene, A.F., Steeneveld, G.J., Hartogensis, O.K. and Holtslag, A.A.M. (2007) Predicting the collapse of turbulence in stably stratified boundary layers. *Flow, Turbulence and Combustion*, 79, 251–274. https://doi.org/10.1007/s10494-007-9094-2.

Van de Wiel, B.J.H., Vignon, E., Baas, P., van Hooijdonk, I.G.S., van der Linden, S.J.A., van Hooft, J.A., Bosveld, F.C., de Roode, S.R., Moene, A.F. and Genthon, C. (2017) Regime transitions in near-surface temperature inversions: a conceptual model. *Journal of the Atmospheric Sciences*, 74, 1057–1073.

Van Hooijdonk, I.G.S., Donda, J.M.M., Clercx, J.H., Bosveld, F.C. and van de Wiel, B.J.H. (2015) Shear capacity as prognostic for nocturnal boundary layer regimes. *Journal of the Atmospheric Sciences*, 72, 1518–1532.

How to cite this article: Acevedo OC, Maroneze R, Costa FD, *et al*. The nocturnal boundary layer transition from weakly to very stable. Part I: Observations. *Q J R Meteorol Soc*. 2019;1–16. https://doi.org/10.1002/qj.3642

5 ARTIGO 3 - THE NOCTURNAL BOUNDARY LAYER TRANSITION FROM WEAKLY TO VERY STABLE. PART II: NUMERICAL SIMULATION WITH A SECOND-ORDER MODEL

Received: 26 March 2019 | Revised: 7 June 2019 | Accepted: 7 August 2019

DOI: 10.1002/qj.3643

RESEARCH ARTICLE

Quarterly Journal of the Royal Meteorological Society RMetS

The nocturnal boundary layer transition from weakly to very stable. Part II: Numerical simulation with a second-order model

Rafael Maroneze[1] | Otávio C. Acevedo[1] | Felipe D. Costa[2] | Franciano S. Puhales[1] | Giuliano Demarco[3] | Luca Mortarini[1,4]

[1]Departamento de Física, Universidade Federal de Santa Maria, Santa Maria, Brazil

[2]Universidade Federal do Pampa-Campus Alegrete, Brazil

[3]Departamento de Engenharia Mecânica, Universidade Federal de Santa Maria, Santa Maria, Brazil

[4]Institute of Atmospheric Sciences and Climate - National Research Council, Turin, Italy

Correspondence
Rafael Maroneze, Departamento de Física, Universidade Federal de Santa Maria, Santa Maria, Brazil.
Email: rafaelmaroneze@gmail.com

Abstract

Observations of the vertical and temporal structure of the nocturnal boundary layer before and after a transition from the weakly to the very stable regime have been presented in Part I. Here, similar transitions are investigated using a one-dimensional second-order closure numerical model, with an energy budget solved at the surface. The transition is driven by a decreasing mean wind at the top of the domain, and simulations with different cloud covers and surface thermal properties are considered. The time of the transition depends on the wind speed at the top of the domain and on the "coupling strength" between the surface and the atmosphere, which is affected by the cloud cover and surface thermal properties. The vertical profiles and temporal evolutions of the terms of the budgets of turbulent kinetic energy (TKE), heat flux and temperature variance are presented. Of these, only TKE budget presents the same dominant terms in both regimes. Absolute heat flux in the model is proportional to the cube of the wind speed in the very stable regime.

KEYWORDS

regime transitions, second-order closure model, stable boundary layer, very stable regime, weakly stable regime

1 | INTRODUCTION

The existence of two distinct regimes in the stable boundary layer (SBL) has been firmly established in recent years. In both observational (Mahrt, 1998; Acevedo and Fitzjarrald, 2003; Van de Wiel *et al.*, 2003; Sun *et al.*, 2012; Lan *et al.*, 2018) and modeling (McNider *et al.*, 1995; Van de Wiel *et al.*, 2002; Costa *et al.*, 2011; Maroneze *et al.*, 2019) studies, it is evident that under strong winds there is a *weakly stable* regime of fully developed turbulence, while under weak winds turbulence may be intermittent or absent, leading the SBL to be commonly referred to as *very stable*. Although it is certain that the mean wind speed has a crucial role in determining the SBL regime (Sun *et al.*, 2012; Van de Wiel *et al.*, 2012), it has also been observed that the threshold wind speed varies between sites and between nights at the same site. Therefore, other conditions are also important, and Van de Wiel *et al.* (2012) suggested that those are related to the radiative loss at the surface. Mahrt *et al.* (2013) found that transition wind speed increases with decreasing surface roughness and this result has been later confirmed both by Sun and French (2016) and Guerra *et al.* (2018). In this case, rougher surfaces tend to be more turbulent for the same mean wind speed, allowing the coupling between surface and atmosphere to occur at lower mean wind speeds. Sun and French (2016) found that the regime transition happens at higher wind speeds over the ocean than over land, showing that the coupling becomes less effective with increased surface heat capacity. This reasoning has been expanded by Van de Wiel *et al.* (2017), who attributed the control of the regime transition to the "coupling strength" between the surface and the atmosphere. It is affected by the surface energy budget, being

therefore dependent on the quantities that control this budget, such as cloudiness and the surface thermal properties. A general review on the external controls on the internal SBL flow and its coupling state is provided by Steeneveld (2014).

Baas *et al.* (2018) used a single column model that solves first-order equations and TKE to simulate the SBL over a large range of stabilities as observed at the Cabauw tower, in the Netherlands. Their model was found to "… represent regime transitions in a natural way". Later, Baas *et al.* (2019) used a similar model to simulate regime transitions observed in Antarctica, finding that such a model reproduces the complex relationship between surface thermal inversion and mean wind speed. Holdsworth and Monahan (2019) looked at the weakly to very stable transition using a first-order model with turbulent mixing determined by stability functions. They performed idealized equilibrium simulations for different geostrophic winds and found that external factors such as cloudiness, soil thermal conductivity or the Coriolis parameter also affect the SBL regime. Their study, therefore, corroborates the assertion that the wind speed that triggers the regime transition depends largely on the coupling strength.

In a companion article, Acevedo *et al.* (2019), hereinafter A19) analyzed 36 nights when a transition from the weakly to the very stable regime was evident, using 10 levels of turbulence observations taken at a 140 m tower. The transition from weakly to SBL happened systematically at the site of the tower, being driven by a superposition of a northerly synoptic flow with a sea-breeze forcing in the east–west direction. Such a superposition caused the mean large-scale wind to continually decrease in magnitude throughout the night. As a consequence, the shear production term in the turbulent kinetic energy (TKE) budget equation also continually decreases in magnitude and a regime transition occurs at some point along the night. In A19, many aspects of the vertical structure of the SBL in each regime and at the transition between regimes have been analyzed in detail. However, there were also important aspects that locally control the regime transition, such as cloudiness, that could not be addressed because of limitations of the dataset. Moreover, those observations refer to a single location, so that their analysis precludes any conclusion on how the transition is affected by different site characteristics that affect the coupling strength, such as the surface thermal properties.

In the present study, a complete second-order model is used to simulate a situation that mimics the transitions described by A19. To do that, the mean wind speed at the top of the domain model is forced to decrease continually throughout the night. The radiative budget is solved at the surface, allowing variations in processes that affect it, such as cloud cover and the surface thermal properties. Therefore, the use of such a model allows addressing the role of cloudiness and of the large-scale wind together. Furthermore, it allows generalizing the conclusions to different locations, by considering different values of soil properties such as its heat capacity and its temperature at larger depths. In contrast with previous studies that used first-order (Holdsworth and Monahan, 2019) or TKE models (Baas *et al.*, 2018; 2019), the present use of a complete second-order version allows investigating the budgets of high-order moments such as TKE, heat flux and temperature variance both in terms of temporal evolution and vertical structure. The analysis identifies the terms that dominate the respective budgets in the different SBL regimes. Therefore, the main purpose of this second part is to explain certain aspects of the transitions that cannot be analyzed with turbulence observations alone.

2 | THE MODEL

An idealized dry boundary layer is represented by the following set of equations (Blackadar, 1979; McNider *et al.*, 1995; Costa *et al.*, 2011; Maroneze *et al.*, 2019):

$$\frac{\partial \overline{u}}{\partial t} = f(\overline{v} - v_G) - \frac{\partial \overline{u'w'}}{\partial z}, \tag{1}$$

$$\frac{\partial \overline{v}}{\partial t} = f(u_G - \overline{u}) - \frac{\partial \overline{v'w'}}{\partial z}, \tag{2}$$

$$\frac{\partial \overline{\theta}}{\partial t} = -\frac{\partial \overline{w'\theta'}}{\partial z}. \tag{3}$$

Assumptions of horizontal homogeneity, incompressibility and of no radiative flux divergence in the atmosphere have been made. The ground surface temperature is determined by a force-restore method proposed by Blackadar (1979):

$$\frac{\partial \overline{\theta_g}}{\partial t} = \frac{1}{c_g}(I_\downarrow - \sigma\overline{\theta_g^4} - H_0) - k_m(\overline{\theta_g} - \overline{\theta_m}). \tag{4}$$

In Equations 1–4, $\overline{u}$, $\overline{v}$, θ, θ_g are respectively the zonal and meridional wind components, potential temperature and ground surface temperature. The Coriolis parameter is given by f, while u_G and v_G are the zonal and meridional components of the geostrophic wind. The geostrophic wind components are used in single-column models to specify the large-scale pressure gradients, which represent an external mechanical forcing. The turbulent momentum fluxes are given by $\overline{u'w'}$ and $\overline{v'w'}$, while $\overline{w'\theta'}$ is the turbulent heat flux. In Equation 4, c_g is the thermal capacity of the soil layer per unit area; σ is the Stefan–Boltzmann constant; $k_m = 1.18\,\omega$ is the soil heat transfer coefficient (where ω is Earth's angular frequency) and θ_m is the soil temperature below the surface. The term $H_0 = \rho c_P \overline{w'\theta'}_0$ is the surface sensible-heat flux, where ρ is the air density, and c_P is the specific heat of air at constant pressure. Following Staley and Jurica (1972), the long-wave radiation from the atmosphere $I_\downarrow$ is given by:

$$I_\downarrow = \sigma[Q_c + 0.67(1 - Q_c)(1670Q_a)^{0.08}]\theta_a^4, \tag{5}$$

where Q_c is the cloud fraction, Q_a the specific humidity at a reference height, and θ_a is the potential temperature at the boundary-layer top (140 m). The thermal capacity of the soil layer per unit area c_g can be determined as:

$$c_g = 0.95\left(\frac{\lambda c_s \rho_s}{2\omega}\right)^{\frac{1}{2}}, \tag{6}$$

where λ is the ground thermal conductivity, c_s is the soil specific heat and ρ_s represents soil density (Blackadar, 1979).

For a horizontally homogeneous atmosphere, the prognostic equation for TKE ($\overline{e}$) is:

$$\frac{\partial \overline{e}}{\partial t} = -\overline{u'w'}\frac{\partial \overline{u}}{\partial z} - \overline{v'w'}\frac{\partial \overline{v}}{\partial z} + \frac{g}{\Theta}\overline{w'\theta'} - \frac{\partial}{\partial z}\left[\overline{w'e} + \frac{\overline{p'w'}}{\rho_0}\right] - \varepsilon_e, \tag{7}$$

where p is pressure, ρ_0 is a reference density and Θ is a reference temperature. On the right-hand side (r.h.s) of Equation 7, the first and second terms represent the turbulence shear production (SP); the third term is the turbulence buoyant destruction under stable conditions (BD_e); the fourth term is the vertical transport of TKE both by turbulence and by pressure fluctuations (TR_e) and the fifth term is TKE viscous dissipation (DIS_e).

The prognostic equations for the momentum flux components ($\overline{u'w'}$, $\overline{v'w'}$) are:

$$\frac{\partial \overline{u'w'}}{\partial t} = -\overline{w'^2}\frac{\partial \overline{u}}{\partial z} - \frac{\partial \overline{w'u'w'}}{\partial z} + \overline{\frac{p'}{\rho_0}\left[\frac{\partial u'}{\partial z} + \frac{\partial w'}{\partial x}\right]}, \tag{8}$$

$$\frac{\partial \overline{v'w'}}{\partial t} = -\overline{w'^2}\frac{\partial \overline{v}}{\partial z} - \frac{\partial \overline{w'v'w'}}{\partial z} + \overline{\frac{p'}{\rho_0}\left[\frac{\partial v'}{\partial z} + \frac{\partial w'}{\partial y}\right]}, \tag{9}$$

where the first terms on the r.h.s of Equations 8 and 9 are the production of momentum flux by the mean wind shear, and the second and third terms represent the transport of momentum flux by turbulence and pressure fluctuations, respectively.

The prognostic equations for the horizontal velocity variances components ($\overline{u'^2}$, $\overline{v'^2}$) are:

$$\frac{\partial \overline{u'^2}}{\partial t} = -2\overline{u'w'}\frac{\partial \overline{u}}{\partial z} - \frac{\partial \overline{w'u'^2}}{\partial z} - \frac{2}{\rho_0}\frac{\partial \overline{u'p'}}{\partial x} + \overline{\frac{2p'}{\rho_0}\frac{\partial u'}{\partial x}} - \varepsilon_u, \tag{10}$$

$$\frac{\partial \overline{v'^2}}{\partial t} = -2\overline{v'w'}\frac{\partial \overline{v}}{\partial z} - \frac{\partial \overline{w'v'^2}}{\partial z} - \frac{2}{\rho_0}\frac{\partial \overline{v'p'}}{\partial y} + \overline{\frac{2p'}{\rho_0}\frac{\partial v'}{\partial y}} - \varepsilon_v, \tag{11}$$

where the first terms on the r.h.s of Equations 10 and 11 are the production of velocity variance by the mean wind shear, while the second and third terms represent the transport of velocity variance by turbulence and pressure fluctuations, respectively. The fourth term is the pressure redistribution term (return to isotropy) and the fifth is the molecular dissipation of velocity variance.

The prognostic equation for the heat flux ($\overline{w'\theta'}$) is:

$$\frac{\partial \overline{w'\theta'}}{\partial t} = -\overline{w'^2}\frac{\partial \overline{\theta}}{\partial z} + \frac{g}{\Theta}\overline{\theta'^2} - \frac{\partial \overline{w'w'\theta'}}{\partial z} + \frac{1}{\rho_0}\overline{\theta'\frac{\partial p'}{\partial z}}, \tag{12}$$

where the first term on the r.h.s represents the thermal gradient production of downward heat flux in an SBL (TGP), the second term is heat flux buoyant destruction (BD_f), and the third and fourth terms represent the transport of heat flux by turbulence and pressure fluctuations, respectively.

The prognostic equation for temperature variance is:

$$\frac{\partial \overline{\theta'^2}}{\partial t} = -2\overline{w'\theta'}\frac{\partial \overline{\theta}}{\partial z} - \frac{\partial \overline{w'\theta'^2}}{\partial z} - \varepsilon_\theta, \tag{13}$$

where the first term in the r.h.s is the heat flux production of temperature variance (Pr), the second is its turbulent transport (TR_θ) and the third term is its molecular dissipation (DIS_θ).

The prognostic equation for the vertical velocity variance is:

$$\frac{\partial \overline{w'^2}}{\partial t} = 2\frac{g}{\Theta}\overline{w'\theta'} - \frac{\partial \overline{w'w'w'}}{\partial z} - \frac{2}{\rho_0}\frac{\partial \overline{w'p'}}{\partial z} + \overline{\frac{2p'}{\rho_0}\frac{\partial w'}{\partial z}} - \varepsilon_w, \tag{14}$$

where the first term on the r.h.s represents the turbulence buoyant destruction (for stable conditions), the second and third terms represent the transport of vertical velocity variance by turbulence and pressure fluctuations, respectively. The fourth term is the pressure redistribution of turbulence among the different components and the fifth is the molecular dissipation of velocity variance. It is interesting to verify that the main source term in Equation 14 is the pressure redistribution term, which transfers energy from the horizontal velocity variances to the vertical component. As this source term is not fully understood and it plays a major role in the equation, the vertical velocity variance is determined, following Deardorff (1974), from the TKE definition:

$$\overline{w'^2} = 2\overline{e} - \overline{u'^2} - \overline{v'^2}. \tag{15}$$

Following Deardorff (1973), the last term of Equations 8 and 9 is parametrized as

$$\overline{\frac{p'}{\rho_0}\left[\frac{\partial u'}{\partial z} + \frac{\partial w'}{\partial x}\right]} = c_1\overline{e}\frac{\partial \overline{u}}{\partial z} - c_2\frac{\overline{e}^{1/2}}{l}\overline{u'w'} \quad \text{and}$$
$$\overline{\frac{p'}{\rho_0}\left[\frac{\partial v'}{\partial z} + \frac{\partial w'}{\partial y}\right]} = c_1\overline{e}\frac{\partial \overline{v}}{\partial z} - c_2\frac{\overline{e}^{1/2}}{l}\overline{v'w'}, \tag{16}$$

where c_1, c_2 are numerical constants.

The dissipation terms in Equations 7, 10, 11 and 13 are parameterized as

$$\varepsilon_e = c_8\frac{\overline{e}^{3/2}}{l}, \quad \varepsilon_u = \varepsilon_v = c_3\frac{\overline{e}^{3/2}}{l} \quad \text{and} \quad \varepsilon_\theta = c_7\frac{\sqrt{\overline{e}}}{l}\overline{\theta'^2}, \tag{17}$$

where c_3, c_8 and c_9 are numerical constants.

Following Rotta (1951), the third term on the r.h.s of Equations 10 and 11 is parametrized as

$$\overline{\frac{2p'}{\rho_0}\frac{\partial u'}{\partial x}} = -c_4\frac{\sqrt{\overline{e}}}{l}\left(\overline{u'^2} - \frac{2\overline{e}}{3}\right) \quad \text{and}$$
$$\overline{\frac{2p'}{\rho_0}\frac{\partial v'}{\partial y}} = -c_4\frac{\sqrt{\overline{e}}}{l}\left(\overline{v'^2} - \frac{2\overline{e}}{3}\right), \tag{18}$$

where c_4 is a numerical constant.

Following Therry and Lacarrere (1983) the last term of Equation 12 can be parametrized as a sum of two contributions, the first being proportional to the heat flux ($P1$) itself and the second being proportional to the temperature variance ($P2$):

$$\frac{1}{\rho_0}\overline{\theta'\frac{\partial p'}{\partial z}} = P1 + P2, \tag{19}$$

where

$$P1 = -c_6\frac{\overline{e}^{1/2}}{l}\overline{w'\theta'} \quad \text{and} \quad P2 = -c_5\frac{g}{\Theta}\overline{\theta'^2}, \tag{20}$$

c_5 and c_6 are numerical constants.

Following Duynkerke (1988), the TKE transport term is given by:

$$-\frac{\partial}{\partial z}\left[\overline{w'e} + \overline{\frac{p'w'}{\rho_0}}\right] = \frac{\partial}{\partial z}\left[\frac{K_m}{\sigma_e}\frac{\partial\overline{e}}{\partial z}\right], \tag{21}$$

where σ_e is the turbulent Prandtl number for TKE, and K_m is the exchange coefficient for momentum, which is parametrized as $K_m = 0.325\overline{e}^{1/2}l$. A value of 2.5 is assumed for σ_e in the simulation (Costa *et al.*, 2011).

Baas *et al.* (1962) suggested that:

$$\frac{1}{l} = \frac{1}{\kappa z} + \frac{1}{\lambda_0}, \tag{22}$$

where l is a mixing length, κ is von Karman constant, and following Therry and Lacarrere (1983) λ_0 is assumed to be 50 m.

In analogy with Equation 21, the transport terms are parametrized as

$$-\frac{\partial\overline{w'u'w'}}{\partial z} = \frac{\partial}{\partial z}\left[K_m\frac{\partial\overline{u'w'}}{\partial z}\right],$$
$$-\frac{\partial\overline{w'v'w'}}{\partial z} = \frac{\partial}{\partial z}\left[K_m\frac{\partial\overline{v'w'}}{\partial z}\right],$$
$$-\frac{\partial\overline{w'u'^2}}{\partial z} = \frac{\partial}{\partial z}\left[K_m\frac{\partial\overline{u'^2}}{\partial z}\right], -\frac{\partial\overline{w'v'^2}}{\partial z} = \frac{\partial}{\partial z}\left[K_m\frac{\partial\overline{v'^2}}{\partial z}\right],$$
$$-\frac{\partial\overline{w'\theta'^2}}{\partial z} = \frac{\partial}{\partial z}\left[K_m\frac{\partial\overline{\theta'^2}}{\partial z}\right] \text{ and}$$
$$-\frac{\partial\overline{w'w'\theta'}}{\partial z} = \frac{\partial}{\partial z}\left[K_m\frac{\partial\overline{w'\theta'}}{\partial z}\right].$$

With all approximations, the final set of second-order prognostic equations is:

$$\frac{\partial\overline{u'w'}}{\partial t} - \frac{\partial}{\partial z}\left[K_m\frac{\partial\overline{u'w'}}{\partial z}\right] = -\overline{w'u'}\frac{\partial\overline{u}}{\partial z} - c_1\frac{\sqrt{\overline{e}}}{l}\overline{u'w'} + c_2\overline{e}\frac{\partial\overline{u}}{\partial z}, \tag{23}$$

$$\frac{\partial\overline{v'w'}}{\partial t} - \frac{\partial}{\partial z}\left[K_m\frac{\partial\overline{v'w'}}{\partial z}\right] = -\overline{w'v'}\frac{\partial\overline{v}}{\partial z} - c_1\frac{\sqrt{\overline{e}}}{l}\overline{v'w'} + c_2\overline{e}\frac{\partial\overline{u}}{\partial z}, \tag{24}$$

$$\frac{\partial\overline{v'^2}}{\partial t} - \frac{\partial}{\partial z}\left[K_m\frac{\partial\overline{v'^2}}{\partial z}\right] = -2\overline{v'w'}\frac{\partial\overline{v}}{\partial z} - c_3\frac{\overline{e}^{3/2}}{l} - c_4\frac{\sqrt{\overline{e}}}{l}\left(\overline{v'^2} - \frac{2\overline{e}}{3}\right), \tag{25}$$

$$\frac{\partial\overline{u'^2}}{\partial t} - \frac{\partial}{\partial z}\left[K_m\frac{\partial\overline{u'^2}}{\partial z}\right] = -2\overline{v'w'}\frac{\partial\overline{u}}{\partial z} - c_3\frac{\overline{e}^{3/2}}{l} - c_4\frac{\sqrt{\overline{e}}}{l}\left(\overline{u'^2} - \frac{2\overline{e}}{3}\right), \tag{26}$$

$$\frac{\partial\overline{w'\theta'}}{\partial t} - \frac{\partial}{\partial z}\left[K_m\frac{\partial\overline{w'\theta'}}{\partial z}\right] = -\overline{w'^2}\frac{\partial\overline{\theta}}{\partial z} - (1-c_5)\frac{g}{\Theta}\overline{\theta'^2} - c_6\frac{\sqrt{\overline{e}}}{l}\overline{w'\theta'}, \tag{27}$$

$$\frac{\partial\overline{\theta'^2}}{\partial t} - \frac{\partial}{\partial z}\left[K_m\frac{\partial\overline{\theta'^2}}{\partial z}\right] = -2\overline{w'\theta'}\frac{\partial\theta}{\partial z} - c_7\frac{\sqrt{\overline{e}}}{l}\overline{\theta'^2}, \tag{28}$$

$$\frac{\partial\overline{e}}{\partial t} - \frac{\partial}{\partial z}\left[\frac{K_m}{\sigma_e}\frac{\partial\overline{e}}{\partial z}\right] = -\overline{u'w'}\frac{\partial\overline{u}}{\partial z} - \overline{v'w'}\frac{\partial\overline{v}}{\partial z} - \frac{g}{\Theta}\overline{w'\theta'} - C_8\frac{(\overline{e})^{3/2}}{l}. \tag{29}$$

A 140 m high domain is assumed from the ground surface ($z = 0$) to $h = 140$ m. Forty main levels are considered in this layer, with the first one fixed at $z_1 = 0.20$ m. The grid spacing increases linearly with height as $z_i = z_{i-1} + \Delta z_i$, where

$$\Delta z_i = \frac{z_1 + (i-1)A}{B}. \tag{30}$$

A and B are arbitrary constants (Degrazia *et al.*, 2009; Schmengler *et al.*, 2015), assumed as 3.5 and 20.6, respectively, in this simulation. As in previous studies (Costa *et al.*, 2011; Maroneze *et al.*, 2019), the second-order equations are solved at intermediate levels, located in between the main levels. It makes it easier to determine the turbulent flux divergences at the main levels.

A fourth-order Runge–Kutta algorithm is used to integrate Equations 1–4, 23–29 for 13 h, using a time step of 0.1 s.

At the domain top, the mean wind components are assumed as $u\,(t,h) = u_G$, $v\,(t,h) = v_G\,(t)$. The u_G component is assumed as constant and equal to 2 m s^{-1}, while v_G is assumed constant in the first 3 h of simulation and linearly decreasing in magnitude after this initial time at a rate of 1 m s^{-1} per hour:

$$v_G(t) = \begin{cases} -10\ \mathrm{m\,s^{-1}}, & \text{if } t < 3\ \text{h} \\ -10 + (t-3)\ \mathrm{m\,s^{-1}}, & \text{if } t > 3\ \text{h}. \end{cases} \tag{31}$$

Such a wind speed decrease is similar to the average conditions observed in the nights analyzed by A19, where it was driven by the superposition of a mean southerly flow to a time-evolving sea breeze. The first three hours of simulation before the mean wind starts to decrease are necessary for the model to reach an equilibrium. At the surface, a no slip condition is assumed ($u\,(t,0) = v\,(t,0) = 0$).

At the first level, the initial conditions for zonal and meridional wind components are $v\,(0,z_1) = u\,(0,z_1) = 0.1$ m s^{-1} and a linear profile is assumed from this level to the domain top where the wind is geostrophic. The initial conditions for ground and air temperatures are: $\theta_g\,(0) = 300$ K and $\theta\,(0,z) = 300$ K for the entire domain. The surface heat flux $\overline{u'\theta'}_0$ is assumed to be the heat flux calculated at the first intermediate level from Equation 27. The surface temperature variance is assumed to be zero.

The constants for peat soil are shown in Table 1. The peat soil heat capacity is $C_g = 14{,}600$ J K^{-1} m^{-2}, the same used in the study of McNider *et al.* (1995). To infer the role of soil properties on the regime transitions, other soil heat capacities have been considered: 1,000, 5,000, 10,000, 15,000, 20,000 and 50,000 J K^{-1} m^{-2}. In most simulations, the substrate temperature was assumed as $\theta_m = 275$ K. The role of different substrate temperatures has been considered by varying this value from 265 to 295 K with 5 K steps. The values of the constants in Equations 23–29 are shown in Table 2. These are the same used by Mellor and Yamada (1974), with the exception of c_6 and c_7 which are slightly smaller than in Mellor and Yamada (1974) for numerical stability purposes, and c_5, which is the same as that suggested by Therry and Lacarrere (1983).

TABLE 1 Peat soil parameters

λ	Ground thermal conductivity	0.06 W m^{-1} K^{-1}
c_s	Soil specific heat	1.92×10^3 J kg^{-1} K^{-1}
ρ_s	Soil density	0.3 kg/m^3
c_g	Thermal capacity of the soil layer per unit area	14,600 J K^{-1} m^{-2}

TABLE 2 Closure constants

Constants	
c_1	0.6
c_2	0.112
c_3	0.126
c_4	0.6
c_5	0.4
c_6	0.3
c_7	0.1
c_8	0.168
σ_e	2.5

3 | TEMPORAL AND VERTICAL STRUCTURE

The wind speed at the different model levels generally follows the geostrophic wind pattern forced at the domain top: a nearly linear decrease after 3 h of simulation (Figure 1a). The wind speed is only slightly affected by the cloud fraction (Figure 1a) and by the surface thermal properties (not shown), with higher values happening when there are more clouds and smaller surface heat capacity. Once the wind speed starts decreasing at 3 h, temperature drops at a rate that is different from that of wind speed, therefore not being linear (Figure 1b,d,f). The initially small temperature cooling rate steadily increases to a maximum at a time that depends on the cloud cover (Figure 1b), surface heat capacity (Figure 1d) and substrate temperature (Figure 1f). Such a maximum cooling rate, which marks an inflection point in the temperature time series, happens earlier with clear skies than otherwise. Larger surface heat capacity and colder substrate temperatures also favor earlier transitions. Fitzjarrald and Lala (1989) and Acevedo and Fitzjarrald (2001) have associated the temperature inflection point at the evening transition to surface layer decoupling from the upper boundary layer, while Acevedo *et al.* (2019) have shown that the temperature inflection point marks the regime transition from weakly to very stable on nights when the decoupling does not immediately follow the evening transition. Therefore, using the temperature inflection point to identify the regime transition, it is possible to infer that the coupling strength (Van de Wiel *et al.*, 2017) increases with increasing cloud cover, decreasing surface heat capacity and increasing substrate temperature. Increased cloud cover provides more long-wave radiation towards the surface, keeping

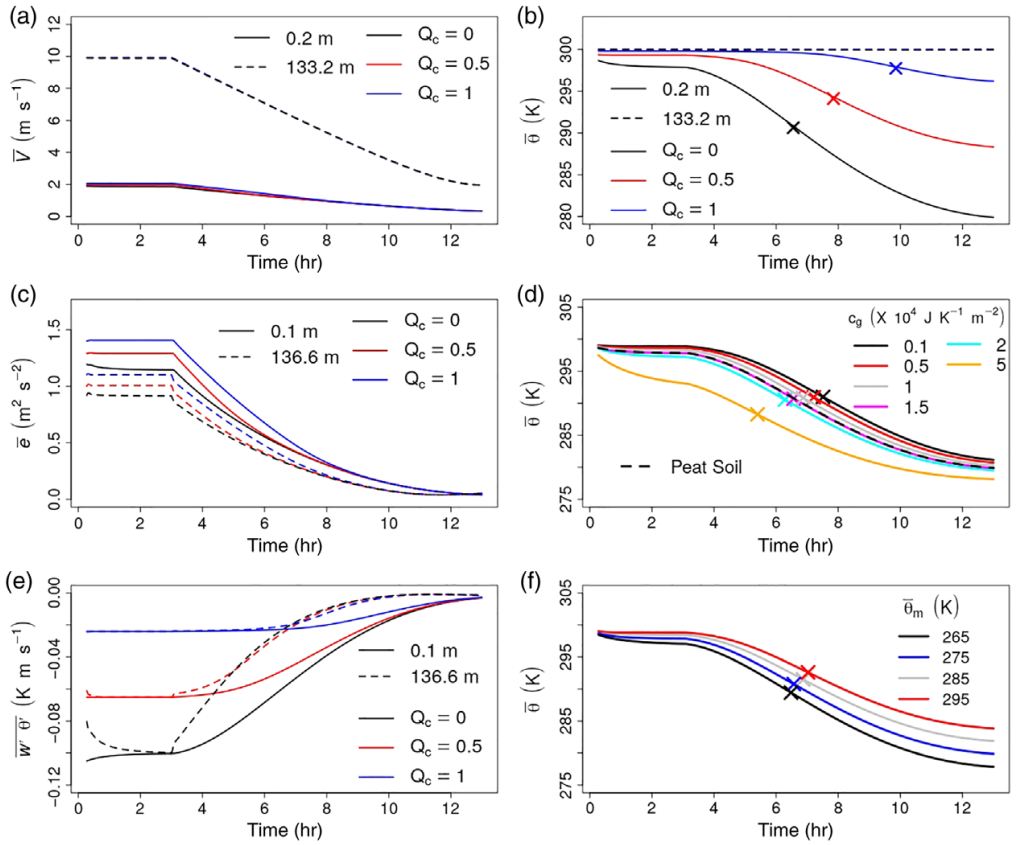

FIGURE 1 Temporal evolution of (a) wind velocity, (b,d,f) potential temperature, (c) TKE and (e) heat flux, for two distinct heights. In (a–c,e) the different lines represent different cloud covers for peat soil and $\overline{\theta}_m = 275$ K, according to legend. In (d), they represent different surface heat capacities for $Q_c = 0$ and $\overline{\theta}_m = 275$ K. In (f) they are for different substrate temperatures with $Q_c = 0$ and peat soil. In (b,d,f) the crosses identify the temperature inflection points [Colour figure can be viewed at wileyonlinelibrary.com].

it warmer, less stable and more turbulent than what occurs at a similar geostrophic wind in cloudless conditions. A similar effect is obtained when the surface heat capacity is reduced, because in this case the surface cools less (decreasing stability and increasing turbulence) than if the same radiative loss occurs with a larger surface heat capacity. Finally, a warmer substrate provides enhanced heat transfer from the deeper soil layers towards the surface, also keeping it warmer than in a similar case with a colder substrate. Therefore, when there are clouds, smaller surface heat capacity or warmer substrates, the turbulence collapses at smaller wind speeds than under clear skies, large heat capacity or cold soil substrate. TKE, on the other hand, starts decaying at a large rate that steadily decreases (Figure 1c). At the end of the simulation, TKE becomes nearly independent of the cloud cover both at lower and higher levels. At lower levels, the heat flux has an inflection point at a similar time to the temperature inflection point, but at higher levels the heat flux inflection point occurs earlier (Figure 1e).

The very small TKE and heat flux, as well as the reduced cooling rate at the end of the simulations, indicate that the surface layer is in the very stable regime and, therefore, that the SBL has experienced the transition from weakly to very stable. Sun *et al.* (2012) have proposed that the SBL regime may be determined from the relationship between a turbulence-related quantity, such as the turbulence velocity scale (V_{TKE}) or the friction velocity (u_*) and the mean wind speed ($\overline{V}$), and this criterion has been used for that purpose by a large number of studies since (Martins *et al.*, 2013; Mahrt *et al.*, 2015; Russell *et al.*, 2016; Dias-Júnior *et al.*, 2017; Vignon *et al.*, 2017; Acevedo *et al.*, 2018; *inter alia*). The comparison between V_{TKE} and $\overline{V}$ from the simulations shows that they have a linear relationship for the first hours of the simulation (Figure 2), deviating from it later. For the cloudless simulation (black lines), such a deviation from linearity occurs between 6 and 7 h from the start at 136.6 m, and after 8 h at 31.1 m. For the overcast simulation, with $Q_c = 0.8$ (blue lines), the deviation from linearity in Figure 2

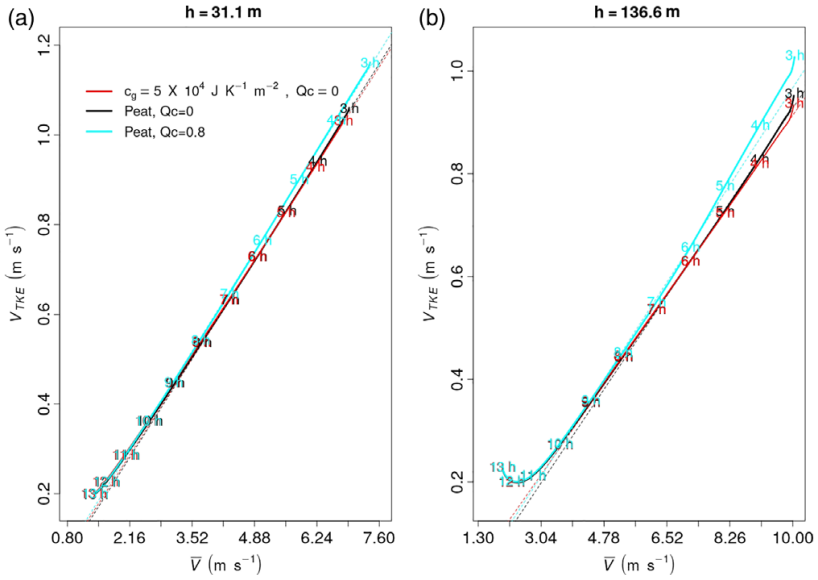

FIGURE 2 (a,b) Average dependence of the turbulence velocity scale on mean wind speed for different cloud covers and surface heat capacity, as given by legend. In all cases, $\overline{\theta}_m = 275$ K. Dotted lines show the extrapolation of a linear relationship for the first 5 h of simulation [Colour figure can be viewed at wileyonlinelibrary.com].

occurs between 9 and 10 h at 136.6 m. In the simulation with increased surface heat capacity (red lines), it happens between 5 and 6 h. In the three cases shown in Figure 2, the temperature inflection point near the surface occurs at the time when the relationship between V_{TKE} and $\overline{V}$ stops being linear at higher levels. This indicates that the decoupling in the model happens aloft, immediately affecting surface temperature as it marks the end of continuous communication across the entire vertical domain through turbulence. Therefore, from this point onwards, the temperature inflection point at the lowest level will be considered as the indicator of the regime transition in the model. Other changes that happen earlier at higher levels than near the surface are TKE becoming independent of cloud cover (Figure 1c) and the heat flux inflection point (Figure 1d). A19 also observed that the temperature inflection point marks the regime transition and that the maximum absolute heat flux near the surface occurs before the transition.

The vertical structure of the different variables before and after the transition is shown in Figure 3 for the clear-sky case and peat soil. The cooling starts near the surface, where it is also more intense (Figure 3a), but the transition affects a large vertical extension of the domain, as was also observed at Linhares from A19 and at the continental sites of Cabauw, Hamburg, Karlsruhe and Los Alamos (Abraham, 2019). Wind speed (Figure 3b) continually decays at all levels, while the observations from A19 show that it tends to a vertically dependent constant value in the very stable regime. This result shows that although the simulated transition is not as abrupt as often observed at the Linhares site in A19, the simulated wind speed values are as low as those observed. It is important to notice that A19 selected the nights with most abrupt transitions, to more precisely determine when the transition occurs. In many other cases the transition was less abrupt or smooth, resembling the model simulations more closely. TKE starts decaying in the model at higher levels (Figure 3a), as it does in the observations at Linhares (A19) and at Cabauw and Hamburg (Abraham, 2019). In the very stable regime, modeled TKE decays continually, following wind speed. The heat flux generally follows TKE, decaying in magnitude first at higher levels, similarly to the Linhares observations (Figure 3e). In the weak-wind regime, the heat flux magnitude decreases with height, consistently with the progressive cooling simulated, but contrasting with the observations that show occasional episodes of heat flux convergence and subsequent warming events (A19). These are associated with intermittent events, which are not captured by the model.

Temperature variance $\overline{\theta'^2}$ is a relevant quantity, because it constitutes one of the two heat flux destruction mechanisms in a stratified flow (Shah and Bou-Zeid, 2014). In the model, it reaches a maximum near the surface just before the transition (Figure 3f), while the observations from A19 show a broad maximum that ends at the transition. In the model, the peak is largest in the middle of the layer, near 60 m (Figure 3f). Sun *et al.* (2012) found that $\theta_* \equiv \overline{w'\theta'}/u_*$ peaks at the transition and that θ_* increases linearly with σ_θ, while Acevedo *et al.* (2016) showed that σ_θ peaks around the transition near the surface, but not at higher levels. Figure 4 shows that for

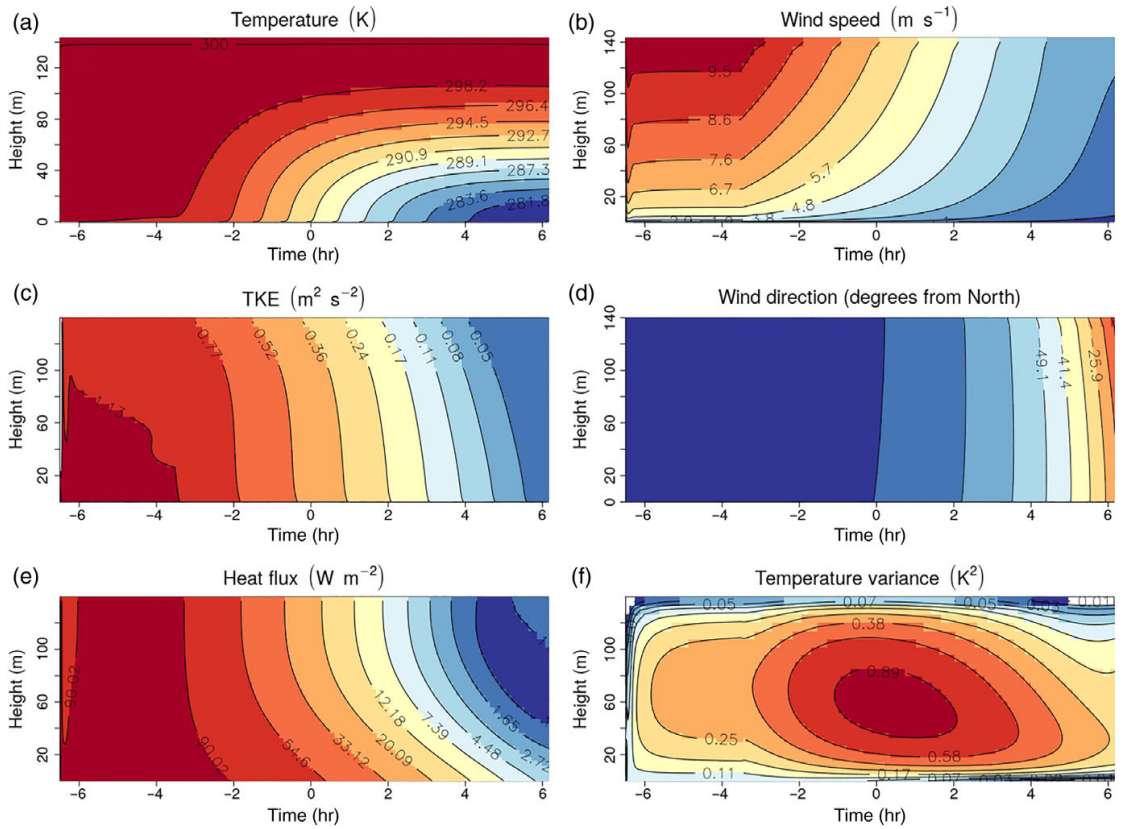

FIGURE 3 The vertical structure of (a) potential temperature, (b) wind speed, (c) TKE, (d) wind direction, (e) absolute heat flux and (f) temperature variance, before and after the transition for the clear-sky case [Colour figure can be viewed at wileyonlinelibrary.com].

any cloud cover, the $\overline{\theta'^2}$ peaks before the temperature inflection point at 1.6 m and near the domain top, at 98.8 m. At intermediate levels, such as 49.4 m, it peaks slightly after the temperature inflection point. These results suggest a close connection between $\overline{\theta'^2}$ maximum and the transition, which possibly arises from the control it exerts on the heat flux. Similar results are obtained when different surface thermal properties are considered (figure not shown).

4 | BUDGETS

In this section, the role of the coupling strength is generally assessed by considering variations in cloudiness alone. As shown previously, increased cloudiness affects the transition in a similar manner as reduced surface thermal capacity and increased substrate temperature, as all these are perturbations that increase the coupling strength between the surface and the atmosphere.

The TKE budget is dominated by shear production and dissipation terms (Figure 5a,b), as shown by Acevedo *et al.* (2016) with data from the FLOSSII experiment. For clear skies, buoyant destruction (BD_e) in the weakly stable regime is about an order of magnitude smaller than both dominant terms. When $Q_c = 0.8$ the role of BD_e is further reduced, so that the dissipation term approaches the shear production. In the very stable regime, the relative role of BD_e increases, as will be detailed later, when the Richardson number evolution will be addressed. The heat flux budget, on the other hand, shows different dominant terms in the different regimes (Figure 5c,d). The thermal gradient production term is the most important production term in both cases (notice that in this case, as the heat flux is negative, production terms are also negative). In the weakly stable regime, prior to the transition, TGP is mostly opposed by $P1$, which, following Therry and Lacarrere (1983), is parametrized similarly to a heat flux dissipation rate. After the transition, on the other hand, the most important heat flux destruction mechanism is buoyant destruction (BD_f), which is proportional to the temperature variance. Regardless of cloud cover, BD_f exceeds TGP magnitude not long after the transition, in agreement with the FLOSSII observations (Acevedo *et al.*, 2016) and

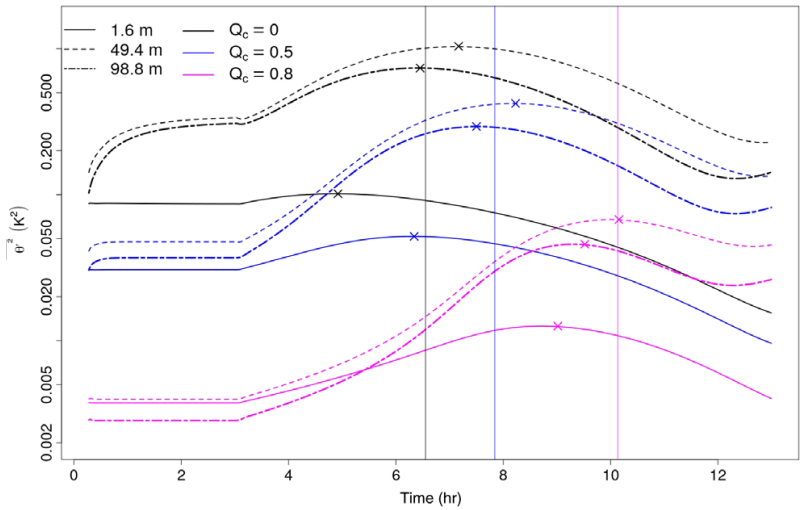

FIGURE 4 Temporal evolution of temperature variance for three distinct heights and three different cloud covers. Vertical lines show the regime transition as shown in Figure 1. Crosses identify the temporal maximum of each curve [Colour figure can be viewed at wileyonlinelibrary.com].

suggesting that the ratio between both terms might be a good indicator of the SBL regime. The other production term is the return-to-isotropy, $P2$, parametrized as proportional to the temperature variance, and it peaks in the very stable regime. The largest term (in magnitude) of the temperature variance budget at lower levels is dissipation (Figure 5e,f). This is only possible because vertical transport is positive and relatively large. The maximum $\overline{\theta'^2}$ dissipation rate happens at the transition, as given by the temperature inflection point.

The general relationship between TKE budget terms is the same throughout the entire vertical domain and regardless of cloud cover (Figure 6). In contrast, different terms dominate the heat flux budget before and after the transition (Figure 7a,b). In the weakly stable regime (Figure 7a,b, dotted lines), TGP decreases in magnitude monotonically in the vertical, while it has a maximum at the middle of the domain in the very stable regime (Figure 7a,b, solid and dashed lines). The vertical profiles of the heat flux budget terms are generally similar to those obtained from the direct numerical simulations (DNS) of Shah and Bou-Zeid (2014). In this association, the role of the return-to-isotropy term in those simulations, a destruction term, is played in the present second-order model by $P1$, a heat flux dissipation term, while the pressure transport, a production term, is simulated here as $P2$, which is proportional to the temperature variance. Acevedo *et al.* (2016) observed that in the FLuxes Over Snow Surfaces (FLOSS-II) dataset TGP exceeds BD_f in magnitude only in the weakly stable regime and near the surface. In the weakly stable regime of the model, BD_f peaks near 80 m (Figure 7a,b, purple dotted lines), which is about the only region where it exceeds TGP in magnitude. In the very stable case, on the other hand, BD_f exceeds TGP in magnitude at all heights, also in agreement with the FLOSS-II observations. For the temperature variance budget terms, the vertical profiles are very similar to those shown by Shah and Bou-Zeid (2014). In the weakly stable regime, the heat flux production term (Pr) is dominant, being larger at lower levels and decaying with height. DIS_θ is the dominant destruction term, also decaying steadily in the vertical, and the transport term is positive at lower levels, switching sign above 40 m, indicating that it transports $\overline{\theta'^2}$ from higher levels towards the surface. As the transition progresses, Pr decreases near the surface, so that it peaks above 20 m in the very stable regime. At the same time, the transport term increases near the surface, where it is larger in the very stable regime than in the weakly stable case. The height where it switches sign is lower in the very stable regime. In this case, TR_θ is the dominant production term near the surface, showing that in very stable conditions, most of the $\overline{\theta'^2}$ existent near the surface is coming from upper levels. This is also in agreement with the DNS results from Shah and Bou-Zeid (2014). This result shows that the most relevant aspects that govern the transition are captured by a simple second-order model.

The model can be used to determine whether there is a dimensionless number that universally distinguishes the two regimes. Numbers traditionally used to quantify stability, such as the flux Richardson number (the ratio between SP and BD_e in Equation 7), the local stability parameter z/Λ (where Λ is the local Obukhov length defined as $\Lambda \equiv -u_*^3\theta/\kappa g\overline{w'\theta'}$) and the gradient Richardson number are considered. The latter is defined as $Ri_g = (g/\Theta)(\partial\theta/\partial z)/((\partial u/\partial z)^2 + (\partial v/\partial z)^2)$ and evaluated by centered finite differences using adjacent model levels. A fourth dimensionless number analyzed is the ratio between the absolute values of BD_f and TGP in the heat flux

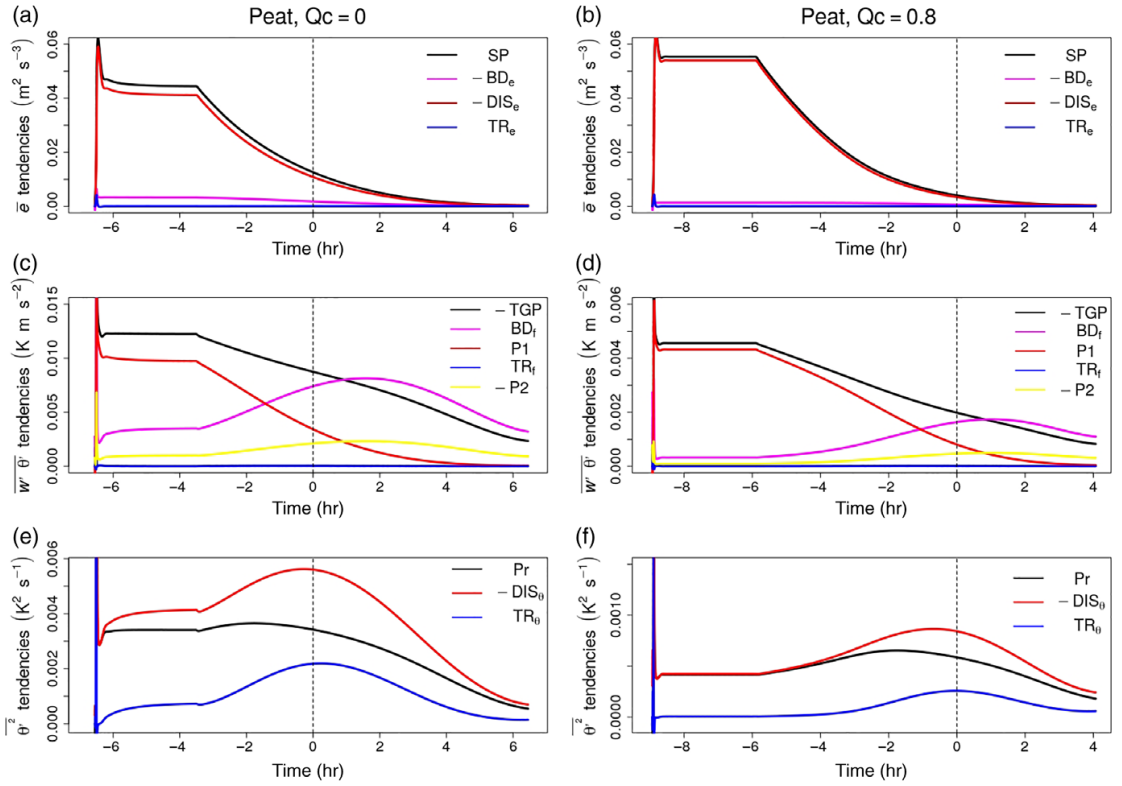

FIGURE 5 The temporal budget of (a,b) TKE, (c,d) heat flux and (e,f) temperature variance, at 8.8 m for two different cloud cover fractions [Colour figure can be viewed at wileyonlinelibrary.com].

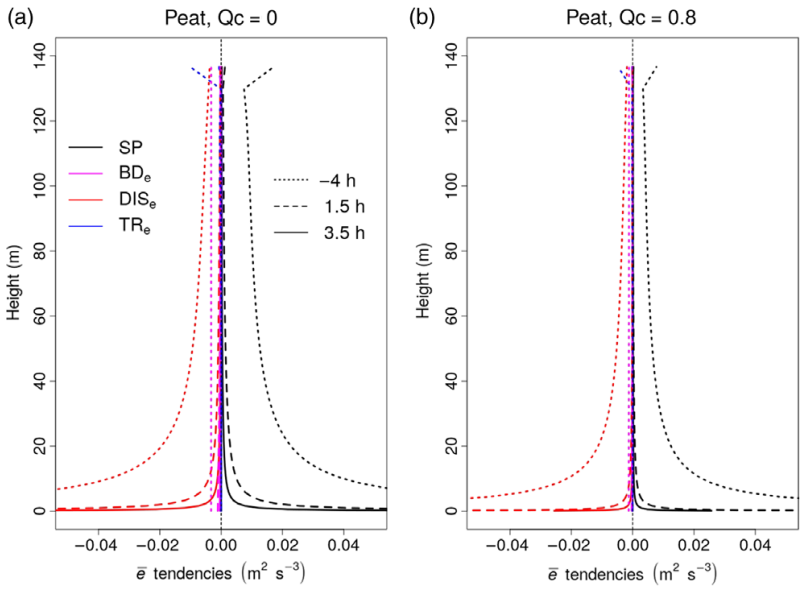

FIGURE 6 Vertical profiles of the TKE budget terms for (a) $Q_c = 0$ and (b) $Q_c = 0.8$, for three different instants of the simulation [Colour figure can be viewed at wileyonlinelibrary.com].

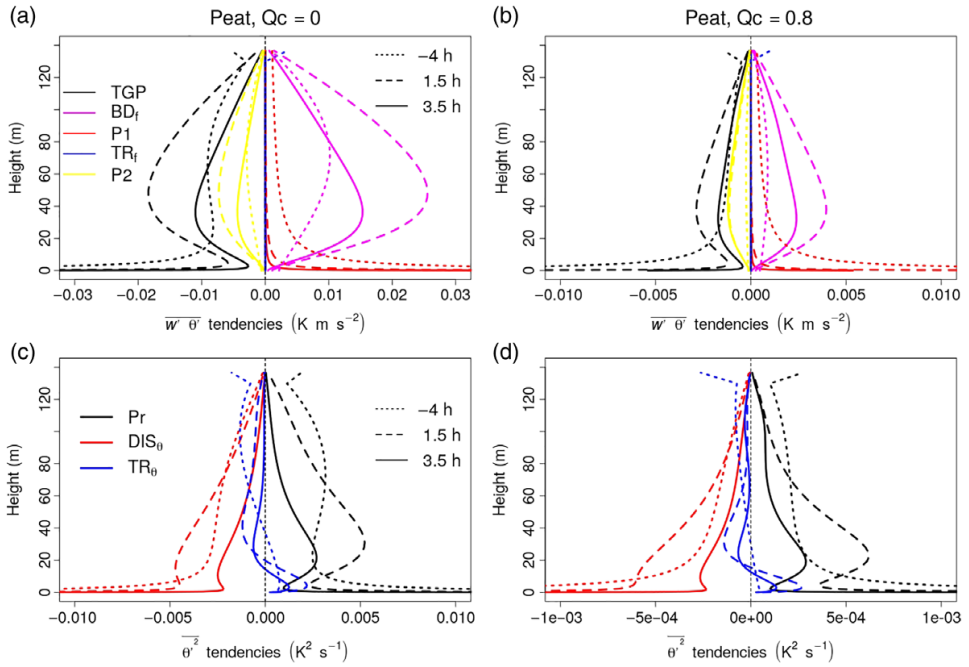

FIGURE 7 Vertical profiles of the (a,b) heat flux budget terms and (c,d) temperature variance budget terms, with (a,c) $Q_c = 0$ and (b,d) $Q_c = 0.8$, for three different instants of the simulation [Colour figure can be viewed at wileyonlinelibrary.com].

budget (Equation 12). This choice is made because, as shown in Figure 5c,d, −TGP is larger than BD_f before the transition, while the opposite happens not long after the transition, in agreement with FLOSSII observations (Acevedo *et al.*, 2016). Besides, this number also corresponds to the ratio between turbulent potential energy (TPE) and the contribution of the vertical turbulent fluctuations to TKE, so that it is a test of the association made by Sun *et al.* (2016) between the existence of two regimes and the relative importance between TPE and TKE. All these dimensionless numbers continually increase as the simulations evolve from the weakly stable to the very stable, but none shows any kind of abrupt change at or near the transition (Figure 8). The value of both Ri_f and Ri_g near the surface at the transition are just below 0.2 (Table 3), which is commonly assumed to be a critical value for the Richardson number (Freire *et al.*, 2019). Similarly, the z/Λ value near the surface at the transition is just above 0.1 (Table 3), which falls within the transition regime proposed by Mahrt (1998). As described in Figure 5, the ratio BD_f/TGP near the surface exceeds unity after the transition, so that its value at the transition is near 0.8. As noted, all numbers exhibit a smooth progression from one to the other regime. Ri_g and BD_f/TGP have critical values that are least dependent on the cloudiness, with a variation of 5% from the cloud-free simulation to that with total cloud cover. BD_f/TGP has the additional advantage of being nearly independent of cloud cover in the weak wind, very stable regime. Near the surface, its limit approaches 1.2 2 h after the transition (Table 4), tending to stay at that value further along (Figure 8j). This behavior is even more evident at upper levels (Figure 8k,l).

The common usage of the Richardson number to classify stability in the SBL, and of its critical value as a threshold for regime transition is justified by these results. It attests the essential role of the heat flux in driving the transition, despite the fact that BD_e is much smaller than both SP and DIS_e in both regimes. Along this line, Maroneze *et al.* (2019) have shown that if the BD_e term is absent in the TKE budget equation, the turbulent velocity scale increases linearly with wind speed even when the mean wind speed approaches zero. Such a controlling character of the heat flux for the regime transition explains why the ratio between the two dominant terms in its budget equation is also a good indicator of the regime. A19 made a similar comparison using the Linhares observations and found that Ri_g is the best indicator of the transition. Their results, however, indicate that the ratio BD_f/TGP is not as good a transition indicator as found in the present modeling study, possibly as a consequence of the difficulties associated with the second-order moment determination from observational data.

The relationship between Ri_g and Ri_f near the surface in the model is universal, being independent of cloud cover and surface heat capacity (Figure 9). Besides, Ri_f never exceeds 0.26, while Ri_g increases steadily along the simulation. The maximum Ri_f in the very stable regime is dependent on

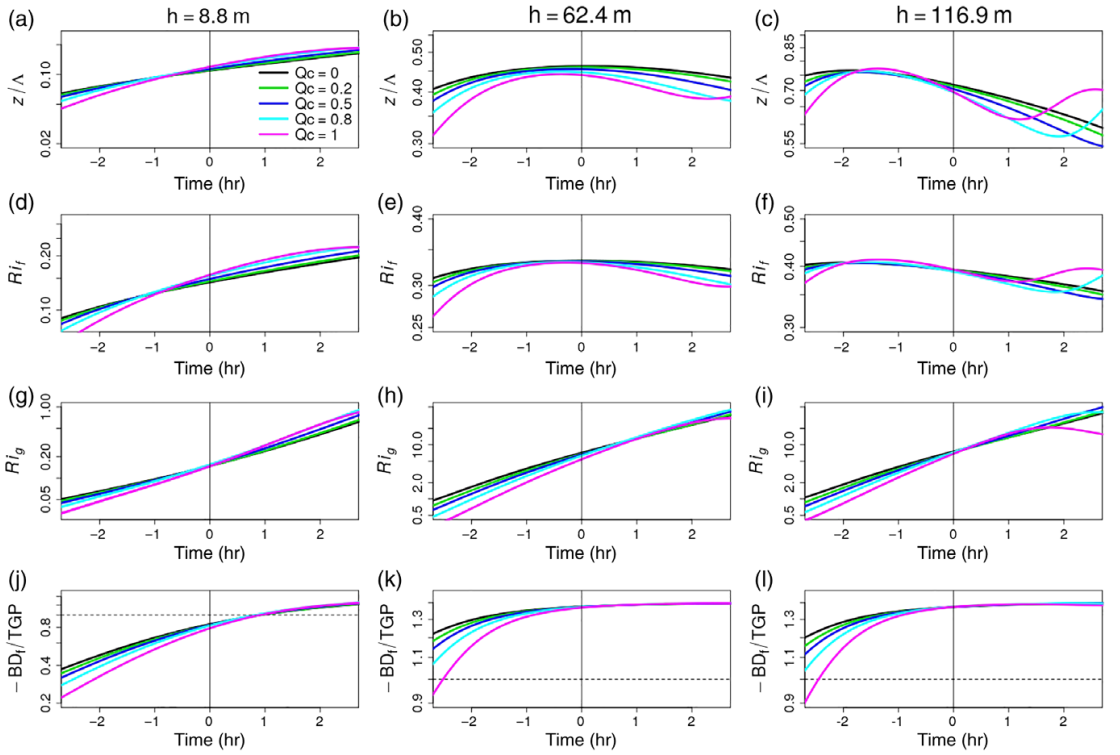

FIGURE 8 Time evolution of (a–c) Z/Λ, (d–f) Richardson flux Ri_f, (g–i) Richardson gradient Ri_g, (j–l) BD/TGP, at different heights, for five different cloud covers [Colour figure can be viewed at wileyonlinelibrary.com].

TABLE 3 Dimensionless numbers in the transition

	$Q_c = 0$	$Q_c = 0.2$	$Q_c = 0.5$	$Q_c = 0.8$	$Q_c = 1.0$
z/Λ	0.109	0.111	0.113	0.118	0.119
Ri_f	0.143	0.144	0.148	0.155	0.157
Ri_g	0.148	0.147	0.151	0.155	0.147
BD_f/TGP	0.847	0.837	0.834	0.826	0.785

TABLE 4 Dimensionless numbers 2 h after the transition

	$Q_c = 0$	$Q_c = 0.2$	$Q_c = 0.5$	$Q_c = 0.8$	$Q_c = 1.0$
z/Λ	0.148	0.151	0.16	0.172	0.177
Ri_f	0.181	0.186	0.196	0.209	0.216
Ri_g	0.41	0.428	0.485	0.566	0.567
BD_f/TGP	1.15	1.15	1.17	1.19	1.18

the surface heat capacity, but only for large values of this property. Bou-Zeid *et al.* (2018) found a theoretical maximum attainable Ri_f of 0.21, associated with the value of the Rotta constant in the return-to-isotropy term of the TKE budget equation. The present result indicates that a similar limit occurs in the second-order model used.

In the model, SP from the TKE budget equation is proportional to the third power of the mean wind speed in both regimes and regardless of cloudiness (Figure 10). BD_e, on the other hand, has a similar cubic dependence, but only in the very stable regime, as also found by A19. Such a cubic dependence is relevant, because Van de Wiel *et al.*

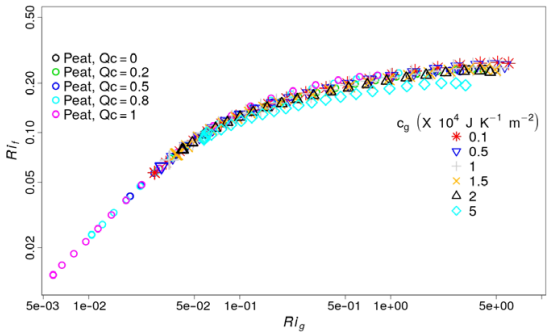

FIGURE 9 Relationship between Ri_f and Ri_g at 8.8 m for different cloud covers and surface heat capacities, as indicated by legend [Colour figure can be viewed at wileyonlinelibrary.com].

(2012) and Van Hooijdonk *et al.* (2015) based the maximum sustainable heat flux theory and the definition of Shear Capacity on a cubic relationship between heat flux and mean wind speed. In that case, the relationship was inferred from a similarity-based expression (Taylor, 1971). Using a simpler model that solved the heat flux and temperature variance, but not the variances of the wind components and the momentum fluxes, Maroneze *et al.* (2019) were not able to find such a cubic dependence in either regime, suggesting that this solution depends on solving the complete set of second-order equations. In the weakly stable regime, the model shows a tendency of independency between BD_e (and consequently, the heat flux) and the mean wind speed, which becomes more evident in the simulation with cloud cover (Figure 10b). It once more shows that in the weakly stable regime, when SP controls turbulence, the role of the heat flux is strongly reduced, such that it becomes independent of the mean wind speed. In the very stable regime, on the other hand, the heat flux affects the flow and is affected by it. In that case, it depends on the mean wind speed as do SP and DIS (not shown).

5 | CONCLUSION

The most relevant characteristics of the transitions from the weakly stable to the very stable regime have been properly simulated by a second-order model. It shows that such models properly describe the two-regime SBL. Besides, some specific findings of the study are:

- Radiative processes and surface thermal properties are determinant of the time of the transition. Under different values of these quantities, the transition takes place at different mean wind speeds. This result supports the reasoning behind the maximum sustainable heat flux theory introduced by Van de Wiel *et al.* (2012) and generalized by Van de Wiel *et al.* (2017) in the concept of a "coupling strength". It increases as cloudiness and substrate temperature increase and as surface thermal capacity decreases. Larger coupling strength causes the transition from weakly to very stable to occur with lower geostrophic wind speeds.
- Around the transition, dimensionless numbers that relate stability to mechanical effects become nearly independent of the coupling strength. It means that these numbers incorporate the role of radiative and surface thermal processes

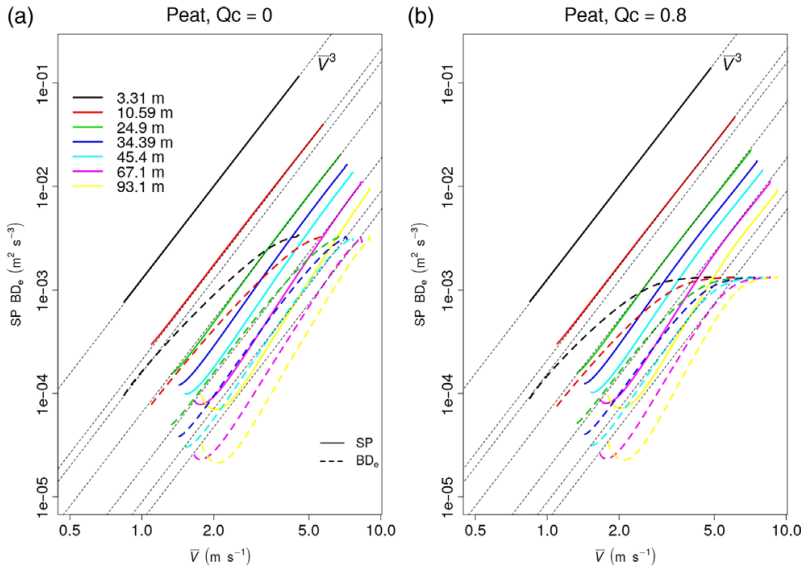

FIGURE 10 Vertical profile of the mechanical production (solid rules) and thermal destruction of TKE (dashed lines) for (a) $Q_c = 0$ and (b) $Q_c = 0.8$. Thin dotted black lines are proportional to $\overline{V}^3$ [Colour figure can be viewed at wileyonlinelibrary.com].

in their definition. This is especially true for the gradient Richardson number and for the ratio between buoyant destruction and thermal gradient production in the heat flux budget, although the latter was not found to describe well the process in the observational study of A19.

- The heat flux controls the transition, despite its small magnitude. The dominant terms in its budget change between regimes. In the heat flux budget, thermal gradient production dominates in the weakly stable case, while buoyant destruction dominates in the very stable regime.
- The temperature variance ($\overline{\theta'^2}$) peaks a little before the transition near the surface and close to the transition at higher levels. This peak is relevant because in the present case $\overline{\theta'^2}$ is numerically solved by a prognostic equation, while A19 found a similar peak from the observations. In that case, the maximum could be contaminated by the rapid cooling experienced around the transition, but the present modeling results indicate it is genuine.
- The relative magnitudes of the TKE budget terms are very little dependent on the SBL regime, while the same does not occur for the terms of the heat flux and temperature variance budgets. In these cases, different dominant terms occur at different times relative to the transition and also at different heights.

The simulations have provided a good representation of the observed quantities, showing the usefulness of the second-order model as a tool to simulate regime transitions in the SBL. A complete validation still demands a comparison of its results to real cases observed at sites with different surface characteristics. Nevertheless, the result sensitivity to external factors such as cloudiness, surface heat capacity and substrate temperature indicate that such a validation is likely to be achieved. Therefore, in the future similar second-order models may be used for describing other cases, even if no corresponding observations are available. As an example, one may consider the opposite process, of a transition from very to weakly stable, which may be forced by increasing the mechanical forcing at domain top. It may also be used to simulate case-studies of particularly interesting and relevant occurrences, such as top-down propagating intermittent events driven by wind speed enhancement aloft, the effects of abrupt variability of cloud cover, or the SBL response to low-frequency variability in the large-scale wind forcing.

ACKNOWLEDGEMENTS

The study has been developed within the context of a Research and Development project sponsored by companies Linhares Geração S.A. and Termelétrica Viana S.A., and named "Desenvolvimento de um modelo operacional para simulação em tempo real da dispersão atmosférica de poluentes emitidos por termelétrica a gás natural". The Project is within the context of the investment programme in Research and Development, regulated by Brazilian National Agency for Electric Energy. The authors thank deeply all support provided by these companies for the development of the present work. The study also has been partially supported by Brazilian funding agencies CNPq and CAPES (Finacial code 001). The latter funds graduate studies of the first author.

ORCID

Rafael Maroneze https://orcid.org/0000-0002-3025-9676
Otávio C. Acevedo https://orcid.org/0000-0003-2606-4726

REFERENCES

Abraham, C. (2019) *Regime occupation and transition information obtained from observable meteorological state variables in the stably stratified nocturnal boundary layer*. PhD Thesis, University of Victoria, Victoria, BC, Canada.

Acevedo, O.C., Degrazia, G.A., Puhales, F.S., Martins, L.G., Oliveira, P.E., Teichrieb, C., Silva, S.M., Maroneze, R., Bodmann, B., Mortarini, L., Cava, D. and Anfossi, D. (2018) Monitoring the micrometeorology of a coastal site next to a thermal power plant from the surface to 140 m. *Bulletin of the American Meteorological Society*, 99, 725–738.

Acevedo, O.C. and Fitzjarrald, D.R. (2001) The early evening surface-layer transition: temporal and spatial variability. *Journal of the Atmospheric Sciences*, 58, 2650–2667.

Acevedo, O.C. and Fitzjarrald, D.R. (2003) In the core of the night-effects of intermittent mixing on a horizontally heterogeneous surface. *Boundary-Layer Meteorology*, 106, 1–33.

Acevedo, O.C., Mahrt, L., Puhales, F.S., Costa, F.D., Medeiros, L.E. and Degrazia, G.A. (2016) Contrasting structures between the decoupled and coupled states of the stable boundary layer. *Quarterly Journal of the Royal Meteorological Society*, 142, 693–702. https://doi.org/10.1002/qj.2693.

Acevedo, O.C., Rafael, M., Costa, F.D., Puhales, F.S., Mortarini, L., Degrazia, G.A., Martins, L.G.N. and Oliveira, P.E.S. (2019) The nocturnal boundary layer transition from weakly to very stable. Part I: Observations. *Quarterly Journal of the Royal Meteorological Society*. https://doi.org/10.1002/qj.3642.

Baas, P., van de Wiel, B., van der Linden, S. and Bosveld, F. (2018) From near-neutral to strongly stratified: adequately modelling the clear-sky nocturnal boundary layer at Cabauw. *Boundary-Layer Meteorology*, 166, 217–238.

Baas, P., van de Wiel, B.J., van Meijgaard, E., Vignon, E., Genthon, C., van der Linden, S.J. and de Roode, S.R. (2019) Transitions in the wintertime near-surface temperature inversion at Dome C, Antarctica. *Quarterly Journal of the Royal Meteorological Society*, 145, 930–946.

Blackadar, A. (1962) The vertical distribution of wind and turbulent exchange in a neutral atmosphere. *Journal of Geophysical Research*, 67, 3095–3102.

Blackadar, A. (1979) High resolution models of the planetary boundary layer. *Advances in Environmental Science and Engineering*, 1, 50–85.

Bou-Zeid, E., Gao, X., Ansorge, C. and Katul, G.G. (2018) On the role of return to isotropy in wall-bounded turbulent flows with buoyancy. *Journal of Fluid Mechanics*, 856, 61–78.

Costa, F.D., Acevedo, O.C., Mombach, J.C. and Degrazia, G.A. (2011) A simplified model for intermittent turbulence in the nocturnal boundary layer. *Journal of the Atmospheric Sciences*, 68, 1714–1729.

Deardorff, J.W. (1973) Three-dimensional numerical modeling of planetary boundary layer. In: Haugen, D.A. (Ed.) *Workshop on Micrometeorology*. Boston, MA: American Meteorological Society, pp. 271–311.

Deardorff, J.W. (1974) Three-dimensional numerical study of the height and mean structure of a heated planetary boundary layer. *Boundary-Layer Meteorology*, 7, 81–106.

Degrazia, G.A., Rizza, U., Puhales, F.S., Goulart, A.G., Carvalho, J., Welter, G.S. and Marques Filho, E.P. (2009) A variable mesh spacing for large-eddy simulation models in the convective boundary layer. *Boundary-Layer Meteorology*, 131, 277–292.

Dias-Júnior, C.Q., Sá, L.D., Marques Filho, E.P., Santana, R.A., Mauder, M. and Manzi, A.O. (2017) Turbulence regimes in the stable boundary layer above and within the Amazon forest. *Agricultural and Forest Meteorology*, 233, 122–132.

Duynkerke, P.G. (1988) Application of the $E - \varepsilon$ turbulence closure model to the neutral and stable atmospheric boundary layer. *Journal of the Atmospheric Sciences*, 45, 865–880. https://doi.org/10.1175/1520-0469(1988)045<0865:AOTTCM>2.0.CO;2.

Fitzjarrald, D.R. and Lala, G.G. (1989) Hudson valley fog environments. *Journal of Applied Meteorology*, 28, 1303–1328.

Freire, L.S., Chamecki, M., Bou-Zeid, E. and Dias, N.L. (2019) Critical flux Richardson number for Kolmogorov turbulence enabled by TKE transport. *Quarterly Journal of the Royal Meteorological Society*, 145(721), 1551–1558. https://doi.org/10.1002/qj.3511.

Guerra, V.S., Acevedo, O.C., Medeiros, L.E., Oliveira, P.E.S. and Santos, D.M. (2018) Small-scale horizontal variability of mean and turbulent quantities in the nocturnal boundary layer. *Boundary-Layer Meteorology*, 169, 395–411. https://doi.org/10.1007/s10546-018-0381-3.

Holdsworth, A.M. and Monahan, A.H. (2019) Turbulent collapse and recovery in the stable boundary layer using an idealized model of pressure-driven flow with a surface energy budget. *Journal of the Atmospheric Sciences*, 76, 1307–1327.

Lan, C., Liu, H., Li, D., Katul, G.G. and Finn, D. (2018) Distinct turbulence structures in stably stratified boundary layers with weak and strong surface shear. *Journal of Geophysical Research: Atmospheres*, 123, 7839–7854.

Mahrt, L. (1998) Nocturnal boundary-layer regimes. *Boundary-Layer Meteorology*, 88, 255–278. https://doi.org/10.1023/A:1001171313493.

Mahrt, L., Sun, J. and Stauffer, D. (2015) Dependence of turbulent velocities on wind speed and stratification. *Boundary-Layer Meteorology*, 155, 55–71.

Mahrt, L., Thomas, C., Richardson, S., Seaman, N., Stauffer, D. and Zeeman, M. (2013) Non-stationary generation of weak turbulence for very stable and weak-wind conditions. *Boundary-Layer Meteorology*, 147, 179–199. https://doi.org/10.1007/s10546-012-9782-x.

Maroneze, R., Acevedo, O.C., Costa, F.D. and Sun, J. (2019) Simulating the regime transition of the stable boundary layer using different simplified models. *Boundary-Layer Meteorology*, 170, 305–321. https://doi.org/10.1007/s10546-018-0401-3.

Martins, H.S., Sá, L.D.A. and Moraes, O.L.L. (2013) Low level jets in the Pantanal wetland nocturnal boundary layer – case studies. *American Journal of Environmental Engineering*, 3, 32–47.

McNider, R.T., England, D.E., Friedman, M.J. and Shi, X. (1995) Predictability of the stable atmospheric boundary layer. *Journal of the Atmospheric Sciences*, 52, 1602–1614. https://doi.org/10.1175/1520-0469(1995)052<1602:POTSAB>2.0.CO;2.

Mellor, G.L. and Yamada, T. (1974) A hierarchy of turbulence closure models for planetary boundary layers. *Journal of the Atmospheric Sciences*, 31, 1791–1806.

Rotta, J.C. (1951) Statistische theorie nichthomogener turbulenz. *Zeitschrift für Physik*, 129, 547–572.

Russell, E.S., Liu, H., Gao, Z., Lamb, B. and Wagenbrenner, N. (2016) Turbulence dependence on winds and stability in a weak-wind canopy sublayer over complex terrain. *Journal of Geophysical Research: Atmospheres*, 121, 11502–11515.

Schmengler, M., Costa, F.D., Acevedo, O.C., Puhales, F.S., Demarco, G., Martins, L.G.N. and Medeiros, L.E. (2015) Comparison of mixing length formulations in a single-column model simulation for a very stable site. *American Journal of Environmental Engineering*, 5, 106–118.

Shah, S.K. and Bou-Zeid, E. (2014) Direct numerical simulations of turbulent Ekman layers with increasing static stability: modifications to the bulk structure and second-order statistics. *Journal of Fluid Mechanics*, 760, 494–539.

Staley, D. and Jurica, G. (1972) Effective atmospheric emissivity under clear skies. *Journal of Applied Meteorology*, 11, 349–356.

Steeneveld, G.-J. (2014) Current challenges in understanding and forecasting stable boundary layers over land and ice. *Frontiers in Environmental Science*, 2, 41. https://doi.org/10.3389/fenvs.2014.00041.

Sun, J. and French, J.R. (2016) Air–sea interactions in light of new understanding of air–land interactions. *Journal of the Atmospheric Sciences*, 73, 3931–3949. https://doi.org/10.1175/JAS-D-15-0354.1.

Sun, J., Lenschow, D.H., LeMone, M.A. and Mahrt, L. (2016) The role of large-coherent-eddy transport in the atmospheric surface layer based on CASES-99 observations. *Boundary-Layer Meteorology*, 160, 83–111. https://doi.org/10.1007/s10546-016-0134-0.

Sun, J., Mahrt, L., Banta, R.M. and Pichugina, Y.L. (2012) Turbulence regimes and turbulence intermittency in the stable boundary layer during CASES-99. *Journal of the Atmospheric Sciences*, 69, 338–351.

Taylor, P.A. (1971) A note on the log-linear velocity profile in stable conditions. *Quarterly Journal of the Royal Meteorological Society*, 97, 326–329.

Therry, G. and Lacarrère, P. (1983) Improving the eddy kinetic energy model for planetary boundary layer description. *Boundary-Layer Meteorology*, 25, 63–88. https://doi.org/10.1007/BF00122098.

Van de Wiel, B.J.H., Moene, A.F., Hartogensis, O.K., de Bruin, H.A.R. and Holtslag, A.A.M. (2003) Intermittent turbulence in the stable boundary layer over land. Part III: A classification for observations during CASES-99. *Journal of the Atmospheric Sciences*, 60, 2509–2522.

Van de Wiel, B.J.H., Ronda, R.J., Moene, A.F., de Bruin, H.A.R. and Holtslag, A.A.M. (2002) Intermittent turbulence and oscillations in the stable boundary layer over land. Part I: A bulk model. *Journal of the Atmospheric Sciences*, 59, 942–958.

Van de Wiel, B.J.H., Moene, A.F., Jonker, H.J.J., Baas, P., Basu, S., Donda, J.M.M., Sun, J. and Holtslag, A.A.M. (2012) The minimum wind speed for sustainable turbulence in the nocturnal boundary

layer. *Journal of the Atmospheric Sciences*, 69, 3116–3127. https://doi.org/10.1175/JAS-D-12-0107.1.

Van de Wiel, B.J.H., Vignon, E., Baas, P., van Hooijdonk, I.G.S., van der Linden, S.J.A., van Hooft, J.A., Bosveld, F.C., de Roode, S.R., Moene, A.F. and Genthon, C. (2017) Regime transitions in near-surface temperature inversions: a conceptual model. *Journal of the Atmospheric Sciences*, 74, 1057–1073. https://doi.org/10.1175/JAS-D-16-0180.1.

Van Hooijdonk, I.G.S., Donda, J.M.M., Clercx, H.J.H., Bosveld, F.C. and van de Wiel, B.J.H. (2015) Shear capacity as prognostic for nocturnal boundary layer regimes. *Journal of the Atmospheric Sciences*, 72, 1518–1532. https://doi.org/10.1175/JAS-D-14-0140.1.

Vignon, E., van de Wiel, B.J.H., van Hooijdonk, I.G.S., Genthon, C., van der Linden, S.J.A., van Hooft, J.A., Baas, P., Maurel, W., Traullé, O. and Casasanta, G. (2017) Stable boundary-layer regimes at Dome C, Antarctica: observation and analysis. *Quarterly Journal of the Royal Meteorological Society*, 143, 1241–1253.

How to cite this article: Maroneze R, Acevedo OC, Costa FD, Puhales FS, Demarco G, Mortarini L. The nocturnal boundary layer transition from weakly to very stable. Part II: Numerical simulation with a second-order model. *Q J R Meteorol Soc*. 2019;1–16. https://doi.org/10.1002/qj.3643

6 ARTIGO 4 - HOW IS THE TWO-REGIME STABLE BOUNDARY LAYER SOLVED BY THE DIFFERENT PBL SCHEMES IN WRF

manuscript submitted to *Geophysical Research Letters*

How is the two-regime stable boundary layer solved by the different PBL schemes in WRF?

Rafael Maroneze [1]

Otavio Costa Acevedo [1]

Felipe Denardin Costa [2]

Franciano Scremim Puhales [1]

Vagner Anabor [1]

Luca Mortarini [13]

[1]Universidade Federal de Santa Maria
[2]Universidade Federal do Pampa Campus-Alegrete
[3]Institute of Atmospheric Sciences and Climate - National Research Council

Key Points:

- Planetary Boundary Layer Schemes
- Stable Boundary Layer regimes
- WRF

Corresponding author: Rafael Maroneze, rafaelmaroneze@gmail.com

Abstract

Five planetary boundary layer (PBL) schemes of the Weather Research and Forecasting (WRF) model are compared with respect to their ability to simulate the very stable and the weakly stable regime of the stable boundary layer. This is done for single column models where the large-scale mechanical forcing, represented by geostrophic winds, ranges from 0.5 to 12 m s^{-1}. The comparison relies on the relationship between turbulence velocity scale and the mean wind speed, between thermal gradient and the mean wind speed and between flux and gradient Richardson numbers. The 2.5-level Mellor-Yamada-Nakanishi-Niino scheme is shown to simulate the very stable regime better than the other schemes, mainly because its heat eddy diffusivity decreases with respect to the momentum eddy diffusivity as the stability increases, while the same is not verified in the other schemes compared.

1 Introduction

Weather Research and Forecasting (WRF) (Skamarock et al., 2008) is currently the most used model for both research and numerical weather prediction (NWP) in the world. WRF applications are beyond NWP, as it is also employed for the prediction of a large range of Earth systems such as air chemistry, hydrology, wind and solar energy, wildland fires, hurricanes, regional climate, and others (Powers et al., 2017). Most of these applications demand a correct simulation of both daytime and nighttime periods, specifically at levels near the surface, within the planetary boundary layer (PBL). The present study addresses a difficulty that affects most PBL numerical schemes: the representation of turbulence in weak wind nocturnal conditions.

The existence of two distinct regimes in the stable boundary layer (SBL) has been known for many years (André & Mahrt, 1982; Mahrt & Gamage, 1987). More recently, the two regimes have been classified both observationally and in modelling as weakly stable and very stable (Mahrt, 1998; Sun et al., 2012; Van de Wiel et al., 2002; Acevedo et al., 2016, among others). In the weakly stable regime, turbulence is relatively well developed and continuous both in space and time. This regime typically occurs in conditions of strong wind and/or large cloud cover (Mahrt, 1998), which determine a weakly stratified or quasi-neutral boundary layer. Usually, this regime is well described by similarity theory (Mahrt, 2014) and, for this reason, it is expected to be well simulated by numerical PBL schemes, such as those employed in WRF. On the other hand, the very stable regime typically occurs with weak winds and clear sky, so that the surface radiative loss is large and, as a consequence, an intense stratification develops. In the very stable regime, turbulent mixing is largely suppressed, being localized (intermittent) both in space and time, or absent. Situations of very strong thermal stratification are not well described by classical concepts and their full description remains a challenge (Mahrt, 2014). Improving the simulation of the very stable regime by numerical schemes is a major micrometeorological challenge (Van de Wiel et al., 2017; Battisti et al., 2017; Baas et al., 2019; Holdsworth & Monahan, 2019; Lapo et al., 2019; Maroneze et al., 2019, n.d.).

Sun et al. (2012) and Van de Wiel et al. (2012) have identified that the transition between SBL regimes at a given vertical level is controlled by the mean wind speed at that level. Since then, the practice of analyzing turbulent quantities as a function of the wind speed has become common (Acevedo et al., 2016; Vignon et al., 2017; Lan et al., 2018). However, the local wind speed used in such classifications is a variable internal to the SBL dynamics, being largely dependent on other quantities such as the thermal stratification and turbulent mixing. For this reason, specially in modelling studies, it is interesting to relate the SBL regimes to external parameters. In that regard, the most commonly used parameter to represent the large-scale mechanical forcing is the geostrophic wind (McNider et al., 1995; Van de Wiel et al., 2002; Costa et al., 2011; van der Linden et al., 2017).

In the present study, five different PBL schemes of WRF are compared regarding specifically their ability to represent the two different SBL regimes: Mellor-Yamada-Nakanishi-Niino (MYNN, Nakanishi and Niino (2006), Nakanishi and Niino (2009) and Olson et al. (2019)), Mellor-Yamada-Janjic (MYJ, Janjić (1994)), Quasi-normal scale elimination (QNSE, Sukoriansky et al. (2005)), University of Washington boundary-layer scheme (UW-BLS, Bretherton and Park (2009)) and Bougeault-Lacarrere (BouLac, Bougeault and Lacarrere (1989)). Moreover, four different options of MYNN are used. The comparison is done for WRF single-column model version with the purpose of isolating how the SBL regime in each scheme responds solely to the geostrophic wind. Previous studies that compared WRF PBL schemes for stable conditions used 3D simulations, where the SBL regimes were not necessarily determined by the large-scale forcing alone (Tastula et al., 2015; Dimitrova et al., 2016; Battisti et al., 2017), as their purpose was not specifically addressing how the SBL regimes are solved.

2 Model Setup

Three days from the Cooperative Atmosphere Surface Exchange Study 1999 (CASES-99) experiment (Poulos et al., 2002) are simulated. These are the days used in GEWEX (Global Energy and Water cycle Experiment) Atmospheric Boundary Layer Study 2 (GABLS2) study, where two consecutive clear days from CASES-99 were chosen for comparing turbulence parameterizations in single column models (Svensson et al., 2011).

A 12-km single column is used with 170 levels between the surface ($z = 0$) and the top of the domain ($z = 12$ km). The initial conditions (table S1, supporting information) are the same as those in GABLS2 between the surface and 4 km, and above this level the variables are vertically uniform. As in GABLS2, a large-scale synoptic divergence is assumed to drive a mean vertical velocity of w =-0.005(z/1000) m s^{-1} until z =1000 m and w =-0.005 m s^{-1} for $z > 1000$ m, and advection is neglected. In GABLS2 simulations, skin temperature is imposed as a function of local time. Differently, in the present case it is estimated from the solar forcing according to the date, latitude and longitude.

For evaluating how the different PBL regimes solve the two SBL regimes in WRF, the geostrophic wind zonal component u_G, assumed constant in time and height for each simulation, varies from 0.5 m s^{-1} to 12 m s^{-1} with 0.5 m s^{-1} steps, totalling 23 simulations for each PBL scheme. The geostrophic wind meridional component v_g is assumed constant and equal to zero in all cases. The initial conditions are shown in Table S1.

Soil temperature is estimated through Unified Noah Land Surface Model (sf-surface-physics= 2, Mukul Tewari et al. (2004)), which depends on the longwave and shortwave radiation, determined by RRTM Longwave Scheme (ra-lw-physics= 1, Mlawer et al. (1997)) and Dudhia Shortwave Scheme (ra-sw-physics= 1, Dudhia (1989)) respectively. Kessler micro physics scheme is used in all simulations (mp-physics=1,Kessler (1969)). Dryland cropland and pasture land vegetation (scm-lu-index= 2) with vegetation fraction of 0.5 are considered.

The PBL schemes compared are MYNN, MYJ, QNSE, UWBLS and BouLac. These are the available schemes in WRF 3.9 version that explicitly solve turbulent kinetic energy (TKE). As the SBL regime definition relies on the relationship between TKE and mean wind speed, regimes are not clearly characterized in schemes where TKE is not defined, which are, therefore, not included in the comparison. Both 2.5- and 3-level versions of MYNN are considered, and in each of them two different mixing length formulations are used, so that 4 versions of this scheme are compared, totalling 8 different schemes in the study (Table S2, supporting information). A detailed description on how they represent turbulence-related quantities is given in the supporting information (SI).

3 Results

The time series of near-surface quantities are shown in Fig.1 for a special case that uses the same geostrophic forcing ($u_G = 3$ m s^{-1} and $v_G = -9$ m s^{-1}) as in GABLS2 (Svensson et al., 2011). Nocturnal temperatures differences approach 5 K between the warmest (BouLac) and coldest (MYJ) schemes, although all of them are much warmer than the CASES 99 observations (Fig. 1a). This discrepancy is mainly driven by the fact that all schemes lie in the weakly stable regime for the geostrophic forcing used, while the large observed cooling indicates that the CASES SBL was in the very stable regime when the observations were collected. It, therefore, indicates that in all PBL schemes there is a range of geostrophic winds that cause a weakly stable boundary layer in cases the observations indicate the occurrence of a very stable one. The single-column model schemes used by Svensson et al. (2011) compared better to the CASES observation at nighttime than is shown in Fig. 1a because Svensson et al. (2011) forced a data-fitted skin temperature.

In most cases, the wind speed profiles show a maximum near the surface (Fig. 2), and its vertical location may be used as a proxy for the SBL height (Cuxart et al., 2006). Boulac simulates the deepest SBL among all schemes, with a wind speed maximum near 700 m for geostrophic winds that exceed 11 m s^{-1}. This is a consequence of Boulac presenting the largest mixing lengths (Figure S1a in the SI) and lacking a stability function. Other schemes show comparable heights of the maximum wind speed. For cases of weaker geostrophic forcing, when the SBL near the surface is in the very stable regime, a sharp wind maximum close to the surface is evident for the schemes with smaller momentum eddy diffusivity (K_M). Sharpest and lowest wind maxima are associated with the smallest K_M at weak geostrophic forcing (UWBLS and QNSE being the smallest and MYNN2.5L-B coming next).

In general, thermal stratification decreases as u_G increases for all schemes (Fig. 3). The schemes with smaller eddy diffusivities in the very stable regime, MYNN2.5, MYNN2.5L-B, QNSE and UWBLS (Fig. S1b,c in SI) also simulate the most stable conditions close to the surface. MYNN3 and MYNN3l-B simulate a small stratification when the geostrophic wind is weak (Figs. 3b, c). This is a consequence of these two schemes having a countergradient contribution that causes positive heat fluxes in these situations (Eq. 68 in the SI). For large u_G, only in Boulac scheme (Fig. 3h) the stratification is almost entirely suppressed and this scheme also simulates a deeper SBL than any other scheme in this condition.

To evaluate u_G associated with SBL regime change near the surface, its value when the thermal gradient between 1.3 and 30.8 m presents a inflection point is shown as vertical dashed lines in Fig. 3 (shown in more detail in Fig. S2 in the SI). For most schemes, the regime transition determined this way happens with u_G ranging from 4.0 (UWBLS) to 5.5 m s^{-1} (MYNN2.5 and MYNN2.5L-B). The exception is MYJ, where it happens at $u_G = 9.0$ m s^{-1}, and in this case it is a consequence of the large minimum TKE imposed by this scheme, 0.1 m^2 s^{-2}. Such a transition in MYJ corresponds to u_G for which near-surface TKE exceeds that minimum. This result explains why in Fig. 1, that shows a simulation driven with $u_G \approx 9.5$ m s^{-1}, all schemes were in the weakly stable regime. Furthermore, it shows that they often simulate weakly stable conditions when very stable conditions actually occur. van der Linden et al. (2017) showed that very small friction velocities are observed when $u_G < 8.0$ m s^{-1}, further indicating that very stable conditions may be observed at values of u_G for which the PBL schemes, except MYJ, are simulating the weakly stable regime. On the other hand, the large minimum TKE of MYJ implies that the very stable regime simulated by this scheme is more turbulent than it should be.

The classical shape of the V_{TKE} x $\overline{V}$ diagram, as presented by Sun et al. (2012) using CASES99 data, obtained at flat uniform terrain, shows V_{TKE} increasing with $\overline{V}$

at a slow rate in the very stable regime and at a much larger rate at the weakly wind regime, with an abrupt transition between both regimes. Other studies have shown slight variations in this shape, which are attributed to specific site features, such as hilly terrain (Acevedo et al., 2016), vegetation (Dias-Júnior et al., 2017) or ocean (Sun & French, 2016). It is, therefore, assumed here that the CASES99 observations from Sun et al. (2012) represent the canonical form of the diagram. In the present simulations, all schemes simulate both regimes (Fig. 4), but there are appreciable differences among them regarding the regime thresholds and the behavior in the very stable, weak-wind regime. The best approximations to the CASES99 observations are obtained by MYNN2.5L-B (Fig. 4a) and MYNN2.5 (Fig. 4b). The main advantages of these two schemes lie in the very stable regime, when $VTKE$ has a slight dependence on $\overline{V}$. UWBLS performs well close to the surface , where a reduced increase of V_{TKE} with $\overline{V}$ occurs (Fig. 4g). However, as this scheme effectively suppresses turbulence when $Ri > 0.19$ (Figure S1d), it may produce $V_{TKE} = 0$, therefore independent on $\overline{V}$, at upper levels, where such stability condition may be verified. The main problem of QNSE (Fig. 4e) is its minimum imposed TKE of 0.005 $m^2\ s^{-2}$, which implies that V_{TKE} is very often at the minimum value in the very stable regime, restricting the SBL dynamics in this case. A similar, but enhanced, problem affects MYJ (Fig. 4f), whose minimum TKE is larger, 0.1 $m^2\ s^{-2}$. In both MYNN3L-B (Fig. 4c) and MYNN3 (Fig. 4d), V_{TKE} decreases with $\overline{V}$ in the very stable regime, even close to the surface. This non-physical behavior occurs along with positive heat fluxes (not shown), despite the existence of a stable stratification at the same time. This is a consequence of negative stability functions, driven by the term that depends on temperature variance (Equation 66-67 in the SI), which has been introduced in these schemes to express countergradient diffusion (Nakanishi and Nino, 2009). The V_{TKE} x $\overline{V}$ diagram for the Boulac scheme is generally similar to that for UWBLS, but the transition between regimes happens at much lower wind speeds in the Boulac scheme. This is a consequence of Boulac simulating reduced thermal stratification and enhanced turbulence than any other scheme, for the same mean wind speeds. The schemes that explicitly solve a prognostic equation for TKE (all versions of MYNN, QNSE and Boulac) show a well-behaved relationship between V_{TKE} and $\overline{V}$ once the $\overline{V}$ threshold for the weakly stable regime is exceeded. UWBLS, which does not solve TKE prognostically but, rather, estimates it diagnostically from the balance between TKE shear production, buoyancy destruction and dissipation (equation 80 in SI), simulates a more variable V_{TKE} for similar values of $\overline{V}$. A similarly large variability is simulated by MYJ, which solves a linearized form of a prognostic equation for the ratio between the mixing length and TKE (equation 26-27 in SI).

Vignon et al. (2017) showed that there are two asymptotic limits for the SBL thermal gradient, one for each regime. In the very stable regime, this limit is much larger than zero, while the weakly stable limit approaches zero. In between these two limits, the thermal gradient depends on wind speed, and Vignon et al. (2017) showed that such dependence varies according to external parameters, such as the radiative loss near the surface. The thermal gradient reduction with wind speed may be more or less abrupt, but it is always large near the wind speed threshold for regime separation. This behavior has since been also found at other sites (Van de Wiel et al., 2017; Acevedo et al., 2019). The comparison between thermal gradients and mean wind speed for the different schemes (Fig. 5a) shows that they differ regarding the abruptness and the mean wind threshold for the transition between regimes and the magnitude of the thermal stratification in both regimes, but specially in the very stable one. Very abrupt transitions are simulated by UWBLS and QNSE, the two schemes with smallest eddy diffusivities in the very stable case (Figs. S1b, c). This result is in agreement with those from Van de Wiel et al. (2017), who showed that more abrupt transitions happen in short-tail schemes that totally suppress turbulence once a stability threshold is exceeded. This is the case for UWBLS, a short-tail scheme, but not for QNSE, where the very small eddy diffusivities produce a behavior that mimics those of a short-tail scheme. Acevedo et al. (2012) have shown that the regime transition becomes less abrupt when stability functions are used, and this re-

sult explains why the Boulac scheme also simulates an abrupt transition, although in this case it happens at a much smaller wind speed threshold than in any other scheme. Smooth transitions, in that sense resembling those observed by Van de Wiel et al. (2017) and by Vignon et al. (2017) when the radiative loss is not large are simulated by the TKE long-tail schemes MYNN2.5L-B and MYNN2.5. These two schemes are also those where the wind speed threshold for the transition between schemes is largest, a feature of TKE schemes with a long-tail stability function (Acevedo et al., 2012). Very large thermal gradients, that exceed a 5-C difference between 1 and 30 m are simulated by the QNSE scheme. Again, this is a consequence of the very small heat eddy difuusivity in this scheme under weak geostrophic forcing (Fig. S1c). Although UWBLS heat eddy diffusivities are similarly small in the very stable regime, in this case the thermal stratification is limited by the forced constraint of a maximum gradient Richardson number of 0.19. Both 2;5-level MYNN schemes also simulate a large thermal stratification in the very stable regime. This is a consequence of one ot the most relevant features of these schemes regarding the two-regime SBL: a reduced heat eddy diffusivity with respect to the momentum eddy diffusivity (increased turbulent Prandtl number) in the very stable regime.

Such a relationship between momentum (K_M) and heat (K_H) eddy diffusivities is evident when one compares flux and gradient Richardson numbers (Ri and Ri_g, respectively), whose ratio equals K_M/K_H (Zilitinkevich et al., 2013; Katul et al., 2014; Bou-Zeid et al., 2018). Both observations (Ohya, 2001; Pardyjak et al., 2002) and LES results (Nakanish, 2001) show that Ri_f increases approximately linearly with Ri_g in the weakly stable regime. When Ri_g exceeds a critical value (typically around 0.25), Ri_f becomes nearly constant and independent on Ri_g, characterizing the very stable regime. The ratio Ri_g/Ri_f is also known as the turbulent Prandtl number (Pr_T), which therefore is nearly constant in the weakly stable regime, increasing linearly with Ri_g in the very stable regime, in such case implying the reduction of the heat diffusion with respect to the momentum diffusion (Zilitinkevich et al., 2013).

Only the two 2.5-level MYNN schemes consistently present reduced K_H with respect to K_M in the very stable regime (Fig. 5b), a consequence of the stability functions used in these schemes. However even in these two schemes Ri_f keeps increasing steadily (although at a much smaller rate) with Ri_g for large values of Ri_g, and no asymptotic limit for Ri exists. Among the other schemes, the two 3-level MYNN have a confuse definition of Ri in the very stable regime, caused by the frequent occurrence of positive heat fluxes in this situation, driven by the contergradient terms in their stability functions. QNSE presents a regime transition near $Ri_g = 0.25$, where K_H starts to decrease with respect to K_M, but this condition does not exist for the most stable conditions when both decrease at a similar rate. It is important, however, to notice that both K_M and K_H are very small in QNSE (Fig. S1b, c), and this is its most important feature in this regard, causing very large thermal gradients near the surface (Fig. 2e) and low level wind maximums (Fig. 3e). The UWBLS scheme imposes a critical Ri_g of 0.19, beyond which turbulence is suppressed and, for this reason, the analysis of its dynamics in the very stable regime is not possible, although its Ri x Ri_g relationship starts to bend as Ri_g approaches 0.19. Similarly, the behavior of MYJ in the very stable regime is compromised by the imposition of a relatively large minimum TKE value, which also translates in minimums for both K_M and K_H, equal to each other. Similarly to UWBLS, MYJ shows a consistent relationship between Ri and Ri_g in the weakly stable regime, that is interrupted by the minimum TKE imposition as the SBL approaches thegeostrophic very stable regime. Finally, Boulac, lacking a stability function, has always $K_M = K_H$ and, therefore, excessive heat diffusion in the very stable regime.

4 Conclusion

The analysis has indicated that the two 2.5-level MYNN perform better than the others regarding the ability to solve both the weakly and the very stable regimes of the

stable boundary layer (SBL). QNSE also performs well, but its very small eddy diffusivities cause it to often simulate TKE at its imposed minimum value (0.005 m^2 s^{-2}) when it is very stable. Most advantages of the aforementioned schemes lie in the very stable regime where the other schemes have large difficulties. These include an unrealistic negative stability function (MYNN3 and MYNN3l-b); a maximum imposed gradient Richardson number (UWBLS); an excessively large minimum TKE in a scheme that solves a linearized form of the TKE prognostic equation (MYJ) or excessive turbulence driven by the lack of a stability function (Boulac).

All schemes tend to simulate weakly stable regimes near the surface in situations that observations indicate the occurrence of a very stable regime. MYJ simulates very stable boundary layer with larger geostrophic winds than the other schemes, but this is caused by its minimum imposed TKE, that is too large. The very stable regime in this scheme has, therefore, a constant, not physically resolved TKE. Therefore, a necessary improvement in the PBL schemes regards the ability of simulating very stable boundary layers at larger geostrophic winds than they currently do.

The present results have been obtained from single-column simulations as a means to certify that the SBL regime is solely determined by the geostrophic wind forcing. For that reason, it is possible that the schemes perform somewhat differently in full 3D simulations, where advection and cloud cover may also affect the SBL regime.

None of the boundary layer schemes available at WRF prognostically solves the heat flux, possibly because this variable is not determine at the planetary boundary layer (PBL) module but, rather, at the surface layer (SL) module, where it is typically done from similarity relationships. However, there are recent indications that this is the variable that controls the SBL regime (Van de Wiel et al., 2012; Maroneze et al., 2019), so that the determination of the heat flux from a prognostic equation in the PBL module may represent an important advance in WRF ability to simulate both regimes, although it is certainly not a trivial task, as it demands adjustments in both PBL and SL modules.

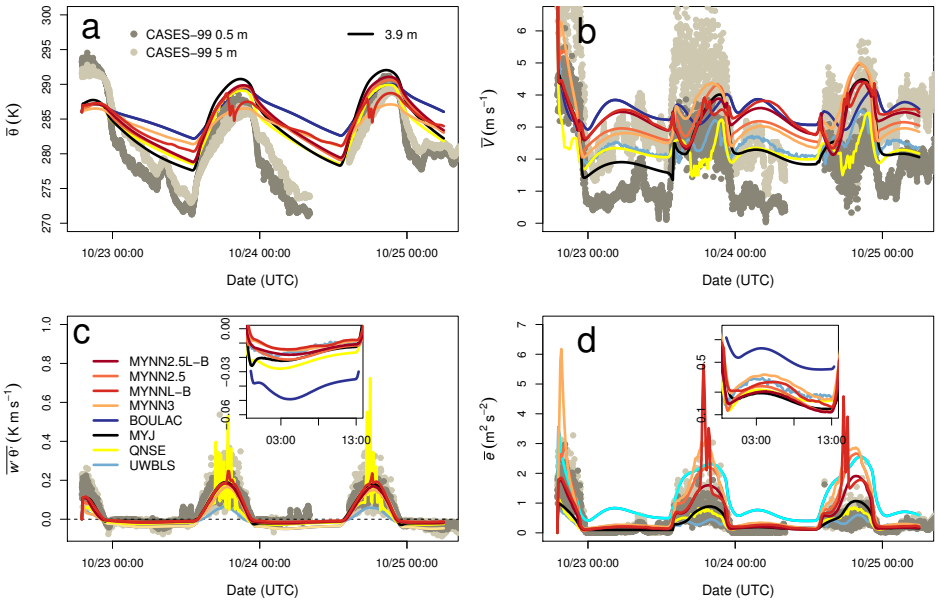

Figure 1. Temporal evolution of 3.9-m potential temperature $\overline{\theta}$ (a), mean wind speed $\overline{V}$ (b), heat flux $\overline{w'\theta'}$ (c) and TKE $\overline{e}$ (d) over the entire period of the simulations with the same geostrophic wind as in GABLS2, for the different PBL schemes used, as shown in legend at panel c. Points refer to CASES99 observations from the same days at 0.5 m (dark gray) and 5 m (light gray).

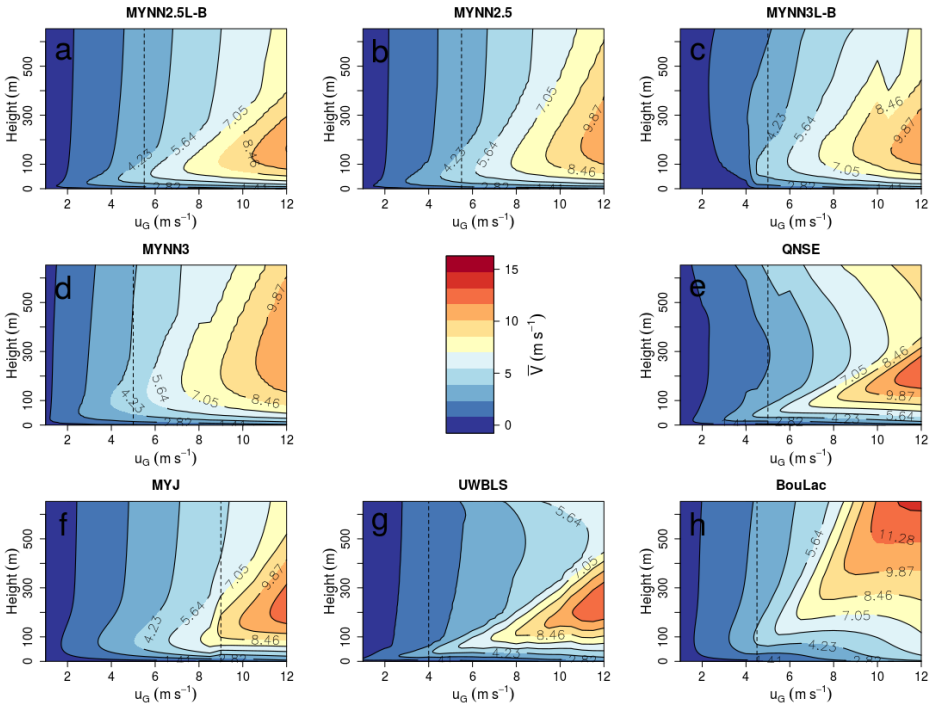

Figure 2. Average mean wind speed as a function of height and geostrophic wind for each PBL scheme as indicated at the top of each panel. For each value of geostrophic wind, values shown are the averages over the last hour of the second night of simulation. Vertical dashed line mark the geostrophic wind in which the thermal gradient between 1.3 and 30.8 m has an inflection point.

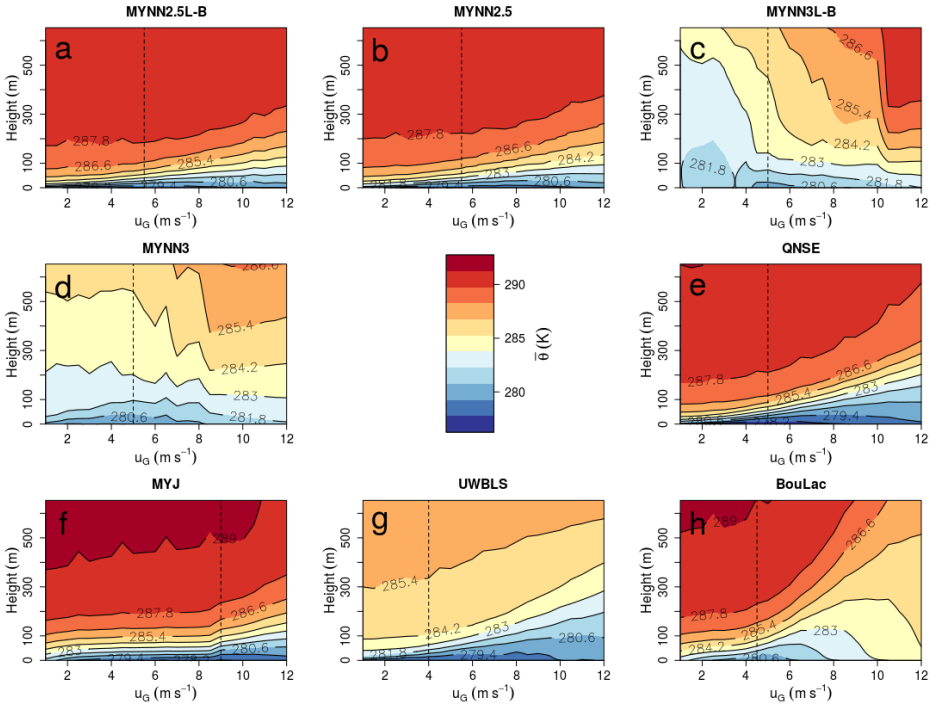

Figure 3. The same as in Figure 2, but for potential temperature. Vertical dashed line mark the geostrophic wind in which the thermal gradient between 1.3 and 30.8 m has an inflection point.

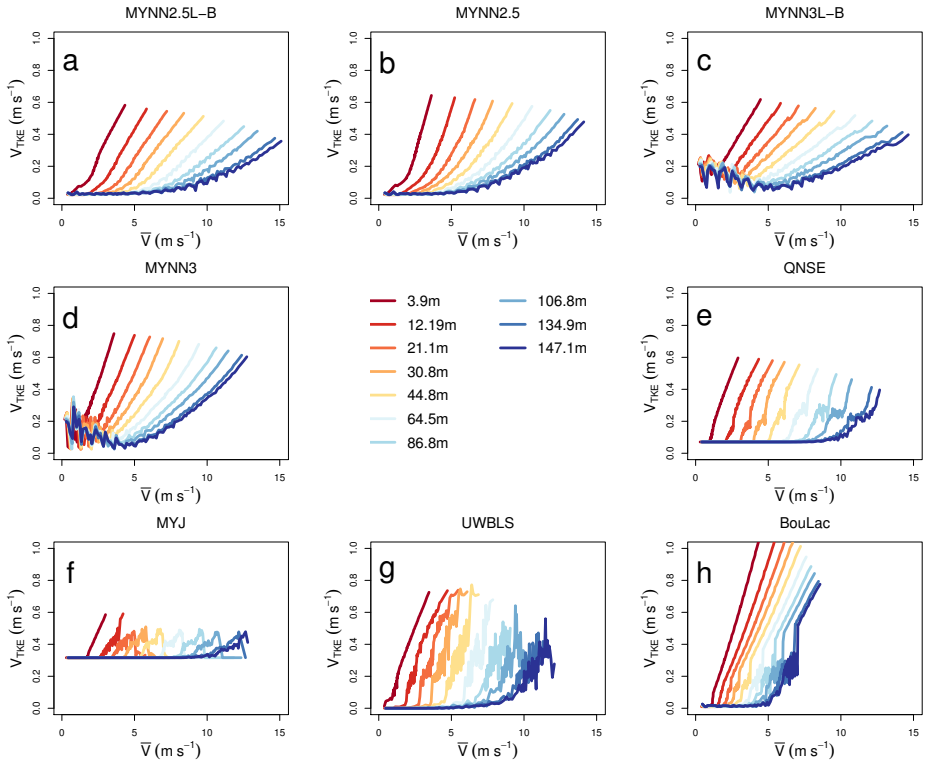

Figure 4. Average turbulence velocity scale V_{TKE} as a function of mean wind speed $\overline{V}$ for each PBL scheme, as identified at the top of each panel and for different heights as given in legend in the midlle of the plot. All panels show bin-averaged values taken from the second night of simulation, for all values of geostrophic wind considered.

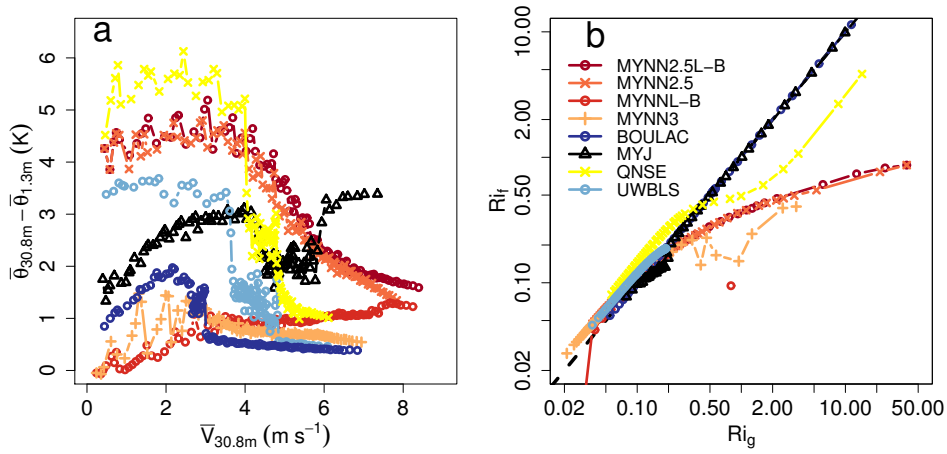

Figure 5. (a) Average potential temperature difference beteen 30.8 and 1.3 m as a function of the 30.8-m wind speed for each PBL scheme, according to legend in panel b. (b) Average flux Richardson number as a function of gradient Richardson number for each PBL scheme, according to legend. Both panels show bin-averaged values taken from the second night of simulation, for all values of geostrophic wind considered.

Acknowledgments

This study has been carried out within the scope of the Research & Development program of Brazilian energy sector, regulated by ANEEL with financial support from ENEVA. RM graduate studies have been supported by CAPES. OCA and FDC have financial support from CNPq.

References

Acevedo, O. C., Costa, F. D., & Degrazia, G. A. (2012). The coupling state of an idealized stable boundary layer. *Boundary-Layer Meteorol.*, *145*(1), 211–228.

Acevedo, O. C., Mahrt, L., Puhales, F. S., Costa, F. D., Medeiros, L. E., & Degrazia, G. A. (2016). Contrasting structures between the decoupled and coupled states of the stable boundary layer. *Q. J. R. Meteorol. Soc.*, *142*(695), 693-702. Retrieved from `https://rmets.onlinelibrary.wiley.com/doi/abs/10.1002/qj.2693` doi: 10.1002/qj.2693

Acevedo, O. C., Rafael, M., Costa, F. D., Puhales, F. S., Mortarini, L., Degrazia, G. A., ... Oliveira, P. E. S. (2019). The nocturnal boundary layer transition from weakly to very stable. part 1: Observations. *Quarterly Journal of the Royal Meteorological Society*, *0*(ja).

André, J. C., & Mahrt, L. (1982). The nocturnal surface inversion and influence of clear-air radiative cooling. *Journal of the Atmospheric Sciences*, *39*(4), 864-878. Retrieved from `https://doi.org/10.1175/1520-0469(1982)039<0864:TNSIAI>2.0.CO;2` doi: 10.1175/1520-0469(1982)039⟨0864:TNSIAI⟩2.0.CO;2

Baas, P., van de Wiel, B. J., van Meijgaard, E., Vignon, E., Genthon, C., van der Linden, S. J., & de Roode, S. R. (2019). Transitions in the wintertime near-surface temperature inversion at dome c, antarctica. *Quarterly Journal of the Royal Meteorological Society*.

Battisti, A., Acevedo, O. C., Costa, F. D., Puhales, F. S., Anabor, V., & Degrazia, G. A. (2017). Evaluation of nocturnal temperature forecasts provided by the weather research and forecast model for different stability regimes and terrain characteristics. *Boundary-Layer Meteorol.*, *162*(3), 523–546.

Bougeault, P., & Lacarrere, P. (1989). Parameterization of orography-induced turbulence in a mesobeta–scale model. *Monthly Weather Review*, *117*(8), 1872-1890. Retrieved from https://doi.org/10.1175/1520-0493(1989)117<1872:POOITI>2.0.CO;2 doi: 10.1175/1520-0493(1989)117⟨1872:POOITI⟩2.0.CO;2

Bou-Zeid, E., Gao, X., Ansorge, C., & Katul, G. G. (2018). On the role of return to isotropy in wall-bounded turbulent flows with buoyancy. *Journal of Fluid Mechanics*, *856*, 61–78.

Bretherton, C. S., & Park, S. (2009). A new moist turbulence parameterization in the community atmosphere model. *Journal of Climate*, *22*(12), 3422-3448. Retrieved from https://doi.org/10.1175/2008JCLI2556.1 doi: 10.1175/2008JCLI2556.1

Costa, F. D., Acevedo, O. C., Mombach, J. C., & Degrazia, G. A. (2011). A simplified model for intermittent turbulence in the nocturnal boundary layer. *J. Atmos. Sci.*, *68*(8), 1714–1729.

Cuxart, J., Holtslag, A. A. M., Beare, R. J., Bazile, E., Beljaars, A., Cheng, A., ... Xu, K.-M. (2006). Single-column model intercomparison for a stably stratified atmospheric boundary layer. *Boundary-Layer Meteorol.*, *118*(2), 273–303.

Dias-Júnior, C. Q., Sá, L. D., Marques Filho, E. P., Santana, R. A., Mauder, M., & Manzi, A. O. (2017). Turbulence regimes in the stable boundary layer above and within the amazon forest. *Agricultural and forest meteorology*, *233*, 122–132.

Dimitrova, R., Silver, Z., Zsedrovits, T., Hocut, C. M., Leo, L. S., Di Sabatino, S., & Fernando, H. J. S. (2016, Jun 01). Assessment of planetary boundary-layer schemes in the weather research and forecasting mesoscale model using materhorn field data. *Boundary-Layer Meteorology*, *159*(3), 589–609. Retrieved from https://doi.org/10.1007/s10546-015-0095-8 doi: 10.1007/s10546-015-0095-8

Dudhia, J. (1989). Numerical study of convection observed during the winter monsoon experiment using a mesoscale two-dimensional model. *Journal of the Atmospheric Sciences*, *46*(20), 3077-3107. Retrieved from https://doi.org/10.1175/1520-0469(1989)046<3077:NSOCOD>2.0.CO;2 doi: 10.1175/1520-0469(1989)046⟨3077:NSOCOD⟩2.0.CO;2

Holdsworth, A. M., & Monahan, A. H. (2019). Turbulent collapse and recovery in the stable boundary layer using an idealized model of pressure-driven flow with a surface energy budget. *Journal of the Atmospheric Sciences*(2019).

Janjić, Z. I. (1994). The step-mountain eta coordinate model: Further developments of the convection, viscous sublayer, and turbulence closure schemes. *Monthly Weather Review*, *122*(5), 927-945. Retrieved from https://doi.org/10.1175/1520-0493(1994)122<0927:TSMECM>2.0.CO;2 doi: 10.1175/1520-0493(1994)122⟨0927:TSMECM⟩2.0.CO;2

Katul, G. G., Porporato, A., Shah, S., & Bou-Zeid, E. (2014, Feb). Two phenomenological constants explain similarity laws in stably stratified turbulence. *Phys. Rev. E*, *89*, 023007. Retrieved from https://link.aps.org/doi/10.1103/PhysRevE.89.023007 doi: 10.1103/PhysRevE.89.023007

Kessler, E. (1969). On the distribution and continuity of water substance in atmospheric circulations. In *On the distribution and continuity of water substance in atmospheric circulations* (pp. 1–84). Boston, MA: American Meteorological Society. Retrieved from https://doi.org/10.1007/978-1-935704-36-2_1 doi: 10.1007/978-1-935704-36-2_1

Lan, C., Liu, H., Li, D., Katul, G. G., & Finn, D. (2018). Distinct turbulence structures in stably stratified boundary layers with weak and strong surface shear.

Journal of Geophysical Research: Atmospheres, *123*(15), 7839–7854.

Lapo, K., Nijssen, B., & Lundquist, J. D. (2019). Evaluation of turbulence stability schemes of land models for stable conditions. *Journal of Geophysical Research: Atmospheres*, *124*(6), 3072-3089. Retrieved from https://agupubs.onlinelibrary.wiley.com/doi/abs/10.1029/2018JD028970 doi: 10.1029/2018JD028970

Mahrt, L. (1998, Aug 01). Nocturnal boundary-layer regimes. *Boundary-Layer Meteorol.*, *88*(2), 255–278. Retrieved from https://doi.org/10.1023/A:1001171313493 doi: 10.1023/A:1001171313493

Mahrt, L. (2014). Stably stratified atmospheric boundary layers. *Annual Review of Fluid Mechanics*, *46*(1), 23-45. Retrieved from https://doi.org/10.1146/annurev-fluid-010313-141354 doi: 10.1146/annurev-fluid-010313-141354

Mahrt, L., & Gamage, N. (1987). Observations of turbulence in stratified flow. *Journal of the Atmospheric Sciences*, *44*(7), 1106-1121. Retrieved from https://doi.org/10.1175/1520-0469(1987)044<1106:OOTISF>2.0.CO;2 doi: 10.1175/1520-0469(1987)044⟨1106:OOTISF⟩2.0.CO;2

Maroneze, R., Acevedo, O. C., Costa, F. D., Puhales, F. S., Demarco, G., & Mortarini, L. (n.d.). The nocturnal boundary layer transition from weakly to very stable. part 2: Numerical simulation with a second order model. *Quarterly Journal of the Royal Meteorological Society*, *0*(0), 16. doi: 10.1002/qj.3643

Maroneze, R., Acevedo, O. C., Costa, F. D., & Sun, J. (2019, Feb 01). Simulating the regime transition of the stable boundary layer using different simplified models. *Boundary-Layer Meteorology*, *170*(2), 305–321. Retrieved from https://doi.org/10.1007/s10546-018-0401-3 doi: 10.1007/s10546-018-0401-3

McNider, R. T., England, D. E., Friedman, M. J., & Shi, X. (1995). Predictability of the stable atmospheric boundary layer. *J. Atmos. Sci.*, *52*(10), 1602-1614. Retrieved from https://doi.org/10.1175/1520-0469(1995)052<1602:POTSAB>2.0.CO;2 doi: 10.1175/1520-0469(1995)052⟨1602:POTSAB⟩2.0.CO;2

Mlawer, E. J., Taubman, S. J., Brown, P. D., Iacono, M. J., & Clough, S. A. (1997). Radiative transfer for inhomogeneous atmospheres: Rrtm, a validated correlated-k model for the longwave. *Journal of Geophysical Research: Atmospheres*, *102*(D14), 16663-16682. Retrieved from https://agupubs.onlinelibrary.wiley.com/doi/abs/10.1029/97JD00237 doi: 10.1029/97JD00237

Mukul Tewari, N., Tewari, M., Chen, F., Wang, W., Dudhia, J., LeMone, M., ... others (2004). Implementation and verification of the unified noah land surface model in the wrf model (formerly paper number 17.5). In *20th conference on weather analysis and forecasting/16th conference on numerical weather prediction* (pp. 11–15).

Nakanish, M. (2001, Jun 01). Improvement of the mellor–yamada turbulence closure model based on large-eddy simulation data. *Boundary-Layer Meteorology*, *99*(3), 349–378. Retrieved from https://doi.org/10.1023/A:1018915827400 doi: 10.1023/A:1018915827400

Nakanishi, M., & Niino, H. (2006, May 01). An improved mellor–yamada level-3 model: Its numerical stability and application to a regional prediction of advection fog. *Boundary-Layer Meteorology*, *119*(2), 397–407. Retrieved from https://doi.org/10.1007/s10546-005-9030-8 doi: 10.1007/s10546-005-9030-8

Nakanishi, M., & Niino, H. (2009). Development of an improved turbulence closure model for the atmospheric boundary layer. *Journal of the Meteorological Society of Japan. Ser. II*, *87*(5), 895-912. doi: 10.2151/jmsj.87.895

Ohya, Y. (2001, Jan 01). Wind-tunnel study of atmospheric stable boundary layers over a rough surface. *Boundary-Layer Meteorology*, *98*(1), 57–82. Retrieved from https://doi.org/10.1023/A:1018767829067 doi: 10.1023/A:

436 1018767829067
437 Olson, J. B., Kenyon, J. S., Angevine, W., Brown, J. M., Pagowski, M., Sušelj, K.,
438 et al. (2019). A description of the mynn-edmf scheme and the coupling to
439 other components in wrf–arw.
440 Pardyjak, E. R., Monti, P., & Fernando, H. J. S. (2002). Flux richardson number
441 measurements in stable atmospheric shear flows. *Journal of Fluid Mechanics*,
442 *459*, 307–316. doi: 10.1017/S0022112002008406
443 Poulos, G. S., Blumen, W., Fritts, D. C., Lundquist, J. K., Sun, J., Burns,
444 S. P., ... Jensen, M. (2002). Cases-99: A comprehensive investigation
445 of the stable nocturnal boundary layer. *Bulletin of the American Mete-*
446 *orological Society*, *83*(4), 555-582. Retrieved from `https://doi.org/`
447 `10.1175/1520-0477(2002)083<0555:CACIOT>2.3.CO;2` doi: 10.1175/
448 1520-0477(2002)083⟨0555:CACIOT⟩2.3.CO;2
449 Powers, J. G., Klemp, J. B., Skamarock, W. C., Davis, C. A., Dudhia, J., Gill,
450 D. O., ... Duda, M. G. (2017). The weather research and forecasting model:
451 Overview, system efforts, and future directions. *Bulletin of the American*
452 *Meteorological Society*, *98*(8), 1717-1737. Retrieved from `https://doi.org/`
453 `10.1175/BAMS-D-15-00308.1` doi: 10.1175/BAMS-D-15-00308.1
454 Skamarock, W. C., Klemp, J. B., Dudhia, J., Gill, D. O., Barker, D. M., Wang, W.,
455 & Powers, J. G. (2008). A description of the advanced research wrf version 3.
456 ncar technical note-475+ str.
457 Sukoriansky, S., Galperin, B., & Perov, V. (2005, Nov 01). 'application of a new
458 spectral theory of stably stratified turbulence to the atmospheric bound-
459 ary layer over sea ice'. *Boundary-Layer Meteorology*, *117*(2), 231–257.
460 Retrieved from `https://doi.org/10.1007/s10546-004-6848-4` doi:
461 10.1007/s10546-004-6848-4
462 Sun, J., & French, J. R. (2016). Air–sea interactions in light of new understanding of
463 air–land interactions. *Journal of the Atmospheric Sciences*, *73*(10), 3931-3949.
464 Retrieved from `https://doi.org/10.1175/JAS-D-15-0354.1` doi: 10.1175/
465 JAS-D-15-0354.1
466 Sun, J., Mahrt, L., Banta, R. M., & Pichugina, Y. L. (2012). Turbulence regimes
467 and turbulence intermittency in the stable boundary layer during "cases-99".
468 *J. Atmos. Sci.*, *69*(1), 338–351.
469 Svensson, G., Holtslag, A. A. M., Kumar, V., Mauritsen, T., Steeneveld, G. J.,
470 Angevine, W. M., ... Zampieri, M. (2011). Evaluation of the diurnal cycle in
471 the atmospheric boundary layer over land as represented by a variety of single-
472 column models: the second "gabls" experiment. *Boundary-Layer Meteorol.*,
473 *140*(2), 177–206.
474 Tastula, E.-M., Galperin, B., Dudhia, J., LeMone, M. A., Sukoriansky, S., &
475 Vihma, T. (2015). Methodical assessment of the differences between
476 the qnse and myj pbl schemes for stable conditions. *Quarterly Journal*
477 *of the Royal Meteorological Society*, *141*(691), 2077-2089. Retrieved from
478 `https://rmets.onlinelibrary.wiley.com/doi/abs/10.1002/qj.2503` doi:
479 10.1002/qj.2503
480 van der Linden, S. J. A., Baas, P., van Hooft, J. A., van Hooijdonk, I. G. S.,
481 Bosveld, F. C., & van de Wiel, B. J. H. (2017). Local characteristics of the
482 nocturnal boundary layer in response to external pressure forcing. *J. Appl.*
483 *Meteorol. Climat.*, *56*(11), 3035-3047. Retrieved from `https://doi.org/`
484 `10.1175/JAMC-D-17-0011.1` doi: 10.1175/JAMC-D-17-0011.1
485 Van de Wiel, B. J. H., Moene, A. F., Jonker, H. J. J., Baas, P., Basu, S., Donda,
486 J. M. M., ... Holtslag, A. A. M. (2012). The minimum wind speed for sustain-
487 able turbulence in the nocturnal boundary layer. *Journal of the Atmospheric*
488 *Sciences*, *69*(11), 3116-3127. Retrieved from `https://doi.org/10.1175/`
489 `JAS-D-12-0107.1` doi: 10.1175/JAS-D-12-0107.1
490 Van de Wiel, B. J. H., Ronda, R. J., Moene, A. F., De Bruin, H. A. R., & Holt-

slag, A. A. M. (2002). Intermittent turbulence and oscillations in the stable boundary layer over land. part i: A bulk model. *Journal of the Atmospheric Sciences*, *59*(5), 942-958. Retrieved from https://doi.org/10.1175/1520-0469(2002)059<0942:ITAOIT>2.0.CO;2 doi: 10.1175/1520-0469(2002)059⟨0942:ITAOIT⟩2.0.CO;2

Van de Wiel, B. J. H., Vignon, E., Baas, P., van Hooijdonk, I. G. S., van der Linden, S. J. A., Antoon van Hooft, J., ... Genthon, C. (2017). Regime transitions in near-surface temperature inversions: A conceptual model. *Journal of the Atmospheric Sciences*, *74*(4), 1057-1073. Retrieved from https://doi.org/10.1175/JAS-D-16-0180.1 doi: 10.1175/JAS-D-16-0180.1

Vignon, E., van de Wiel, B. J., van Hooijdonk, I. G., Genthon, C., van der Linden, S. J., van Hooft, J. A., ... Casasanta, G. (2017). Stable boundary-layer regimes at dome c, antarctica: observation and analysis. *Quarterly Journal of the Royal Meteorological Society*, *143*(704), 1241–1253.

Zilitinkevich, S. S., Elperin, T., Kleeorin, N., Rogachevskii, I., & Esau, I. (2013, Mar 01). A hierarchy of energy- and flux-budget (efb) turbulence closure models for stably-stratified geophysical flows. *Boundary-Layer Meteorology*, *146*(3), 341–373. Retrieved from https://doi.org/10.1007/s10546-012-9768-8 doi: 10.1007/s10546-012-9768-8

GEOPHYSICAL RESEARCH LETTERS

Supporting Information for "How is the two-regime stable boundary layer solved by the different PBL schemes in WRF?"

Rafael Maroneze [1]

Otavio Costa Acevedo [1]

Felipe Denardin Costa [2]

Franciano Scremim Puhales [1]

Vagner Anabor [1]

Luca Mortarini [13]

[1]Universidade Federal de Santa Maria

[2]Universidade Federal do Pampa Campus-Alegrete

[3]Institute of Atmospheric Sciences and Climate - National Research Council

Contents of this file

1. Description of the PBL schemes

2. Figures S1-S2

3. Tables S1-S3

1. Description of the PBL schemes

The following description regards the PBL schemes representations available in WRF 3.9 version. In some cases, the code differs in details from the papers on which the scheme is based. When it happens, the present description refers to the information from the WRF 3.9-version code. Furthermore, in some cases different stability conditions and mixing lengths exist for day and nighttime. The present description regards the nocturnal case alone, as this is the one that affectes the SBL regimes.

All numerical constants used in the schemes are presented in Table S3.

1.1. BouLac

For BouLac PBL scheme (Bougeault & Lacarrere, 1989), a characteristic length is defined as the vertical distance that a fluid particle may travel upward (l_{up}) or downward (l_{down}) in response to a local amount of TKE. The lengths l_{up} and l_{down} are given, respectively by

$$\int_{z}^{z+l_{up}} \beta \left(\overline{\theta}\left(z\right) - \overline{\theta}\left(z'\right) \right) dz' = \overline{e}\left(z\right), \tag{1}$$

and

$$\int_{z-l_{down}}^{z} \beta \left(\overline{\theta}\left(z'\right) - \overline{\theta}\left(z\right) \right) dz' = \overline{e}\left(z\right). \tag{2}$$

In this formulation, the eddies characteristic length is

$$l_K = min\left(l_{up}, l_{down}\right). \tag{3}$$

The vertical turbulent diffusion coeficients are related to both TKE and l_K as

$$K_m = C_K l_K \overline{e}^{1/2}, \tag{4}$$

$$K_h = \alpha_T K_m, \tag{5}$$

and

$$K_e = \alpha_e K_m, \tag{6}$$

where C_K is a numerical constant, and α_T is the inverse of the turbulent Prandtl number. Using K-theory, the second-order statistical moments are parameterized as

$$\overline{u'w'} = -K_m \frac{\partial \overline{u}}{\partial z}, \tag{7}$$

$$\overline{v'w'} = -K_m \frac{\partial \overline{v}}{\partial z} \tag{8}$$

$$\overline{w'\theta'} = -K_h \frac{\partial \overline{\theta}}{\partial z} \tag{9}$$

and

$$\overline{w'e} = -K_e \frac{\partial \overline{e}}{\partial z}. \tag{10}$$

TKE dissipation rate is estimated as

$$\epsilon = C_\epsilon \frac{\overline{e}^{3/2}}{l_\epsilon}, \tag{11}$$

where C_ϵ is a numerical constant, and l_ϵ is the characteristic length of the energy-containing eddies, given by

$$l_\epsilon = \left(l_{up} l_{down}\right)^{1/2}. \tag{12}$$

Therefore, the prognostic equation for TKE solved by the scheme is

$$\frac{\partial \overline{e}}{\partial z} = K_m \left[\left(\frac{\partial \overline{u}}{\partial z} \right)^2 + \left(\frac{\partial \overline{v}}{\partial z} \right)^2 \right] - \frac{g}{\Theta} K_h \frac{\partial \overline{\theta}}{\partial z} + \frac{\partial}{\partial z} \left(K_e \frac{\partial \overline{e}}{\partial z} \right) - C_\epsilon \frac{\overline{e}^{3/2}}{l_\epsilon}. \tag{13}$$

Minimum values for K_m and for TKE are assumed as 0.1 m^2 s^{-1} and 0.0001 m^2 s^{-2} respectively. BouLac scheme does not use a stability function.

1.2. Mellor Yamada Janjic

For the Mellor Yamada Janjic PBL scheme (Janji, 1994), the turbulent length scale is defined as (Mellor & Yamada, 1974):

$$l_t = \frac{l_0 \kappa z}{\kappa z + l_0}, \tag{14}$$

where

$$l_0 = \frac{\int_0^\infty \alpha \left| z \right| q dz}{\int_0^\infty q dz}. \tag{15}$$

As in Mellor and Yamada (1974), q^2 is defined as twice TKE ($q^2 = 2\overline{e}$) In (14) and (15), κ is the von Karman constant and α is a numerical constant, whose values are given in table S1. The dimensionless vertical gradients of wind speed and temperature are defined, respectively, as

$$G_M \equiv \frac{l_t^2}{q^2} \left[\left(\frac{\partial \overline{u}}{\partial z} \right)^2 + \left(\frac{\partial \overline{v}}{\partial z} \right)^2 \right], \tag{16}$$

and

$$G_H \equiv \frac{l_t^2}{q^2} \beta g \frac{\partial \overline{\theta}_V}{\partial z}. \tag{17}$$

In (16), $\beta = 1/\Theta$. For MYJ the stability functions form momentum (S_M) and heat (S_H) are the same as those in Mellor and Yamada (1982), but written in terms of the

above defined quantities:

$$S_M = \frac{A_{S_M} G_H + B_{S_M}}{\left(C_{S_M} G_M + D_{S_M} G_H\right) G_H + F_{S_M} G_M + G_{S_M} G_H + 1}, \tag{18}$$

and

$$S_H \equiv \frac{\left(A_{S_H} G_M + B_{S_H} G_H\right) + A_2}{\left(C_{S_M} G_M + D_{S_M} G_H\right) G_H + F_{S_M} G_M + G_{S_M} G_H + 1}, \tag{19}$$

where A_{S_M}, B_{S_M},C_{S_M},D_{S_M},F_{S_M},G_{S_M},A_{S_H},B_{S_H} and C_{S_H} are numerical constants given by

$$A_{S_M} = -3A_1A_2\left(3A_2 + 3B_2C_1 + 12A_1C_1 - B2\right),$$

$$B_{S_M} = A_1\left(1 - 3C_1\right),$$

$$C_{S_M} = 18A_1^2A_2\left(B_2 - 3A_2\right),$$

$$D_{S_M} = 9A_1A_2^2\left(12A_1 + 3B_2\right),$$

$$F_{S_M} = 6A_1^2,$$

$$G_{S_M} = 3A_2\left(7A_1 + B_2\right),$$

$$A_{S_H} = 18A_1^2A_2C_1,$$

$$B_{S_H} = 9A_1A_2^2,$$

$$C_{S_H} = A_2,$$

where the numerical constants A_1,A_2,B_1,B_2 and C_1 values are shown in table S1.

The vertical turbulent diffusion coeficients are related to S_M, S_H and q:

$$K_M = l_t q S_M, \tag{20}$$

$$K_H = l_t q S_H, \tag{21}$$

and the second-order statistical moments are parameterized as in equations 7-9. MYJ TKE disipation is assumed as

$$\epsilon_q = \frac{q^3}{B_1 l_t}. \tag{22}$$

Lacking a transport term, the prognostic equation for q is

$$\frac{\partial q}{\partial t} = \left(\frac{q^2}{l_t}\right)\left[S_M G_M + S_H G_H - \frac{1}{B_1}\right], \tag{23}$$

Equation 23 may be rewritten as

$$\frac{d}{dt}\left(\frac{l_t}{q}\right) = \frac{A\left(\frac{l_t}{q}\right)^4 + B\left(\frac{l_t}{q}\right)^2}{C\left(\frac{l_t}{q}\right)^4 + D\left(\frac{l_t}{q}\right)^2 + 1} - \frac{1}{B1}, \tag{24}$$

where the right-hand side is defined as R. Its derivative with respect to l_t/q is defined as R':

$$\frac{dR}{d\left(\frac{l_t}{q}\right)} = R' = -2\frac{\left[(AD - BC)\left(\frac{l_t}{q}\right)^5 + 2A\left(\frac{l_t}{q}\right)^3 + B\left(\frac{l_t}{q}\right)\right]}{\left[C\left(\frac{l_t}{q}\right)^4 + D\left(\frac{l_t}{q}\right)^2 + 1\right]^2}. \tag{25}$$

The functions A, B, C and D are given by

$$A = \left\{\left[-3A_1A_2\left(3A_2 + 3B_2c_1 + 18A_1C_1 - B2\right)(\beta g)\right] g_M - \left[B_{S_H}(\beta g)^2\right] g_H\right\} g_H,$$

$$B = B_{S_M} g_M - (A_2 \beta g)\, g_H,$$

$$C = \left\{\left[C_{S_M}(\beta g)\right] g_M - \left[D_{S_H}(\beta g)^2\right] g_H\right\} g_H$$

and

$$D = F_{S_M} g_M - G_{S_H}(\beta g)\, g_H.$$

where the dimensionless vertical gradients of mean wind speed and virtual temperature are defined as

$$g_M = \frac{G_M}{\frac{l_t^2}{q^2}}$$

and

$$g_H = \frac{G_H}{\frac{l_t^2}{q^2}\beta g}$$

Equation 24 is linearized as

$$\frac{d\left(\frac{l_t}{q}\right)_{i+1}}{dt} = R_i + R_i' \left[\left(\frac{l_t}{q}\right)_{i+1} - \left(\frac{l_t}{q}\right)_i \right] \tag{26}$$

whose solution is

$$\left(\frac{l_t}{q}\right)_{i+1} = \left(\frac{l}{q}\right)_i - \left[\frac{R}{R'}\right]_i + \left\{ \left[\frac{R}{R'}\right]_i + \left[\left(\frac{l_t}{q}\right)_0 - \left(\frac{l_t}{q}\right)_i \right] \right\} \exp\left[\Delta t R_i'\right] \tag{27}$$

which needs to be found iteratively. In general, two interactions are sufficient, so that q^2 depends on $(l/q)_3$, given by eq. 27 after two interactions:

$$q^2 = \frac{l_t^2}{\left(\frac{l_t}{q}\right)_3^2}. \tag{28}$$

Equations 24-28 do not solve TKE transport. It is estimated at a later step where TKE is vertically diffused as its value at a given value is adjusted with respect to the value at neighbor levels:

$$q^2(z_i) = \frac{-C_r(z_i)q^2(z_{i+1}) + R_Q(z_i)}{C_M(z_i)} \tag{29}$$

where

$$C_R(z_i) = -DTZ(z_i)AK_q(z_i)$$

$$C_M = C_R(z_{i-1})C_F(z_i) + (AK_q(z_{i-1}) + AK_q(z_i))DTZ(z_i) + 1$$

$$R_Q(z_i) = R_Q(z_{i-1})C_F(z_i) + q^2(z_i)$$

$$AK_q(z_i) = \frac{5\sqrt{q^2(z_i)}l(z_i)}{z_{i+1} - z_{i+2}}$$

$$DTZ(z_i) = \frac{2\Delta t}{z_i - z_{i+2}}$$

$$C_F = \frac{-DTZ(z_i)AK_q(z_{i-1})}{C_M(z_{i-1})}.$$

A TKE minimum value of 0.1 m^2 s^{-2} is assumed.

1.3. QNSE

For stable conditions the mixing length in QNSE is given by

$$l_q = \frac{1}{l_b^{-1} + l_s^{-1}} \tag{30}$$

where l_b and l_s are defined as

$$l_b = \frac{\kappa z}{1 + \frac{\kappa z}{\lambda}}$$

and

$$l_s = \frac{\sqrt{0.5q^2}}{N}$$

where q^2 is TKE, N is the BruntVisl frequency and $\lambda = 0.0063u_*/f$.

The stability functions are defined in terms of the gradient Richradson number (Sukoriansky et al., 2005)

$$\alpha_M = \frac{1 + A_{M1}Ri_g^2}{1 + A_{M2}Ri_g + A_{M3}Ri_g^2} \tag{31}$$

$$\alpha_H = \frac{A_{H1} + A_{H2}Ri_g + A_{H3}Ri_g^2}{1 + A_{H4}Ri_g + A_{H5}Ri_g^2} \tag{32}$$

where A_{M1}, A_{M2}, A_{M3}, A_{H1}, A_{H2}, A_{H3}, A_{H4} and A_{H5} are numerical constants.

The vertical turbulent diffusion coeficients are related to α_M, α_H and q:

$$K_M = l_q q \alpha_M, \tag{33}$$

$$K_H = l_q q \alpha_H, \tag{34}$$

and the second-order statistical moments are parameterized as in equations 7-9.

Lacking a transport term, the prognostic equation for TKE is

$$\frac{\partial q^2}{\partial z} = 2\left\{K_m\left[\left(\frac{\partial \overline{u}}{\partial z}\right)^2 + \left(\frac{\partial \overline{v}}{\partial z}\right)^2\right] - \frac{g}{\Theta}K_h\frac{\partial \overline{\theta}_V}{\partial z} - C_e\frac{(0.5q^2)^{3/2}}{l_q}\right\} \tag{35}$$

TKE transport is determined as in MYJ (equation 29). A minimum TKE of 0.005 m^2s^{-2} is imposed.

1.4. MYNN

The original MYNN length mixing (bl-mynn-mixlength=0) is calculated as the harmonic average between a turbulent (l_T), a surface-layer (l_S) and a buyoant (l_B) length scale:

$$\frac{1}{l} = \frac{1}{l_T} + \frac{1}{l_S} + \frac{1}{l_B} \tag{36}$$

where:

$$l_T = \frac{\int_0^{H_{PBL}} 0.23\,|z|\,q dz}{\int_0^{H_{PBL}} q dz}. \tag{37}$$

$$l_S = \kappa z\left[1 + 2.7\ min\left(\frac{z}{L}, 1\right)\right] \tag{38}$$

$$l_B = \frac{q}{N} \tag{39}$$

where L is the MoninObukhov length and N is the BruntVisl frequency. In the L-B versions of MYNN (bl-mynn-mixlength=1), an additional correction for the mixing length is used, originating mixing-length l':

$$l' = l(1 - W_T) + 0.4L_{BouLac} * W_T \tag{40}$$

where L_{BouLac} is given by eq. 3, and W_T:

$$W_T = 0.5tgh\left[\frac{z-(z_{i2}+h_1)}{h_2}\right]+0.5 \tag{41}$$

where z_{i2} is the PBL height and $h_1 = 0.3z_{i2}$ and $h_2 = h_1/2$.

Level 2

Although no level-2 MYNN PBL schemes are explicitly used in the present study, it is necessary to define its equations before showing those for levels 2.5 and 3.

As defined in Mellor and Yamada (1974, 1982), in level-2 parameterizations TKE is estimated through the balance between shear production, buoyant destruction and dissipation

$$q_2^2 = b_1 l^2\left\{s_m\left[\left(\frac{\partial\overline{u}}{\partial z}\right)^2+\left(\frac{\partial\overline{v}}{\partial z}\right)^2\right]+s_h\frac{g}{\Theta}\frac{\partial\overline{\theta}_V}{\partial z}\right\} \tag{42}$$

where s_h and s_m are the stability functions for heat and momentum, respectively:

$$s_h = 3a_2\left(g_1+g_2\right)\frac{r_{fc}-rf}{1-rf} \tag{43}$$

and

$$s_m = \frac{a_1}{a_2}\frac{f_1}{f_2}\frac{r_{f1}-rf}{r_{f2}-rf}s_h. \tag{44}$$

which are functions of the level-2 flux Richardson number (rf), defined as

$$rf = min\left[ri1\left(Ri_g+r_{i2}-\sqrt{Ri_g^2-r_{i3}Ri_g+r_{i2}^2}\right), r_{fc}\right] \tag{45}$$

where Ri_g is the gradient Richardson number, r_{fc} is the critical flux Richardson number:

$$r_{fc} = \frac{g_1}{g_1+g_2}. \tag{46}$$

The other quantities in eqs. 43-45 are numerical constants:

$$f_1 = b_1\left(g_1-c_1\right)+3a_2\left(1-c_2\right)\left(1-c_5\right)+2g_1\left(1-c_2\right),$$

$$f_2 = b_1 (g_1 + g_2) - 3a_1 (1 - c_2),$$

$$r_{f1} = \frac{b_1 (g_1 - c_1)}{f_1},$$

$$r_{f2} = \frac{b_1 g_1}{f_2},$$

$$r_{i1} = \frac{1}{2}\frac{a_2}{a_1}\frac{f_2}{f_1},$$

$$r_{i2} = r_{f1}\frac{a_1}{a_2}\frac{f_1}{f_2}$$

and

$$r_{i3} = 4r_{f2}\frac{a_1}{a_2}\frac{f_1}{f_2} - 2r_{i2}.$$

A correction that allows a variable critical Richardson number and avoids negative TKE in stable condions uses

$$a_2 = \frac{a_2'}{1 + Ri_g}$$

following Canuto, Cheng, Howard, and Esau (2008) and Kitamura (2010).

Level 2.5

In level 2.5, a prognostic equation for q^2 is solved

$$\frac{\partial q^2}{\partial t} = 2lq\left\{s_{m2.5}\left[\left(\frac{\partial \overline{u}}{\partial z}\right)^2 + \left(\frac{\partial \overline{v}}{\partial z}\right)^2\right] + s_{h2.5}\frac{g}{\Theta}\frac{\partial \overline{\theta}_V}{\partial z}\right\} + \frac{\partial}{\partial z}\left[3lqs_{m2.5}\frac{\partial q^2}{\partial z}\right] - \frac{2q^3}{b_1 l} \quad (47)$$

If $q^2 < q_2^2$ (level-2 TKE, equation 42), the stability functions for momentum ($s_{m2.5}$) and heat ($s_{m2.5}$) are

$$s_{m2.5} = s_m\sqrt{\frac{q^2}{q_2^2}}, \quad (48)$$

$$s_{h2.5} = s_h\sqrt{\frac{q^2}{q_2^2}}, \quad (49)$$

while, on the other hand, if $q^2 > q_2^2$, these stability functions are:

$$s_{m2.5} = \frac{q^2 a_1 (e_2 - 3c_1 e_4)}{D_{2.5}}, \quad (50)$$

$$s_{h2.5} = \frac{q^2 \left(e_2 + 3c_1 e_5\right)}{D_{2.5}}, \tag{51}$$

where e_1, e_2, e_3, e_4, e_5 and $D_{2.5}$ are

$$e_1 = q^2 - 3a_2 b_2 \left(1 - c_3\right) l^2 \frac{g}{\Theta} \frac{\partial \overline{\theta}_V}{\partial z},$$

$$e_2 = q^2 - 9a_1 a_2 \left(1 - c_2\right) l^2 \frac{g}{\Theta} \frac{\partial \overline{\theta}_V}{\partial z},$$

$$e_3 = e_1 + 9a_2^2 \left(1 - c_2\right) \left(1 - c_5\right) l^2 \frac{g}{\Theta} \frac{\partial \overline{\theta}_V}{\partial z},$$

$$e_4 = e_1 - 12a_1 a_2 \left(1 - c_2\right) l^2 \frac{g}{\Theta} \frac{\partial \overline{\theta}_V}{\partial z},$$

$$e_5 = 6a_1^2 l^2 \left[\left(\frac{\partial \overline{u}}{\partial z}\right)^2 + \left(\frac{\partial \overline{v}}{\partial z}\right)^2\right]$$

and

$$D_{2.5} = e_2 e_4 + e_3 e_5.$$

The vertical eddy diffusivities are related to $s_{m2.5}$, $s_{h2.5}$, l and q:

$$K_M = lqs_{m2.5}, \tag{52}$$

$$K_H = lqs_{h2.5}, \tag{53}$$

and the second-order statistical moments are parameterized as in equations 7-9.

The variance of temperature, variance of total water content and covariance of $\overline{\theta_l}$ and $\overline{q}_w$ are diagnostically estimated as

$$\overline{\theta_l'^2}_{2.5} = \alpha_c b_2 lqs_{h2.5} \left(\frac{\partial \overline{\theta_l}}{\partial z}\right)^2, \tag{54}$$

$$\overline{q_w'^2}_{2.5} = \alpha_c b_2 lqs_{h2.5} \left(\frac{\partial \overline{q}_w}{\partial z}\right)^2, \tag{55}$$

$$\overline{\theta_l' q_w'}_{2.5} = \alpha_c b_2 lqs_{h2.5} \frac{\partial \overline{q}_w}{\partial z} \frac{\partial \overline{\theta}_l}{\partial z} \tag{56}$$

These quantities are not used in 2.5 level schemes, but they are important to calculate the contergradients and stability functions of MYNN 3-level. The parameter α_c is defined as (Nakanishi & Niino, 2009)

$$\alpha_c = \begin{cases} q/q_2, & \text{if } q < q_2 \\ 1, & \text{if } q \geq q_2 \end{cases} . \tag{57}$$

Level 3

In level 3, the stability function for momentum (s_m) is split in two parts, the first is the stability functions from level-2.5 ($s_{m2.5}$), and the second part is a correction ($s_{m'}$) (Nakanishi & Niino, 2009):

$$s_m = s_{m2.5} + s_{m'}, \tag{58}$$

The second part $s_{m'}$ is defined as

$$s_{m'} = \frac{l^2 \alpha_c e'_6 \frac{g}{\Theta} \left(\overline{\theta'^2_V} - \overline{\theta'^2_{V2.5}} \right)}{D_3} \alpha_c^2 \left(9a_2^2 (1-c_2)(1-c_5) + 12 a_1 a_2 (1-c_2) \right) \frac{a_1}{a_2} \tag{59}$$

where e'_2, e'_3, e'_4, e'_5, e'_6 and D_3 are given by

$$D_3 = e'_2 e'_4 + e'_3 e'_5,$$

$$e'_2 = q^2 - 9a_1 a_2 (1-c_2) l^2 \frac{g}{\Theta} \frac{\partial \overline{\theta}_V}{\partial z} \alpha_c^2,$$

$$e'_3 = q^2 + 9a_2^2 (1-c_2)(1-c_5) l^2 \frac{g}{\Theta} \frac{\partial \overline{\theta}_V}{\partial z} \alpha_c^2,$$

$$e'_4 = q^2 - 12 a_1 a_2 (1-c_2) l^2 \frac{g}{\Theta} \frac{\partial \overline{\theta}_V}{\partial z} \alpha_c^2,$$

$$e'_5 = 6 a_1^2 l^2 \left[\left(\frac{\partial \overline{u}}{\partial z} \right)^2 + \left(\frac{\partial \overline{v}}{\partial z} \right)^2 \right] \alpha_c^2$$

and

$$e'_6 = 3a_2 (1-c_3) \frac{g}{\Theta}.$$

The vertical eddy difuusivitys are related to s_m, $s_{h2.5}$, l and q as:

$$K_M = lqs_m, \tag{60}$$

$$K_H = lqs_{h2.5} \tag{61}$$

and the second-order statistical moments parameterized are given by

$$\overline{u'w'} = -K_M \frac{\partial \overline{u}}{\partial z} \tag{62}$$

$$\overline{v'w'} = -K_M \frac{\partial \overline{v}}{\partial z} \tag{63}$$

$$\overline{w'\theta'_l} = -lq \left[s_{h2.5} \frac{\partial \overline{\theta_l}}{\partial z} + \Gamma_\theta \right] \tag{64}$$

$$\overline{w'\theta'_V} = -lq \left[s_{h2.5} \frac{\partial \overline{\theta_V}}{\partial z} + \Gamma_V \right] \tag{65}$$

$$\overline{w'q'_w} = -lq \left[s_{h2.5} \frac{\partial \overline{q_w}}{\partial z} + \Gamma_q \right] \tag{66}$$

The quantities Γ_{theta}, Γ_q and Γ_V are countergradient contributions

$$\Gamma_\theta = \frac{-e'_7 \alpha_c e'_6 \left(\overline{\theta'_l \theta'_V} - \overline{\theta'_l \theta'_{V\,2.5}} \right)}{D_3}, \tag{67}$$

$$\Gamma_V = \frac{e'_7 \alpha_c e'_6 \frac{g}{\Theta} \left(\overline{\theta'^2_V} - \overline{\theta'^2_{V\,2.5}} \right)}{D_3}, \tag{68}$$

$$\Gamma_q = \frac{-e'_7 \alpha_c e'_6 \left(\overline{q'_w \theta'_V} - \overline{q'_w \theta'_{V\,2.5}} \right)}{D_3}, \tag{69}$$

where $\overline{\theta'_l \theta'_V}$, $\overline{q'_w \theta'_V}$, $\overline{\theta'_V{}^2}$ and e'_7 are given by

$$\overline{\theta'_l \theta'_V} = \beta_\theta \overline{\theta'^2_l} + \beta_q \overline{\theta'_l q'_w},$$

$$\overline{q'_w \theta'_V} = \beta_\theta \overline{\theta'_l q_w} + \beta_q \overline{q'^{\,2}_w},$$

$$\overline{\theta_V'^2} = \beta_\theta \overline{\theta_l' \theta_V'} + \beta_q \overline{q_w' \theta_V'}$$

and

$$e_7' = e_2' + e_5',$$

In the expressions above, β_θ and β_q are functions related to the condensation process (Nakanishi & Niino, 2009).

The prognostic equations solved by level-3 MYNN are:

$$\frac{\partial q^2}{\partial t} = 2lq \left\{ s_m \left[\left(\frac{\partial \overline{u}}{\partial z} \right)^2 + \left(\frac{\partial \overline{v}}{\partial z} \right)^2 \right] + s_{h2.5} \frac{g}{\Theta} \frac{\partial \overline{\theta_V}}{\partial z} + \Gamma_V \right\} + \frac{\partial}{\partial z} \left[3lqs_m \frac{\partial q^2}{\partial z} \right] - \frac{2q^3}{b_1 l} \quad (70)$$

$$\frac{\partial \overline{\theta_l'^2}}{\partial t} = 2lq \left[s_{h2.5} \left(\frac{\partial \overline{\theta_l}}{\partial z} \right) + \Gamma_\theta \right] \left(\frac{\partial \overline{\theta_l}}{\partial z} \right) + \frac{\partial}{\partial z} \left[lqs_m \frac{\partial \overline{\theta_l'^2}}{\partial z} \right] - \frac{2q\overline{\theta_l'^2}}{b_2 l} \quad (71)$$

$$\frac{\partial \overline{q_w'^2}}{\partial t} = 2lq \left[s_{h2.5} \left(\frac{\partial \overline{q_w}}{\partial z} \right) + \Gamma_q \right] \left(\frac{\partial \overline{q_w}}{\partial z} \right) + \frac{\partial}{\partial z} \left[lqs_m \frac{\partial \overline{q_w'^2}}{\partial z} \right] - \frac{2q\overline{q_w'^2}}{b_2 l} \quad (72)$$

$$\frac{\partial \overline{\theta_l' q_w'}}{\partial t} = lq \left\{ \left[s_{h2.5} \left(\frac{\partial \overline{\theta_l}}{\partial z} \right) + \Gamma_\theta \right] \left(\frac{\partial \overline{q}_w}{\partial z} \right) + \left[s_{h2.5} \left(\frac{\partial \overline{q_w}}{\partial z} \right) + \Gamma_q \right] \left(\frac{\partial \overline{\theta_l}}{\partial z} \right) \right\} + \frac{\partial}{\partial z} \left[lqs_m \frac{\partial \overline{\theta_l' q_w'}}{\partial z} \right] - \frac{2q\overline{\theta_l' q_w'}}{b_2 l} \quad (73)$$

1.5. UWBLS

The UWBLS (Bretherton & Park, 2009) turbulent master length scale has been formulated by Blackadar (1962),

$$l_e = \frac{l_\infty}{1 + \frac{l_\infty}{\kappa z}} \quad (74)$$

where l_∞ =30 m for stable conditions.

For known TKE ($\overline{e}$) and l_e, the momentum and heat eddy diffusivities are, respectively:

$$K_M = l_e \sqrt{\overline{e}} S_m \quad (75)$$

and

$$K_H = l_e \sqrt{\overline{e}} S_h \tag{76}$$

where S_h, S_m are stability functions:

$$S_h = \frac{\alpha_5}{1 + \alpha_3 G_h}, \tag{77}$$

and

$$S_m = \frac{\alpha_1 + \alpha_2 G_h}{(1 + \alpha_3 G_h)(1 + \alpha_4 G_h)}. \tag{78}$$

The stability functions depend on a dimensionless stability ratio G_h:

$$G_h = \frac{-N_h^2 l_e^2}{2\overline{e}}, \tag{79}$$

where N_h is the squared moist buoyancy frequency (Bretherton & Park, 2009) and α_1, α_2, α_3, α_4 and α_5 are numerical constansts. In stable conditions, TKE is computed diagnostically, assuming a balance between shear production, buoyant destruction and dissipation:

$$e = b_1 l_e^2 \left(-S_h N_h^2 + S_m S^2 \right), \tag{80}$$

where S^2 is

$$S^2 = \left[\left(\frac{\partial \overline{u}}{\partial z} \right)^2 + \left(\frac{\partial \overline{v}}{\partial z} \right)^2 \right]. \tag{81}$$

A maximum gradient Richardson number of 0.19 is assumed.

References

Blackadar, A. K. (1962). The vertical distribution of wind and turbulent exchange in a neutral atmosphere. *J Geophys Res*, *67*(8), 3095–3102.

Bougeault, P., & Lacarrere, P. (1989). Parameterization of orography-induced turbulence in a mesobeta–scale model. *Monthly Weather Review*, *117*(8), 1872-1890. Retrieved from https://doi.org/10.1175/1520-0493(1989)117<1872:POOITI>2.0.CO;2 doi: 10.1175/1520-0493(1989)117⟨1872:POOITI⟩2.0.CO;2

Bretherton, C. S., & Park, S. (2009). A new moist turbulence parameterization in the community atmosphere model. *Journal of Climate*, *22*(12), 3422-3448. Retrieved from https://doi.org/10.1175/2008JCLI2556.1 doi: 10.1175/2008JCLI2556.1

Canuto, V. M., Cheng, Y., Howard, A. M., & Esau, I. N. (2008). Stably stratified flows: A model with no ri(cr). *Journal of the Atmospheric Sciences*, *65*(7), 2437-2447. Retrieved from https://doi.org/10.1175/2007JAS2470.1 doi: 10.1175/2007JAS2470.1

Janji, Z. I. (1994). The step-mountain eta coordinate model: Further developments of the convection, viscous sublayer, and turbulence closure schemes. *Monthly Weather Review*, *122*(5), 927-945. Retrieved from https://doi.org/10.1175/1520-0493(1994)122<0927:TSMECM>2.0.CO;2 doi: 10.1175/1520-0493(1994)122⟨0927:TSMECM⟩2.0.CO;2

Kitamura, Y. (2010). Modifications to the mellor-yamada-nakanishi-niino (mynn) model for the stable stratification case. *Journal of the Meteorological Society of Japan. Ser. II*, *88*(5), 857–864.

Mellor, G. L., & Yamada, T. (1974). A hierarchy of turbulence closure models for planetary boundary layers. *J. Atmos. Sci.*, *31*(7), 1791–1806.

Mellor, G. L., & Yamada, T. (1982). Development of a turbulence closure model for

geophysical fluid problems. *Rev. Geophys.*, *20*(4), 851–875.

Nakanishi, M., & Niino, H. (2009). Development of an improved turbulence closure model for the atmospheric boundary layer. *Journal of the Meteorological Society of Japan. Ser. II*, *87*(5), 895-912. doi: 10.2151/jmsj.87.895

Sukoriansky, S., Galperin, B., & Perov, V. (2005, Nov 01). 'application of a new spectral theory of stably stratified turbulence to the atmospheric boundary layer over sea ice'. *Boundary-Layer Meteorology*, *117*(2), 231–257. Retrieved from `https://doi.org/10.1007/s10546-004-6848-4` doi: 10.1007/s10546-004-6848-4

Table S1. Initial vertical profiles

z(m)	$\overline{u}$ (m s^{-1})	$\overline{v}$ (m s^{-1})	θ (K)	$\overline{q_w}$ (kg kg^{-1})
0	u_G	v_G	288	0.0025
200	u_G	v_G	286	0.0025
850	u_G	v_G	286	0.0025
900	u_G	v_G	288	0.0025
1000	u_G	v_G	292	0.0005
2000	u_G	v_G	300	0.0030
3500	u_G	v_G	310	0.0020
4000	u_G	v_G	312	0.0015
6000	u_G	v_G	312	0.0001
12000	u_G	v_G	312	0.0001

Table S2. Namelist

	bl-pbl-physics	sf-sfclay-physics	bl-mynn-mixlength
MYNN2.5	5	1	0
MYNN2.5L-B	5	1	1
MYNN3	6	1	0
MYNN3L-B	6	1	1
QNSE	4	4	-
MYJ	2	2	-
UWBLS	9	1	-
BouLac	8	1	-

Table S3. Numerical Constants

BouLac	MYJ	QNSE	MYNN	UWBLS
$C_K = 0.4$	$\alpha = 0.3$	$A_{M1} = 8$	$a_1 = b_1(1 - 3g_1)/6$	$\alpha_1 = 0.5562$
$\alpha_e = 1$	$A_1 = 0.6599$	$A_{M2} = 2.3$	$a_2' = a_1(g_1 - c_1)/(g_1 p_r)$	$\alpha_2 = -4.364$
$\alpha_T = 1$	$A_2 = 0.6574$	$A_{M3} = 35$	$b_1 = 24$	$\alpha_3 = -34.6764$
$C_\epsilon = 1/1.4$	$B_1 = 11.878$	$A_{H1} = 1.4$	$b_2 = 15$	$\alpha_4 = -6.1272$
	$B_2 = 7.227$	$A_{H2} = -0.01$	$c_1 = g_1 - 1/(3a_1 2.88)$	$\alpha_5 = 0.6986$
	$C_1 = 0.00083$	$A_{H3} = 1.29$	$c_2 = 0.729$	$b_1 = 5.8$
		$A_{H4} = 2.44$	$c_3 = 0.340$	
		$A_{H5} = 19.8$	$c_4 = 0$	
		$C_e = 0.166$	$c_5 = 0.2$	
			$g_1 = 0.235$	
			$g_2 = b_2/b_1(1 - c_3) + 2a_1/b_1(3 - 2c_2)$	
			$p_r = 0.74$	

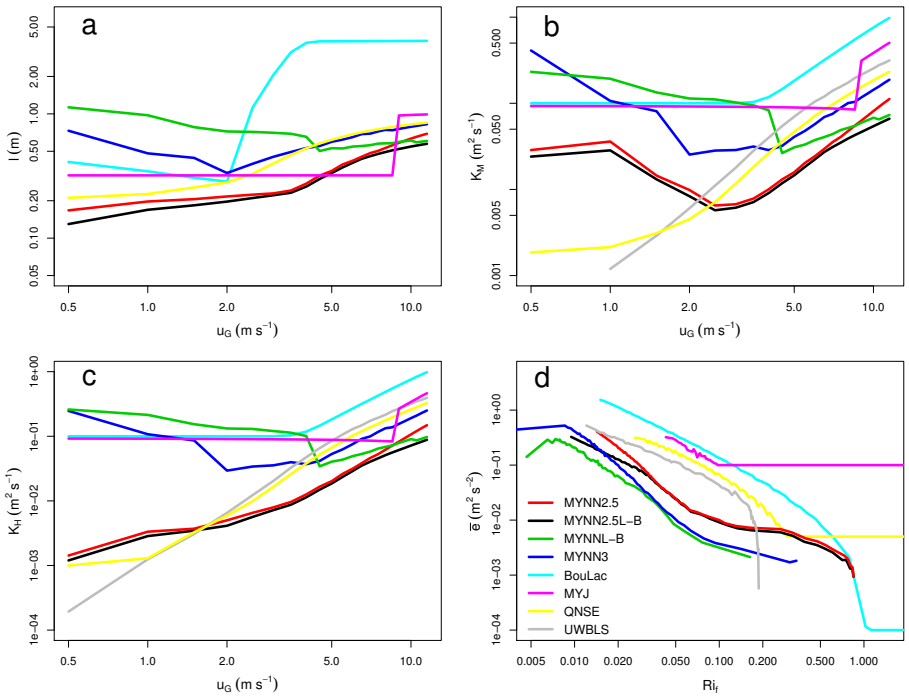

Figure S1. Average 3.9-m mixing length l (a), momentum eddy diffusivity K_M (b) and heat eddy diffusivity K_H (c) as a function of geostrophic wind speed u_G. Panel d shows average TKE $\overline{e}$ as a function of the flux Richardson number Ri_f. In all panels, each line represents a different PBL scheme, as given in legend at panel d and the values correspond to bin averages taken over the second night of simulation, for all values of geostrophic wind considered.

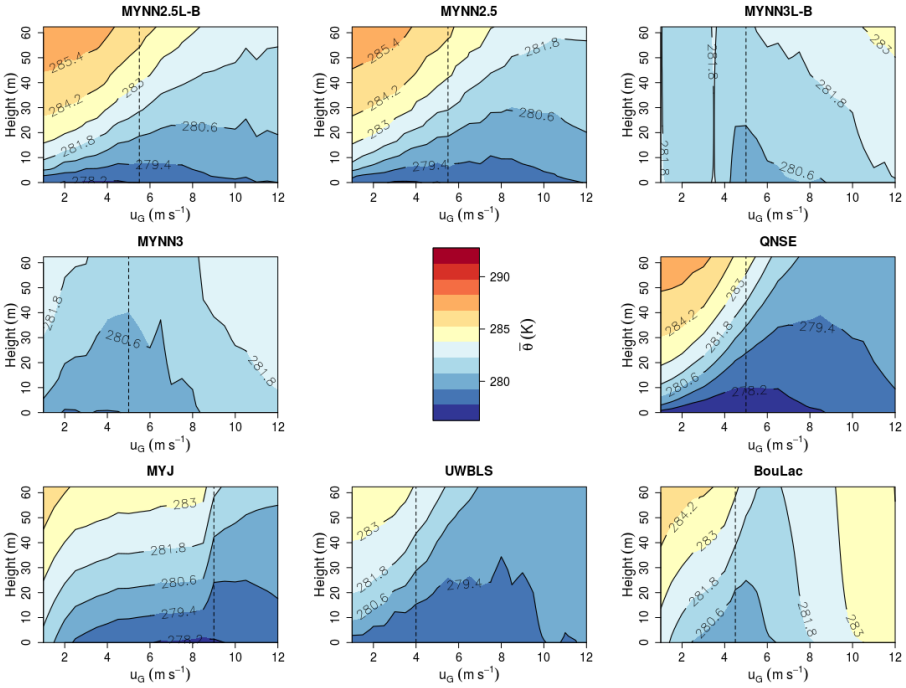

Figure S2. Average potencial temperature as a function of height and geostrophic wind for each PBL scheme as indicated at the top of each panel. For each value of geostrophic wind, values shown are the averages over the last hour of the second night of simulation. Vertical dashed line mark the geostrophic wind in which the thermal gradient between 1.3 and 30.8 m has an inflection point.

7 DISCUSSÃO

Nos modelos apresentados no artigo 1 ("Simulating the Regime Transition of the Stable Boundary Layer Using Different Simplified Models"), os fluxos de momentum são estimados através da mistura local, determinada pela ECT através da seguinte expressão matemática $u_* = \sqrt{\overline{e}/4}$. Observações evidenciam que essa relação não pode ser considerada constante, sendo que em casos muito estáveis (condições de vento fraco), essa razão aumenta (PAHLOW; PARLANGE; PORTé-AGEL, 2001; QUAN; HU, 2009; ACEVEDO et al., 2014). Portanto, o uso de uma relação constante, como a utilizada no artigo 1, produz uma superestimativa da velocidade de fricção (u_*) e, consequentemente, dos fluxos de momentum, produzindo ainda valores excessivos de V_{TKE} em condições de vento pouco intenso, fazendo que a transição entre os regime ocorra com ventos de menor intensidade em relação ao que é observado na natureza. Do ponto de vista físico, a utilização de equações prognósticas para os fluxos aumentam o realismo físico do modelo, e o seu número de graus de liberdade, pois permitirá que a velocidade de fricção evolua de maneira relativamente independente da ECT. Devido a motivos, como o descrito anteriormente, equações prognóstica para os fluxos de momentum são incorporadas ao modelo apresentado no artigo 3 ("The nocturnal boundary layer transition from weakly to very stable. Part II: Numerical simulation with a second-order model").

O artigo 1 ("Simulating the Regime Transition of the Stable Boundary Layer Using Different Simplified Models") mostra que regime pouco estável é aproximadamente independente do fluxo de calor (uma vez que ele pode ser removido do balanço da ECT), e do número de equações prognósticas resolvidas (Figura 7.1). Portanto, no regime pouco estável, a turbulência é impulsionada, principalmente, pela produção devido ao cisalhamento do vento e pela dissipação molecular. Já, no regime muito estável, a turbulência é controlada pelo fluxo de calor.

Acevedo et al. (2016) que mostraram que o termo da destruição térmica de turbulência na equação de balanço de ECT tem importância relativa no balanço total muito maior no regime desacoplado ou regime muito estável. Essa afirmação pode ser corroborado com os resultado apresentados na figura 7.1, em que as linhas tracejadas apresentam os resultados dos modelos quando o termo de destruição térmica é considerado constante e igual a zero. Nessa situação é observado apenas um único regime, que coincide com o regime pouco estável, em que tanto o termo de produção mecânica quanto o termo de dissipação de ECT, em módulo, crescem proporcionalmente com ao cubo da velocidade do vento. Essas simulações hipotéticas mostram que o termo de destruição térmica desempenha um papel fundamental no regime muito estável, evidenciando que uma solução adequada para a equação prognóstica do fluxo de calor é fundamental para que os modelos numéricos, que descrevam o comportamento médio de uma CLE, consigam reproduzir

Figura 7.1 – Perfil vertical dos termos associados à produção mecânica de ECT (linha preta), destruição térmica de ECT (linha vermelha) e dissipação de ECT (linha azul clara) provenientes dos modelos e, $e-F_H$ e $e-F_H-\sigma_\theta$. Já as linhas tracejadas são os resultados obtidos pelo modelos quando a distruição térmica é considera constante e igual a zero.

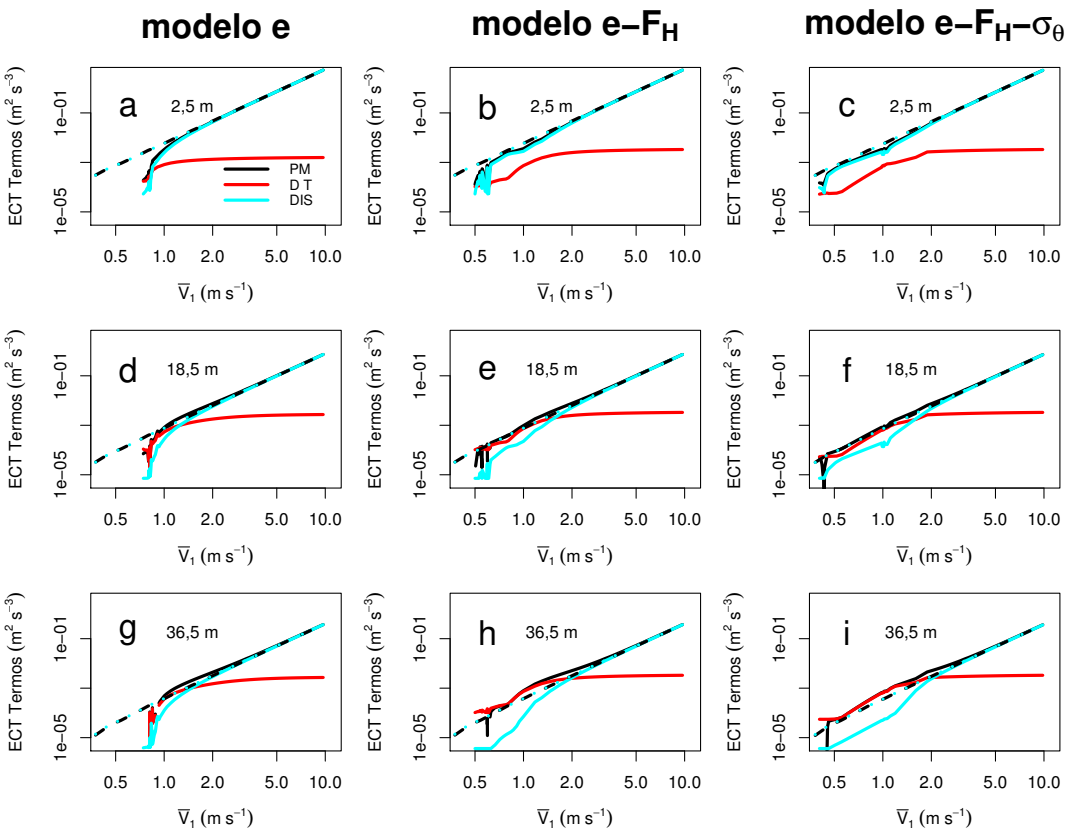

de forma correta os dois regimes da CLE. Uma solução para fluxo de calor só pode ser obtida de forma completamente adequada se e somente se a variância de temperatura e a componente vertical da variância da velocidade do vento forem estimados através de equações prognósticas. Por este motivo equações prognósticas para a componentes da variância da velocidade do vento foram incluídas no modelo apresentado no artigo 3 ("The nocturnal boundary layer transition from weakly to very stable. Part II: Numerical simulation with a second-order model"), tornando-o um modelo de segundo ordem completo, ou conforme a classificação de Mellor e Yamada (1974) um modelo de nível 4.

Acevedo et al. (2019) (artigo 2, "The nocturnal boundary layer transition from weakly to very stable. Part I: Observations") observaram, em muitas noites, um resfriamento abrupto da camada acompanhado de uma redução na energia cinética turbulenta (ECT), e na intensidade da velocidade do vento. Nesse estudo a transição entre o regime pouco estável e o muito estável foi marcada exatamente no instante de tempo em que ocorre resfriamento máximo nos níveis inferiores da camada limite. No artigo 3 ("The nocturnal boundary layer transition from weakly to very stable. Part II: Numerical simulation with a second-order model"), transições semelhantes, as observadas por Acevedo et al. (2019),

foram investigadas com auxilio de um modelo numérico unidimensional de segunda ordem completo. Além disso esse artigo mostra que as principais características da transição entre o regime pouco estável e o muito estável são adequadamente simuladas por um modelo de segunda ordem. Isso mostrou que esses modelos conseguem descrever adequadamente os dois regimes da CLE, e reiterou novamente a importância do fluxo de calor no controle dos regimes da camada limite estável.

Até o terceiro artigo, os regimes da CLE, pouco estável e muito estável, foram investigados com o auxílio de modelos numéricos completamente idealizados, que não podem ser empregados de forma direta nos modelos numéricos de previsão de tempo e clima (MNPTC). Então, as diferentes parametrizações de CLP presentes no "Weather Research and Forecasting - Single Column Model" (WRF-SCM) foram comparadas e avaliadas quanto a sua capacidade de resolver os regimes da CLE. Dentre todos os esquemas de turbulência analisados na presente tese, ambos os Mellor-Yamada-Nakanishi-Niino de nível 2.5 apresentaram o melhor desempenho, sendo capaz de resolver tanto o regime pouco estável quanto o regime muito estável da CLE. Porém, a transição entre os regimes da CLE ocorre sob condições de vento geostrófico de menor intensidade que observado na natureza.

O esquema de turbulência proposto por Bougeault e Lacarrere (1989) (BouLac) é o único modelo, presente no WRF, que resolve ECT prognosticamente e não possui funções de estabilidade, isso significa que a difusividade turbulenta de momentum e de calor são sempre iguais ($K_M = K_H$) e, acarretando, em uma excessiva difusão de calor no regime muito estável. Então, devido a isso, e ao valor mínimo imposto à difusividade de calor e de momentum ($K_M = K_H = 0.1$ m^2 s^{-1}), o esquema de turbulência, BouLac, não é capaz desenvolver uma camada limite fortemente estratificada em situações que o forçante mecânico é pouco intenso ($u_g \leq 3$ m s^{-1}). Esse fato poder ser verificado nas figura 7.4-a e 7.2 (linhas em preto).

O número de Prandtl turbulento (Pr_T) também pode ser definido como,

$$Pr_T = \frac{K_M}{K_H}. \tag{7.1}$$

Tanto observações quanto simulação numéricas mostram que Pr_T é aproximadamente constante no regime pouco estável, e passa a crescer linearmente com Ri_g no regime muito estável, implicando na redução da difusão turbulenta de calor em relação à difusão turbulenta de momentum (ZILITINKEVICH et al., 2013), esse comportamento não é reproduzido pelo esquema de turbulência BouLac (Figura 5-b, no artigo 4). Zilitinkevich et al. (2013) propuseram a seguinte aproximação para o número de Prandtl turbulento,

$$Pr_T = 0.8 + 0.45 Ri_g. \tag{7.2}$$

Uma expressão matemática para o número de Prandtl turbulento pode desempe-

nhar um papel semelhante a uma função de estabilidade. Logo, a difusividade turbulenta de calor pode ser estimada por,

$$K_H = \frac{K_M}{Pr_T}, \tag{7.3}$$

forçando que a difusividade térmica turbulenta seja reduzida em relação a difusão turbulenta de momentum, principalmente em situações muitos estáveis ($Ri_g \gg 0.25$). Portanto, a inclusão das equações 7.2-7.3 ao esquema de turbulência BouLac, no WRF, pode melhorar significativamente os resultados desse esquema. Porém, a velocidade de transição entre os regimes não é alterado com a inclusão dessas equações.

Figura 7.2 – a) Diferença de temperatura potencial entre 30,8 e 1,3 metros em função da velocidade do vento em 30,8 m para Boulac original (linhas em pretos) e para o BouLac com a Pr_T proposta por Zilitinkevich et al. (2013) (linhas em vermelho). b) Diferença de temperatura potencial entre 30,8 e 1,3 metros em função da vento geostrófico para Boulac original (linhas em pretos) e para o BouLac com a Pr_T proposta por Zilitinkevich et al. (2013) (linhas em vermelho)

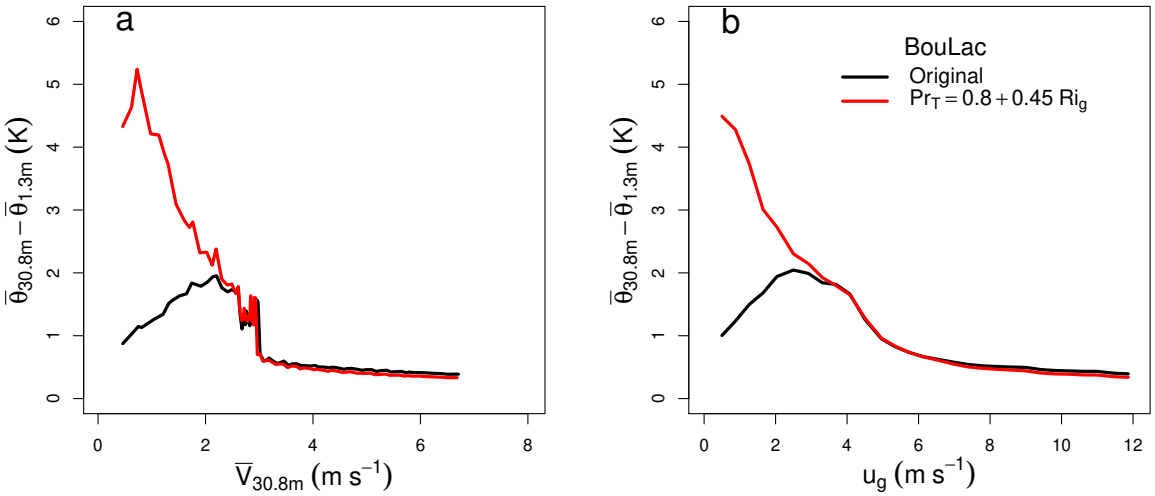

A inclusão da expressão para o número de Prandtl turbulento proposto por Zilitinkevich et al. (2013) no esquema BouLac altera insignificante a relação entre $V_{TKE} \times \overline{V}$ (Figura 7.3), ainda não conseguindo simular uma situação semelhante a observada por Sun et al. (2012) para o regime muito estável. Porém, a inclusão da equação 7.2 altera significativamente o comportamento da inversão térmica em função da velocidade do vendo no regime muito estável (Figura 7.2), tornando a camada mais estratificada e estável em condições de vento de baixa intensidade (Figura 7.4). Já, o perfil vertical da velocidade do vento não é alterado com a inclusão dessa equação ao BouLac, conforme pode ser visto nos painéis c e d da figura 7.4.

Uma melhora significativa pode ser observada para relação entre o módulo do fluxo de calor e a velocidade do vento com a inclusão das equações 7.2 e 7.3 ao BouLac, onde o fluxo de calor tende a crescer com $\overline{V}^3$, principalmente nos níveis mais altos, se aproxi-

Figura 7.3 – Relação entre V_{TKE} e $\overline{V}$ obtida pelo BouLac original (linhas sólidas), com o número de Prandtl turbulento proposto por Zilitinkevich et al. (2013) (linhas tracejadas).

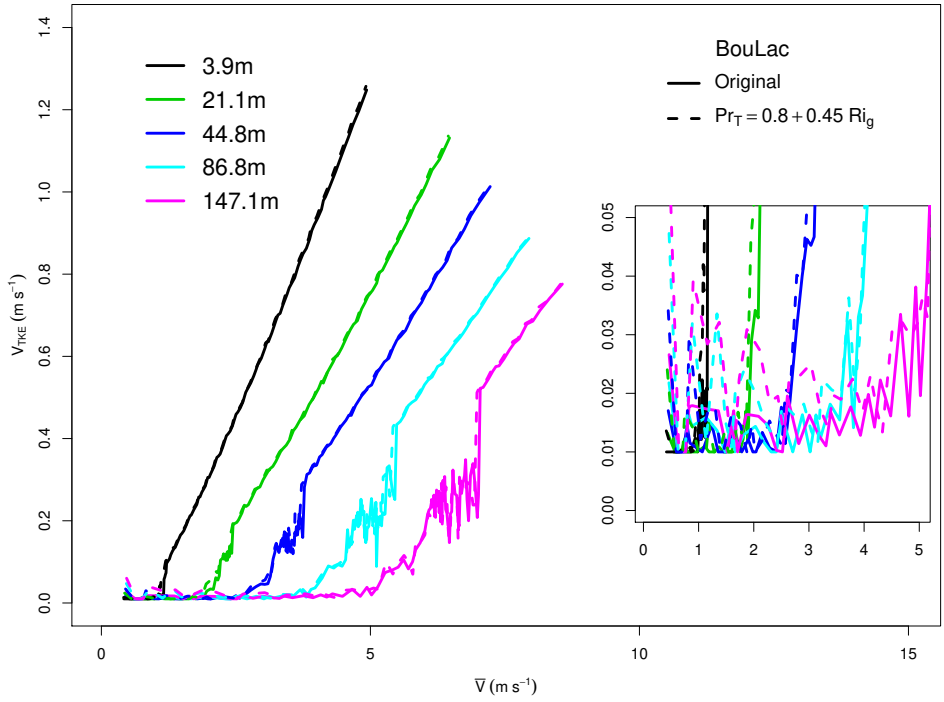

mando da relação observada na natureza. A fim de melhorar esses resultados, o valor mínimo imposto para difusividade de momentum ($K_M = 0.1$ m^2 s^{-1}), em torno de uma ordem de grandeza maior que os apresentados pelo MYNN2.5 (Figura S1-b), pode ser relaxado, pois esse valor continua sendo muito superior aos observados na natureza. Outro fato importante a ser destacado é que o BouLac apresenta os maiores comprimentos de mistura dentre todos os modelos apresentados nessa tese, e em torno de duas a três vezes maiores que os apresentados pelos demais modelos (Figura S1-a). A inclusão da expressão matemática para Pr_T faz com que o comprimento de mistura reduzido aproximadamente pela metade (Figura 7.6), e se aproxime dos comprimentos de mistura apresentados por ambos MYNN2.5 e pelo QNSE.

O simples fato de adicionar uma expressão matemática para o Pr_T ao BouLac melhorou os resultados desse modelo, principalmente na estimativa do fluxo de calor. Logo, a inclusão de uma equação prognóstica para o fluxo de calor ao BouLac pode fazer com que ele consiga reproduzir o regime muito estável da CLE de forma mais adequada.

Figura 7.4 – Temperatura potencial (a-c) e velocidade (b-d) média em função da altura e do vento geostrófico para BouLac original e com o número de Prandtl turbulento proposto por Zilitinkevich et al. (2013) , conforme indicado na parte superior do painel.

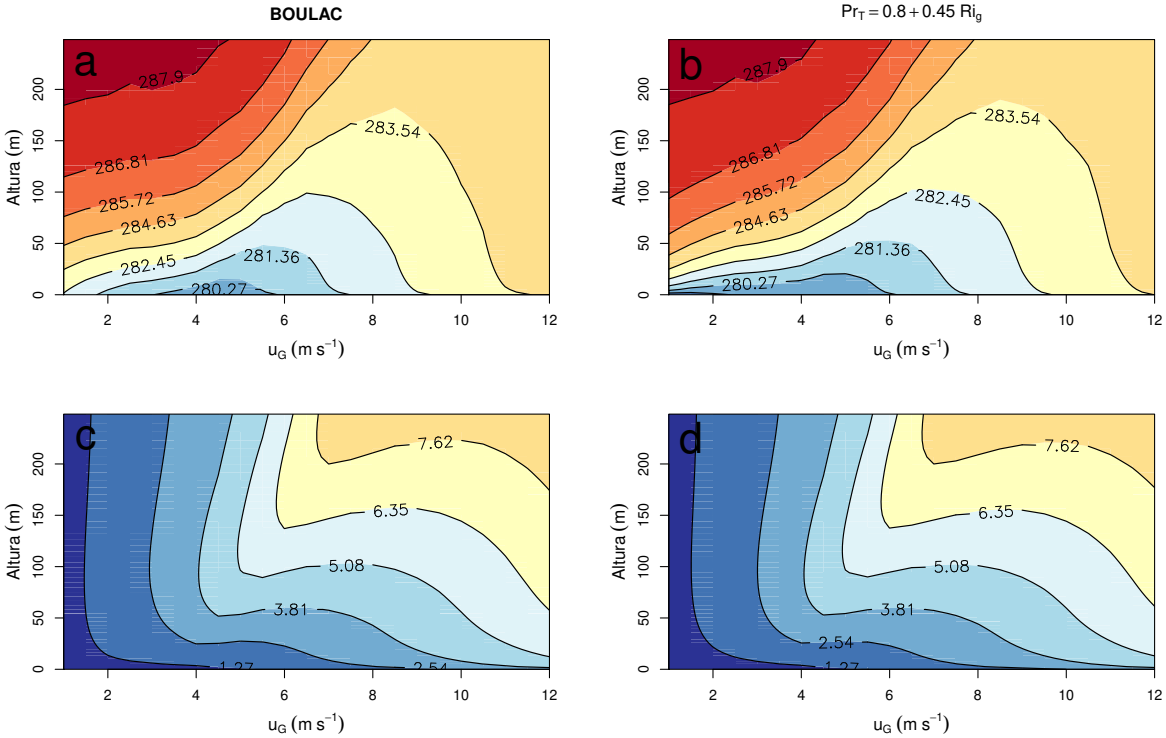

Figura 7.5 – Relação entre $\overline{w'\theta'}$ e $\overline{V}$ obtida pelo BouLac original (a), com o número de Prandtl turbulento proposto por Zilitinkevich et al. (2013) (b).

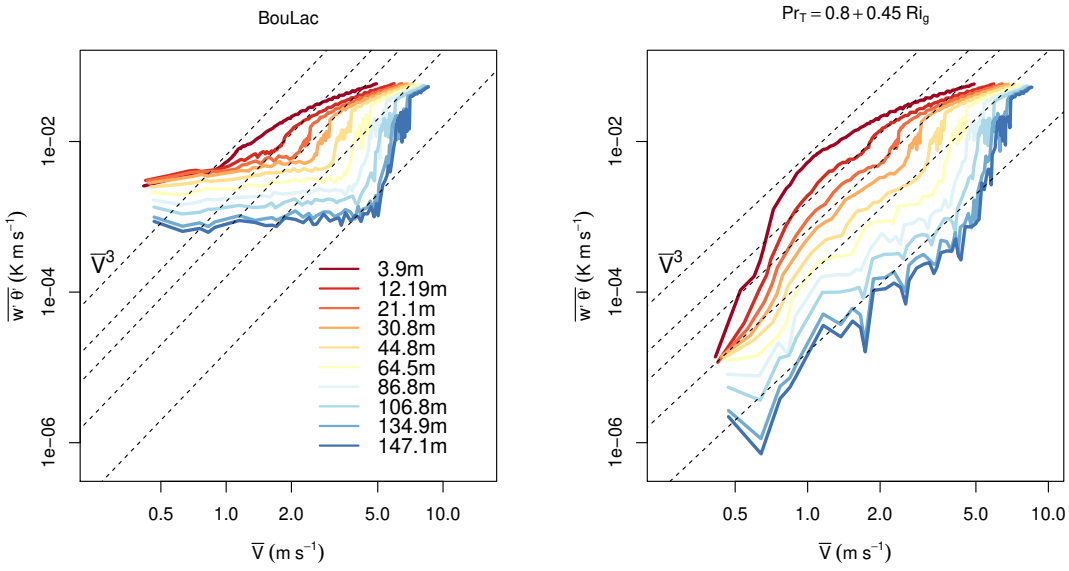

Figura 7.6 – Comprimento de mistura a 3.9 m proveniente do BouLac original (a), com o número de Prandtl turbulento proposto por Zilitinkevich et al. (2013) (b).

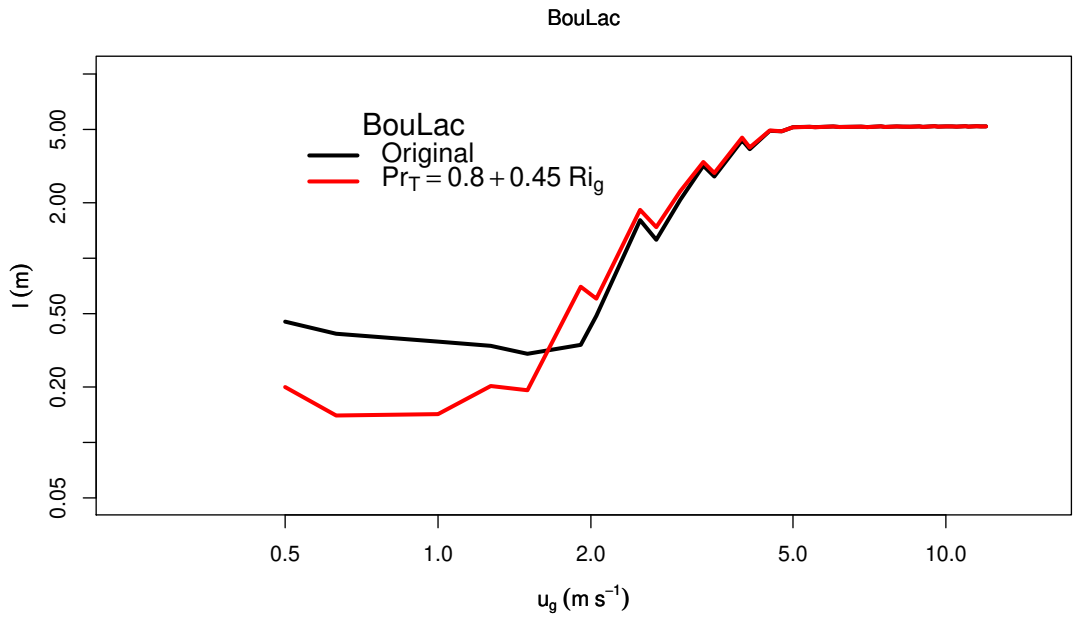

8 CONCLUSÕES

A presente tese foi divida em 4 diferentes artigos. No primeiro deles ("Simulating the Regime Transition of the Stable Boundary Layer Using Different Simplified Models") 3 diferentes modelos numéricos, utilizados para descrever o comportamento médio de uma camada limite estável, são comparados quanto a sua capacidade de reproduzir dois regimes da CLE. Esses modelos são: e, em que a energia cinética turbulenta (ECT) é o único momento estatístico de segunda ordem resolvido através de uma equação prognóstica; o $e - F_H$, em o fluxo de calor sensível é estimado através de uma equação prognóstica; o modelo $e - F_H - \sigma_\theta$, em que a variância de temperatura passa a ser calculada através de uma equação prognóstica.

No segundo artigo (The nocturnal boundary layer transition from weakly to very stable. Part I: Observations), a transição do regime pouco estável para muito estável da CLE, é analisada através dos dados micrometeorológicos provenientes de uma torre de 140 metros situada em Linhares, no estado de Espírito Santos, sudoeste do Brasil. Foi observado que a transição entre os regimes era precedida por um resfriamento abrupto da camada, acompanhado de uma redução na energia cinética turbulenta, e da intensidade da velocidade do vento. No terceiro artigo ("The nocturnal boundary layer transition from weakly to very stable. Part II: Numerical simulation with a second-order model"), transições semelhantes, às apresentadas no segundo artigo, foram investigadas com auxilio de um modelo numérico unidimensional de segunda ordem, em que a transição é impulsionada pelo decréscimo da intensidade do vento no topo do domínio. Nesse artigo o papel dos processos radiativos e das propriedades térmicas da superfície do solo sob a transição também foi investigado.

No quarto artigo ("How is the two-regime stable boundary layer solved by the different PBL schemes in WRF?"), seis diferentes parametrizações de camada limite planetária (CLP) presentes no "Weather Research and Forecasting - Single Column Model" (WRF-SCM) foram comparados e avaliados quanto a sua capacidade de simular os regimes da CLE: Mellor-Yamada-Nakanishi-Niino nível 2.5 (MYNN2.5, MYNN2.5L-B), Mellor-Yamada-Nakanishi-Niino nível 3 (MYNN3, MYNN3L-B), Mellor-Yamada-Janjic (MYJ), "Quasi-Normal Scale Elimination" (QNSE), "University of Washington (TKE) Boundary Layer Scheme" (UWBLS) e Bougeault-Lacarrere (BouLac).

Os principais resultados obtidos na presente tese podem ser sumarizados como:

- Os regimes da CLE não são apenas controlados pela intensidade da velocidade do vento, mas também pelos processos térmicos.

- No regime muito estável a energia cinética turbulenta cresce com a intensidade do vento a uma pequena taxa. Essa situação só pode ser simulada quando equações

prognósticas para o fluxo de calor e para variância de temperatura são incluídas ao modelo. Porém um efeito semelhante pode ser obtido quando funções de estabilidade adequadas são utilizadas, como ocorre no esquema de turbulência proposto por Nakanishi e Niino (2006) .

- Os presentes resultados indicam que a inclusão de mais equações prognósticas ao modelo fazem com que os regimes da CLE sejam reproduzidos de uma maneira mais semelhantes às observadas na natureza.

- Processos radiativos e propriedades térmicas da superfície do solo são determinantes para transição entre os regimes da camada limite estável (CLE). Diferentes valores dessas quantidades fazem com que a transição entre o regime pouco estável e o muito estável ocorra com ventos de diferentes intensidade. Este resultado está de acordo com conceito do “intensidade de acoplamento”, proposto por Wiel et al. (2017). Quando maior for a "intensidade de acoplamento" entre a superfície do solo e a atmosfera, vento geostróficos de menor intensidade são necessários para que a transição entre regime pouco estável e o muito estável ocorra.

- O máximo do fluxo de calor , em módulo, ocorre no regime pouco estável. Portanto, o máximo fluxo de calor, em módulo, não pode ser utilizado como um marcador da transição entre os regime da CLE, como sugerido por estudos anteriores (MAHRT, 1998; ACEVEDO; FITZJARRALD, 2003; HOOIJDONK et al., 2015; BAAS et al., 2019).

- Tanto no regime pouco estável quanto no regime muito estável, o termo de produção mecânica da ECT é proporcional à intensidade da velocidade do vento ao cubo.

- O fluxo de calor é proporcional à intensidade da velocidade do vento ao cubo, apenas no regime muito estável, se aproximando de um valor máximo, como proposto por Wiel et al. (2012).

- No regime pouco estável, o termo de produção de fluxo de calor devido ao gradiente térmico é o termo dominante no balanço do fluxo de calor. Já, no regime muito estável, o termo de destruição devido as flutuações de temperatura passa a ser o termo dominante do balanço.

- Dentre todos os esquemas de turbulência do WRF, analisados na presente tese, ambos os Mellor-Yamada-Nakanishi-Niino de nível 2.5 apresentam o melhor desempenho, conseguindo resolver tanto o regime pouco estável quanto o regime muito estável da CLE. Porém, a transição entre os regimes da CLE ocorre sob condições de vento geostrófico de menor intensidade que observado na natureza.

Nenhum dos esquemas de camada limite disponíveis no WRF resolve prognosticamente o fluxo calor. Porém, os resultados apresentados nessa tese, assim como os

resultados apresentados por Wiel et al. (2012), indicam que o fluxo de calor exerce um grande controle nos regimes da CLE. Logo, a inclusão de uma equação prognóstica para o fluxo de calor nos esquemas de turbulência, presentes no WRF, significaria um importante avanço. Espera-se que, assim o WRF consiga simular de forma adequada ambos os regimes da CLE.

Diante ao exposto na presente tese, esforços foram concentrados na inclusão de uma equação prognóstica no esquemas de turbulência, BouLac, presente na versão 3.9 do WRF. Porém, ao realizar essa tarefa foi deparado com os seguintes desafios, o fluxo de calor superficial é estimado através de similaridade (Monin Obukhov) no módulo "Surface Layer" e na sequência essa quantidade é utilizada para estimar a temperatura do solo e atualizada no módulo "Land-Surface". No desenvolvimento da presente tese foi possível realizar as alterações os esquemas de turbulência, das quais foi apresentada na seção de discussão. Já, a inclusão da equação prognóstica para o fluxo de calor nos esquemas de turbulência não é uma tarefa trivial, pois essa ação exige ajustes tanto módulos de "Surface-Layer" quanto no de "Land-Surface". A inclusão de uma equação ao esquema de turbulência já foi finalizada. Porém, as alterações dos módulos "Surface Layer" e "Land Surface" ainda estão em desenvolvimento. Essas alterações são necessárias para que não ocorra conflito entre o fluxo de calor obtido pelo esquema de turbulência e o obtido pelo "Surface Layer". Como perspectivas pretende-se finalizar as alterações necessárias ao "Surface Layer" e ao "Land Surface", e futuramente a inclusão de equações prognóstica para o fluxo de momentum, uma vez que foi mostrado que um modelo de segundo ordem é capaz de reproduzir de forma satisfatória muitas características da transição entre o regime pouco estável e o muito estável. Com isso, espera-se implementar uma parametrização completa que seja mais adequada na simulação das características que contrastam entre os dois regimes. Também espera-se que esta parametrização resolva situações muito estáveis com valores de forçante mecânico maiores do que ocorre nas parametrizações existentes atualmente, e mais próximas ao que é observado na natureza.

ANEXO A – ENERGIA CINÉTICA TURBULENTA

As equações de Navier-Stokes, equações diferenciais que descrevem o comportamento do escoamento de um fluido, pode ser escrita em notação tensorial como:

$$\frac{\partial u_i}{\partial t} + u_j \frac{\partial u_i}{\partial x_j} = -\delta_{i3}\left[g - \left(\frac{\theta'}{\overline{\theta}}\right) g\right] + f\varepsilon_{ij3}u_j - \frac{1}{\overline{\rho}}\frac{\partial p}{\partial x_i} + \gamma\frac{\partial^2 u_i}{\partial x_j^2}, \tag{A.1}$$

onde os termos do lado esquerdo da equação representam a variação euleriana de velocidade e o transporte advectivo de velocidade, respectivamente. Já os termos do lado direito da igualdade representam a aceleração gravitacional efetiva, aceleração devido à força de Coriolis, aceleração devido a um gradiente de pressão e a dissipação devido a viscosidade do fluido, respectivamente.

As variáveis, associadas a um escoamento turbulento, podem ser decompostas em uma parte média e outra turbulenta (denominada Decomposição de Reynolds). Então, as grandezas u_i e p podem ser decompostas como:

$$u_i = \overline{u_i} + u_i',$$

e p=$\overline{p} + p'$.

Substituindo as equações acima na equação A.1, obtém-se:

$$\frac{\partial\left(\overline{u_i} + u_i'\right)}{\partial t} + \left(\overline{u_j} + u_j'\right)\frac{\partial\left(\overline{u_i} + u_i'\right)}{\partial x_j} = -\delta_{i3}\left[g - \left(\frac{\theta'}{\overline{\theta}}\right) g\right] + f\varepsilon_{ij3}\left(\overline{u_j} + u_j'\right) -$$

$$\left(\frac{1}{\overline{\rho}}\right)\frac{\partial\left(\overline{p} + p'\right)}{\partial x_i} + \gamma\frac{\partial^2\left(\overline{u_i} + u_i'\right)}{\partial x_j^2}, \tag{A.2}$$

que pode ser reescrita como:

$$\frac{\partial\overline{u_i}}{\partial t} + \frac{\partial u_i'}{\partial t} + \overline{u_j}\frac{\partial\overline{u_i}}{\partial x_j} + \overline{u_j}\frac{\partial u_i'}{\partial x_j} + u_j'\frac{\partial\overline{u_i}}{\partial x_j} + u_j'\frac{\partial u_i'}{\partial x_j} = -\delta_{i3}\left[g - \left(\frac{\theta'}{\overline{\theta}}\right) g\right] + f\varepsilon_{ij3}\overline{u_j} + f\varepsilon_{ij3}u_j' +$$

$$\gamma\frac{\partial^2 u_i'}{\partial x_j^2} + \gamma\frac{\partial^2\overline{u_i}}{\partial x_j^2} - \frac{1}{\overline{\rho}}\frac{\partial\overline{p}}{\partial x_i} - \frac{1}{\overline{\rho}}\frac{\partial p'}{\partial x_i}. \tag{A.3}$$

Tomando a média de Reynolds em ambos os lados da igualdade acima, obtém-se:

$$\frac{\partial\overline{u_i}}{\partial t} + \overline{u_j}\frac{\partial\overline{u_i}}{\partial x_j} + \overline{u_j'\frac{\partial u_i'}{\partial x_j}} = \delta_{i3}g + f\varepsilon_{ij3}\overline{u_j} - \frac{1}{\overline{\rho}}\frac{\partial\overline{p}}{\partial x_i} + \gamma\frac{\partial^2\overline{u_i}}{\partial x_j^2} \tag{A.4}$$

Através da equação da continuidade, sabe-se que

$$\frac{\partial u_j'}{\partial x_j} = 0,$$

logo,

$$u_i' \frac{\partial u_j'}{\partial x_j} = 0.$$

Tomando a média de Reynolds na equação acima, temos que:

$$\overline{u_i' \frac{\partial u_j'}{\partial x_j}} = 0,$$

que pode ser somado a equação A.4 sem alterá-la. Portanto,

$$\frac{\partial \overline{u_i}}{\partial t} + \overline{u_j}\frac{\partial \overline{u_i}}{\partial x_j} + \overline{u_i' \frac{\partial u_j'}{\partial x_j}} + \overline{u_j' \frac{\partial u_i'}{\partial x_j}} = \delta_{i3} g + f \varepsilon_{ij3} \overline{u_j} - \frac{1}{\overline{\rho}} \frac{\partial \overline{p}}{\partial x_i} + \gamma \frac{\partial^2 \overline{u_i}}{\partial x_j^2}. \tag{A.5}$$

Através da regra do produto sabemos que:

$$\overline{u_i' \frac{\partial u_j'}{\partial x_j}} + \overline{u_j' \frac{\partial u_i'}{\partial x_j}} = \frac{\partial \overline{u_j' u_i'}}{\partial x_j}.$$

Logo, a equação A.5 pode ser reescrita como:

$$\frac{\partial \overline{u_i}}{\partial t} + \overline{u_j}\frac{\partial \overline{u_i}}{\partial x_j} + \frac{\partial \overline{u_j' u_i'}}{\partial x_j} = \delta_{i3} g + f \varepsilon_{ij3} \overline{u_j} - \frac{1}{\overline{\rho}} \frac{\partial \overline{p}}{\partial x_i} + \gamma \frac{\partial^2 \overline{u_i}}{\partial x_j^2}, \tag{A.6}$$

Subtraindo A.6 de A.3, temos que:

$$\frac{\partial u_i'}{\partial t} + \overline{u_j}\frac{\partial \overline{u_i'}}{\partial x_j} + u_j' \frac{\partial \overline{u_i}}{\partial x_j} + u_j' \frac{\partial u_i'}{\partial x_j} - \frac{\partial \overline{u_i' u_j'}}{\partial x_j} = \delta_{i3} \left(\frac{\theta'}{\overline{\theta}} \right) g +$$

$$f \varepsilon_{ij3} u_j' - \frac{1}{\overline{\rho}} \frac{\partial p'}{\partial x_i} + \gamma \frac{\partial^2 u_i'}{\partial x_j^2}. \tag{A.7}$$

Quando multiplicada por $2u_i'$, a equação acima pode ser escrita como:

$$2u_i' \frac{\partial u_i'}{\partial t} + 2u_i' \overline{u_j} \frac{\partial \overline{u_i'}}{\partial x_j} + 2u_i' u_j' \frac{\partial \overline{u_i}}{\partial x_j} + 2u_i' u_j' \frac{\partial u_i'}{\partial x_j} - 2u_i' \frac{\partial \overline{u_i' u_j'}}{\partial x_j} = 2u_i' \delta_{i3} \left(\frac{\theta'}{\overline{\theta}} \right) g + 2u_i' f \varepsilon_{ij3} u_j' -$$

$$2u_i' \frac{1}{\overline{\rho}} \frac{\partial p'}{\partial x_i} + 2u_i' \gamma \frac{\partial^2 u_i'}{\partial x_j^2} \tag{A.8}$$

Através da regra do produto, sabemos que:

$$2u_i'\frac{\partial u_i'}{\partial t} = \frac{\partial u_i'^2}{\partial t}.$$

Então,

$$\frac{\partial u_i'^2}{\partial t} + \overline{u_j}\frac{\partial \overline{u_i'^2}}{\partial x_j} + 2u_i'u_j'\frac{\partial \overline{u_i}}{\partial x_j} + u_j'\frac{\partial u_i'^2}{\partial x_j} - 2u_i'\frac{\partial \overline{u_i'u_j'}}{\partial x_j} = 2u_i'\delta_{i3}\left(\frac{\theta'}{\overline{\theta}}\right)g +$$

$$2u_i'f\varepsilon_{ij3}u_j' - 2u_i'\frac{1}{\overline{\rho}}\frac{\partial p'}{\partial x_i} + 2u_i'\gamma\frac{\partial^2 u_i'}{\partial x_j^2}. \tag{A.9}$$

Tomando a média de Reynolds e considerando que $\overline{u_i'} = 0$, temos que:

$$\frac{\partial \overline{u_i'^2}}{\partial t} + \overline{u_j}\frac{\partial \overline{u_i'^2}}{\partial x_j} + 2\overline{u_i'u_j'}\frac{\partial \overline{u_i}}{\partial x_j} + \overline{u_j'\frac{u_i'^2}{\partial x_j}} = 2\delta_{i3}\frac{\overline{u_i'\theta'}}{\overline{\theta}}g + 2f\varepsilon_{ij3}\overline{u_j'u_i'} + 2\gamma\overline{u_i'\frac{\partial^2 u_i'}{\partial x_j^2}} - \frac{2}{\overline{\rho}}\overline{u_i'\frac{\partial p'}{\partial x_i}}. \tag{A.10}$$

Através da equação da continuidade, sabemos que $\overline{u_i'^2\frac{\partial u_j'}{\partial x_j}} = 0$, que pode ser somada na equação acima:

$$\frac{\partial \overline{u_i'^2}}{\partial t} + \overline{u_j}\frac{\partial \overline{u_i'^2}}{\partial x_j} + 2\overline{u_i'u_j'}\frac{\partial \overline{u_i}}{\partial x_j} + \overline{u_j'\frac{u_i'^2}{\partial x_j}} + \overline{u_i'^2\frac{\partial u_j'}{\partial x_j}} = 2\delta_{i3}\frac{\overline{u_i'\theta'}}{\overline{\theta}}g +$$

$$2f\varepsilon_{ij3}\overline{u_j'u_i'} + 2\gamma\overline{u_i'\frac{\partial^2 u_i'}{\partial x_j^2}} - \frac{2}{\overline{\rho}}\overline{u_i'\frac{\partial p'}{\partial x_i}}. \tag{A.11}$$

Através da regra da cadeia, sabe-se que:

$$\overline{u_j'\frac{u_i'^2}{\partial x_j}} + \overline{u_i'^2\frac{\partial u_j'}{\partial x_j}} = \frac{\partial\left(\overline{u_j'u_i'^2}\right)}{\partial x_j}.$$

Então, a equação A.11 pode ser reescrita como:

$$\frac{\partial \overline{u_i'^2}}{\partial t} + \overline{u_j}\frac{\partial \overline{u_i'^2}}{\partial x_j} + 2\overline{u_i'u_j'}\frac{\partial \overline{u_i}}{\partial x_j} + \frac{\partial\left(\overline{u_j'u_i'^2}\right)}{\partial x_j} = 2\delta_{i3}\frac{\overline{u_i'\theta'}}{\overline{\theta}}g + 2f\varepsilon_{ij3}\overline{u_j'u_i'}$$

$$-\frac{2}{\overline{\rho}}\overline{u_i'\frac{\partial p'}{\partial x_i}} + 2\gamma\overline{u_i'\frac{\partial^2 u_i'}{\partial x_j^2}}. \tag{A.12}$$

Analisaremos separadamente os 3 últimos termos da equação acima, para o primeiro deles:

$$2f\varepsilon_{ij3}\overline{u_j'u_i'} = 2f\overline{u_1'u_2'} - 2f\overline{u_2'u_1'} = 2f\overline{u_1'u_2'} - 2f\overline{u_1'u_2'} = 0. \tag{A.13}$$

Para o próximo termo

$$-\frac{2}{\overline{\rho}}\overline{u_i'\frac{\partial p'}{\partial x_i}} = -\frac{2}{\overline{\rho}}\frac{\partial \overline{u_i'p'}}{\partial x_i} + 2\overline{\frac{p'}{\overline{\rho}}\left[\frac{\partial u_i'}{\partial x_i}\right]}, \tag{A.14}$$

sabemos que $\frac{\partial u_i'}{\partial x_i} = 0$, então

$$-\frac{2}{\overline{\rho}}\overline{u_i'\frac{\partial p'}{\partial x_i}} = -\frac{2}{\overline{\rho}}\frac{\partial \overline{u_i'p'}}{\partial x_i}. \tag{A.15}$$

Para o último termo,

$$\frac{\partial^2\overline{(u_i')}}{\partial x_j^2} = 2\overline{\left(\frac{\partial u_i'}{\partial x_j}\right)^2} + \overline{u_i'\frac{\partial^2 u_i'}{\partial x_j^2}}. \tag{A.16}$$

Então,

$$2\gamma\overline{u_i'\frac{\partial^2 u_i'}{\partial x_j^2}} = \frac{\partial^2\overline{(u_i')}}{\partial x_j^2} - 2\gamma\overline{\left(\frac{\partial u_i'}{\partial x_j}\right)^2}, \tag{A.17}$$

onde o primeiro termo representa a difusão molecular da variância de velociadade que é da ordem de 10^{-11} e 10^{-7}, que pode ser neglicenciado em relação ao segundo termo,

$$2\gamma\overline{u_i'\frac{\partial^2 u_i'}{\partial x_j^2}} \approx -2\gamma\overline{\left(\frac{\partial u_i'}{\partial x_j}\right)^2}. \tag{A.18}$$

A dissipação viscosa é definido como

$$\varepsilon = \gamma\overline{\left(\frac{\partial u'}{\partial x_j}\right)^2}. \tag{A.19}$$

Portanto, a equação A.12 pode ser aproximada por:

$$\frac{\partial\overline{u_i'^2}}{\partial t} = -\overline{u_j}\frac{\partial\overline{u_i'^2}}{\partial x_j} + 2\delta_{i3}\frac{\left(\overline{u_i'\theta'}\right)}{\overline{\theta}} - 2\overline{u_i'u_j'}\frac{\partial\overline{u_i}}{\partial x_j} - \frac{\partial\left(\overline{u_j'u_i'^2}\right)}{\partial x_j} - \frac{2}{\overline{\rho}}\frac{\partial\left(\overline{u_i'p'}\right)}{\partial x_i} - 2\varepsilon \tag{A.20}$$

A energia cinética turbulenta é definida como:

$$\overline{e} = \frac{1}{2}\left(\overline{u'^2} + \overline{v'^2} + \overline{w'^2}\right), \tag{A.21}$$

a equação prognóstica para energia cinética turbulenta:

$$\frac{\partial\overline{e}}{\partial t} = \frac{1}{2}\left(\frac{\partial\overline{u'^2}}{\partial t} + \frac{\partial\overline{v'^2}}{\partial t} + \frac{\partial\overline{w'^2}}{\partial t}\right). \tag{A.22}$$

Sabemos que i=1,2,3 correspondem respectivamente as componentes u,v e w do vento, então

$$\frac{\partial\overline{e}}{\partial t} = -\overline{u_j}\frac{\partial\overline{e}}{\partial x_j} + \delta_{i3}\frac{g}{\overline{\theta}}\overline{u_i'\theta'} - \overline{u_i'u_j'}\frac{\partial\overline{u_i}}{\partial x_j} - \frac{\partial\overline{u_j'e}}{\partial x_j} - \frac{1}{\overline{\rho}}\frac{\partial\overline{u_i'p'}}{\partial x_i} - \varepsilon \tag{A.23}$$

Considerando homogeneidade horizontal, a equação prognóstica para ECT pode ser escrita como:

$$\frac{\partial \overline{e}}{\partial t} = -\overline{u'w'}\frac{\partial \overline{u}}{\partial z} - \overline{v'w'}\frac{\partial \overline{v}}{\partial z} + \frac{g}{\overline{\theta}}\overline{w'\theta'} - \frac{\partial \overline{ew'}}{\partial z} - \frac{1}{\overline{\rho}}\frac{\partial \overline{w'p'}}{\partial z} - \varepsilon. \tag{A.24}$$

ANEXO B – FLUXO DE CALOR SENSÍVEL

A derivada parcial de $\overline{w'\theta'}$ em relação ao tempo, pode ser escrita como:

$$\frac{\partial \overline{w'\theta'}}{\partial t} = \overline{\theta' \frac{\partial w'}{\partial t}} + \overline{w' \frac{\partial \theta'}{\partial t}}. \tag{B.1}$$

A partir da decomposição de Reynolds, temos que:

$$\frac{\partial \theta'}{\partial t} = \frac{\partial \theta}{\partial t} - \frac{\partial \overline{\theta}}{\partial t}. \tag{B.2}$$

A equação associada a conservação da energia térmica pode ser escrita como:

$$\frac{\partial \theta}{\partial t} + u_j \frac{\partial \theta}{\partial x_j} = \nu_\theta \frac{\partial^2 \theta}{\partial x_j^2}, \tag{B.3}$$

quando os termos de divergência de radiação e o termo de calor latente são desprezados. A equação acima pode ser escrita como:

$$\frac{\partial \theta}{\partial t} = -u\frac{\partial \theta}{\partial x} - v\frac{\partial \theta}{\partial y} - w\frac{\partial \theta}{\partial z} + \nu_\theta \frac{\partial^2 \theta}{\partial x_j^2} \tag{B.4}$$

Lembrando que

$$u = \overline{u} + u',\ v = \overline{v} + v',\ w = w' \ e\ \theta = \overline{\theta} + \theta'.$$

Logo, a equação B.4 pode ser escrita como:

$$\frac{\partial \theta}{\partial t} = -(\overline{u} + u')\frac{\partial (\overline{\theta} + \theta')}{\partial x} - (\overline{v} + v')\frac{\partial (\overline{\theta} + \theta')}{\partial y} - w'\frac{\partial (\overline{\theta} + \theta')}{\partial z} +$$

$$\nu_\theta \frac{\partial^2 (\overline{\theta} + \theta')}{\partial x^2} + \nu_\theta \frac{\partial^2 (\overline{\theta} + \theta')}{\partial y^2} + \nu_\theta \frac{\partial^2 (\overline{\theta} + \theta')}{\partial z^2}, \tag{B.5}$$

que pode ser reescrito como:

$$\frac{\partial \theta}{\partial t} = -\overline{u}\frac{\partial \overline{\theta}}{\partial x} - \overline{u}\frac{\partial \theta'}{\partial x} - u'\frac{\partial \overline{\theta}}{\partial x} - u'\frac{\partial \theta'}{\partial x} - \overline{v}\frac{\partial \overline{\theta}}{\partial x} - \overline{v}\frac{\partial \theta'}{\partial x} - v'\frac{\partial \overline{\theta}}{\partial x} - v'\frac{\partial \theta'}{\partial x} - w'\frac{\partial \theta'}{\partial z} - w'\frac{\partial \overline{\theta}}{\partial z}$$

$$\nu_\theta \frac{\partial^2 \overline{\theta}}{\partial x^2} + \nu_\theta \frac{\partial^2 \theta'}{\partial x^2} + \nu_\theta \frac{\partial^2 \overline{\theta}}{\partial y^2} + \nu_\theta \frac{\partial^2 \overline{\theta}}{\partial y^2} + \nu_\theta \frac{\partial^2 \theta'}{\partial y^2} + \nu_\theta \frac{\partial^2 \overline{\theta}}{\partial z^2} + \nu_\theta \frac{\partial^2 \theta'}{\partial z^2} \tag{B.6}$$

Podemos adicionar $-\theta' \frac{\partial u'}{\partial x} - \theta' \frac{\partial v'}{\partial y} - \theta' \frac{\partial w'}{\partial z} = 0$ a equação acima sem altera-lá. Logo,

$$\frac{\partial \theta}{\partial t} = -\overline{u}\frac{\partial \overline{\theta}}{\partial x} - \overline{u}\frac{\partial \theta'}{\partial x} - u'\frac{\partial \overline{\theta}}{\partial x} - u'\frac{\partial \theta'}{\partial x} - \overline{v}\frac{\partial \overline{\theta}}{\partial x} - \overline{v}\frac{\partial \theta'}{\partial x} - v'\frac{\partial \overline{\theta}}{\partial x} - v'\frac{\partial \theta'}{\partial x} - w'\frac{\partial \theta'}{\partial z} - w'\frac{\partial \overline{\theta}}{\partial z} -$$

$$\theta' \frac{\partial u'}{\partial x} - \theta' \frac{\partial v'}{\partial y} - \theta' \frac{\partial w'}{\partial z} + \nu_\theta \frac{\partial^2 \overline{\theta}}{\partial x^2} + \nu_\theta \frac{\partial^2 \theta'}{\partial x^2} + \nu_\theta \frac{\partial^2 \overline{\theta}}{\partial y^2} + \nu_\theta \frac{\partial^2 \overline{\theta}}{\partial y^2} + \nu_\theta \frac{\partial^2 \overline{\theta}}{\partial z^2} + \nu_\theta \frac{\partial^2 \theta'}{\partial z^2}. \quad \text{(B.7)}$$

Aplicando a regra do produto, a equação acima pode ser reescrita como:

$$\frac{\partial \theta}{\partial t} = -\overline{u}\frac{\partial \overline{\theta}}{\partial x} - \overline{u}\frac{\partial \theta'}{\partial x} - u'\frac{\partial \overline{\theta}}{\partial x} - \overline{v}\frac{\partial \overline{\theta}}{\partial x} - \overline{v}\frac{\partial \theta'}{\partial x} - v'\frac{\partial \overline{\theta}}{\partial x} - w'\frac{\partial \overline{\theta}}{\partial z} - \frac{\partial u'\theta'}{\partial x} - \frac{\partial v'\theta'}{\partial y} - \frac{\partial w'\theta'}{\partial z} +$$

$$\nu_\theta \frac{\partial^2 \overline{\theta}}{\partial x^2} + \nu_\theta \frac{\partial^2 \theta'}{\partial x^2} + \nu_\theta \frac{\partial^2 \overline{\theta}}{\partial y^2} + \nu_\theta \frac{\partial^2 \overline{\theta}}{\partial y^2} + \nu_\theta \frac{\partial^2 \overline{\theta}}{\partial z^2} + \nu_\theta \frac{\partial^2 \theta'}{\partial z^2}. \quad \text{(B.8)}$$

Tomando média de Reynolds na equação acima, obtém-se:

$$\frac{\partial \overline{\theta}}{\partial t} = -\overline{u}\frac{\partial \overline{\theta}}{\partial x} - \overline{v}\frac{\partial \overline{\theta}}{\partial y} - \frac{\partial \overline{u'\theta'}}{\partial x} - \frac{\partial \overline{v'\theta'}}{\partial y} - \frac{\partial \overline{w'\theta'}}{\partial z} + \nu_\theta \frac{\partial^2 \overline{\theta}}{\partial x^2} + \nu_\theta \frac{\partial^2 \overline{\theta}}{\partial y^2} + \nu_\theta \frac{\partial^2 \overline{\theta}}{\partial z^2}. \quad \text{(B.9)}$$

Lembrando que,

$$\frac{\partial \theta'}{\partial t} = \frac{\partial \theta}{\partial t} - \frac{\partial \overline{\theta}}{\partial t}, \quad \text{(B.10)}$$

temos que:

$$\frac{\partial \theta'}{\partial t} = -\overline{u}\frac{\partial \overline{\theta}}{\partial x} - \overline{u}\frac{\partial \theta'}{\partial x} - u'\frac{\partial \overline{\theta}}{\partial x} - \overline{v}\frac{\partial \overline{\theta}}{\partial x} - \overline{v}\frac{\partial \theta'}{\partial x} - v'\frac{\partial \overline{\theta}}{\partial x} - w'\frac{\partial \overline{\theta}}{\partial z} - \frac{\partial u'\theta'}{\partial x} - \frac{\partial v'\theta'}{\partial y} - \frac{\partial w'\theta'}{\partial z} -$$

$$\left(-\overline{u}\frac{\partial \overline{\theta}}{\partial x} - \overline{v}\frac{\partial \overline{\theta}}{\partial y} - \frac{\partial \overline{u'\theta'}}{\partial x} - \frac{\partial \overline{v'\theta'}}{\partial y} - \frac{\partial \overline{w'\theta'}}{\partial z}\right) + \nu_\theta \frac{\partial^2 \theta'}{\partial x^2} + \nu_\theta \frac{\partial^2 \theta'}{\partial y^2} + \nu_\theta \frac{\partial^2 \theta'}{\partial z^2}, \quad \text{(B.11)}$$

que pode ser escrita como:

$$\frac{\partial \theta'}{\partial t} = -\overline{u}\frac{\partial \theta'}{\partial x} - u'\frac{\partial \overline{\theta}}{\partial x} - \overline{v}\frac{\partial \theta'}{\partial x} - v'\frac{\partial \overline{\theta}}{\partial x} - w'\frac{\partial \overline{\theta}}{\partial z} - \frac{\partial u'\theta'}{\partial x} - \frac{\partial v'\theta'}{\partial y} - \frac{\partial w'\theta'}{\partial z} + \frac{\partial \overline{u'\theta'}}{\partial x} + \frac{\partial \overline{v'\theta'}}{\partial y} + \frac{\partial \overline{w'\theta'}}{\partial z}$$

$$+\nu_\theta \frac{\partial^2 \theta'}{\partial x^2} + \nu_\theta \frac{\partial^2 \theta'}{\partial y^2} + \nu_\theta \frac{\partial^2 \theta'}{\partial z^2}. \quad \text{(B.12)}$$

Sabemos também que

$$\frac{\partial w'}{\partial t} = \frac{\theta'}{\overline{\theta}} g - \frac{1}{\overline{\rho}} \frac{\partial p'}{\partial z}, \quad \text{(B.13)}$$

multiplicando por θ', temos que:

$$\theta' \frac{\partial w'}{\partial t} = \frac{\theta'^2}{\overline{\theta}} g - \frac{\theta'}{\overline{\rho}} \frac{\partial p'}{\partial z}. \quad \text{(B.14)}$$

Tomando a média de Reynolds da equação acima, obtém-se que:

$$\overline{\theta' \frac{\partial w'}{\partial t}} = \frac{\overline{\theta'^2}}{\overline{\theta}} g - \overline{\frac{\theta'}{\overline{\rho}} \frac{\partial p'}{\partial z}} \tag{B.15}$$

Multiplicando a equação B.12 por w',

$$w' \frac{\partial \theta'}{\partial t} = w' \left(-\overline{u} \frac{\partial \theta'}{\partial x} - u' \frac{\partial \overline{\theta}}{\partial x} - \overline{v} \frac{\partial \theta'}{\partial z} - v' \frac{\partial \overline{\theta}}{\partial z} - w' \frac{\partial \overline{\theta}}{\partial z} - \frac{\partial u'\theta'}{\partial x} - \frac{\partial v'\theta'}{\partial y} - \frac{\partial w'\theta'}{\partial z} \right) +$$

$$w' \left(\frac{\partial \overline{u'\theta}}{\partial x} + \frac{\partial \overline{v'\theta}}{\partial y} + \frac{\partial \overline{w'\theta}}{\partial z} \right) + w' \left(\nu_\theta \frac{\partial^2 \theta'}{\partial x^2} + \nu_\theta \frac{\partial^2 \theta'}{\partial y^2} + \nu_\theta \frac{\partial^2 \theta'}{\partial z^2}. \right) \tag{B.16}$$

Subtraindo $w'\theta' \left(\frac{\partial u'}{\partial x} + \frac{\partial v'}{\partial y} + \frac{\partial w'}{\partial z} \right) = 0$ da equação acima e tomando a média de Reynolds obtemos:

$$\overline{w' \frac{\partial \theta'}{\partial t}} = -\overline{u} \overline{w' \frac{\partial \theta'}{\partial x}} - \overline{u'w'} \frac{\partial \overline{\theta}}{\partial x} - \overline{v} \overline{w' \frac{\partial \theta'}{\partial y}} - \overline{v'w'} \frac{\partial \overline{\theta}}{\partial y} - \overline{w'^2} \frac{\partial \overline{\theta}}{\partial z} - \overline{w' \frac{\partial u'\theta'}{\partial x}} - \overline{w' \frac{\partial v'\theta'}{\partial y}} - \overline{w' \frac{\partial w'\theta'}{\partial z}} -$$

$$\overline{w'\theta' \left(\frac{\partial u'}{\partial x} + \frac{\partial v'}{\partial y} + \frac{\partial w'}{\partial z} \right)} + \overline{w' \left(\nu_\theta \frac{\partial^2 \theta'}{\partial x^2} + \nu_\theta \frac{\partial^2 \theta'}{\partial y^2} + \nu_\theta \frac{\partial^2 \theta'}{\partial z^2}. \right)} \tag{B.17}$$

Considerando a turbulência horizontalmente homogenia, a equação acima pode ser escrita como:

$$\overline{w' \frac{\partial \theta'}{\partial t}} = -\overline{w'^2} \frac{\partial \overline{\theta}}{\partial z} - \overline{w'\theta' \frac{\partial w'}{\partial z}} - \overline{w' \frac{\partial w'\theta'}{\partial z}} = -\overline{w'^2} \frac{\partial \overline{\theta}}{\partial z} - \overline{\frac{\partial w'w'\theta'}{\partial z}} + \overline{\nu_\theta w' \frac{\partial^2 \theta'}{\partial z^2}}, \tag{B.18}$$

simulações numéricas mostram que o último termo da equação acima é muitas ordens de grandezas menor que os demais termos da equação, podendo ser desprezado. Voltando a equação B.1, obtém-se que

$$\frac{\partial \overline{w'\theta'}}{\partial t} = \overline{\theta' \frac{\partial w'}{\partial t} + w' \frac{\partial \theta'}{\partial t}} = -\overline{w'^2} \frac{\partial \overline{\theta}}{\partial z} - \overline{\frac{\partial w'w'\theta'}{\partial z}} + \frac{\overline{\theta'^2}}{\overline{\theta}} g - \overline{\frac{\theta'}{\overline{\rho}} \frac{\partial p'}{\partial z}} \tag{B.19}$$

Portanto, a equação prognóstica para o fluxo de calor pode ser dada por:

$$\frac{\partial \overline{w'\theta'}}{\partial t} = -\overline{w'^2} \frac{\partial \overline{\theta}}{\partial z} + \frac{\overline{\theta'^2}}{\overline{\theta}} g - \overline{\frac{\partial w'w'\theta'}{\partial z}} - \overline{\frac{\theta'}{\overline{\rho}} \frac{\partial p'}{\partial z}}. \tag{B.20}$$

ANEXO C – VARIÂNCIA DE TEMPERATURA

Partindo da equação B.12,

$$\frac{\partial \theta'}{\partial t} = -\overline{u}\frac{\partial \theta'}{\partial x} - u'\frac{\partial \overline{\theta}}{\partial x} - \overline{v}\frac{\partial \theta'}{\partial x} - v'\frac{\partial \overline{\theta}}{\partial x} - w'\frac{\partial \overline{\theta}}{\partial z} - \frac{\partial u'\theta'}{\partial x} - \frac{\partial v'\theta'}{\partial y} - \frac{\partial w'\theta'}{\partial z} + \frac{\partial \overline{u'\theta'}}{\partial x} + \frac{\partial \overline{v'\theta'}}{\partial y} + \frac{\partial \overline{w'\theta'}}{\partial z} +$$

$$\nu_\theta \frac{\partial^2 \theta'}{\partial x^2} + \nu_\theta \frac{\partial^2 \theta'}{\partial y^2} + \nu_\theta \frac{\partial^2 \theta'}{\partial z^2}. \tag{C.1}$$

Sabemos que

$$\frac{\partial \theta'^2}{\partial t} = 2\theta' \frac{\partial \theta'}{\partial t} \tag{C.2}$$

então a equação C.1 pode ser substituída em C.2, obtendo:

$$\frac{\partial \theta'^2}{\partial t} = 2\theta' \left(-\overline{u}\frac{\partial \theta'}{\partial x} - u'\frac{\partial \overline{\theta}}{\partial x} - \overline{v}\frac{\partial \theta'}{\partial x} - v'\frac{\partial \overline{\theta}}{\partial x} - w'\frac{\partial \overline{\theta}}{\partial z} - \frac{\partial u'\theta'}{\partial x} - \frac{\partial v'\theta'}{\partial y} - \frac{\partial w'\theta'}{\partial z} \right) +$$

$$2\theta' \left(\frac{\partial \overline{u'\theta'}}{\partial x} + \frac{\partial \overline{v'\theta'}}{\partial y} + \frac{\partial \overline{w'\theta'}}{\partial z} + \nu_\theta \frac{\partial^2 \theta'}{\partial x^2} + \nu_\theta \frac{\partial^2 \theta'}{\partial y^2} + \nu_\theta \frac{\partial^2 \theta'}{\partial z^2} \right). \tag{C.3}$$

Pode ser somado $\theta'^2(\frac{\partial u'}{\partial x} + \frac{\partial v'}{\partial y} + \frac{\partial w'}{\partial z}) = 0$ à equação acima sem altera-lá, obtendo

$$\frac{\partial \theta'^2}{\partial t} = 2\theta' \left(-\overline{u}\frac{\partial \theta'}{\partial x} - u'\frac{\partial \overline{\theta}}{\partial x} - \overline{v}\frac{\partial \theta'}{\partial x} - v'\frac{\partial \overline{\theta}}{\partial x} - w'\frac{\partial \overline{\theta}}{\partial z} - \frac{\partial u'\theta'}{\partial x} - \frac{\partial v'\theta'}{\partial y} - \frac{\partial w'\theta'}{\partial z} \right) +$$

$$2\theta' \left(\frac{\partial \overline{u'\theta'}}{\partial x} + \frac{\partial \overline{v'\theta'}}{\partial y} + \frac{\partial \overline{w'\theta'}}{\partial z} + \nu_\theta \frac{\partial^2 \theta'}{\partial x^2} + \nu_\theta \frac{\partial^2 \theta'}{\partial y^2} + \nu_\theta \frac{\partial^2 \theta'}{\partial z^2} \right) +$$

$$\theta'^2 \left(\frac{\partial u'}{\partial x} + \frac{\partial v'}{\partial y} + \frac{\partial w'}{\partial z} \right) \tag{C.4}$$

tomando a média de Reynolds e considerando a turbulência horizontalmente homogênea, obtemos:

$$\frac{\partial \overline{\theta'^2}}{\partial t} = -2\overline{w'\theta'}\frac{\partial \overline{\theta}}{\partial z} - \frac{\partial \overline{w'\theta'^2}}{\partial z} + 2\nu_\theta \overline{\theta' \frac{\partial^2 \theta'}{\partial z^2}}. \tag{C.5}$$

considerando o termos de dissipação $2\nu_\theta \overline{\theta' \frac{\partial^2 \theta'}{\partial z^2}} = -\varepsilon_{\theta'^2}$. A equação prognóstica para variância de temperatura pode ser dada por:

$$\frac{\partial \overline{\theta'^2}}{\partial t} = -2\overline{w'\theta'}\frac{\partial \overline{\theta}}{\partial z} - \frac{\partial \overline{w'\theta'^2}}{\partial z} - \varepsilon_{\theta'^2}. \tag{C.6}$$

REFERÊNCIAS BIBLIOGRÁFICAS

ACEVEDO, O. C. et al. The influence of submeso processes on stable boundary layer similarity relationships. **Journal of the Atmospheric Sciences**, v. 71, n. 1, p. 207–225, 2014. Disponível em: <https://doi.org/10.1175/JAS-D-13-0131.1>.

____. Monitoring the micrometeorology of a coastal site next to a thermal power plant from the surface to 140 m. **Bulletin of the American Meteorological Society**, v. 99, n. 4, p. 725–738, 2018.

ACEVEDO, O. C.; FITZJARRALD, D. In the core of the night – effects of intermittent mixing on a horizontally heterogeneous surface. **Bound.-Layer Meteor.**, v. 106, p. 1–33, 2003.

ACEVEDO, O. C. et al. Contrasting structures between the decoupled and coupled states of the stable boundary layer. **Q.J.R. Meteorol. Soc.. doi: 10.1002/qj.269**, 2016.

____. The nocturnal boundary layer transition from weakly to very stable. part 1: Observations. **Quarterly Journal of the Royal Meteorological Society**, v. 0, n. ja, p. 16, 2019.

ARYA, P. S. **Introduction to micrometeorology**. [S.l.]: Elsevier, 2001. v. 79.

BAAS, P. et al. Transitions in the wintertime near-surface temperature inversion at dome c, antarctica. **Quarterly Journal of the Royal Meteorological Society**, Wiley Online Library, 2019.

BLACKADAR, A. High resolution models of the planetary boundary layer. **Adv Environ Sci Eng**, Gordon and Breach, v. 1, n. 1, p. 50–85, 1979.

BOU-ZEID, E. et al. On the role of return to isotropy in wall-bounded turbulent flows with buoyancy. **Journal of Fluid Mechanics**, Cambridge University Press, v. 856, p. 61–78, 2018.

BOUGEAULT, P.; LACARRERE, P. Parameterization of orography-induced turbulence in a mesobeta–scale model. **Monthly Weather Review**, v. 117, n. 8, p. 1872–1890, 1989. Disponível em: <https://doi.org/10.1175/1520-0493(1989)117<1872:POOITI>2.0.CO;2>.

BRETHERTON, C. S.; PARK, S. A new moist turbulence parameterization in the community atmosphere model. **Journal of Climate**, v. 22, n. 12, p. 3422–3448, 2009. Disponível em: <https://doi.org/10.1175/2008JCLI2556.1>.

COSTA, F. D. et al. A simplified model for intermittent turbulence in the nocturnal boundary layer. **Journal of the Atmospheric Sciences**, v. 68, n. 8, p. 1714–1729, 2011. Disponível em: <https://doi.org/10.1175/2011JAS3655.1>.

DEARDORFF, J. W. Three-dimensional numerical study of the height and mean structure of a heated planetary boundary layer. **Boundary-Layer Meteorology**, Springer, v. 7, n. 1, p. 81–106, 1974.

DIAS-JÚNIOR, C. Q. et al. Turbulence regimes in the stable boundary layer above and within the amazon forest. **Agricultural and forest meteorology**, Elsevier, v. 233, p. 122–132, 2017.

HOLTON, J. R. **An Introduction to Dynamic Meteorology. 4. ed.** [S.l.]: Elsevier Academic Press, 2004. 535 p.

HOOIJDONK, I. G. S. van et al. Shear capacity as prognostic for nocturnal boundary layer regimes. **J. Atmos. Sci.**, v. 72, n. 4, p. 1518–1532, 2015. Disponível em: <https://doi.org/10.1175/JAS-D-14-0140.1>.

JANJIć, Z. I. The step-mountain eta coordinate model: Further developments of the convection, viscous sublayer, and turbulence closure schemes. **Monthly Weather Review**, v. 122, n. 5, p. 927–945, 1994. Disponível em: <https://doi.org/10.1175/1520-0493(1994)122<0927:TSMECM>2.0.CO;2>.

LAN, C. et al. Distinct turbulence structures in stably stratified boundary layers with weak and strong surface shear. **Journal of Geophysical Research: Atmospheres**, Wiley Online Library, v. 123, n. 15, p. 7839–7854, 2018.

MAHRT, L. Nocturnal boundary-layer regimes. **Boundary-Layer Meteorology**, v. 88, n. 2, p. 255–278, Aug 1998. ISSN 1573-1472. Disponível em: <https://doi.org/10.1023/A:1001171313493>.

____. Stably stratified atmospheric boundary layers. **Annual Review of Fluid Mechanics**, v. 46, n. 1, p. 23–45, 2014. Disponível em: <https://doi.org/10.1146/annurev-fluid-010313-141354>.

MAHRT, L. et al. Non-stationary generation of weak turbulence for very stable and weak-wind conditions. **Boundary-Layer Meteorology**, v. 147, n. 2, p. 179–199, May 2013. ISSN 1573-1472. Disponível em: <https://doi.org/10.1007/s10546-012-9782-x>.

MALHI, Y. S. The significance of the dual solutions for heat fluxes measured by the temperature fluctuation method in stable conditions. **Boundary-Layer Meteorology**, v. 74, n. 4, p. 389–396, Jun 1995. ISSN 1573-1472. Disponível em: <https://doi.org/10.1007/BF00712379>.

MARONEZE, R. et al. Simulating the regime transition of the stable boundary layer using different simplified models. **Boundary-Layer Meteorology**, v. 170, n. 2, p. 305–321, Feb 2019. ISSN 1573-1472. Disponível em: <https://doi.org/10.1007/s10546-018-0401-3>.

MCNIDER, R. T. et al. Predictability of the stable atmospheric boundary layer. **Journal of the Atmospheric Sciences**, v. 52, n. 10, p. 1602–1614, 1995. Disponível em: <https://doi.org/10.1175/1520-0469(1995)052<1602:POTSAB>2.0.CO;2>.

MELLOR, G. L.; YAMADA, T. A hierarchy of turbulence closure models for planetary boundary layers. **J. Atmos. Sci.**, v. 31, n. 7, p. 1791–1806, 1974.

____. Development of a turbulence closure model for geophysical fluid problems. **Rev. Geophys.**, Wiley Online Library, v. 20, n. 4, p. 851–875, 1982.

MONAHAN, A. H. et al. Multiple regimes of wind, stratification, and turbulence in the stable boundary layer. **Journal of the Atmospheric Sciences**, v. 72, n. 8, p. 3178–3198, 2015. Disponível em: <https://doi.org/10.1175/JAS-D-14-0311.1>.

NAKANISH, M. Improvement of the mellor–yamada turbulence closure model based on large-eddy simulation data. **Boundary-Layer Meteorology**, v. 99, n. 3, p. 349–378, Jun 2001. ISSN 1573-1472. Disponível em: <https://doi.org/10.1023/A:1018915827400>.

NAKANISHI, M.; NIINO, H. An improved mellor–yamada level-3 model: Its numerical stability and application to a regional prediction of advection fog. **Boundary-Layer Meteorology**, v. 119, n. 2, p. 397–407, May 2006. ISSN 1573-1472. Disponível em: <https://doi.org/10.1007/s10546-005-9030-8>.

____. Development of an improved turbulence closure model for the atmospheric boundary layer. **Journal of the Meteorological Society of Japan. Ser. II**, v. 87, n. 5, p. 895–912, 2009.

OHYA, Y. Wind-tunnel study of atmospheric stable boundary layers over a rough surface. **Boundary-Layer Meteorology**, v. 98, n. 1, p. 57–82, Jan 2001. ISSN 1573-1472. Disponível em: <https://doi.org/10.1023/A:1018767829067>.

OHYA, Y.; NEFF, D. E.; MERONEY, R. N. Turbulence structure in a stratified boundary layer under stable conditions. **Boundary-Layer Meteorology**, v. 83, n. 1, p. 139–162, Apr 1997. ISSN 1573-1472. Disponível em: <https://doi.org/10.1023/A:1000205523873>.

PAHLOW, M.; PARLANGE, M. B.; PORTé-AGEL, F. On monin–obukhov similarity in the stable atmospheric boundary layer. **Boundary-Layer Meteorol.**, v. 99, p. 225–248, 2001.

PARDYJAK, E. R.; MONTI, P.; FERNANDO, H. J. S. Flux richardson number measurements in stable atmospheric shear flows. **Journal of Fluid Mechanics**, Cambridge University Press, v. 459, p. 307–316, 2002.

QUAN, L. H.; HU, F. Relationship between turbulent flux and variance in the urban canopy. **Meteorol. Atmos. Phys.**, v. 104, p. 29–36, 2009.

STULL, R. B. **An Introduction to Boundary Layer Meteorology**. Dordrecht, The Netherlands: Kluwer Academic Publishers, 1988. 666 p.

SUKORIANSKY, S.; GALPERIN, B.; PEROV, V. 'application of a new spectral theory of stably stratified turbulence to the atmospheric boundary layer over sea ice'. **Boundary-Layer Meteorology**, v. 117, n. 2, p. 231–257, Nov 2005. ISSN 1573-1472. Disponível em: <https://doi.org/10.1007/s10546-004-6848-4>.

SUN, J.; FRENCH, J. R. Air–sea interactions in light of new understanding of air–land interactions. **Journal of the Atmospheric Sciences**, v. 73, n. 10, p. 3931–3949, 2016. Disponível em: <https://doi.org/10.1175/JAS-D-15-0354.1>.

SUN, J. et al. Turbulence regimes and turbulence intermittency in the stable boundary layer during cases-99. **Journal of the Atmospheric Sciences**, v. 69, n. 1, p. 338–351, 2012. Disponível em: <https://doi.org/10.1175/JAS-D-11-082.1>.

VIGNON, E. et al. Stable boundary-layer regimes at dome c, antarctica: observation and analysis. **Quarterly Journal of the Royal Meteorological Society**, Wiley Online Library, v. 143, n. 704, p. 1241–1253, 2017.

WIEL, B. J. H. V. de et al. The minimum wind speed for sustainable turbulence in the nocturnal boundary layer. **Journal of the Atmospheric Sciences**, v. 69, n. 11, p. 3116–3127, 2012. Disponível em: <https://doi.org/10.1175/JAS-D-12-0107.1>.

____. Intermittent turbulence and oscillations in the stable boundary layer over land. part ii: A system dynamics approach. **Journal of the Atmospheric Sciences**, v. 59, n. 17, p. 2567–2581, 2002. Disponível em: <https://doi.org/10.1175/1520-0469(2002)059<2567:ITAOIT>2.0.CO;2>.

WIEL, B. J. H. Van de et al. Intermittent turbulence and oscillations in the stable boundary layer over land. part i: A bulk model. **Journal of the Atmospheric Sciences**, v. 59, n. 5, p. 942–958, 2002. Disponível em: <https://doi.org/10.1175/1520-0469(2002)059<0942:ITAOIT>2.0.CO;2>.

____. Regime transitions in near-surface temperature inversions: A conceptual model. **Journal of the Atmospheric Sciences**, v. 74, n. 4, p. 1057–1073, 2017. Disponível em: <https://doi.org/10.1175/JAS-D-16-0180.1>.

ZILITINKEVICH, S. S. et al. A hierarchy of energy- and flux-budget (efb) turbulence closure models for stably-stratified geophysical flows. **Boundary-Layer Meteorology**, v. 146, n. 3, p. 341–373, Mar 2013. ISSN 1573-1472. Disponível em: <https://doi.org/10.1007/s10546-012-9768-8>.